

Interfacial Fluid Dynamics in Porous Media

by

Bauyrzhan K. Primkulov

B.Sc. Petroleum Engineering, University of Alberta, 2011

M.Sc. Chemical Engineering, University of Alberta, 2015

Submitted to the Department of Civil and Environmental Engineering
in partial fulfillment of the requirements for the degree of

Doctor of Philosophy

at the

MASSACHUSETTS INSTITUTE OF TECHNOLOGY

May 2022

© Massachusetts Institute of Technology 2022. All rights reserved.

Author
Department of Civil and Environmental Engineering
May 13, 2022

Certified by
Ruben Juanes
Professor of Civil and Environmental Engineering
Professor of Earth, Atmospheric and Planetary Sciences
Thesis Supervisor

Accepted by
Colette L. Heald
Professor of Civil and Environmental Engineering
Chair, Graduate Program Committee

Interfacial Fluid Dynamics in Porous Media

by
Bauyrzhan K. Primkulov

Submitted to the Department of Civil and Environmental Engineering
on May 13, 2022, in partial fulfillment of the
requirements for the degree of
Doctor of Philosophy

Abstract

A beautiful array of patterns emerges when one fluid displaces another in porous media, a physical situation prevalent in many clean energy production and storage applications. These patterns can be reminiscent of dielectric breakdown, diffusion-limited growth of crystals, or percolation clusters in polymer gelation, depending on the relative affinity of the two fluids to the porous medium (wettability) and the balance of viscous and capillary forces. Examining this rich system at microscopic and macroscopic scales is at the center of this dissertation.

In Part I, we build computational models to capture macroscopic fluid-fluid displacement patterns in disordered porous media, which helps synthesize decades' worth of experimental observations. We draw parallels between electrical circuits and flow in porous media, where resistors model viscous effects and a combination of batteries and capacitors model capillary forces. This simple analogy, augmented with wettability-dependent pore-invasion mechanisms, allows capturing the rich dynamics of pattern formation within a single pore-network model and helps delineate the role of wettability. Finally, we explore intriguing features of self-organized criticality during fluid-fluid displacement in disordered porous media.

In Part II, we examine fluid displacement at a scale of a single capillary. We use lubrication theory to produce precise predictions of film evolution during spin-coating of capillary tubes—a technique one can use to fabricate capillaries with controlled surface properties. We then study the spontaneous imbibition of liquids in capillary tubes, where classical imbibition front slows with time. We propose a simple modification that renders imbibition constant-rate in capillary tubes and allows tuning of viscous dissipation; we use this system to characterize sources of dissipation during fluid-fluid displacement. We conclude Part II by revisiting the theory of moving contact lines over heterogeneous surfaces and rationalizing the transition from stick-slip to steady sliding.

The physical problems we investigate in this dissertation may prove helpful in addressing our current environmental challenges by inspiring physics-informed advances in CO₂ storage, electrolyzers and fuel cells, design of sustainable micromechanical devices and self-cleaning surfaces.

Thesis Supervisor: Ruben Juanes

Title: Professor of Civil and Environmental Engineering

Professor of Earth, Atmospheric and Planetary Sciences

Acknowledgments

When I look back on my journey in science so far, it is difficult to underestimate the importance of outstanding teachers and mentors I was fortunate to encounter along the way. Ruben has been one of the most significant influences on how and why I continue along the academic path. He taught me through his own example that you can be a successful scientist and remain kind to your students and colleagues. His humanity is apparent to anyone who interacted with him. As a mentor, he encourages ambitious intellectual challenges, he lifts you in your lows, and celebrates your successes more than his own. In the age when academia is more competitive than ever, it is very encouraging to have caring mentors like Ruben.

“Choose a mentor who would say your name in a room full of opportunities.” Ruben has been that person for me throughout my PhD studies. Through small but intentionally generous acts, he consistently lends the spotlight to his students. As a result, many of us have a sense of belonging in the scientific community by the time we graduate from the PhD program. It is not surprising that many of his students enjoy very successful academic careers. Thank you for everything, Ruben!

My sincere gratitude goes to Chris, John, and Lydia for the encouragement, advice, and mentorship. I also thank Juanes Group members (present and past), my teachers in Kazakhstan, mentors/friends/colleagues from University of Alberta, and MIT CEE support staff for our shared journey. I would not have made it this far without my family. Thank you!

Өмір – Бәйге

Өмір – бәйге, түскін балам жарысқа,
Жаныңды сал жүйріктерден қалыспа.
Мыңнан озып тұлпар шығу үшін сен
Ешкімде жоқ дүлей күшті сарыпта.

Жетер мәрең болсын мейлі алыста
Жет қалайда, қиындыққа қайыспа!
Жинақтаған өнер, білім, тәрбиен,
Үстем етсін мәртебеңді сайыста.

Қарсыласың мойндасын, мықты деп
Мықтылықтан туын биік тікті деп.
Ұмытпағын әр-бір шыққан биігің
Еңбекпен тер нәтижесі жемісті.

Жету үшін биік шыңға жарқыным
Мықтылардың оқы, үйрен бар сырын
Мен секілді шабандарды сүйреумен
Қысқа өмірдің сарп етпегін жартысын.

Мықтылармен жарысқа түс, бақ сына
Төреліктің туралығын-ақ сұра.
Жабылардан оңай озып кеттім деп,
Шын тұлпарлардан шаң қаппағын қапыда.

Үміт артып, жеңіс күтем мен сенен
Топты жарып озғаныңды көксегем
Бағындырып мен алмаған биікті
Мен жетпеген мұраттарға жет дер ем.

Адалдық пен шындық болсын ұраның
Топқа қостым, жолың болсын, шырағым!
Құрбан ата әруағы жар болып,
Жаратушым төксін саған шуағын!

Сен келгенде топтан озып бәйгеден
Мен мәреде сені күтіп тұрамын.

Contents

1	Introduction	15
I	Fluid-fluid displacement patterns in porous media	17
2	Quasi-static fluid-fluid displacement in porous media: invasion-percolation through a wetting transition	19
2.1	Introduction	19
2.2	Method	21
2.2.1	Burst event	23
2.2.2	Touch event	24
2.2.3	Overlap event	24
2.2.4	Drainage overlap event	24
2.2.5	Corner and capillary bridge events	25
2.2.6	Invasion algorithm	26
2.3	Results and discussion	27
2.3.1	Invasion front morphology through the wetting transition	27
2.3.2	Sensitivity of macroscopic invasion to local contact angle perturbations	28
2.3.3	Influence of drainage overlap and post spacing on cooperative pore filling	30
2.3.4	Three-dimensional effects: out-of-plane curvature	31
2.4	Conclusions	32
3	Signatures of fluid-fluid displacement in porous media: wettability, patterns, and pressures	35
3.1	Introduction	35
3.2	Moving capacitor model	37
3.3	Invasion patterns	39
3.4	Pressure signature	40
3.5	Conclusion	43
4	Wettability and Lenormand’s diagram	45
4.1	Introduction	45
4.2	Method	48
4.2.1	Pore-network construction	49
4.2.2	Single-phase flow	50
4.2.3	Two-phase flow: moving capacitors	50
4.2.4	Moving-capacitor model in strong imbibition	52
4.3	Principal flow regimes	53

4.3.1	Stable displacement	54
4.3.2	Viscous fingering	55
4.3.3	Invasion percolation	55
4.3.4	Cooperative pore filling	56
4.3.5	Corner flow	57
4.4	Crossover from viscous-dominated to capillary-dominated flow	58
4.5	Extending Lenormand's phase diagram	59
4.6	Conclusion	64
5	Avalanches in strong imbibition	65
5.1	Introduction	65
5.2	Pore-scale physics and intermittency	67
5.3	SOC signature in waiting time	68
5.4	SOC signature in avalanche size	68
5.5	Furuberg scaling	69
5.6	Furuberg scaling in strong imbibition	69
5.7	Discussion and conclusion	70
II	Moving fluid interfaces and contact lines	72
6	Spin coating of capillary tubes	73
6.1	Introduction	73
6.2	Experimental method	74
6.3	Theory	75
6.3.1	Inertial slug-flow	76
6.3.2	Viscous slug-flow	77
6.3.3	Film thinning	77
6.4	Self-similar solution of film thinning	79
6.5	Rayleigh-Plateau instability	80
6.6	Coating with curable polymers	82
6.7	Conclusion	83
7	Characterizing dissipation in fluid–fluid displacement using constant-rate spontaneous imbibition	85
7.1	Introduction	85
7.2	Experimental method	86
7.3	Theory	87
7.4	Contact-line dissipation	88
7.5	Conclusion	90
8	Moving contact lines over heterogeneous surfaces: from stick–slip to steady sliding	93
8.1	Introduction	93
8.2	Physical setup and governing equations	94
8.3	Results and Discussion	97
8.3.1	Constant-force analog	97
8.3.2	Constant-rate analog	97
8.3.3	Energy dissipation	99

8.3.4	Phase-field simulations	100
8.4	Conclusions	100
9	Summary	103
A	Corner meniscus and characteristics of displacement patterns	105
A.1	Corner meniscus	105
A.1.1	Corner meniscus shape	105
A.1.2	Corner meniscus growth	107
A.2	Measuring fractal dimension	108
A.3	Measuring finger width	108
B	Corner-flow parameter and pore-scale disorder	111
B.1	Fitting parameter for corner flow	111
B.2	Impact of pore-scale disorder on displacement patterns	112
C	Experimental and computational protocols for strong imbibition	117
C.1	Experimental details	117
C.2	Simulation protocol	118
C.3	Influence of trapping on the displacement statistics	118
D	Spin-coater speed and experimental details	121
D.1	Spin-coater speed and experimental data	121
D.1.1	Deviation of 50 cSt oil from more viscous oils in figure 2b	121
D.1.2	Estimating film thickness variation in comparison to Taylor’s coating method	121
E	Spontaneous imbibition experiments and classical imbibition	123
E.1	Details of the experimental setup	123
E.2	Generalized Cox equation	123
E.3	Classical imbibition	124
F	Contact-line dynamics over imperfect surfaces	127
F.1	Experimental details	127
F.2	Force-velocity relations	127
F.2.1	Constant-force displacement	127
F.2.2	Constant-rate displacement	130
F.2.3	Total force	134
F.3	Phase-field simulations of the viscous slug displacement at a constant rate	136

List of Figures

2-1	Invasion front configuration and pore-scale invasion events.	23
2-2	Overlap trapping.	25
2-3	Pore geometry: post diameter and pore throat size histograms	27
2-4	Displacement patterns, from $\theta = 160^\circ$ to $\theta = 10^\circ$	28
2-5	Cooperative pore filling and fractal dimension plots.	29
2-6	Percentage of cooperative pore filling events for posts spaced out by a factor of λ from the original post geometry.	31
2-7	Figure shows how post heights alter the shapes of the invasion fronts.	32
3-1	Schematic diagram of in-plane and out-of-plane curvatures within the flow cell.	36
3-2	Phase diagram of the invading fluid morphology at breakthrough.	38
3-3	Temporal evolution of the injection pressure.	41
3-4	Pore-scale perspective for the scaling of pressure fluctuations.	42
4-1	Lenormand's phase diagram for a nonwetting fluid displacing a wetting fluid in a porous medium.	46
4-2	Schematic of flow through a porous medium and the analog electrical circuit.	49
4-3	Burst, touch, overlap, and corner-flow events.	51
4-4	Stable displacement in the benchmark geometry for $Ca = 10^{-1}$, $M = 10^3$, and $\theta = 170^\circ$	54
4-5	Viscous fingering in the benchmark geometry for $Ca = 10^{-1}$, $M = 10^{-3}$, and $\theta = 170^\circ$	55
4-6	Invasion percolation in the benchmark geometry for $Ca = 10^{-7}$, $M = 1$, and $\theta = 170^\circ$	56
4-7	Cooperative pore filling in the benchmark geometry for $Ca = 10^{-7}$, $M = 1$, and $\theta = 46^\circ$	57
4-8	Corner flow in the benchmark geometry for $Ca = 5 \cdot 10^{-7}$, $M = 0.1$, and $\theta = 4^\circ$	58
4-9	Histogram of the distance (Δs) between consecutive pore-invasion events.	59
4-10	Evolution of D_f in M - Ca - θ space.	60
4-11	Viscous-dominated and capillary-dominated regions of M - Ca - θ space.	60
4-12	Extended Lenormand diagram.	62
4-13	A sketch of Lenormand's phase diagram.	63
5-1	Temporal evolution of slow fluid-fluid displacement.	66
5-2	Scale-free distribution of waiting times and avalanches in the strong imbibition experiment.	68
5-3	Verification of Eq. (5.1) in slow strong imbibition.	71
6-1	Diagram of the computer fan repurposed as a spin-coater.	74
6-2	Exponential change in the slug-center position x_c with time.	75
6-3	Temporal evolution of the deposited film thickness long after the slug-motion.	75
6-4	Film thickness profiles at various times.	78

6-5	Rayleigh-Plateau instability of 500 cSt silicone oil films.	81
6-6	Capillary imbibition of silicone oil in two horizontal capillary tubes coated with NOA81.	82
7-1	Experimental snapshots of the classical and constant-rate spontaneous imbibition.	86
7-2	Constant-rate imbibition experiments for a range of viscosities and slug lengths.	87
7-3	Phase diagram of forced, rate-controlled imbibition of viscous oil slugs.	89
8-1	Viscous slug schematic and experimental transition from stick–slip to steady sliding	94
8-2	Mechanical analog of the spring oscillator model	96
8-3	Quasi-static motion of the pendulum in the constant-rate displacement	98
8-4	Fraction of the total dissipation Ξ due to stick–slip motion	99
A-1	Shape of the corner meniscus around the post.	106
A-2	Interface shape of a corner meniscus outside a post.	107
A-3	Laplace pressure for a growing corner meniscus.	108
A-4	Fractal dimensions calculated with the box-counting method.	109
A-5	Ratio of the invading pattern finger width to mean pore size.	110
B-1	Transition to corner-flow regime as a function of post height h	112
B-2	Experimental image sequences of corner flow taken from Zhao <i>et al.</i> (2016).	113
B-3	Viscous-fingering simulations on a regular triangular lattice.	114
B-4	Capillary-dominated simulations on a regular triangular lattice.	115
B-5	Quasi-static strong imbibition simulations on a triangular post lattice.	115
C-1	Optical measurements of water-oil contact angle on flat substrates.	117
C-2	Post-size distribution for (a) the benchmark geometry and (b) micromodel with regular triangular lattice and random post-size assignment.	118
C-3	Verification of Eq. (5.1) using invasion percolation model on a square lattice.	119
E-1	PIV measurements of the velocity profile in spontaneously moving slug.	124
E-2	Evolution of $z(t)$ during classical imbibition of 50 cSt silicon oil.	125
F-1	Examples of stick–slip motion of contact lines	128
F-2	Crystalline structures growing on cured NOA81 surfaces	128
F-3	Evolution of α_c in Eq. 8.14 for $\omega_0 \in (B, 2B]$	129
F-4	Diminishing amplitude of oscillations with ω_0/B in constant force setting	130
F-5	Adiabatic approximation leading up to Eq. 8.14	130
F-6	Quasi-static vs. dynamic force integral	131
F-7	Solution to equation F.18	133
F-8	Scaling of force-velocity terms	133
F-9	Evolution of $\tilde{\alpha}_c$ in Eq. 8.17 for $\omega_u/B \in [10^{-3}, 10^2]$	134
F-10	Change in the amplitude of oscillations	135
F-11	Total force scaling	135
F-12	Phase-field simulation of constant-rate fluid-fluid displacement	136

List of Tables

5.1	Critical exponents for invasion percolation.	70
5.2	Result of data collapse analogous to Fig. 5-3c for simulations on the benchmark geometry.	70

Chapter 1

Introduction

One fluid displacing another inside porous environments is a very rich problem where experiments often produce compelling visual patterns, theory offers clever approximations and analogies, and computation allows probing conditions well outside the experimental and analytical reach. Evidence of that is, hopefully, sprinkled throughout this dissertation.

The first part of my thesis examines fluid-fluid displacement patterns at the scale of hundreds or thousands of pores. These patterns emerge in many practical applications like CO₂ storage (Szulczewski *et al.*, 2012), fuel cells and electrolyzers (Anderson *et al.*, 2010), porous chemical reactor beds (Hill, 1952), paper-based medical diagnostic devices (Yetisen *et al.*, 2013), and hydrocarbon recovery (Lake, 1989; Blunt, 2017).

In Chapter 2, we explore fluid-fluid displacement in a quasi-static setting and present an invasion-percolation algorithm that accounts for the wettability of the system, which is the relative affinity of the two fluids to the porous medium. Here, similarly to cellular automata, we define several pore-scale displacement mechanisms, which determine the overall macroscopic displacement patterns. The relative frequency of these pore-scale events, and therefore fluid-front morphology, are strongly linked to the system’s wettability. The resulting model extends the traditional range of invasion-percolation algorithms to all wettability conditions. This chapter appeared as a research article in *Physical Review Fluids* (Primkulov *et al.*, 2018).

In Chapter 3, we extend our fluid-fluid displacement model to arbitrary flow rates. We build an analogy between flow in porous media and currents in electrical circuits. In particular, we recognize that fluid-fluid interfaces in pore spaces act analogously to capacitors: they build Laplace pressure (charge) until pore-invasion events (dielectric breakdown) occur. However, unlike electric circuits, our analog allows the movement of these capacitors to new locations after a dielectric breakdown. This approach reproduces the rich physics of fluid-fluid displacement observed in microfluidic experiments. This chapter appeared as a rapid communication in *Journal of Fluid Mechanics* (Primkulov *et al.*, 2019).

In Chapter 4, we utilize our model’s low computational cost and add a wettability axis to the seminal phase diagram of Lenormand (Lenormand *et al.*, 1988). Lenormand’s diagram has historically been the primary tool for communicating the physics of fluid-fluid displacement in porous media. The original diagram delineated the displacement dynamics through two dimensionless groups: (i) the capillary number, or ratio of viscous to capillary forces, and (ii) the ratio of fluid viscosities. As valuable as the diagram has been for researchers of porous media flow, the practitioners in the field have been aware of wettability-induced deviations from displacement patterns of the original diagram for as long as the diagram existed (Stokes *et al.*, 1986). The first glance of Lenormand’s diagram with the wettability axis we show in this chapter (and the corresponding

paper) systematizes decades of experimental and numerical results on pattern formation during fluid-fluid displacement in porous media. This chapter appeared as a research article in *Journal of Fluid Mechanics* (Primkulov *et al.*, 2021).

In Chapter 5, we conclude the first part of this thesis by exploring the self-organized criticality (SOC) features of slow capillary-dominated invasion of a strongly wetting fluid. The displacement evolves through avalanches, where bursts of rapid coating of post clusters are separated by periods of apparent inactivity of the displacement front. We demonstrate with experiments and numerical simulations that many SOC features thought to be exclusive to non-wetting displacement carry over to strongly-wetting conditions, despite their marked differences in pore-scale mechanisms. This chapter appeared as a research article in *Communications Physics* (Primkulov *et al.*, 2022).

The second part of the thesis targets the physics of fluid displacement at the scale of a single pore, conceptualized as a single capillary tube. Here, the intersection of the fluid-fluid interface with the solid (i.e., moving contact line) offers complex dynamics that are not yet fully understood. Moving contact lines are relevant to many practical applications like industrial coating of solids (Scriven, 1988), design of self-cleaning surfaces (Richard & Quéré, 1999; Aussillous & Quéré, 2001), and fabrication of micro-mechanical devices (Zimmermann *et al.*, 2007).

In Chapter 6, we develop a spin coating technique for capillary tubes. We repurpose a computer fan as a spin-coating device with the aid of 3D printing. This device houses capillary tubes partially filled with a liquid polymer; axisymmetric rotation of the device expels most of the liquid, leaving a uniform layer of polymer on the inner walls of the tubes. We use theoretical arguments to accurately predict the film thickness evolution during the spin-coating process, demonstrating that one can easily tune the coating layer thickness down to a micrometer scale. This chapter appeared as a research article in *Journal of Fluid Mechanics* (Primkulov *et al.*, 2020b).

In Chapter 7, we introduce constant-rate spontaneous imbibition in capillary tubes. Exposing one end of a capillary tube to an oil reservoir results in spontaneous wetting of the tube, where the fluid front slows down as it gets further into the tube, following $z \sim t^{1/2}$ Lucas-Washburn scaling (Lucas, 1918; Washburn, 1921). One can achieve $z \sim t$ scaling instead by placing a high-viscosity oil slug into the tube and then exposing the same end to reservoir of water. We use this setup to show that in some cases, most of the energy dissipation occurs very close to the contact line. This chapter appeared in *Physical Review Letters* (Primkulov *et al.*, 2020b).

Finally, in Chapter 8, we revisit the theoretical arguments of Raphaël & De Gennes (1989); Joanny & Robbins (1990) on moving contact lines over heterogeneous surfaces. We extend their analysis to higher displacement rates, away from the depinning limit. We demonstrate that one should expect the transition from stick-slip motion to steady sliding of the contact line at high displacement rates, where the amplitude of contact-line oscillations dampens linearly with velocity and applied force. We show that the oscillatory motion of contact lines can be responsible for the majority of energy dissipation during slow fluid-fluid displacement on heterogeneous surfaces with strong pinning. This chapter has been submitted for publication as a research article.

Part I

Fluid-fluid displacement patterns in porous media

Chapter 2

Quasi-static fluid-fluid displacement in porous media: invasion-percolation through a wetting transition

This chapter has been published in [Primkulov et al. \(2018\)](#).

2.1 Introduction

Fluid-fluid displacement in porous media is a rich phenomenon, where the interplay between wettability, pore-scale disorder, viscosity ratio of invading and defending fluids, and magnitude of viscous forces relative to that of capillary forces (defined by the capillary number, Ca) generates a wide spectrum of interface patterns. The study of the mechanisms behind these patterns is of relevance to many practical applications. For instance, in the limit of high capillary numbers, the displacement of high-viscosity fluid by a low-viscosity fluid develops a morphology akin to diffusion-limited aggregation ([Chen & Wilkinson, 1985](#); [Måløy et al., 1985](#); [Paterson, 1984](#)), and hence serves as an analog system to dielectric breakdown ([Niemeyer et al., 1984](#)), electrodeposition ([Meakin et al., 1989](#)), and propagation of forest fires ([Conti & Marconi, 2010](#)). Furthermore, both high and low capillary number displacement regimes have direct practical significance in soil remediation and chemical filters ([Hill, 1952](#)), fuel cell technology ([Anderson et al., 2010](#)), carbon sequestration ([Cinar et al., 2007](#)), oil recovery ([Lake, 1989](#)), and design of microfluidic devices ([Lee et al., 2017](#)).

For a given fluid pair, the wettability of the porous medium plays a fundamental role in defining the nature of the displacement both at pore ([Hoffman, 1975](#); [Levaché & Bartolo, 2014](#); [Zhao et al., 2018](#)) and macroscopic scales ([Stokes et al., 1986](#); [Trojer et al., 2015](#)). Wettability is often defined through the contact angle θ between the fluid-fluid interface and the solid. We adopt the convention that θ is measured from the invading phase, such that $\theta > 90^\circ$ corresponds to drainage, and $\theta < 90^\circ$ corresponds to imbibition. In the limit of low capillary number and strong drainage (i.e. strongly non-wetting invading fluid), the fluid-fluid interface advances through capillary fingering and forms a jagged interface that tends to trap defending fluid throughout the displacement ([Lenormand et al., 1983](#); [Lenormand & Zarcone, 1985](#); [Lenormand et al., 1988](#); [Chandler et al., 1982](#)). In weak imbibition (i.e. weakly wetting invading fluid), in contrast, the interface tends to move as a compact front ([Stokes et al., 1986](#); [Trojer et al., 2015](#); [Jung et al., 2016](#); [Singh et al., 2017](#)), where capillary forces work to flatten the interface through cooperative pore filling ([Cieplak & Robbins, 1988, 1990](#)). While the mechanisms of fluid-fluid displacement in drainage are fairly well explored, fluid-fluid displacement in imbibition continues to challenge our mathematical descriptions.

Patterned microfluidic devices offer a convenient way to visualize the fluid-fluid displacement in a controlled and repeatable environment. As a quasi-two-dimensional analog of natural porous media, these microfluidic devices are typically fabricated by generating a pattern of posts on a solid surface and confining it between two flat plates, allowing careful control of both pore geometry and wettability. Early microfluidic experiments (Chen & Wilkinson, 1985; Lenormand & Zarcone, 1985; Lenormand *et al.*, 1988, 1983) explored the interplay between viscous and capillary forces in drainage and weak imbibition, and their findings are in line with the theory (Saffman & Taylor, 1958; Chuoke *et al.*, 1959; Stokes *et al.*, 1986; Trojer *et al.*, 2015). Only recently has this body of work been extended to strong imbibition, where new displacement patterns emerge (Zhao *et al.*, 2016; Odier *et al.*, 2017).

Zhao *et al.* (2016) conducted a series of viscously unstable experiments on microfluidic devices with an irregular pattern of circular posts, where water displaced oil radially from the center of the flow cell at different injection rates and different contact angles between 150° (strong drainage) and 7° (strong imbibition). The authors reported a new wetting transition in the strong imbibition regime ($7^\circ < \theta < 45^\circ$): flow reverts from compact displacement to a corner-flow regime, where the invading fluid advances by preferentially coating the corners between the posts and top/bottom plates of the flow cell. Similar observations were recently reported on a regularly patterned microfluidic cell with square posts (Odier *et al.*, 2017). These new findings may have significant implications for physical modeling of the displacement processes with tunable wetting conditions.

Several computational approaches are available to model pore-scale fluid-fluid displacement. These include, in decreasing order of fidelity (and required computational power): (Meakin & Tartakovsky, 2009) (1) molecular dynamic simulations; (2) numerical solutions of the Navier-Stokes equations with interface and contact-line tracking; (3) lattice or dissipative particle dynamics based models; and (4) pore-network models. The first three approaches require a detailed description of the pore geometry, and are not yet practical for obtaining macroscopic invasion patterns. Pore-network models, on the other hand, rely on a simplified pore geometry and a simplified description of the flow, and are therefore less computationally demanding (Blunt, 2001). The geometric details as well as simplifying assumptions of the interface vary widely from one study to another (Holtzman & Segre, 2015; Holtzman, 2016; Blunt, 1998; Al-Gharbi & Blunt, 2005).

Two particular subclasses of pore-network models are of interest in reproducing the experimental observations of Zhao *et al.* (2016) in the limit of very low Ca: invasion-percolation algorithms (Chandler *et al.*, 1982; Lenormand *et al.*, 1988) and the quasi-static interface tracking method of Cieplak & Robbins (1988, 1990). Invasion-percolation algorithms are robust, but can only capture the invading interface morphology in strong drainage. The interface-tracking algorithm of Cieplak & Robbins (1988, 1990) is applicable to wettabilities from strong drainage to weak imbibition, although it is susceptible to the biases of user-defined conventions in injection pressure increments and scanning order of pore invasion mechanisms. Neither method extends to the corner-flow regime of strong imbibition.

Here, we implement an invasion-percolation algorithm that qualitatively reproduces fluid-fluid displacement morphologies for all wettabilities, from strong drainage to strong imbibition. By building on the work of Cieplak & Robbins (1988, 1990), we are able to explicitly calculate the critical pressures of pore-scale instabilities, including the instability events potentially responsible for the corner flow regime in strong imbibition (Zhao *et al.*, 2016). This new approach eliminates the need for user-assigned pressure increments, instead advancing the interface in the manner of invasion-percolation. Our quasi-static algorithm captures the fluid-fluid displacement in the limit of very low Ca, where viscous forces can be neglected.

The algorithm was implemented on a two-dimensional flow geometry similar to the one in the experiments of Zhao *et al.* (2016). We used the model to capture the wetting transition in strong

imbibition and explored the sensitivity of the flow pattern to pore-scale heterogeneity in contact angle, post spacing, and to three-dimensional effects of finite post height.

2.2 Method

Experimental observations of fluid-fluid displacement in different wettability regimes provide an intuitive way to understand the underlying assumptions behind different models of multiphase flow.

In drainage, the invasion pattern advances by overcoming local capillary entry pressures within the porous medium (Lenormand & Zarcone, 1985). In the limit of vanishing Ca, viscous dissipation can be neglected and the invasion process is well captured by the invasion-percolation algorithm (Lenormand & Bories, 1980; Chandler *et al.*, 1982; Wilkinson & Willemsen, 1983). This approach replaces the pore space with a network of nodes (pores) and edges (throats). Throats that contain a fluid-fluid interface are considered active. Every active throat is ranked according to its critical capillary pressure, which can be calculated from the throat size. The invading fluid moves by advancing locally into the throat with the lowest critical capillary pressure, resulting in invasion avalanches and displacement fronts that often loop on themselves and trap clusters of the defending fluid behind the advancing front.

While the invasion-percolation algorithm is in good agreement with experiments in drainage (Lenormand & Zarcone, 1985), it fails to reproduce the invading fluid pattern during imbibition. Here, cooperative pore filling mechanisms make the invading pattern smoother, and invasion proceeds through compact fronts (Lenormand *et al.*, 1988).

Cieplak & Robbins (1990, 1988) showed that in order to capture cooperative pore filling effects during imbibition one needs to account for the local pore geometry (Cieplak & Robbins, 1988, 1990). They approximated the porous medium by placing posts on a regular 2D lattice; every post was assigned a random radius from a uniform distribution. The interface consisted of a collection of arcs between the posts. Every arc intersected nearby posts at a prescribed contact angle and curvature defined by the Laplace pressure Δp .

Cieplak & Robbins (1988, 1990) introduced three types of instabilities: “burst” (no stable arc at given Δp), “touch” (interface touches opposite post), and “overlap” (two neighbouring interfaces coalesce within the pore). The algorithm moves the fluid-fluid interface at fixed injection pressures by searching for unstable arcs and replacing them with new stable configurations (pore invasion). When no unstable arcs are found, the invading fluid pressure is increased to induce further advance.

Unlike the invasion-percolation algorithm, local interface instabilities are sensitive to geometric configurations of neighbouring arcs, allowing for cooperative pore filling (mostly dominated by touch and overlap instabilities) during imbibition. Moreover, the algorithm produces results nearly identical to invasion-percolation algorithm in drainage, where burst instabilities are prevalent (Cieplak & Robbins, 1990). Thus, the model of Cieplak & Robbins (1988, 1990) extends the description of quasi-static fluid-fluid displacement in porous media from strong drainage to weak imbibition.

At the same time, Cieplak & Robbins (1988, 1990) acknowledged that the arbitrary sequence of pressure increments affects the morphology of simulated invasion fronts. Unlike the invasion-percolation algorithm, where the sequence of local interface advances is determined through global critical pressure ranking, the Cieplak & Robbins (1988, 1990) model advances unstable arcs in the order they are discovered by a user-defined search convention. Moreover, the choice of pressure increments often results in more than one type of instability within the same arc; instabilities are removed by authors’ convention where touch instabilities are removed first and burst instabilities are removed last.

We found that by reformulating the original approach of Cieplak & Robbins (1988, 1990), one

can explicitly calculate critical pressures of all instability events and advance the interface in an invasion-percolation-like manner. The interface moves based on the ranking of critical pressures that are calculated from local arc and post geometries. Thus, this new formulation eliminates the need for arbitrary pressure increments and allows the least stable arcs to advance first. Below we describe the details of the new formulation followed by the algorithm in the spirit of invasion-percolation.

Consider a set of neighboring posts (FIG. 2-1). On every image, posts are numbered from 1 to 3 (where applicable): left post is 1, right post is 2, and the top post is 3 (FIG. 2-1(b)-(d)). Each post is defined through its radius, location expressed in Cartesian coordinates, and a contact angle. For example post 1 has radius r_1 , location (x_1, y_1) , and contact angle θ_1 measured from the invading fluid between posts 1 and 2 (FIG. 2-1(a)). Without loss of generality, we rotate and translate the coordinate system so that points (x_1, y_1) , (x_2, y_2) , (x_3, y_3) turn into $(0, 0)$, $(X_2, 0)$, (X_3, Y_3) .

For the description that follows, we assume that the posts are tall enough that the events considered in FIG. 2-1(b)-(d) can be formulated in a two-dimensional sense. The validity and limitations of this assumption are further explored in section 2.3.

Consider an interface of radius of curvature r_p that meets post 1 at contact angle θ_1 (FIG. 2-1(a)). We define d_1 to be the distance from the center of interface curvature to the center of post 1. Given an expression for value of $\angle ACP$, the distance d_1 can be determined from the law of cosines for $\triangle ACP$. Both $\angle PCU$ and $\angle TCA$ are equal to $\pi/2$ and $\angle UCT$ is $\pi - \theta_1$. Since $\angle ACP + \angle PCU + \angle UCT + \angle TCA = 2\pi$, then $\angle ACP = \theta_1$. Therefore,

$$d_1(r_p, \theta_1) = AP = \sqrt{r_1^2 + r_p^2 - 2r_1r_p \cos \theta_1}. \quad (2.1)$$

Equation (2.1) defines the distance between the center of curvature (X_p, Y_p) and the center of post 1 $(0, 0)$. This means that point (X_p, Y_p) lies on a circle concentric with post 1 and radius d_1 , where the interface satisfies the contact angle θ_1 and has radius of curvature r_p . All points satisfying this requirement are shown as a dashed line on FIG. 2-1(a).

A similar construction for an interface intersecting with a second post of radius r_2 and a contact angle θ_2 centered at $(X_2, 0)$ defines a second circle centered at post 2. For a given r_p , this second circle (dashed line FIG. 2-1(a) opening to the right) will share either two, one or zero common points with the set of potential centers of curvature for the interfaces which stably contact post 1. FIG. 2-1(a) shows a case where the interface is stable. Considering only the case when the invading fluid is sourced from below the X -axis, the stable interface touching both posts will be centered at a point (X_p, Y_p) which is determined to simultaneously satisfy

$$X_p^2 + Y_p^2 = d_1(r_p, \theta_1)^2, \quad (2.2a)$$

$$(X_p - X_2)^2 + Y_p^2 = d_2(r_p, \theta_2)^2, \quad (2.2b)$$

$$Y_p \leq 0. \quad (2.2c)$$

Subtraction of (2.2a) and (2.2b), allows for the direct calculation of X_p and then Y_p can be trivially found as the negative root of equation (2.2a). Equation (2.2c) ensures that one selects the correct root when solving for Y_p (FIG. 2-1(a)).

The equations considered here are simplified significantly by the choice of post placement. For posts located at generic grid points, the post centers can be simply translated and subsequently rotated to achieve this configuration. Following calculations in this modified coordinate system the results can be simply rotated and translated back to the original coordinate system.

We are now ready to define several instability events that determine interface propagation. Following the work of Cieplak and Robbins (Cieplak & Robbins, 1988, 1990), we consider ‘‘burst’’,

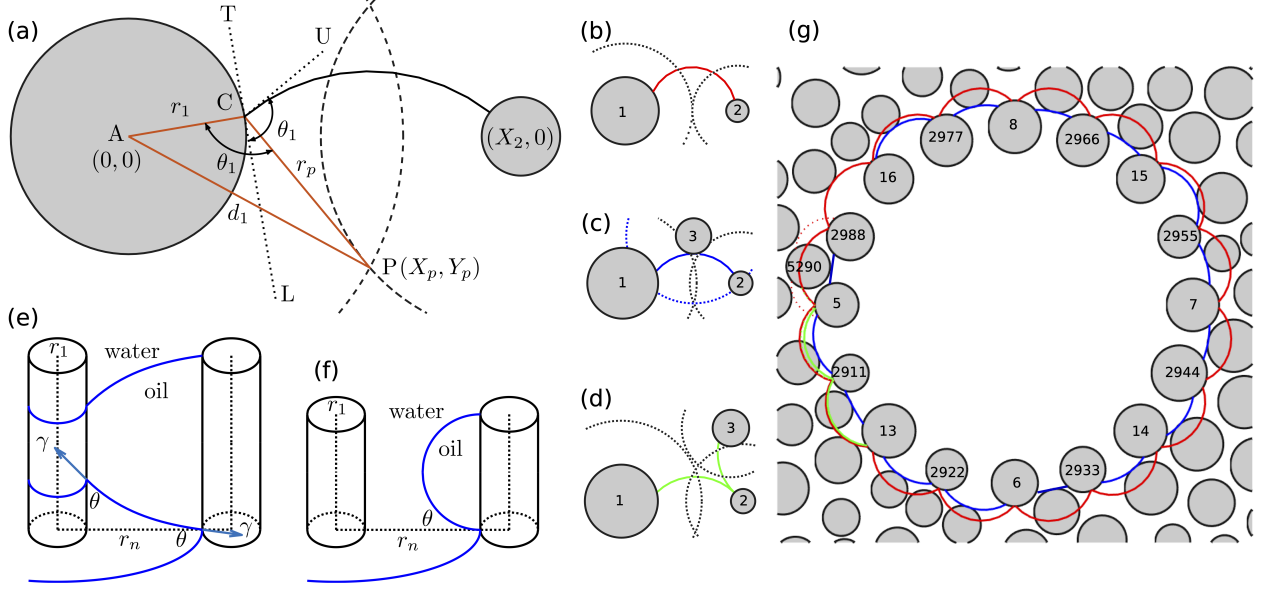


Figure 2-1: (a) Invasion front configuration between two posts; (b) Burst event: unstable interface (red line) advances into the pore; (c) Touch event: interface touches the nearest post; (d) Overlap event: two fronts (green lines) coalesce on post surface and fill the pore; (e) Corner flow event: corner meniscus touches and coats the neighbouring post; (f) Capillary bridge event: corner menisci coalesce mid-post before reaching the next post; (g) Invading front configuration with post IDs: red, blue, green interfaces correspond to “burst”, “touch”, “overlap” critical interfaces.

“touch”, and “overlap” events, and we additionally introduce a new class of “corner” events. The order and frequency of these pore-level events ultimately define the shape of the quasi-static invasion pattern. Below we find the critical Laplace pressures Δp (corresponding to radius of curvature r_p via the Young-Laplace equation, $1/r_p = \Delta p/\gamma$) at which each event takes place.

2.2.1 Burst event

As the pressure of the invading phase increases, the radius of interface curvature r_p decreases. This results in lower values for both d_1 and d_2 . As a result, increasing Δp reduces the radii of the dashed lines in FIG. 2-1(a), and the number of their intersection points (solutions for Equation (2.2)) changes from 2 to 1, and eventually 0. This means that there is no longer a stable interface between posts 1 and 2; this event is referred to as “burst” (see FIG. 2-1(b)). The “burst” event coincides with the last stable configuration of the interface between two posts at given contact angles θ_1 and θ_2 . This occurs when there is only a single root to Equation (2.2), and also corresponds to the case when $Y_p = 0$ (which implies a zero discriminant in the quadratic equation). Introducing this condition in Equation (2.2) allows finding the critical radius of curvature r_p that corresponds to “burst” as a tangential intersection of dashed circles in FIG. 2-1(a):

$$X_p^2 = d_1(r_p, \theta_1)^2, \quad (2.3a)$$

$$(X_p - X_2)^2 = d_2(r_p, \theta_2)^2. \quad (2.3b)$$

Equations (2.3) can be rearranged to give a quadratic equation in r_p ; with the burst radius

chosen to yield a positive burst pressure.

2.2.2 Touch event

The “touch” event refers to the configuration depicted in FIG. 2-1(c). Here, the interface tangentially intersects the third post centered at (X_3, Y_3) and with radius r_3 . This configuration can be viewed as the intersection of black dotted lines and the circle of radius $r_p + r_3$ centered at (X_3, Y_3) , represented by the blue dotted line in FIG. 2-1(c):

$$X_p^2 + Y_p^2 = d_1(r_p, \theta_1)^2, \quad (2.4a)$$

$$(X_p - X_2)^2 + Y_p^2 = d_2(r_p, \theta_2)^2, \quad (2.4b)$$

$$(X_p - X_3)^2 + (Y_p - Y_3)^2 = (r_p + r_3)^2. \quad (2.4c)$$

Equation (2.4) can be solved analytically for the critical value of r_p that satisfies the “touch” condition. Again, the touch condition given by the solution of Equation (2.4) can be reduced to a quadratic equation in r_p , although the expansion to this form involves some laborious algebra.

2.2.3 Overlap event

Cieplak & Robbins (1988, 1990) defined the “overlap” event as an instability where two advancing contact lines meet on the surface of a post (see FIG. 2-1(d)). The solution to the overlap radius of curvature can be written as the intersection of three circles—the interface between posts 1 and 2, the interface between posts 2 and 3, and the circle corresponding to the surface of post 2:

$$(X - X_{p12})^2 + (Y - Y_{p12})^2 = r_p^2, \quad (2.5a)$$

$$(X - X_{p23})^2 + (Y - Y_{p23})^2 = r_p^2, \quad (2.5b)$$

$$(X - X_2)^2 + Y^2 = r_2^2. \quad (2.5c)$$

Here (X_{p12}, Y_{p12}) and (X_{p23}, Y_{p23}) , which are also functions of r_p , denote the centers of curvature for interfaces between posts 1 and 2, and 2 and 3, respectively. Equation (2.5) coupled with solutions for (X_{p12}, Y_{p12}) and (X_{p23}, Y_{p23}) can be solved numerically for a critical value of r_p .

The underlying assumption in the above equations is that both interfaces in FIG. 2-1(d) have the same radius of curvature r_p . In a quasi-static process, as assumed here, the pressure is spatially uniform in both invading and defending fluids with a Laplace pressure drop between them. Thus, we can assume that $\Delta p_{12} = \Delta p_{23}$ in overlap event calculations. Therefore, from the Young-Laplace equation, we have that $\frac{\gamma}{r_{p12}} = \frac{\gamma}{r_{p23}}$ or $r_{p12} = r_{p23} = r_p$.

2.2.4 Drainage overlap event

The original definition of “overlap” event by Cieplak & Robbins (1990) is valid only for $\theta \leq 90^\circ$. When $\theta > 90^\circ$, the two menisci coalesce away from the post, trapping some defending liquid on the post wall (Lee *et al.*, 2017), as illustrated for $\theta = 120^\circ$ in FIG. 2-2(b). This effect has been largely ignored in pore-level simulations, and a careful experimental investigation was only reported recently by Lee *et al.* (2017).

Consider the “drainage overlap” configuration in FIG. 2-2(a), where overlap occurs at $\theta > 90^\circ$ and a distance a away from post 2. The solution for this coalescence can be obtained as an intersection

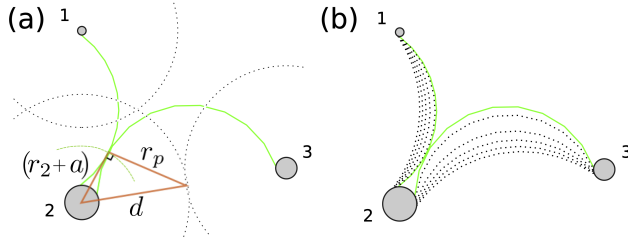


Figure 2-2: (a) Schematic diagram of menisci coalescence away from the post surface. (b) The diagram demonstrates *drainage overlap* at $\theta > 90^\circ$: menisci coalesce inside the pore space, leaving trapped oil on the wall of the invaded post.

of the two menisci and a circle of radius $(r_2 + a)$ concentric with post 2:

$$(X - X_{p12})^2 + (Y - Y_{p12})^2 = r_p^2, \quad (2.6a)$$

$$(X - X_{p23})^2 + (Y - Y_{p23})^2 = r_p^2, \quad (2.6b)$$

$$(X - X_2)^2 + Y^2 = (r_2 + a)^2. \quad (2.6c)$$

Noting that $(r_2 + a)^2 = d^2 - r_p^2$, where d^2 is analogous to equation (2.1), unknown a can be eliminated from the above expressions. This allows solving “drainage overlap” numerically for the critical value of r_p .

2.2.5 Corner and capillary bridge events

In addition to the events described above, all of which apart from “overlap” for $\theta > 90^\circ$ had already been identified previously (Cieplak & Robbins, 1988, 1990), Zhao *et al.* (2016) experimentally observed a transition from pore invasion in weak imbibition to *corner flow* in strong imbibition. In order to capture this transition it is necessary to consider the shape of the fluid-fluid interface in 3D. When the solid walls have high affinity for the invading liquid, the liquid accumulates in corners between the posts and the top/bottom plates of the cell, adopting a constant-curvature configuration shown in FIG. 2-1(e).

In our model, a “corner” event occurs when the interface swells sufficiently to touch a neighboring post; this allows flow towards the corner of the neighbor post. The distance from the center of the wetted post to the surface of its nearest neighbor is denoted by r_n . This distance can be estimated from a force balance on the corner liquid in the vertical direction (de Gennes *et al.*, 2004):

$$2r_1 \cos \theta_1 - 2r_n \sin \theta_1 + (r_n^2 - r_1^2) \Delta p / \gamma = 0. \quad (2.7)$$

Equation (2.7) can be used to determine the critical pressure differential across the interface that is required for a “corner” event for every post on the invasion front. This equation is valid when the height of the posts is significantly taller than the spacing between the posts.

When the post height is comparable to the post spacing, the top and bottom corner menisci might intersect in the middle of the post before a corner event. This results in the coalescence of the two interfaces, and invading liquid coats the post in the shape of a *capillary bridge* (FIG. 2-1(f)). In this case, we use the constant interface curvature equation shown in Appendix A.1 to find the pressure at which mid-post coalescence takes place. A more detailed discussion of the corner liquid interface shape and validity of Equation (2.7) is given in Appendix A.1.

2.2.6 Invasion algorithm

The closest analog to the invasion algorithm presented here is the invasion-percolation method (Wilkinson & Willemsen, 1983; Lenormand & Bories, 1980; Chandler *et al.*, 1982), where the invasion front advances by overcoming threshold pressures associated with pore throats. At every step, a pore with the lowest threshold pressure gets invaded first; the interface is updated and the algorithm proceeds to the next invasion step. The simplicity of invasion-percolation leaves very little room for misinterpretation, but it has traditionally been applied only in strong drainage.

The quasi-static invasion of the fluid-fluid interface is governed entirely by the critical pressures of “burst”, “touch”, “overlap”, and “corner” events. To illustrate how the pore-level threshold pressures combine to determine the evolution of the invasion front, consider the initial configuration in FIG. 2-1(g). This initial invasion front is obtained by connecting the innermost posts, a procedure which does not necessarily produce a stable front. Here, every post has an identification number.

We calculate the critical invasion pressures for pore-scale events by solving Equations (2.3)–(2.7) for every post on the invasion front. To advance the invading fluid, we traverse the invasion front and select the post with the smallest critical invasion pressure Δp (e.g., a “touch” instability for the interface at post 5 in FIG. 2-1(g)).

The manner in which the invasion front changes following an event depends on the type of instability that takes place. If a “burst” or “touch” instability occurs, the nearest post to the interface is added to invasion front (FIG. 2-1(b)-(c)). If the least stable event is “overlap”, the post where the contact lines meet is removed from the invasion front.

Finally, if a “corner” flow event occurs, a newly captured post is added to the list of *corner invasion* posts. We keep track of this list separately from all other events because the manner in which corner menisci advance is distinctly different. As we show later, this leads to competition between corner invasion and cooperative pore filling invasion at some contact angles, leading to the transition in pore-level displacement mechanism observed by Zhao *et al.* (2016). We assume that cooperative pore filling front posts are also coated in their corners, so the corner list is at least as long as the other list; an assumption that is reasonable for the quasi-static description we employ here, but which will likely be inaccurate at very high capillary numbers, when viscous forces dominate and films of the defending fluid are left behind.

By following these simple rules, one can capture the complexity of invasion patterns and their relation to substrate wettability. Although this method was built with the framework initially proposed by Cieplak & Robbins (1990) in mind, there are several features of our approach that are important to note.

Firstly, the evolution of the interface in the algorithm of Cieplak & Robbins (1990) was somewhat sensitive to the arbitrary selection of pressure increments and the order in which the invasion mechanisms were scanned. In the Cieplak & Robbins (1990) study, after each pressure increment, every interface was scanned for “burst”, “touch”, and “overlap” in sequence, and an unstable interface was allowed a single step forward. This means that the natural order of the instability events could be disturbed with a poor choice of pressure increments or scanning order; a shortcoming acknowledged by the authors (Cieplak & Robbins, 1988, 1990). In contrast, our algorithm always advances the *least stable* interface within the invasion front, therefore eliminating arbitrariness.

Secondly, by maintaining the list of critical pressures, new computations only need to be performed in the neighborhood of newly invaded pores. This feature may prove to be especially useful should the algorithm be extended to a dynamic invasion front (i.e. when taking into consideration the pressure changes associated with viscous forces during the motion of the invasion front as in Holtzman & Segre (2015)).

Finally, within the current framework, we can easily assign unique contact angles to individual

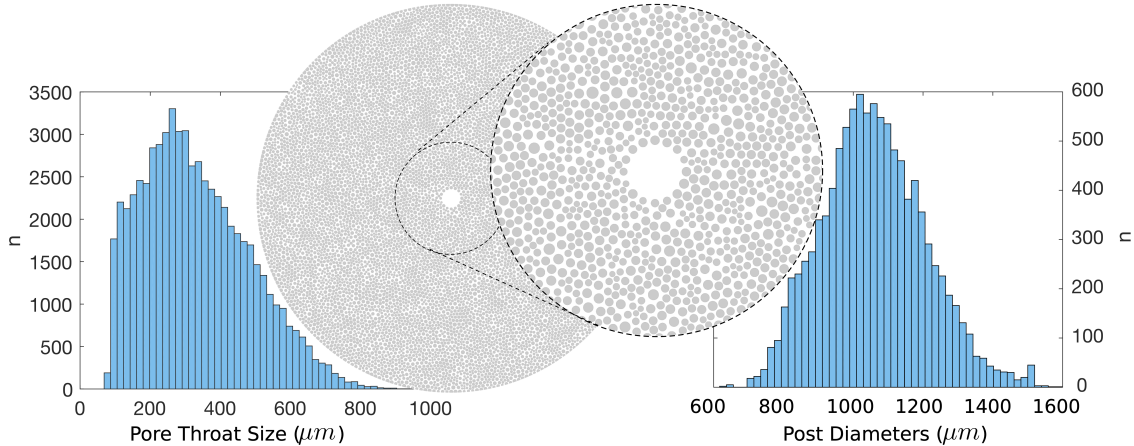


Figure 2-3: Generated pore geometry along with post diameter and pore throat size histograms. Posts were placed on irregular triangular lattice generated with MATLAB’s `pdemesh`, and post radii were assigned to 45% of the smallest connected edge.

posts. We utilize this feature to generate different realizations of the same invasion experiment. That is, for every realization, we assign a random contact angle for every post from a narrow distribution centered around a global mean. This brings us closer to experimental conditions, where small local deviations from the average contact angle of the substrate exist due to material impurities and inhomogeneity from the fabrication process.

2.3 Results and discussion

We use the model described in the previous section to address the following objectives: (1) we test whether our method is able to fully capture the invasion-pattern morphology through the wetting transition from strong drainage to strong imbibition; (2) we explore the sensitivity of the wetting transition to local perturbations in contact angles through pore-level event statistics and the macroscopic fractal dimension; (3) we study the links between pore spacing and mechanisms of pore-level displacement; (4) finally, we explore the limits of our model by introducing three-dimensional effects with finite post heights within the flow geometry.

The baseline pore geometry used in this work was generated in a similar manner to [Zhao *et al.* \(2016\)](#). MATLAB’s `pdemesh` was used to generate a circular Hele-Shaw cell configuration with diameter of 15cm. Centers of the posts were placed at the nodes of the generated irregular mesh. Then the radius of each individual post was assigned to 45% of the smallest edge at a corresponding node. The final geometry of posts and the histograms of the resulting post radii and throat sizes are shown in [FIG. 2-3](#).

2.3.1 Invasion front morphology through the wetting transition

We simulated radial invasion of water into the oil-filled microfluidic cell described above, with substrate contact angles between 160° (strong drainage) and 10° (strong imbibition). Pore invasion simulations in [FIG. 2-4](#) demonstrate that the morphology of the invasion pattern depends strongly on the wettability of the substrate. In particular, the invasion pattern becomes more compact as the scenario changes from strong drainage ($\theta = 160^\circ$) to weak imbibition ($\theta = 45^\circ$), and this is accompanied with a reduction in the amount of trapped oil behind the invasion front. In strong

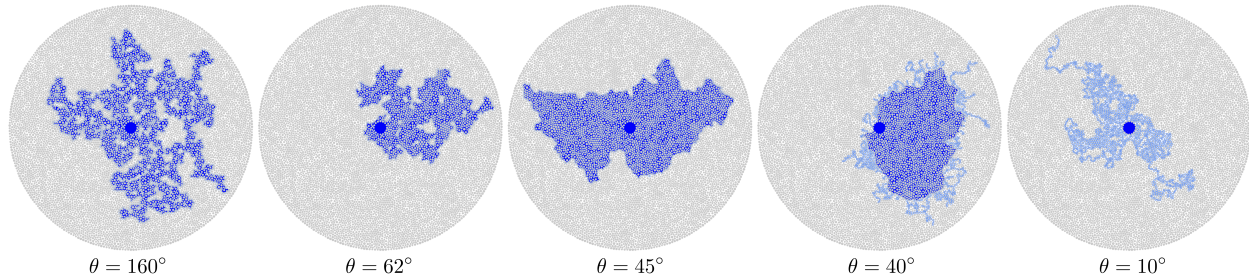


Figure 2-4: Immiscible fluid invasion simulation results: algorithm presented in section 2.2 covers the full range of pore wettabilities, from strong drainage ($\theta = 160^\circ$) to strong imbibition ($\theta = 10^\circ$). Dark blue regions represent fully invaded pores; light blue regions represent partially invaded pores with coated post corners. We include video files of the invasion process at different wettabilities in supplementary materials.

imbibition, the invading fluid starts to preferentially accumulate in the corners formed by the posts with the top and bottom plates. This results in an invasion mechanism that competes with “burst”, “touch”, and “overlap” events.

Consider a single post with invading liquid accumulating in its corners with top/bottom plates. As the pressure of the invading fluid increases, the size of the “corner” meniscus increases, and at some critical pressure the liquid extends far enough to reach the post’s closest neighbour. At this point, the invading liquid flows into the corner of the next post. Here, invasion proceeds akin to invasion-percolation, albeit on a dual network, where the sites are the posts and the links are the edges of the corresponding Delaunay tessellation. This mode of invasion leads to fingering patterns, in contrast with the compact invasion characteristic of weak imbibition. The pattern at $\theta = 40^\circ$ in FIG. 2-4 is particularly noteworthy: here, frequencies of *cooperative pore filling* and *corner flow* events are comparable, and the invasion front advances in a mixed regime.

More generally, the invading front morphology in FIG. 2-4 can be classified into three categories: (1) invasion-percolation in strong drainage (mostly “burst” events, $\theta = 160^\circ$), (2) cooperative pore filling in weak imbibition (mostly “touch” and “overlap” events, $\theta = 45^\circ$), (3) and “post chaining” due to “corner flow” or “capillary bridge” events in strong imbibition ($\theta = 10^\circ$). The first two categories take place at contact angles between 160° and 45° , and they are very much in line with the quasi-static simulations of Cieplak & Robbins (1988, 1990). The latter category was experimentally observed only recently (Zhao *et al.*, 2016).

Furthermore, we find that the finger width measurements (FIG. A-5) of the emerging patterns are in line with experimental observations (Stokes *et al.*, 1986; Trojer *et al.*, 2015; Zhao *et al.*, 2016) and numerical predictions (Cieplak & Robbins, 1988, 1990). In strong drainage, the invading patterns have finger width comparable to the size of a typical pore. When the flow is dominated by cooperative pore filling events, the finger width diverges to a size of about 18 pores. Finally, the finger width reduces to a fraction of a pore size in corner flow dominated regime. We include the detailed discussion on finger width measurements in Appendix A.3, and we include video files of the invasion process at different wettabilities in supplementary materials.

2.3.2 Sensitivity of macroscopic invasion to local contact angle perturbations

Any real substrate is bound to have imperfections that perturb local contact angles from the global mean. In the context of the experiments by Zhao *et al.* (2016), local imperfections in contact angle could arise from dust deposition on the substrate during fabrication of the microfluidic cell, and one

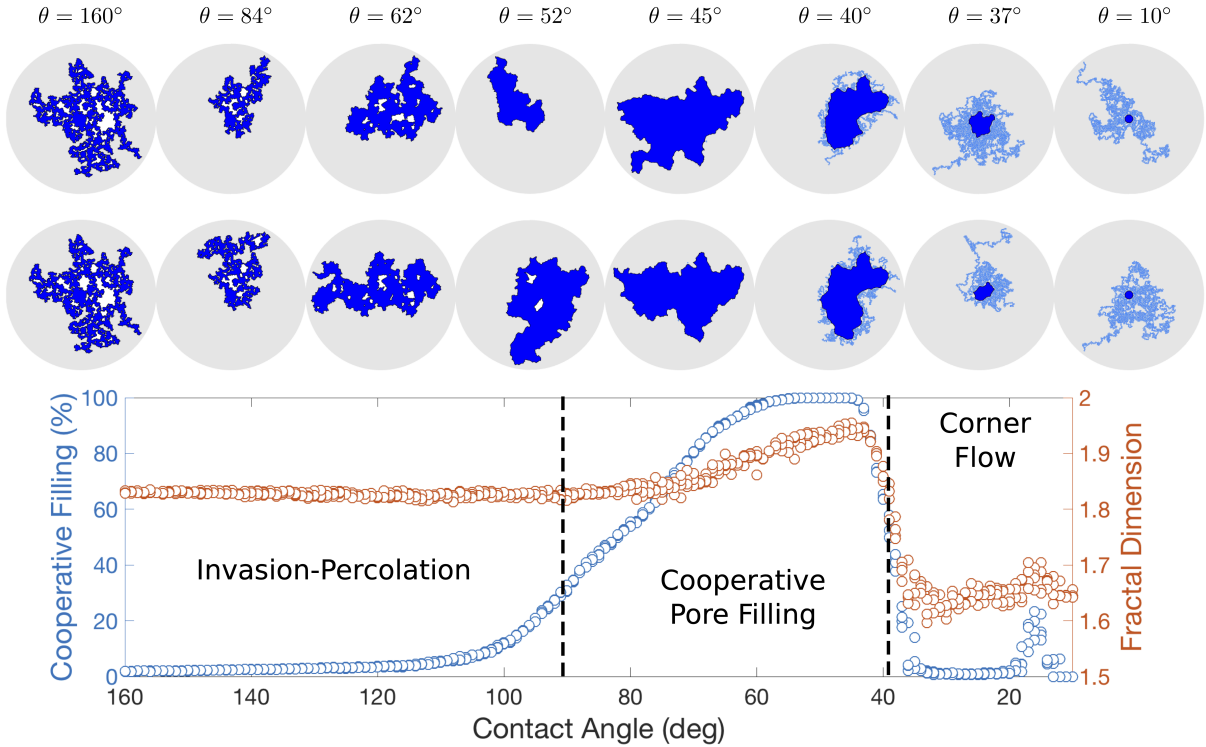


Figure 2-5: Cooperative pore filling and fractal dimension plots. Invasion patterns for different realizations at each fixed global contact angle. As the system moves from strong drainage ($\theta = 160^\circ$) to weak imbibition ($\theta = 45^\circ$), the percentage of cooperative pore-filling events gradually increases. The transition from weak to strong imbibition is marked with a sharp drop in both fraction of cooperative pore filling events and fractal dimension.

typically takes a great deal of care in minimizing these effects.

In practice, no two invasion tests look exactly the same, even when conducted following the same experimental protocol. However, while different realizations of the same experimental conditions can be expected to produce non-identical invasion patterns, those patterns should possess a common quality. This raises an interesting question of quantifying the similarity of the invasion patterns.

We mimic local imperfections in contact angle by assigning unique contact angles to every post in the flow geometry. In particular, we select the contact angles from a uniform distribution with 2° range centered around the global mean. FIG. 2-5 presents the summary from multiple realizations. Every “experiment” was repeated four times for contact angles between 160° and 10° , producing four different realizations for each set of invasion conditions.

The degree of similarity of the resulting invasion patterns was assessed by means of two metrics: (1) the percentage of cooperative pore filling events (“touch” and “overlap”), and (2) the fractal dimension of the invasion pattern. The fractal dimension was calculated using the box counting method (Kenkel & Walker, 1996; Iannaccone & Khokha, 1996). The details of the box counting calculations are included in Appendix A.2.

The results in FIG. 2-5 demonstrate that the percentage of cooperative pore filling events is a robust classifying metric for the invasion shapes; it exhibits negligible variability among realizations. As the contact angle changes from 160° to 45° , “touch” and “overlap” events become dominant. At contact angles below 45° , “corner flow” events take over.

In contrast, the fractal dimension shows a higher variability from one realization to another, and here we can appreciate the difference in invasion shapes quantitatively. For example, consider the two realizations with $\theta = 84^\circ$ in FIG. 2-5. At a glance, the two invasion patterns look similar, but there are subtle differences in the invaded regions and clusters of trapped oil. The fractal dimension reflects this difference, resulting in appreciable scatter of points at $\theta = 84^\circ$ in FIG. 2-5.

The fractal dimension data reported in FIG. 2-5 is computed with box counting method, and shows reasonable values for all flow regimes. The mean fractal dimension for invasion-percolation is 1.83; for cooperative pore filling is between 1.83 and 1.96; and in the corner flow regime is 1.65.

Overall, we were able to mimic the simulation of the same experimental conditions with local imperfections in the wetting properties of the substrate. While every simulation produces a “unique” pattern, each pattern falls into one of the shape categories (invasion-percolation, cooperative filling, corner flow) based on the percentage of cooperative pore filling events plot.

2.3.3 Influence of drainage overlap and post spacing on cooperative pore filling

Consider the schematic diagrams of “drainage overlap” and the original “overlap” events in FIG. 2-6(a). During the invasion process, the “drainage overlap” always precedes the original “overlap” event of Cieplak and Robbins (Cieplak & Robbins, 1988, 1990) and thus corresponds to a lower critical pressure. Since we advance the invasion front into pores with lowest critical pressures, by overestimating the critical pressures of “overlap” events, one would erroneously advance the invasion front through spurious “burst” instabilities. This is especially likely to happen when the spacing between the posts is large. We examine the significance of “drainage overlap” by increasing the spacing between posts in the original pore geometry by a factor $\lambda > 1$.

FIG. 2-6(b) shows that by considering “drainage overlap”, we recover a considerable number of cooperative pore filling events otherwise lost if one follows the original definition of “overlap” event of Cieplak and Robbins (Cieplak & Robbins, 1988, 1990). Simulations with “drainage overlap” result in about 30% cooperative pore filling event ratio at $\theta = 160^\circ$ for $\lambda = 4$, while the original “overlap” produces no cooperative filling events at $\theta = 160^\circ$ for all λ .

One can intuitively understand why larger spacing between posts increases the frequency of cooperative pore filling events by examining two posts and a fluid-fluid interface between them at $\lambda = 1$ and $\lambda = 4$ (FIG. 2-6(c)). In drainage, as the pressure of the invading fluid increases, the interface approaches its “burst” configuration. When the spacing between the posts is small ($\lambda = 1$), the fluid-fluid interface remains mainly within the gap between the two posts. In contrast, when the spacing is wide ($\lambda = 4$), the interface extrudes significantly away from the gap between two posts before reaching the “burst” configuration. As a result, this interface is more likely to encounter — and coalesce with — the neighboring fluid interfaces. In the extreme limit, when $\lambda \gg 1$, we expect the fluid front to advance mainly through cooperative pore filling via “drainage overlap” events, even in strong drainage. Therefore, the “drainage overlap” presented in section II is crucial for the validity of the quasi-static invasion model on a wide range of pore geometries, especially in simulating multiphase flow through highly porous materials such as low-density micropillar arrays (Jung *et al.*, 2016) or fibrous media (Peek & Mclean, 1934; Thompson, 2002; Calhoun & Mortensen, 1992).

The “drainage overlap” events (see section II) result in trapping of the defending liquid on the surfaces of the posts at $\theta > 90^\circ$ (FIG. 2(b)). Furthermore, the earlier onset of cooperative pore filling due to λ changes the amount and the manner in which the defending fluid is trapped behind the invasion front. Trapping of the defending liquid is an interesting problem on its own, but it is not the focus of this work.

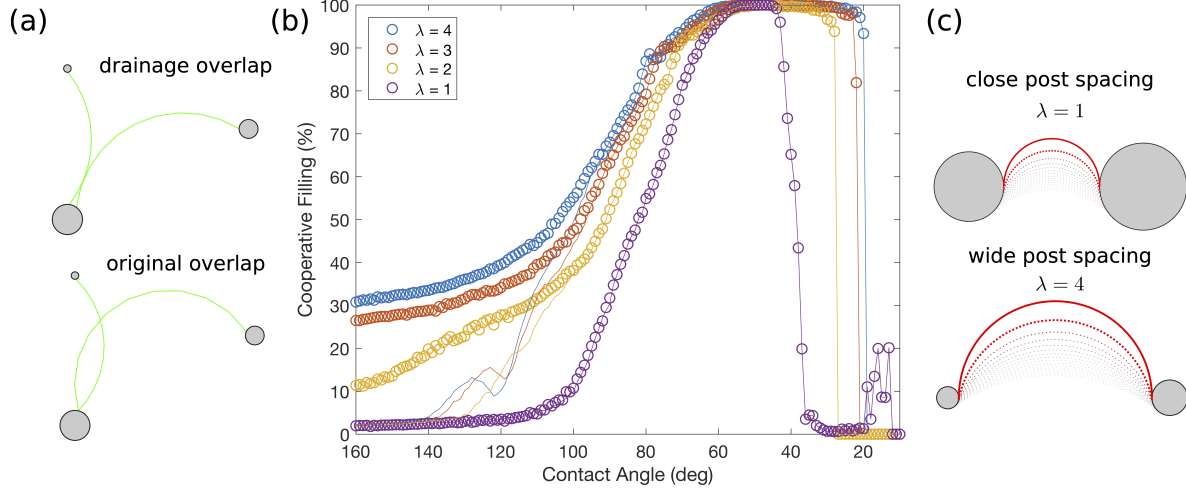


Figure 2-6: (a) Schematic diagrams of “drainage overlap” and “overlap” event of Cieplak and Robbins (Cieplak & Robbins, 1988, 1990). (b) Percentage of cooperative pore filling events for posts spaced out by a factor of λ from the original post geometry. The colored circles represent simulations with “drainage overlap” considered; solid lines represent simulations with the original “overlap” definition of Cieplak and Robbins (Cieplak & Robbins, 1988, 1990). (c) Schematic diagram of post spacing and fluid-fluid interface.

2.3.4 Three-dimensional effects: out-of-plane curvature

In the simulations described so far, we neglected the *out of plane* curvature contributions in the Young-Laplace equation when calculating critical pressures of “burst”, “touch” and “overlap” events in section 2.2, akin to the simulations of Cieplak & Robbins (1988, 1990). The ascribed correction to the critical pressures is that $\frac{\Delta p}{\gamma} = \frac{1}{r_p}$ is replaced by $\frac{\Delta p}{\gamma} = \frac{1}{r_p} - \frac{2\cos\theta}{h}$ for “burst”, “touch”, and “overlap” events.

As the height of the posts decreases, the relative magnitudes of the critical pressures change. This, in turn, alters the final patterns of the invasion fronts (FIG. 2-7). As the post heights approach $100\mu m$, the critical pressures of “burst”, “touch”, “overlap” events become lower than critical pressures of “corner” and “capillary bridge” flow events, leading to a dominance of cooperative pore filling at low contact angles. However, in reality, Zhao *et al.* (2016) observed corner flow dominated regime at $\theta = 7^\circ$.

This discrepancy between the experiment and our quasi-static simulations can be due to several factors. Firstly, this *out of plane* curvature adjustment is rather crude, and was only implemented to test the limits of our 2D model. A full three-dimensional consideration of the invasion would be more accurate, although the formulation would also be significantly more complex. Secondly, and perhaps more importantly, we have likely overestimated the critical pressures of “corner” events. This can be appreciated from a close examination of invasion progression at strong imbibition in the experiments of Zhao *et al.* (2016). There, on average, corner menisci appeared to grow only up to about the middle of pore throats, at which point the neighbouring posts were coated. In our model, the critical pressures of *corner flow* events were calculated assuming the full growth of the *corner meniscus* across the throat, which results in higher critical pressures. Indeed, imposing the *half-throat* rule in our model, produces a transition to *corner flow* at around $\theta = 22^\circ$. This earlier coating of the posts could be due to the establishment of a conductive film ahead of the corner meniscus that was not visible in the experimental images. Indeed, the fluid invasion through thin

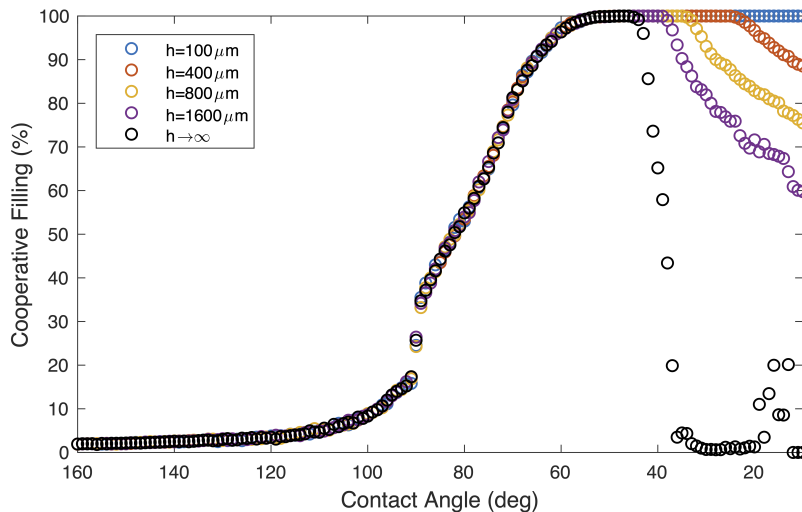


Figure 2-7: Figure shows how post heights alter the shapes of the invasion fronts: the onset of the *corner flow* dominated regime is heavily influenced by the out-of-plane curvature correction of the “burst”, “touch”, and “overlap” instabilities. The magnitude of the correction is controlled by the height of the posts. Invasion fronts on the right are plotted for different h at $\theta = 10^\circ$.

film flow in strong imbibition and accumulation of invading fluid in the corners was also observed by [Odier *et al.* \(2017\)](#). Resolving the detailed dynamics of post bridging in the strong imbibition regime warrants further experimental and theoretical investigations.

Furthermore, solid surface roughness in realistic 3D rock geometries may provide continuity to the wetting layers. In the presence of strong surface roughness, growth of the corner menisci would still dominate in strong imbibition, but the morphology of the invading pattern would likely be controlled by the heterogeneity in surface roughness rather than the spacing between the posts. While the considerations of roughness and film flow in realistic 3D geometries are outside the scope of this work, they are, however, potentially important mechanisms in strong imbibition.

2.4 Conclusions

Overall, our approach to immiscible fluid invasion in disordered micropillar arrays can be viewed as an extension of the invasion-percolation algorithm to include wettability through critical invasion pressures for cooperative filling and corner flow events. This approach eliminates the need for (and thus the sensitivity to) arbitrary increments in the invading pressures and scanning order of the interface for instability events observed in the earlier work ([Cieplak & Robbins, 1988, 1990](#)). Our algorithm also allows assigning a unique contact angle to every post, to study the sensitivity of the invasion patterns to local wettability variations.

The invasion model presented here was coded into an efficient simulation algorithm, making it an attractive starting point for dynamic pore invasion simulations. A natural way of extending this algorithm is through incorporating viscous forces with a coupled pore-network model ([Jain & Juanes, 2009](#); [Holtzman & Juanes, 2010](#); [Holtzman & Segre, 2015](#)).

We have tested the invasion model by comparing the simulation outputs with the experiments of [Zhao *et al.* \(2016\)](#). Our quasi-static model was able to capture the nature of the invasion fronts at low capillary numbers for the full range of substrate wettabilities, including the transition

from *invasion-percolation* to *cooperative filling* to *corner flow* as a function of contact angle. This can have important implications in enhanced oil recovery, carbon sequestration, and microfluidic applications. For example, in petroleum production, a more compact invasion pattern is preferred when displacing oil from the reservoir by water injection. In some instances of reactive transport in microfluidic applications, however, one might want to induce the fingering invasion to maximize the interface area between invading and defending liquids.

Fluid injection can result in localized redistribution of stress loads within porous media accompanied with dilation of the pore space (Jain & Juanes, 2009; Holtzman & Juanes, 2010). Some of the recent experimental observations of pore-scale poroelasticity include localized fluid-induced deformation of hydrogel packs (MacMinn *et al.*, 2015) and glass bead pack deformation caused by immiscible liquid infiltration (Dalbe & Juanes, 2018; Holtzman *et al.*, 2012). The dynamic extension of the model presented here could be further extended to include pore deformations due to changes in effective stress under different wettability conditions, which could capture the potential interplay between pore wettability and deformation during fluid-fluid displacement.

Chapter 3

Signatures of fluid-fluid displacement in porous media: wettability, patterns, and pressures

This chapter has been published in [Primkulov et al. \(2019\)](#).

3.1 Introduction

A beautiful array of flow patterns arises when a low-viscosity fluid displaces a more-viscous fluid in a porous medium. The problem has been extensively examined through laboratory experiments, as well as numerical simulations and theoretical models ([Saffman & Taylor, 1958](#); [Bensimon et al., 1986](#); [Homsy, 1987](#); [Paterson, 1981](#); [Tryggvason & Aref, 1983](#); [Nittmann et al., 1985](#); [Kadanoff, 1985](#); [Arnéodo et al., 1989](#); [Li et al., 2009](#); [Bischofberger et al., 2015](#); [Chen & Wilkinson, 1985](#); [Måløy et al., 1985](#); [Chen, 1987](#); [Fernández et al., 1990](#)). The dynamics of such displacement can be characterized by two dimensionless groups: the ratio of viscous to capillary forces, or the capillary number (Ca), and the ratio of defending to invading fluid viscosities, or viscosity contrast (M). For high Ca , the resulting displacement patterns are reminiscent of diffusion limited aggregation ([Witten et al., 1981](#); [Daccord et al., 1986](#); [Meakin et al., 1989](#); [Niemeyer et al., 1984](#); [Conti & Marconi, 2010](#)). For low Ca , the displacement dynamics becomes more intricate, and the emerging patterns display a strong dependence on the pore geometry ([Lenormand & Zarcone, 1985](#); [Lenormand et al., 1983, 1988](#); [Fernandez et al., 1991](#); [Måløy et al., 1992](#); [Furuberg et al., 1996](#); [Ferer et al., 2004](#); [Toussaint et al., 2005](#); [Holtzman et al., 2012](#)) and the wettability of the medium, that is, the chemical affinity of the solid for each fluid ([Stokes et al., 1986](#); [Trojer et al., 2015](#); [Zhao et al., 2016](#); [Odier et al., 2017](#)). In particular, an intermittent injection pressure signal emerges in the limit of low Ca ([Furuberg et al., 1996](#); [Måløy et al., 1992](#)). Given that in most practical applications visualization of the flow in porous media is not possible, the pressure signal is often the only source of information. Surprisingly, no modeling approach to date has been able to capture the injection pressure signal across different Ca and pore wettabilities. Here, we develop a new pore-network model that fills this gap, and we use it to explore the transition from viscous-dominated to capillary-dominated flow regimes by examining the connections among fluid morphology and pressure signal.

Pore network models of flow in porous media can be broadly classified into two groups: quasi-static and dynamic models ([Blunt, 2001](#); [Meakin & Tartakovsky, 2009](#); [Joekar-Niasar & Hasanzadeh, 2012](#)). Quasi-static models neglect viscous effects and advance the invading fluid through either invasion-percolation ([Chandler et al., 1982](#); [Lenormand et al., 1988](#)) or event-based algorithms

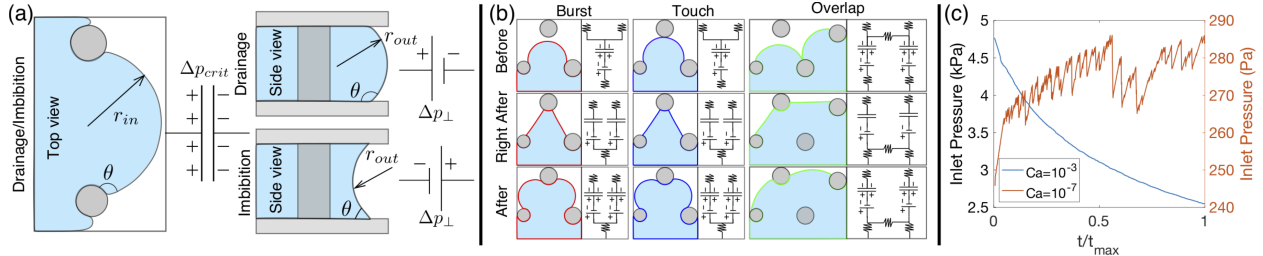


Figure 3-1: (a) Schematic diagram of in-plane and out-of-plane curvatures within the flow cell. Out-of-plane curvature represents the overall affinity of the porous medium to the invading fluid. It is determined by θ and is analogous to a battery. In-plane curvature changes as the local interface evolves while pinned to a pore throat, and it is analogous to a capacitor. (b) Evolution of burst, touch, and overlap events. (c) Temporal profiles of the injection pressure bear close resemblance to similar experiments in the drainage regime at low (orange) and high (blue) Ca (Furuberg *et al.*, 1996; Zhao *et al.*, 2016).

(Cieplak & Robbins, 1990, 1988). Although a quasi-static approach can be effective in reproducing experimental invasion patterns at low Ca (Primkulov *et al.*, 2018), it is unable to capture the temporal evolution of the injection pressure signal. Dynamic network models approximate the flow channels with a network of interconnected capillary tubes. Viscous pressure drops are calculated by assuming fully developed viscous flow within each tube. Local capillary pressures within the network are calculated from either the interface position within pore throats (Aker *et al.*, 1998b; Gjennestad *et al.*, 2018) or through mass balance of the two phases in pore bodies (Al-Gharbi & Blunt, 2005; Joekar-Niasar *et al.*, 2010). Another notable class of models is invasion-percolation in a gradient: a percolation model designed to incorporate buoyancy forces (Wilkinson, 1984; Birovljev *et al.*, 1991; Frette *et al.*, 1992; Meakin *et al.*, 1992), and then extended to model (linear) pressure gradients (Yortsos *et al.*, 1997). None of the invasion-percolation in a gradient studies, however, incorporate any notion of wettability (they all deal exclusively with strong drainage), pore-scale dynamics, or capillary-number-dependent pressure fluctuations.

In fact, most existing pore-network models, both quasi-static and dynamic, are limited to strong drainage (or injection of non-wetting fluid) and do not include wettability-induced cooperative pore filling (Joekar-Niasar *et al.*, 2010; Aker *et al.*, 1998b; Al-Gharbi & Blunt, 2005; Holtzman & Juanes, 2010). The only dynamic pore network model to date that includes cooperative pore filling events (Holtzman & Segre, 2015) does so by combining pore-level invasion events of Cieplak & Robbins (1988, 1990) with viscous relaxation through the pore-network. This viscous-relaxation assumption is at odds with the physics of interface motion in the capillary-dominated regime and, as a result, this model is unable to capture the injection pressure signal observed experimentally in the limit of intermediate and low Ca (Zhao *et al.*, 2016; Furuberg *et al.*, 1996; Måløy *et al.*, 1992). We present in §3.2 a consistent framework that combines viscous, capillary, and wettability effects in a single dynamic network model that builds a direct analogy between local fluid-fluid interfaces and electric capacitors. Our model reproduces, quantitatively, the fluid-fluid displacement patterns for a wide range of Ca and wettabilities (§3.3), and points to a surprising and heretofore unrecognized transition in the pressure fluctuations between the low and high Ca flow regimes (§3.4).

3.2 Moving capacitor model

Consider a moving fluid-fluid interface in a micromodel (FIG 3-1a). Neglecting dynamic-contact-angle effects (Hoffman, 1975) for simplicity, the shape of the meniscus between posts is uniquely defined by the combination of Laplace pressure and substrate wettability defined through a contact angle θ at which the interface meets post surfaces (Cieplak & Robbins, 1988, 1990). As the interface advances, the Laplace pressure increases until the interface encounters a *burst*, *touch* or *overlap* event, as defined by Cieplak & Robbins (1988, 1990). The *burst* event is equivalent to a Haines jump (Haines, 1930; Berg *et al.*, 2013), while the *touch* and *overlap* events take place when the local interface either touches the nearest opposing post or coalesces with a neighboring interface respectively [FIG. 3-1(b)]. If the interface becomes unstable due to *burst* or *touch*, a single pore is invaded and two new interfaces appear. In the case of an *overlap* event, two (in some cases more) pores are filled simultaneously. These pore-level events are an integral part of the model and, indeed, this sensitivity is what permits capturing wettability effects within the model. The events evolve differently at different wettabilities—burst events are most frequent in drainage, while touch and overlap are most frequent in imbibition (or injection of wetting fluid) (Cieplak & Robbins, 1990; Primkulov *et al.*, 2018).

We can explicitly calculate the critical Laplace pressure Δp_{crit} corresponding to all events from the values of the contact angle, radii and coordinates of the posts (Primkulov *et al.*, 2018), and thus can use the analogy between electric capacitors and fluid-fluid interfaces in constructing our network model. A capacitor represents the pinning of the fluid-fluid interface at a pore throat, and is active in both drainage and imbibition: the interface moves only when a local depinning threshold (Δp_{crit}) is reached, and the fluid front moves to restart the pinning-depinning cycle from zero in-plane curvature [Fig. 1(b)]. This progression of the in-plane curvature in our model was motivated by the work of Cieplak and Robbins (Cieplak & Robbins, 1988, 1990) [see also (Rabhani *et al.*, 2018)] and experiments on the progression of the in-plane curvature between the Hele-Shaw cell posts (Jung *et al.*, 2016; Lee *et al.*, 2017). This is what allows capturing pressure fluctuations in the limit of low Ca [Fig. 1(c)]. The battery analogy represents the overall affinity of the porous medium to the invading fluid, set by the out-of-plane curvature at the fluid front. The out-of-plane curvature is fixed throughout a single simulation, and determined by the value of the contact angle (given the constant gap between the flow-cell plates): it is positive in drainage and negative in imbibition [Fig. 1(a)]. To complete the analogy between an electric circuit and a pore network, one can think of a network of resistors being responsible for viscous effects, capacitors and batteries responsible for capillary effects, and local rules for circuit rearrangements responsible for wettability effects [FIG. 3-1(b)].

Therefore, the pressure drop across an edge of the network containing a fluid-fluid interface has three components: (i) pressure drop due to viscous dissipation, (ii) Laplace pressure drop due to in-plane curvature of the interface, and (iii) Laplace pressure drop due to out-of-plane curvature of the interface. We calculate the viscous pressure drop assuming Poiseuille flow in a capillary tube, which is analogous to the potential drop across a resistor. The out-of-plane component of the Laplace pressure can be expressed as either a positive or negative pressure jump ($\Delta p_{\perp} = -\frac{2\gamma \cos \theta}{h}$, where γ is the interfacial tension, and h is the cell height) depending on the substrate wettability; this is analogous to a battery in an electric circuit. The Laplace pressure due to in-plane curvature of the interface is analogous to a capacitor which allows flow until it reaches the critical pressure ($\Delta p_{\text{crit}} = \min\{p_{\text{burst}}, p_{\text{touch}}, p_{\text{overlap}}\}$). Since we can calculate Δp_{crit} for all edges at the invading fluid front, we use a linear estimate of the in-plane Laplace pressure drops within our network ($\Phi(t)\Delta p_{\text{crit}}$), where $\Phi(t)$ stands for the filling ratio of a given throat. When $\Phi(t) \rightarrow 0$, the in-

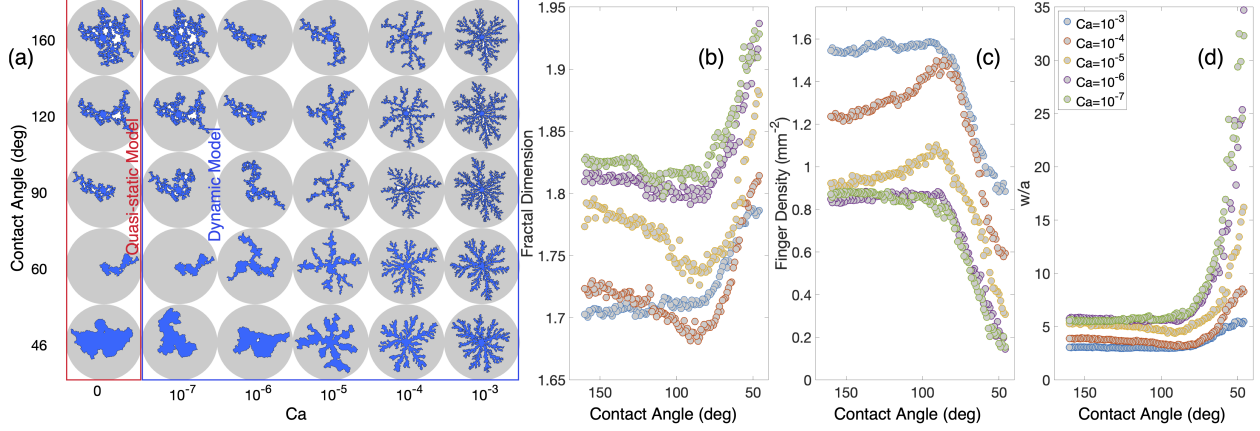


Figure 3-2: (a) Phase diagram of the invading fluid morphology at breakthrough; (b) Fractal dimension, computed by means of the box-counting method; (c) Number of fingers per unit area of injected fluid, which exhibits a maximum near $\theta = 90^\circ$; (d) Normalized finger width (w/a) at different Ca and wettabilities measured at breakthrough. Finger width increases as the posts become more wetting to the invading fluid.

plane Laplace pressure is negligible. When $\Phi(t) \rightarrow 1$, the throat is nearly full and has a critical in-plane Laplace pressure Δp_{crit} . This analogy between local interfaces and capacitors allows us to incorporate local changes in Laplace pressure due to filling of pore throats. Once a node in the network reaches its maximal potential, which coincides with its filling capacity, it becomes unstable and the interface advances. We assume that the in-plane and out-of-plane Laplace pressures are decoupled, and this is done to maintain the simplicity of the overall model. With this assumption, one can run the model for either $\frac{h}{a} \gg 1$ or $\frac{h}{a} \ll 1$, where these conditions would result in negligible or dominant contributions of the out-of-plane curvature in the model, respectively.

The topology of the pore network is captured through the incidence matrix A by examining the adjacency of the pores (Strang, 2007). We number all pores and adopt the convention that pore connections are oriented in the direction of increasing pore numbers. Rows of A represent edges, and columns of A represent nodes of the network. We also make use of the diagonal conductance matrix C , whose elements are hydraulic conductivities of the network edges. The elements of this matrix can be calculated as $c = \frac{\pi r^4}{8\mu L}$, assuming fully developed Hagen-Poiseuille flow through a rectangular tube with hydraulic radius r and length L , where μ is the effective viscosity of the fluid in the channel.

The pressure difference across the network edges can be calculated as $e = b - Ap$, where b and p stand for pressure change due to out-of-plane contribution to Laplace pressure (batteries) and node pressures, respectively. The network flow rates can be calculated from this pressure difference as $q = Ce$. At the same time, flow rates must obey mass conservation, $A^T q = f$, where f stands for flow sources at the nodes. After eliminating e , the flow through the network without the in-plane contribution to Laplace pressure (capacitors) is obtained through the following system of equations:

$$q = C(b - Ap), \quad (3.1)$$

$$A^T q = f. \quad (3.2)$$

We set constant flow boundary conditions at the inlet pores (at the center of the flow cell) and

constant pressure boundary conditions at the outlet pores (at the edges of the flow cell). We note that Ap can be decomposed into components of nodes with prescribed pressure and all other nodes ($Ap = A_{\text{outer}}p_{\text{outer}} + \tilde{A}\tilde{p}$), and therefore Eqs. (3.1)-(3.2) transform to:

$$\begin{bmatrix} C^{-1} & \tilde{A} \\ \tilde{A}^T & 0 \end{bmatrix} \begin{bmatrix} q \\ \tilde{p} \end{bmatrix} = \begin{bmatrix} b - A_{\text{outer}}p_{\text{outer}} \\ \tilde{f} \end{bmatrix} = \begin{bmatrix} \tilde{b} \\ \tilde{f} \end{bmatrix}. \quad (3.3)$$

The solution to (3.3) provides values of both edge flow rates and node pressures for given boundary conditions.

Finally, we incorporate the pressure drop due to in-plane Laplace pressure (capacitors) within the network. Taking into account the direction of the edges (an array $d(t)$ consisting of 1 and -1), the total pressure drop across the network edges can be written as $e = \tilde{b} - \tilde{A}\tilde{p} - d(t)\Phi(t)\Delta p_{\text{crit}}$. In other words, the in-plane Laplace pressure is the product of the filling ratio and the critical pressure from the quasi-static model (Primkulov *et al.*, 2018). Therefore, the equations governing two-phase flow through the network can be written as:

$$\begin{bmatrix} C^{-1}(t) & \tilde{A} \\ \tilde{A}^T & 0 \end{bmatrix} \begin{bmatrix} q(t) \\ \tilde{p}(t) \end{bmatrix} = \begin{bmatrix} \tilde{b} - d(t)\Phi(t)\Delta p_{\text{crit}} \\ \tilde{f} \end{bmatrix}. \quad (3.4)$$

We now discuss the mechanics of the time-stepping in our two-phase flow model. After we initialize the interface locations within the network, we use an adaptive forward Euler time stepping to update the filling ratios of the network edges at the interface $\Phi(t)$. We ensure that only a fraction of the edge total volume at the interface flows within the time-step (Aker *et al.*, 1998b). After every time-step, we use $\Phi(t)$ to update the conductance matrix $C(t)$ and resolve the flow through Eq. (3.4) with updated pressure drops across the fluid-fluid front.

In the spirit of the fundamental contributions from Cieplak and Robbins (Cieplak & Robbins, 1988, 1990), our model takes the form of an arrangement of cylindrical posts confined between the plates of a Hele-Shaw cell. The approach is simple enough to lead to universal findings, yet sufficiently complex to have direct relevance to microfluidic geometries, as well as engineered and natural porous media—much like Lenormand’s phase diagram (Lenormand *et al.*, 1988). By doing so, we demonstrate the ability to reproduce physics—in particular, pressure fluctuations under a wide range of wetting conditions—which, until now, were inaccessible to pore-network modeling. A limitation of the model presented here is that it does not extend to contact angles below 45° , where the wetting fluid preferentially wets the corners of the pore-geometry at low Ca and forms film flow at high Ca (Zhao *et al.*, 2016; Odier *et al.*, 2017).

3.3 Invasion patterns

We simulate immiscible fluid-fluid displacement by setting a constant injection rate at the center of the flow cell and zero pressure at the outlets. The invading and defending fluid viscosities are set to $8.9 \times 10^{-4} \text{ Pa} \cdot \text{s}$ and $0.34 \text{ Pa} \cdot \text{s}$ respectively. The post height h is $100 \mu\text{m}$, and interfacial tension γ is set to $13 \times 10^{-3} \text{ N/m}$. These parameters as well as the pore geometry are chosen to mimic the experiments of Zhao *et al.* (2016). The flow cell has an outer diameter of 30 cm. We perform simulations for wetting conditions from strong drainage ($\theta = 160^\circ$) to weak imbibition ($\theta = 46^\circ$). FIG. 3-1(c) shows the pressure profiles for $\theta = 160^\circ$ at $Ca \in \{10^{-3}, 10^{-7}\}$, respectively. In the limit of high Ca , the more-viscous defending fluid sustains substantial spatial pressure gradients, and the injection pressure gradually drops as more of the defending fluid is displaced (Zhao *et al.*, 2016). In

contrast, in the limit of low Ca, the pressure field is virtually uniform in each fluid, and the injection pressure exhibits intermittent fluctuations typical of slow capillary-dominated drainage (Knudsen & Hansen, 2002; Aker *et al.*, 1998a; Måløy *et al.*, 1992; Moebius & Or, 2012).

The morphology of the invading fluid at breakthrough can be analyzed by means of a binary-image representation of the invasion patterns (Cieplak & Robbins, 1990, 1988; Primkulov *et al.*, 2018) [FIG. 3-2(a)]. We estimate the width and number of fingers in the invading fluid pattern following the protocol outlined in (Cieplak & Robbins, 1988, 1990) and modified in (Primkulov *et al.*, 2018). The binary image is sliced horizontally and vertically, with each slice containing clusters of invading fluid pixels. We calculate the finger width as the mean size of these clusters. FIG. 3-2(d) shows that the finger width, normalized by the typical pore size, increases as $\theta \rightarrow 46^\circ$ for all Ca, which is in agreement with experimental observations (Stokes *et al.*, 1986; Trojer *et al.*, 2015; Zhao *et al.*, 2016). While FIG. 3-2(a) demonstrates that the number of fingers increases with Ca (Lenormand *et al.*, 1988; Fernández *et al.*, 1990; Zhao *et al.*, 2016), we observe an unexpected behavior [FIG. 3-2(b)]: the finger density changes with the substrate wettability, and exhibits a maximum around $\theta = 90^\circ$. This effect is most pronounced for $10^{-6} < \text{Ca} < 10^{-3}$ (when viscous and capillary effects are comparable).

We explain the peak in the viscous finger density at $\theta \approx 90^\circ$ in FIG. 3-2(b) by considering in-plane and out-of-plane contributions to the Laplace pressure. At a fixed Ca, the ratio of viscous and capillary forces in the micromodel changes as a function of substrate wettability. The capillary forces have out-of-plane contributions, which are nominally equal to zero when $\theta = 90^\circ$, so the ratio of viscous and capillary forces increases as θ changes from 160° to 90° at fixed Ca. In addition, when θ changes from 90° to 46° , the cooperative pore filling mechanisms become dominant and widen the largest fingers, which in turn consume the smaller ones and reduce the number of fingers. The combination of these two effects results in the local maximum in the number of viscous fingers around $\theta \approx 90^\circ$ across different Ca [FIG. 3-2(b)].

For a contact angle θ near 160° (strong drainage) and high values of Ca (10^{-3} and 10^{-4}), the invading fluid front advances through viscous fingers with fractal dimension close to 1.71, typical of DLA-type morphology (Witten *et al.*, 1981). As Ca is reduced to a low value (10^{-7}), the fractal dimension increases to about 1.82, characteristic of invasion-percolation (Wilkinson & Willemsen, 1983) [FIG. 3-2(b)]. This increasing trend in fractal dimension is consistent with the decrease in finger density [FIG. 3-2(c)] and the increase in finger width [FIG. 3-2(d)].

As the contact angle approaches 46° , cooperative pore filling becomes the dominant flow mechanism at all values of Ca. This flow regime results in the compact displacement of the defending fluid, and thus the fractal dimension increases, approaching a value of 2 at low Ca, indicative of stable displacement.

3.4 Pressure signature

The fundamental difference in the fluid-fluid displacement process between low and high Ca is reflected in the temporal injection-pressure signals [FIG. 3-3]. When the capillary number is relatively high ($\text{Ca} = 10^{-3}$), viscous forces dominate, and the injection pressure decreases with time for all substrate wettabilities (Zhao *et al.*, 2016) [FIG. 3-3(a)]. Here, most of the pressure drop takes place in the more-viscous defending fluid. Consequently, as more of the defending fluid is displaced, the pressure required to maintain the prescribed injection flow rate decreases. In contrast, at $\text{Ca} = 10^{-7}$, viscous dissipation is negligible, and the injection pressure is determined by the sum of outlet and Laplace pressures. As a result, the injection pressure fluctuates in a stick-slip manner around a mean value [FIG. 3-3(b)], as has been documented in slow drainage experiments (Måløy *et al.*,

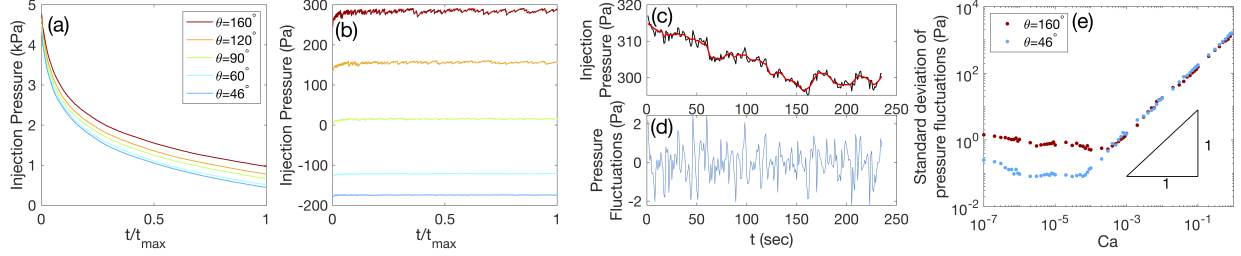


Figure 3-3: (a)-(b) Temporal evolution of the injection pressure at $Ca = 10^{-3}$ and $Ca = 10^{-7}$ respectively. At high Ca , the injection pressure decreases as the viscous fingers approach the outer boundary of the flow cell. At low Ca , the injection pressure is dominated by Laplace pressure fluctuations at the interface. We use wavelet decomposition (Cai, 2002; Sygoumi *et al.*, 2006, 2007) to split the pressure signal ($Ca = 10^{-5}$ and $\theta = 160^\circ$ here) into its (c) global trend and (d) cyclic component. (e) The standard deviation of the pressure fluctuations point at two different regimes. At low Ca , pressure fluctuations are dominated by stick-slip changes in Laplace pressure. At high Ca , pressure fluctuations are dominated by changes in the effective hydraulic conductance of dominant flow channels.

1992; Furuberg *et al.*, 1996; Moebius & Or, 2012). The pressure signals in FIG. 3-3(b) highlight the roles that in-plane and out-of-plane curvatures play in our model. Out-of-plane curvature plays the role of batteries, and thus provides additional resistance/drive (in drainage/imbibition, respectively) to the flow at the interface. The magnitude of the pressure drop/rise at the batteries is a function of wettability, which explains why the mean value of the injection pressure signal also varies with wettability [FIG. 3-3(b)]. The in-plane curvature plays the role of capacitors. As the invading fluid is injected, the in-plane component of Laplace pressure grows at the interface until the meniscus near the pore with lowest critical entry pressure becomes unstable due to *burst*, *touch* or *overlap*. This results in the rapid advance of the local interface, which pressurizes the defending fluid ahead. This overpressure then dissipates (see video S1 in supplemental materials). The critical pressures of *touch* and *overlap* are always smaller than the critical pressures of *burst* events (Primkulov *et al.*, 2018; Cieplak & Robbins, 1990, 1988), so the magnitude of the pressure fluctuations decreases as the substrate becomes more wetting to the invading fluid [FIG. 3-3(b)].

To gain further insight into the difference in the pressure signature between low and high Ca , we decompose the injection pressure signal into its global trend and fluctuating components with Block James-Stein wavelet decomposition (Cai, 2002) (see FIG. 3-3c-d). We compute the standard deviation of the fluctuating component of the pressure signal for both drainage and imbibition conditions ($\theta = 160^\circ$ and 46° , respectively) for a wide range of Ca , and find that it exhibits two distinct regimes [FIG. 3-3(e)]. At low Ca , pressure fluctuations are controlled by the stick-slip-type changes in local Laplace pressures. In contrast, at high Ca , pressure fluctuations are controlled by changes in the effective hydraulic conductance of the dominant flow channels. In the limit of high Ca , the Laplace pressure drop is negligible in comparison with the viscous pressure gradient, but the dominant flow channels are rearranged slightly as the fingers grow (see video S2 in supplementary materials). Since the pore geometry has a heterogeneous distribution of throat sizes, shifts in the dominant flow channels result in viscosity-driven pressure fluctuations at high Ca .

Scaling arguments support the findings from the model simulations. Let us take a pore-scale perspective (see Fig. 3-4). Invading a single pore involves overcoming a capillary pressure and pushing defending fluid out through a throat of width a and height h at a speed proportional to the injection rate. The capillary pressure is $p_{\text{cap}} \approx \gamma(\frac{1}{h} + \frac{1}{af(\theta)})$, where $f(\theta)$ is a wettability-dependent

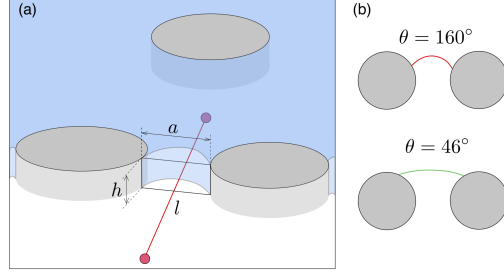


Figure 3-4: (a) Pore-scale perspective for the scaling of pressure fluctuations. The diagram shows a typical pore being invaded. The characteristic distance between the pore centers is l (red line), the pore height is h , and a characteristic throat size is a . (b) Typical configurations of the fluid-fluid interface in drainage and imbibition. Burst events are prevalent in drainage and the typical radius of out-of-plane curvature is of order a . Overlap events are prevalent in imbibition and the typical radius of out-of-plane curvature is an order of magnitude greater than a .

function that takes a value ~ 1 near drainage and ~ 10 near strong imbibition [Fig. 3-4(b)]. Taking variations of p_{cap} with a yields

$$\delta p_{\text{cap}} \sim \frac{\gamma}{a^2 f(\theta)} \delta a. \quad (3.5)$$

The characteristic flow velocity through a typical throat is $u = \frac{k(a,h)}{\mu} \frac{p_{\text{visc}}}{l}$, where $k(a,h) = R_h^2/8$ is the rectangular channel permeability and $R_h = \frac{ah}{2(a+h)}$ the hydraulic radius. Thus the viscous pressure is $p_{\text{visc}} \sim \frac{32(a+h)^2}{a^2 h^2} \mu u l = \frac{32\mu u l}{h^2} (1 + h/a)^2$. Taking variations of p_{visc} with a yields

$$\delta p_{\text{visc}} \sim \frac{64\mu u l}{h^2} (1 + h/a) \frac{h}{a^2} \delta a = \frac{64\mu u l}{ha^2} (1 + h/a) \delta a. \quad (3.6)$$

The magnitude of the total characteristic pressure fluctuation is $\delta p_{\text{cap}} + \delta p_{\text{visc}}$, and its two components are comparable when $\frac{\delta p_{\text{visc}}}{\delta p_{\text{cap}}} \sim 1$. Using equations (3.5) and (3.6),

$$\frac{\delta p_{\text{visc}}}{\delta p_{\text{cap}}} \sim \frac{64\mu u l}{ha^2} (1 + h/a) \frac{a^2 f(\theta)}{\gamma} = \text{Ca} f(\theta) 64 \frac{l}{h} (1 + h/a) \sim 1, \quad (3.7)$$

which implies a crossover Ca ,

$$\text{Ca}^* \sim \frac{h}{64 f(\theta) (1 + h/a) l}, \quad (3.8)$$

between flowrate-independent and flowrate-dependent pressure fluctuations [FIG. 3-3(e)]. The above argument suggests two interesting implications. First, one can potentially infer the characteristic pore size of the material from the fluctuations of the pressure signal in *both* viscously-dominated and capillary-dominated flow regimes. This is especially useful when visualization of the flow in pore space is not possible, which is the case in most porous materials. Second, the characteristic h , a , and l used in this study yield $\text{Ca}^* \approx \frac{10^{-3}}{f(\theta)}$, which reduces to $\text{Ca}^* \sim 10^{-3}$ for drainage and $\text{Ca}^* \sim 10^{-4}$ for imbibition, in agreement with the data in FIG. 3(e). This means that one should expect the transition from capillary-dominated to viscously-dominated flow regimes at different Ca^* in drainage and imbibition. The order of magnitude of $f(\theta)$ was obtained by calculating Δp_{crit} for all pore throats at $\theta \in \{46^\circ, 160^\circ\}$ with the quasi-static model (Primkulov *et al.*, 2018) and taking an average of $f(\theta) = \frac{\gamma}{a \Delta p_{\text{crit}}}$ for each contact angle. Finally, the viscous pressure fluctuation component

scales as $\delta p_{\text{visc}} \sim \mu u$, which is equivalent to $\delta p_{\text{visc}} \sim \text{Ca}$ when interfacial tension is kept constant. This explains the slope of the viscously-dominated portion of the graph in FIG. 3-3(e).

3.5 Conclusion

Overall, our moving-capacitor network model provides new fundamental insights into the dynamics of immiscible fluid-fluid displacement in porous media for a wide range of Ca and wettabilities. The model completes the picture of the displacement by covering both high and low Ca which allows, for the first time, to reproduce experimental observations of invading fluid patterns (Zhao *et al.*, 2016), injection pressure and front velocity in drainage (Måløy *et al.*, 1992; Furuberg *et al.*, 1996; Moebius & Or, 2012) and imbibition. Our observations and scaling arguments on the transition from viscous-dominated to capillary-dominated flow regime suggest that it is possible to infer the character of the multiphase-flow displacement purely from the injection pressure signal. This poses an exciting prospect for detailed experiments.

Chapter 4

Wettability and Lenormand’s diagram

This chapter has been published in [Primkulov et al. \(2021\)](#).

4.1 Introduction

Patterns form during fluid–fluid displacement in porous media in many natural and industrial processes. As sand castles dry, air percolates into the sand matrix and the integrity of the structure depends strongly on the resulting moisture distribution ([Richefeu et al., 2006](#); [Møller & Bonn, 2007](#)). In sugar processing, liquor-saturated charcoal packs are periodically cleansed with water, where channeling of the water phase is undesirable ([Hill, 1952](#)). In refractory ceramics manufacturing, the ceramic matrix is infiltrated by molten metal, where higher degree of infiltration leads to more resilient ceramics ([Léger et al., 2015](#)). In hydrocarbon recovery, oil is produced by displacing it with water and higher displacement efficiency is more economically desirable ([Datta et al., 2014](#)). Understanding morphology of the displacement front during such processes is of great value.

[Lenormand et al. \(1988\)](#) presented a phase diagram (Fig. 4-1) to characterize fluid–fluid displacement in a porous medium with two dimensionless parameters: the mobility ratio $M \equiv \mu_i/\mu_d$ and the capillary number $\text{Ca} \equiv \mu_i u/\gamma$, where u is the characteristic velocity, γ is the interfacial tension, and μ_i and μ_d are the dynamic viscosities of the invading and defending fluids, respectively. For high Ca, viscous forces dominate over capillary forces. For $M > 1$ (favorable displacement) and high Ca, the displacement front is viscously stable and the invading fluid sweeps the porous medium compactly ([Lenormand et al., 1988](#)). For $M < 1$ (unfavorable displacement) and high Ca, the displacement front is subject to the Saffman–Taylor instability ([1958](#)) and develops a self-similar viscous-fingering pattern ([Hill, 1952](#); [Van Meurs, 1957](#); [Chuoque et al., 1959](#); [Paterson, 1984](#); [Chen & Wilkinson, 1985](#); [Måløy et al., 1985](#); [Homsy, 1987](#); [Feder et al., 1989](#); [Hinrichsen et al., 1989](#); [Meakin et al., 1989](#); [Ben Amar, 1991a,b](#); [Li et al., 2009](#); [Patmonoaji et al., 2020](#)). For low Ca, capillary forces dominate over viscous forces and the displacement front advances via capillary invasion regardless of M ([Chandler et al., 1982](#); [Wilkinson & Willemsen, 1983](#); [Lenormand & Zarcone, 1985](#)).

The wetting properties of the fluid–fluid–solid system are not a part of the original [Lenormand et al. \(1988\)](#) diagram, although significance of wettability has been acknowledged in [Lenormand \(1990\)](#). A number of studies have discussed the importance of wettability at both high and low Ca ([Stokes et al., 1986](#); [Cieplak & Robbins, 1988, 1990](#); [Trojer et al., 2015](#); [Holtzman & Segre, 2015](#); [Zhao et al., 2016](#); [Jung et al., 2016](#); [Odier et al., 2017](#); [Singh et al., 2017](#); [Primkulov et al., 2018](#); [Zhao et al., 2019](#); [Primkulov et al., 2019](#)). Wettability can be characterized by the contact angle θ at which the fluid–fluid interface meets the solid surface, measured from the invading fluid (Fig. 4-1b-c). For $\theta < 90^\circ$, a more wetting fluid displaces a less wetting fluid and the process is called

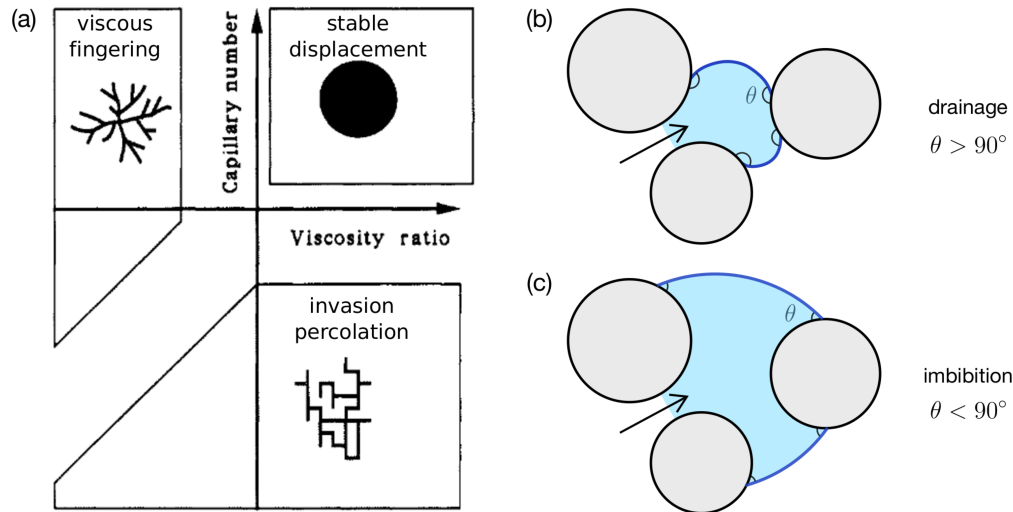


Figure 4-1: (a) Lenormand’s phase diagram for a nonwetting fluid displacing a wetting fluid in a porous medium. The displacement front advances through either viscous fingering, stable displacement, or invasion percolation, depending on the values of Ca and M . Adapted from [Lenormand \(1990\)](#). We endow Lenormand’s phase diagram with wettability, characterized through angle θ : (b) $\theta > 90^\circ$ in drainage, and (c) $\theta < 90^\circ$ in imbibition.

imbibition; for $\theta > 90^\circ$, a less wetting fluid displaces a more wetting fluid and the process is called drainage. As the system transitions from strong drainage to weak imbibition, the displacement becomes more compact: for high Ca and $M < 1$, the viscous fingers become wider ([Stokes *et al.*, 1986](#); [Trojer *et al.*, 2015](#); [Zhao *et al.*, 2016](#)); for low Ca and all M , the displacement patterns are very compact ([Cieplak & Robbins, 1988, 1990](#); [Trojer *et al.*, 2015](#); [Zhao *et al.*, 2016](#); [Primkulov *et al.*, 2018](#)). When a capillary-dominated system (low Ca) is in strong imbibition, the displacement front advances by preferentially filling crevices and corners in the pore-space (corner-flow) ([Levaché & Bartolo, 2014](#); [Zhao *et al.*, 2016](#); [Odier *et al.*, 2017](#); [Primkulov *et al.*, 2018](#)).

The invading fluid does not always displace the defending fluid completely from invaded pores; corner-flow is one such case. Another instance of incomplete displacement takes place in strong drainage at high Ca ([Park & Homsy, 1984](#); [Zhao *et al.*, 2016, 2019](#)). Here, solid surfaces behind the displacement front remain coated with a film of defending fluid ([Landau & Levich, 1988](#); [Bretherton, 1961](#); [Zhao *et al.*, 2016, 2019](#)). The opposite happens in strong imbibition for high Ca and $M < 1$: films of invading fluid advance on the solid surfaces ahead of the bulk displacement front ([Levaché & Bartolo, 2014](#); [Zhao *et al.*, 2016](#); [Odier *et al.*, 2017](#); [Zhao *et al.*, 2019](#)).

Pore-network models are often used to simulate flow in porous media, as they are both intuitive and computationally inexpensive ([Fatt, 1956](#); [Blunt & Scher, 1995](#); [Celia *et al.*, 1995](#); [Øren *et al.*, 1998](#); [Constantinides & Payatakes, 2000](#); [Patzek, 2001](#); [Blunt, 2001](#); [Joekar-Niasar & Hassanizadeh, 2012](#)). The pore geometry in such models is approximated by a network of nodes and links, and the flow within each phase is assumed to be fully developed Poiseuille flow. The relatively low computational cost of such models makes them ideal for exploring full the M – Ca – θ parameter space required for extending the original Lenormand diagram. No study to date, pore-network or otherwise, has produced a three-dimensional version of the Lenormand phase diagram, capturing gradual wettability-induced changes in the displacement patterns. The majority of pore-network studies have targeted only a limited range of wettability conditions. While fluid-fluid displacement has been extensively studied in separate sections of the M – Ca space in drainage ([Chandler *et al.*,](#)

1982; Wilkinson & Willemsen, 1983; Chen & Wilkinson, 1985; Lenormand *et al.*, 1988; Aker *et al.*, 1998b; Joekar-Niasar *et al.*, 2010; Al-Gharbi & Blunt, 2005; Gjennestad *et al.*, 2018), weak imbibition (Øren *et al.*, 1998; Patzek, 2001; Valvatne & Blunt, 2004), and strong imbibition with precursor wetting film flow through crevices and micro-roughness (Blunt & Scher, 1995; Vizika *et al.*, 1994; Tzimas *et al.*, 1997; Constantinides & Payatakes, 2000), only a few pore-network studies have explored the continuous transition in displacement patterns due to changes in θ .

A substantial advance towards capturing continuous wettability-induced changes in displacement patterns was made by Cieplak & Robbins (1988, 1990). Their model, which was designed for a 2D-porous medium comprised of a cylindrical obstacle array, reproduced experimentally observed compaction of the invading fluid as the system shifted from drainage to imbibition. This was done by introducing three pore-scale invasion mechanisms—burst, touch, and overlap (Fig. 4-3a-c)—whose relative frequencies shaped the displacement patterns at a given wettability. While this model was only valid for vanishing injection rates, Holtzman & Segre (2015) extended it by including viscous effects for $M \ll 1$. The model allowed capturing the experimentally observed stabilization of fingering displacement patterns away from $\text{Ca} \rightarrow 0$ (Trojer *et al.*, 2015; Stokes *et al.*, 1986).

At the same time, both pore-network models fell short of capturing three-dimensional effects that become important in strong imbibition. When $\theta < 45^\circ$, the Laplace pressure of a wetting fluid in the corner between a post and a plate can be negative (Fig. 4-3d). Therefore, a strongly wetting invading fluid can advance predominantly through crevices between the top/bottom plates and the cylindrical obstacles. We account for this three-dimensional mode of invasion by introducing a corner-flow event to the quasi-static model of Cieplak and Robbins (Primkulov *et al.*, 2018). Specifically, we incorporate the corner flow event in the “moving-capacitor” framework (Primkulov *et al.*, 2019), where we treat local fluid-fluid interfaces within a micromodel as analogs to capacitors in electrical circuits. Our approach in strong imbibition is similar to models by Blunt & Scher (1995) and Constantinides & Payatakes (2000), where displacement patterns are determined by competing flow through crevices and pore centers. However, unlike the model of Blunt & Scher (1995), our model fully accounts for viscous pressure gradients and is therefore not limited to small length scales. Furthermore, our model does not pre-assign a distribution of micro-channels like the work of Constantinides & Payatakes (2000); instead, connectivity of the invading fluid through crevices is determined by local micromodel geometry, and this connectivity evolves with the sequence of corner flow events. Ours is the first pore-network model to capture the continuous change in displacement patterns across all wettability conditions at arbitrary Ca and M . This feature, along with its computational efficiency, allows conducting an extensive parameter sweep over the entirety of M - Ca - θ space. We utilize this model to build the first picture of a three-dimensional version of Lenormand’s diagram, including an axis that represents wettability.

Recent studies have made strides in this direction, but stopped short of producing the full 3D diagram. Holtzman & Segre (2015) outlined the changes in displacement patterns within Ca - θ space for $M \ll 1$ using a pore-network model, excluding the possibility of corner flow. Hu *et al.* (2018) subsequently used continuum simulations to explore boundaries between viscous-dominated and capillary-dominated regimes for $M \approx 26$. This study was complemented by Lan *et al.* (2020), who used a dynamic pore-network model to explore the interplay between wettability and Ca for $M \approx 3 \cdot 10^{-3}$ which, like the model of Holtzman & Segre (2015), neglected corner flow and was therefore limited to $\theta > 45^\circ$. The phase diagrams produced in these studies correspond to a set of partial Ca - θ slices of the M - Ca - θ diagram we present in this chapter.

In §4.2, we present our “moving-capacitor” pore-network framework in detail (Primkulov *et al.*, 2019), which has been extended to all θ by incorporating corner flow events. Our model is based on the analogy between flow in porous media and currents in electrical circuits (Fatt, 1956), and it treats the local fluid-fluid interfaces as a combination of batteries and capacitors. The model builds

on many existing ideas in the porous-media community (Aker *et al.*, 1998b; Holtzman & Segre, 2015; Cieplak & Robbins, 1988, 1990; Blunt & Scher, 1995; Constantinides & Payatakes, 2000; Primkulov *et al.*, 2018, 2019) and combines them into a single framework that is able to handle M -Ca space over all wettability conditions ($0^\circ < \theta < 180^\circ$). The model is built for the quasi-two-dimensional, paradigmatic case of randomly placed cylindrical pillars between the flat plates of a Hele-Shaw cell. We use the model to explore the principal flow regimes of fluid-fluid displacement in porous media (§4.3). We then discuss the crossover from capillary invasion to viscous fingering under unfavorable displacement ($M < 1$) through pore-scale event statistics, symmetry of the displacement front, and autocorrelation of the flow field (§4.4). Finally, we synthesize the results of over 7000 dynamic simulations into an extension of Lenormand’s phase diagram that accounts for arbitrary wettability in §4.5.

4.2 Method

The model presented below builds on the analogy originally suggested by Fatt (1956), who pointed to the similarities between flow of a single fluid through a porous medium and flow of electrical current through a network of resistors. In this analogy, Ohm’s and Kirchhoff’s laws of electricity are analogous to the Hagen-Poiseuille law and conservation of mass for incompressible fluids, respectively. Therefore, resolving the viscous pressure drop due to flow through a particular network of tubes is equivalent to resolving the potential drop through an electrical circuit with identical topology.

This picture can be extended to two-phase flow by recognizing the similarities between local fluid-fluid interfaces and electrical capacitors. Electrical capacitors are traditionally used to store electrical charge: current builds up opposing charges across the capacitor plates, resulting in a step-change in electrical potential across the capacitor. This potential difference builds with current until a maximum is reached, which may result in dielectric breakdown of the capacitor. Similarly, when one fluid displaces another within a porous medium, the curvature of fluid-fluid interfaces increase as they advance into narrow sections of the pore geometry (*i.e.*, pore throats), corresponding to higher Laplace pressure across the interface. Overcoming the maximum Laplace pressure (*i.e.*, the capillary entry pressure) results in rapid invasion of the pore space ahead. This invasion is analogous to dielectric breakdown; however, unlike capacitors, the fluid-fluid interface will subsequently find the nearest pore throat and start re-building the Laplace pressure (thus curvature). We therefore refer to the model presented here as a “moving-capacitor” model.

We use the paradigmatic case of cylindrical obstacles in a Hele-Shaw cell as a quasi-2D porous medium (Cieplak & Robbins, 1988, 1990; Holtzman & Segre, 2015; Zhao *et al.*, 2016; Jung *et al.*, 2016; Holtzman, 2016; Primkulov *et al.*, 2018, 2019; Borgman *et al.*, 2019; Hu *et al.*, 2019). In this case, there is also an out-of-plane contribution to the Laplace pressure that is analogous to a battery at the displacement front. This “battery” represents the overall affinity of the porous medium to the invading fluid. For a constant and uniform gap between the plates, we assume that this out-of-plane curvature is fixed by the value of the contact angle, and is positive in drainage and negative in imbibition. By doing so, we neglect the effect of dynamic contact angle (Hoffman, 1975; Voinov, 1977; Cox, 1986).

We organize the remainder of this discussion into three subsections. We begin by explaining how we construct the pore network in §4.2.1. Then, we discuss the single-phase-flow model in §4.2.2. Finally we present the details of the two-phase-flow model (*i.e.*, the moving-capacitor model) in §4.2.3.

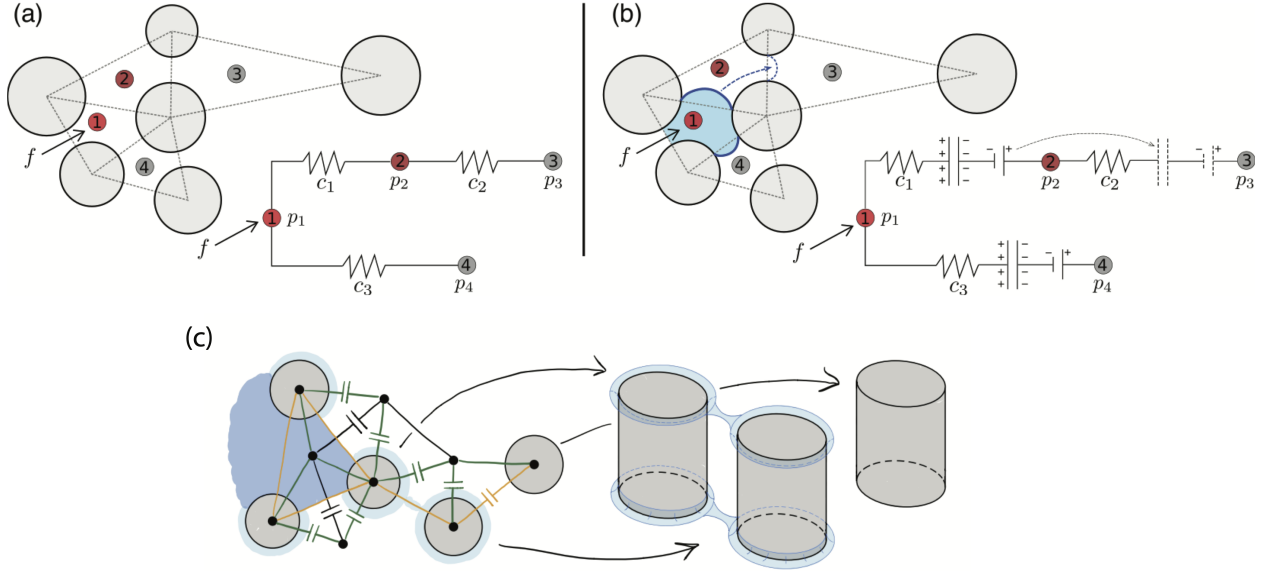


Figure 4-2: Schematic of flow through a porous medium and the analog electrical circuit for (a) single-phase flow and (b) two-phase flow. Nodes of the electrical circuit correspond to pore centres. Viscous pressure drop is analogous to potential drop through resistors, and fluid-fluid interfaces are analogous to a combination of a capacitor and a battery. (c) Schematic of the dynamic pore-network model in strong imbibition ($\theta < 45^\circ$), where capacitors are placed at the fluid-fluid interfaces. Nodes are placed at pore and post centers; black, orange, and green edges correspond to pore-to-pore, post-to-post, and pore-to-post edges respectively.

4.2.1 Pore-network construction

Unless otherwise specified, simulations are conducted in the geometry of a benchmark flow cell: a circular, patterned Hele-Shaw cell with a pore-throat size distribution that has a mean of $665 \mu\text{m}$ and a standard deviation of $337 \mu\text{m}$. The cell is 30 cm in diameter and has a centered injection port. We set the gap between the two plates of our flow cell to $100 \mu\text{m}$. The benchmark flow geometry is constructed using MATLAB's `pdemesh` tool with meshing parameters tuned to match the pore-throat size distribution reported in [Zhao *et al.* \(2016\)](#). In this construction, posts are centered at the nodes of the triangular mesh, and their radii are set to 45% of the length of the shortest adjacent edge.

Each mesh triangle represents a pore [Fig. 4-2(a)], so we can build the pore-network incidence matrix ([Strang, 2007](#)) by examining the adjacency of the triangles. We number all pores and adopt the convention that pore connections are oriented in the direction of increasing pore number. As such, the incidence matrix of the network presented in Fig. 4-2(a) is

$$\mathbf{A} = \begin{bmatrix} -1 & 1 & 0 & 0 \\ 0 & -1 & 1 & 0 \\ -1 & 0 & 0 & 1 \end{bmatrix}, \quad (4.1)$$

where rows and columns of \mathbf{A} represent edges and nodes, respectively. Here, 1 and -1 indicate entering and leaving the node, respectively. For example, edge 1 in eq. (4.1) is directed from node 1 to node 2.

We also make use of the diagonal conductance matrix \mathbf{C} , whose elements are the hydraulic

conductivities of the network edges. The elements of \mathbf{C} can be calculated as $c = \pi r^4 / 8\mu L$, assuming fully developed Hagen-Poiseuille flow through a rectangular tube with hydraulic radius r and length L , which correspond to pore-throat radius and distance between pore centers in a micromodel geometry, respectively.

4.2.2 Single-phase flow

The difference in potential across the network edges can be obtained from the incidence matrix as $\mathbf{e} = -\mathbf{A}\mathbf{p}$ (Strang, 2007). Here, \mathbf{p} is an array of node potentials, which in the example of Fig. 4-2a would read as $\mathbf{p} = (p_1, p_2, p_3, p_4)^T$. The network currents can be calculated from the potential difference as $\mathbf{q} = \mathbf{C}\mathbf{e}$, where the example of Fig. 4-2a would have $\mathbf{q} = (q_1, q_2, q_3)^T$ and

$$\mathbf{C} = \begin{bmatrix} c_1 & 0 & 0 \\ 0 & c_2 & 0 \\ 0 & 0 & c_3 \end{bmatrix}.$$

At the same time, currents must obey Kirchhoff's current law (or mass conservation in fluid flow), $\mathbf{A}^T\mathbf{q} = \mathbf{f}$, where \mathbf{f} is the array of current sources at the nodes and would read $\mathbf{f} = (f, 0, 0, 0)^T$ for the example in Fig. 4-2a. After eliminating \mathbf{e} , single-phase flow through the network is captured by the following system of equations:

$$\mathbf{q} = -\mathbf{C}\mathbf{A}\mathbf{p}, \quad (4.2)$$

$$\mathbf{A}^T\mathbf{q} = \mathbf{f}. \quad (4.3)$$

Eliminating \mathbf{q} , the node potentials are given by

$$\mathbf{p} = -(\mathbf{A}^T\mathbf{C}\mathbf{A})^{-1}\mathbf{f}. \quad (4.4)$$

We set constant-flow boundary conditions at the inlet pores (at the center of the flow cell) and zero-pressure boundary conditions at the outlet pores (at the edges of the flow cell).

4.2.3 Two-phase flow: moving capacitors

To extend the model to two-phase flow, we take advantage of the analogy between a capacitor and a fluid-fluid interface, where the drop in potential across the capacitor plates is analogous to the Laplace pressure. Consider the network diagram in Fig. 4-2(b). Initially, the capacitor is between nodes 1 and 2. As the current flows through the network, the capacitor accumulates charge and the potential difference across its plates builds. Capacitors with high accumulated potential difference hinder further flow, redirecting it elsewhere. Once the capacitor is filled to its maximum capacity, we allow it to advance to the next stable configuration at the neighboring edges (between nodes 2 and 3).

Our previous work on quasi-static fluid-fluid displacement (Primkulov *et al.*, 2018) provides a framework for deciding how and when capacitors move. For any given configuration of the fluid-fluid interface (capacitor locations), the quasi-static model predicts both the critical Laplace pressures (Δp_{crit}) and the type of interface instability. The type of instability event (*i.e.*, *burst*, *touch*, *overlap*, or *corner flow*; see Fig. 4-3) determines the next stable interface configuration (Cieplak & Robbins, 1990, 1988; Primkulov *et al.*, 2018). The critical Laplace pressure for *burst*, *touch*, and *overlap* events can be written as

$$\Delta p_{\text{crit}} = \gamma \left(\frac{1}{r_{\text{in}}} + \frac{1}{r_{\text{out}}} \right), \quad (4.5)$$

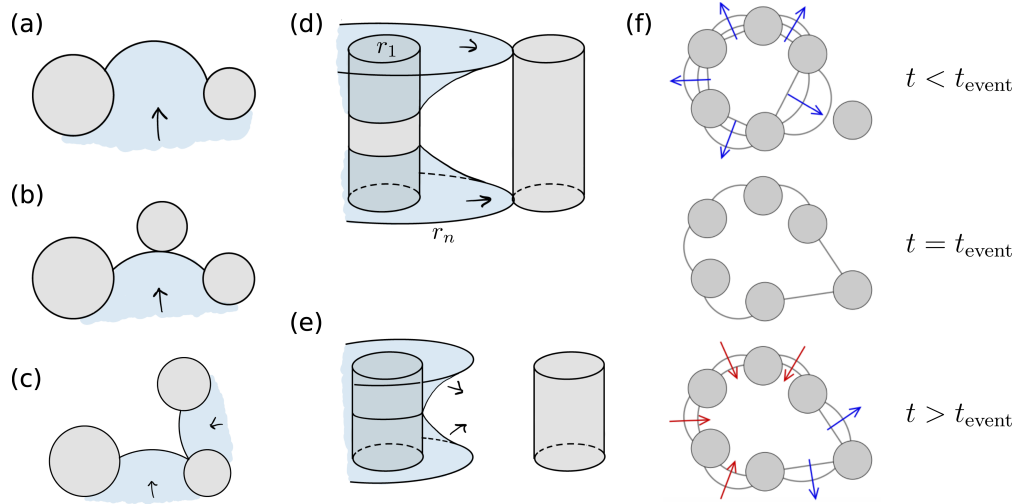


Figure 4-3: (a) A burst event occurs when the interface pushes past its highest stable curvature. (b) A touch event occurs when the interface touches the post ahead; (c) An overlap event occurs when two neighboring interfaces touch and coalesce, filling the pore cooperatively; (d) A corner-flow event occurs when a corner meniscus touches and coats the neighbouring post; (e) A capillary-bridge event occurs when corner menisci coalesce mid-post before reaching the next post; (f) A sequence of interface configurations before and after pore-invasion event at $t = t_{\text{event}}$ in capillary-dominated displacement. Figure adapted from [Primkulov et al. \(2018\)](#).

where $1/r_{\text{out}} = 2 \cos \theta / h$ is the out-of-plane curvature of the fluid-fluid interface and $1/r_{\text{in}}$ is the in-plane curvature that corresponds to either *burst*, *touch*, or *overlap* configuration (Fig. 4-3a-c). *Burst* events correspond to the highest stable in-plane curvature of the interface between two posts (Fig. 4-3a). *Touch* events correspond to the interface coming in contact with a nearby post (Fig. 4-3b). *Overlap* events occur when two neighboring interfaces coalesce within the pore space (Fig. 4-3c). When $\theta < 45^\circ$, the invading fluid tends to coat the corners between the posts and top/bottom plates. *Corner-flow* events occur when the horizontal extent of such meniscus reaches the nearest uncoated post (Fig. 4-3d). If these corner menisci instead overlap mid-post, they form a *capillary bridge* that expands spontaneously to the nearest post (Fig. 4-3e). The value of Δp_{crit} for *corner-flow* and *capillary bridge* events is calculated from the total curvature of the meniscus configurations depicted in Fig. 4-3d-e. A more detailed description of all pore-scale events is given in [Primkulov et al. \(2018\)](#).

We assume that the pressure drop across a capacitor at time t can be written as $\Delta p_{\text{crit}} \Phi(t) + \Delta p_{\text{min}}(1 - \Phi(t))$, where the filling ratio $\Phi(t)$ measures the fraction of the throat filled with invading fluid ([Holtzman & Segre, 2015](#)). A throat volume is defined as $2rLh$. We chose Δp_{min} so that it is equal to the smallest value of Δp_{crit} minus the standard deviation of Δp_{crit} within the network. This choice ensures that all menisci have the same Laplace pressure when corresponding throats are empty. Taking into account the direction of the edges (an array $\mathbf{d}(t)$ consisting of 1 and -1 for edges directed towards and away from the defending fluid, respectively), the total pressure drop across the network edges can be written as $\mathbf{e} = \mathbf{b} - \mathbf{A}\mathbf{p}$, where non-zero components of pressure drop array $\mathbf{b}(t)$ are written as $-\mathbf{d}(t)[\Delta p_{\text{crit}} \Phi(t) + \Delta p_{\text{min}}(1 - \Phi(t))]$. Therefore, the equations governing

two-phase flow through the network are

$$\begin{bmatrix} \mathbf{C}^{-1}(t) & \mathbf{A} \\ \mathbf{A}^T & \mathbf{0} \end{bmatrix} \begin{bmatrix} \mathbf{q}(t) \\ \mathbf{p}(t) \end{bmatrix} = \begin{bmatrix} \mathbf{b}(t) \\ \mathbf{f} \end{bmatrix}. \quad (4.6)$$

We now discuss time-stepping method in our two-phase flow model. After we initialize the interface locations within the “circuit”, we use adaptive Forward Euler time-stepping to update the filling ratios of the network edges at the interface, $\Phi(t)$. We ensure that no pore throat is filled in a single time step (Aker *et al.*, 1998b). After every time step, we use the effective viscosity (Aker *et al.*, 1998b; Holtzman & Segre, 2015) $\mu = \mu_i\Phi(t) + \mu_d(1 - \Phi(t))$ to update the conductivity matrix $\mathbf{C}(t)$ and resolve the flow via Eq. (4.6) with updated pressure drops across capacitors.

Whenever we encounter a time step (Δt) where one of the components of $\Phi(t)$ is greater than 1 we repeat the time step with an adjusted Δt until the unstable edge is exactly filled. Then, we remove the filled capacitor and replace it with empty capacitors at locations based on the type of instability that the quasi-static model outputs for the corresponding network edge (Primkulov *et al.*, 2018). Newly added capacitors are initialized with $\Phi = 0$ and accumulate potential drop as the above steps are repeated.

The typical solution of equation (4.6) in capillary-dominated regime produces the invasion sequence depicted in Fig. 4-3f, which can be separated into three steps: (i) interface curvatures build slowly across the displacement front ($t < t_{\text{event}}$); (ii) one of the interfaces reaches a “burst”, “touch”, or “overlap” configuration, and the corresponding pore is instantaneously invaded with new interfaces having zero in-plane curvature and Φ ($t = t_{\text{event}}$); (iii) the invading fluid redistributes to equalize the Laplace pressures at the displacement front ($t > t_{\text{event}}$). The displacement front spends the majority of its time in step (i). Since capturing the short-time dynamics of invasion events (*e.g.*, Haines, 1930) was not the primary objective of this work, we chose to make step (ii) instantaneous, and chose a relatively coarse Δt , with (iii) taking up only a few time steps between pore-invasion events. As a result, having $\Phi = 0$ correspond to zero in-plane curvature (our model) and having $\Phi = 0$ correspond to a negative in-plane curvature (expected experimentally) would only make an appreciable difference in the short-time single-pore dynamics, which is outside the scope of interest of this study. Indeed, it is likely that a fully resolved model of the interface at the pore level is needed to capture these short-timescale dynamics.

While our model of two-phase flow allows for re-emptying of network edges at the interface (Fig. 4-3f), our current implementation prohibits instability events in the reverse direction for simplicity of bookkeeping.

4.2.4 Moving-capacitor model in strong imbibition

When $\theta < 45^\circ$, a total curvatures of corner a meniscus (Fig. 4-3d,e) can be negative. This means that at some $\theta < 45^\circ$, invading fluid may advance by coating post corners instead of filling pore volumes. This was demonstrated in strong imbibition experiments of Zhao *et al.* (2016). Our treatment of strong imbibition fits naturally into the two-phase model described above, where the lowest Δp_{crit} corresponds to either corner-flow (Fig. 4-3d) or capillary bridge event (Fig. 4-3e). Below, we highlight a few distinguishing features of the “moving-capacitor” model for $\theta < 45^\circ$.

The overall flow network accounts for three distinct components: (i) a pore network, where nodes are pore centers and edges are pore-to-pore channels (black network in Fig. 4-2c), (ii) a post corner network, where nodes are placed at the centers of posts and edges are post-to-post connections (orange network in Fig. 4-2c), and (iii) a network connecting post centers to pore centers (green network in Fig. 4-2c).

Hydraulic radii of post-to-post and pore-to-post connections are taken as twice the ratio of channel cross sectional area to its wetted perimeter, which are calculated from the shape of the corner meniscus at its critical Laplace pressure (Fig. 4-3d,e). Volume assigned to a corner meniscus is defined to be $2\pi r_{\text{post}}\pi r_{\text{hydr}}^2$, where r_{post} and r_{hydr} are radius of the post and hydraulic radius of the meniscus respectively.

In post-to-post and pore-to-post capacitors, the value of Φ is assigned to a post, so that capacitors belonging to the same post have identical Laplace pressures at any given time. When a new post is coated, only one capacitor is removed from the network, the capacitor at the post-to-post connection (Fig. 4-2c), and new capacitors are added at the fluid-fluid boundaries of the new post.

Another distinction between the model we present here from the original “moving-capacitor” model is that the corner events depicted in Fig. 4-3d,e can trigger pore invasion. The volume of each pore in our network is bounded by three posts. Therefore, if all three posts experience corner events, the oil phase within the pore space pinches off and pore gets filled with invading fluid (Odiar *et al.*, 2017).

Finally, our model assumes perfectly smooth surfaces and leaves out the role that surface roughness, dynamic contact angle, and potential precursor films may play in the fluid-fluid displacement experiments. While our model on this idealized substrate predicts no corner flow when $h = 100 \mu\text{m}$ (Primkulov *et al.*, 2018), experiments detect the onset of corner flow for θ somewhere between 7° and 60° (Zhao *et al.*, 2016). This discrepancy between experiment and the model is reconciled through a fitting parameter that we discuss in detail in Appendix B.1.

4.3 Principal flow regimes

We begin our discussion by exploring the five principal regimes of fluid-fluid displacement in porous media: (i) viscous fingering, (ii) stable displacement, (iii) invasion percolation, (iv) cooperative pore filling, and (v) corner flow. We anchor our discussion of principal flow regimes around a few key metrics that help to characterize and distinguish the regimes:

1. *Fractal dimension* D_f is a measure of how a pattern fills the space in which it is embedded. For a two-dimensional pattern, D_f varies between 1 (for a line) and 2 (for a compact object). We calculate D_f with the box-counting method (Kenkel & Walker, 1996). Following this method, we tile our flow patterns with boxes of size ϵ and count the number of boxes N of that size needed to cover the pattern. We repeat this process for a sequence of ϵ and take D_f to be the slope of N against ϵ on a log-log plot (see Primkulov *et al.* (2018) for more details).
2. *Finger width* w/a is the ratio of mean finger width to mean pore size. We estimate w/a following a scheme detailed in Primkulov *et al.* (2018), which is an adaptation of an approach by Cieplak & Robbins (1988, 1990). Briefly, we divide our images into slices and record the mean size w of one-dimensional clusters containing the pattern. We repeat the same process for an image where we treat the entire pore space as a pattern and record the mean pore throat size as a .
3. *Modified capillary number* (Ca^*) measures the fraction of characteristic viscous to capillary pressures in our setup. We take

$$\text{Ca}^* = \frac{\Delta p_{\text{visc}}}{\Delta p_{\text{cap}}} = \frac{\max(\text{Ca}, \text{Ca}/M) \gamma R}{|\Delta p_{\text{crit}}| ah}, \quad (4.7)$$

after expanding the characteristic pressure drop as $\Delta p_{\text{visc}} = \max(\mu_i, \mu_d)uR/ah$, where R is

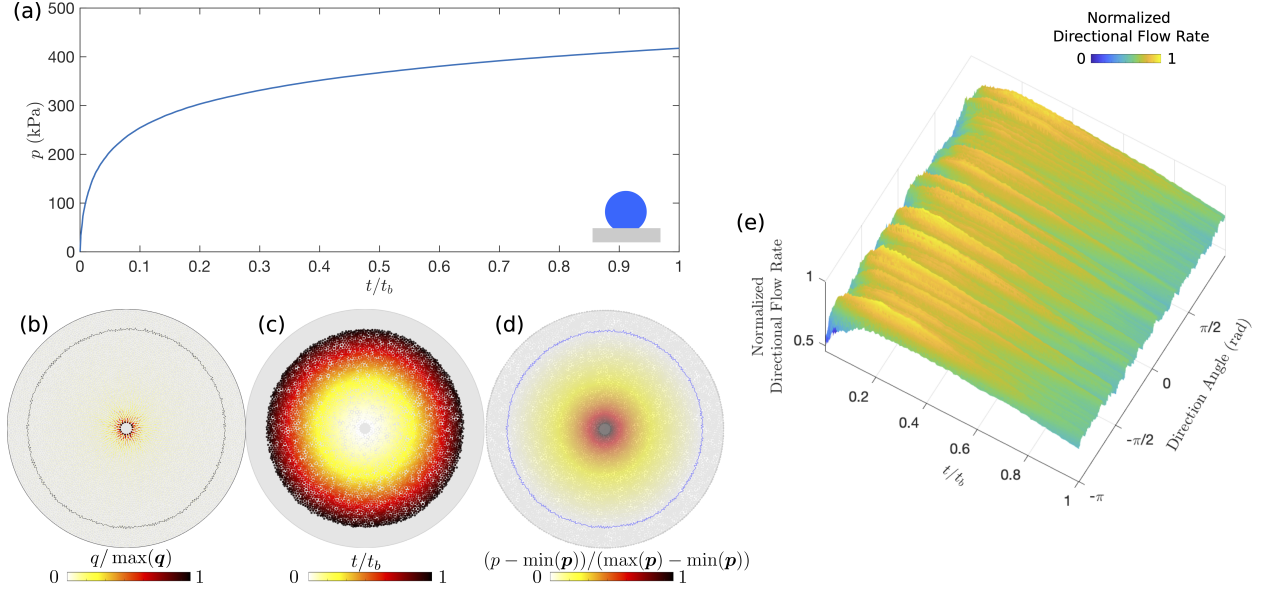


Figure 4-4: Stable displacement in the benchmark geometry for $Ca = 10^{-1}$, $M = 10^3$, and $\theta = 170^\circ$; (a) the injection pressure increases monotonically (t_b is the breakthrough time); (b) flow rates within the network show radial symmetry and radially-decreasing intensity ($\max(\mathbf{q})$ is the largest local flowrate at given t); (c) pore-invasion times reflect the radial symmetry in pattern growth; (d) pore-pressure distribution, where pressure gradients are significant only in the invading fluid ($\max(\mathbf{p})$ is the largest local pressure at given t); (e) the evolution of the directional flow rate is indicative of continuous compact flow, where apparent ridges are artifacts due to discrete pore throats with high flow rates near the cell center.

the radius of the Hele-Shaw cell. The term $\max(Ca, Ca/M)$ ensures that the greater viscous forces are taken into account, and the magnitude of critical Laplace pressure $|\Delta p_{\text{crit}}|$ is taken directly from simulations.

All of these metrics are time-dependent. We evaluate D_f and w/a at the moment of breakthrough, when the invading fluid first reaches the outer boundary of the flow cell. The characteristic velocity u used in calculating Ca and Ca^* is taken as $Q/2\pi r_{\text{min}}$, where r_{min} is the radial distance of the post closest to center of the Hele-Shaw cell. Additionally, we define a *directional flow rate* as the mean flow rate along different directions of the radial flow cell. We do so by dividing the flow cell into 10° sectors and calculating the mean flow rate for each sector as time progresses.

4.3.1 Stable displacement ($D_f = 1.93$, $w/a = 37$, $Ca^* > 1$)

When a more viscous fluid displaces a less viscous fluid ($M > 1$), the displacement front is hydrodynamically stable (Saffman & Taylor, 1958) because viscous forces smooth perturbations.

Simulations at $M = 10^3$, $Ca = 10^{-1}$, $\theta \in [46^\circ, 180^\circ]$ produce nearly perfectly circular patterns (Fig. 4-4). The injection pressure increases as the displacement progresses (Fig. 4-4a), with most of the pressure drop taking place in the invading fluid (Fig. 4-4d). The flow rate is radially symmetric, decreasing with radius (Fig. 4-4b,e), and pattern symmetry is maintained throughout (Fig. 4-4c).

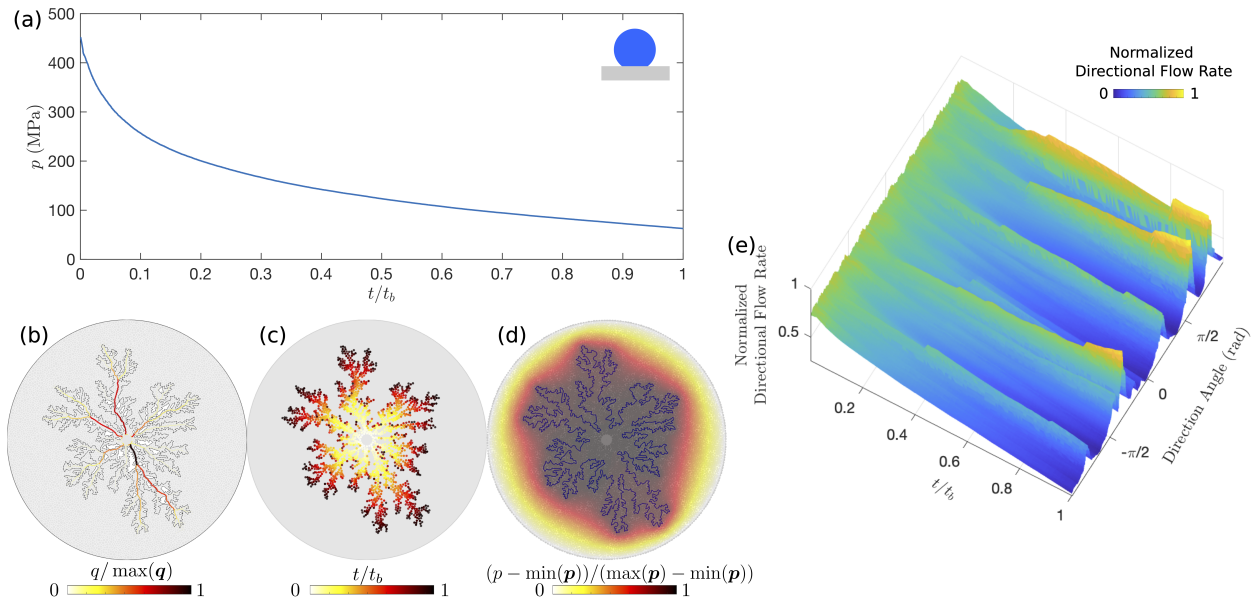


Figure 4-5: Viscous fingering in the benchmark geometry for $Ca = 10^{-1}$, $M = 10^{-3}$, and $\theta = 170^\circ$; (a) the injection pressure decreases monotonically in time (t_b is the breakthrough time); (b) flowrates within the network are pronounced along the main branches of the viscous fingers ($\max(\mathbf{q})$ is the largest local flowrate at given t); (c) pore-invasion times reflect the radial symmetry in pattern growth; (d) pore-pressure distribution, where most pressure changes occur within the defending fluid ($\max(\mathbf{p})$ is the largest local pressure at given t); (e) the evolution of the directional flow rate shows persistent (rather than sporadic) growth of viscous fingers.

4.3.2 Viscous fingering ($D_f = 1.63$, $w/a = 2.1$, $Ca^* > 1$)

Stable displacement is often desirable, but not always attainable in industrial applications like oil recovery (Chuoque *et al.*, 1959) and sugar processing (Hill, 1952). Viscous fingers develop under potential flow when a less-viscous fluid displaces a more viscous one ($M < 1$).

In Fig. 4-5, we highlight the signatures of viscous fingering for the benchmark pore geometry. The simulation in Fig. 4-5 is conducted for $Ca = 10^{-1}$, $M = 10^{-3}$, $\theta = 170^\circ$. As the displacement advances, the injection pressure decreases (Fig. 4-5a) because the majority of the pressure drop takes place in the defending fluid (Fig. 4-5d). Although the pressure appears to decrease smoothly in time, removing the global trend from the signal would expose fluctuations due to intermittent activity at the displacement front (Primkulov *et al.*, 2019). As the fingers develop and grow, they focus the flow along their main branches (Fig. 4-5b,e). The displacement pattern remains radially symmetric throughout (Fig. 4-5c). In fact, the diffusive signature of the pressure field in the defending fluid is what generates the striking similarity between viscous fingering and other patterns in nature, such as diffusion-limited aggregation (DLA) (Meakin *et al.*, 1989), dielectric breakdown of materials (Niemeyer *et al.*, 1984), and spreading of fire fronts (Conti & Marconi, 2010). The diffusive pressure field arises from Darcy flow and incompressibility, which lead to $\nabla^2 p = 0$ in the defending fluid, which is identical to the diffusive solute concentration field in DLA (Paterson, 1984).

4.3.3 Invasion percolation ($D_f = 1.8$, $w/a = 3$, $Ca^* < 1$)

When the invading fluid advances very slowly and viscous forces are negligible ($Ca \rightarrow 0$), the flow is governed exclusively by capillary forces. In drainage ($\theta > 90^\circ$), the invading fluid advances mainly

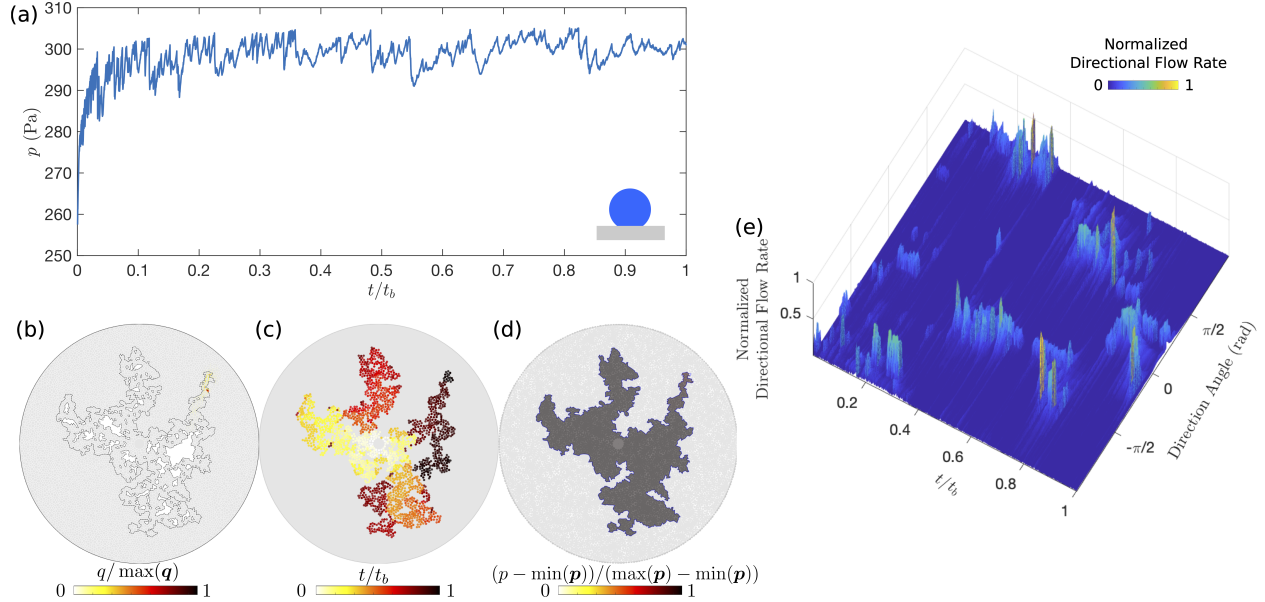


Figure 4-6: Invasion percolation in the benchmark geometry for $\text{Ca} = 10^{-7}$, $M = 1$, and $\theta = 170^\circ$; (a) the injection pressure fluctuates sharply due to pore-invasion events (t_b is the breakthrough time); (b) flowrates within the network are very localized, only a small fraction of the pore space is hydrodynamically active at any given time ($\max(\mathbf{q})$ is the largest local flowrate at given t); (c) pore-invasion times show asymmetric pore invasion clusters; (d) the pore-pressure distribution is uniform within each fluid ($\max(\mathbf{p})$ is the largest local pressure at given t); (e) the evolution of the directional flow rate shows intermittency in flow direction.

through *burst* events and the flow is well captured by the invasion-percolation model (Chandler *et al.*, 1982; Wilkinson & Willemsen, 1983; Lenormand & Zarcone, 1985).

We explore the characteristics of invasion percolation by simulating fluid-fluid displacement at $\text{Ca} = 10^{-7}$, $M = 1$, and $\theta = 170^\circ$ on the benchmark pore geometry (Fig. 4-6). The pressure distribution in the invasion-percolation regime is spatially uniform within each fluid (Fig. 4-6d), with the two fluid pressures differing by the Laplace pressure. As the displacement front advances, the pressure in the invading fluid is modulated by the sequence of lowest capillary entry pressures, and fluctuates sharply (Fig. 4-6a) (Måløy *et al.*, 1992; Furuberg *et al.*, 1996). This intermittency is also reflected in the flow field: only a small fraction of the pore space is active at any given time (Fig. 4-6b), and the flow direction changes frequently (Fig. 4-6e). As a result, the emerging flow pattern lacks radial symmetry throughout the displacement, with invasion-time patches reflecting invasion avalanches (Fig. 4-6c).

4.3.4 Cooperative pore filling ($D_f = 1.93$, $w/a = 15$, and $\text{Ca}^* < 1$)

Cooperative pore filling is a capillary-dominated regime that produces compact displacement patterns. Although cooperative pore filling can take place in viscous flow regimes, they are most prominent in weak imbibition and can dominate the displacement pattern when viscous forces are small. During cooperative pore filling, the displacement front advances mainly through *overlap* and *touch* events (see §2), and the increased fraction of *overlap* events smooths the displacement front (Cieplak & Robbins, 1988, 1990; Holtzman & Segre, 2015; Primkulov *et al.*, 2018). As a result, the displacement front sweeps the defending fluid completely, producing compact displacement patterns

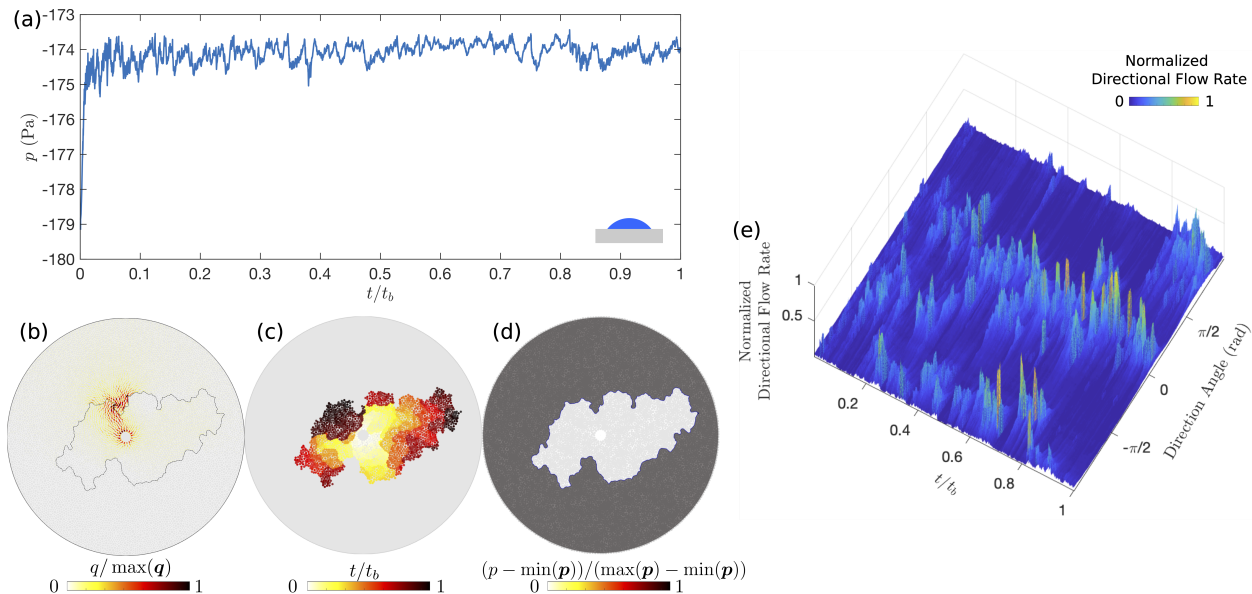


Figure 4-7: Cooperative pore filling in the benchmark geometry for $\text{Ca} = 10^{-7}$, $M = 1$, and $\theta = 46^\circ$; (a) the injection pressure is highly intermittent (t_b is the breakthrough time); (b) flowrates within the network are localized, and only a small fraction of them have appreciable flow; (c) pore-invasion times reveal pore-invasion clusters ($\max(\mathbf{q})$ is the largest local flowrate at given t); (d) the pore-pressure distribution is uniform within each fluid phase ($\max(\mathbf{p})$ is the largest local pressure at given t); (e) the evolution of the directional flow rate shows a high degree of intermittency in the flow direction.

(Fig. B-4).

Cooperative pore-filling simulations on the benchmark pore geometry at $\text{Ca} = 10^{-7}$, $M = 1$, and $\theta = 46^\circ$ (Fig. 4-7) show many similarities to invasion percolation (§4.3.3). The pressure is uniform in each fluid phase (Fig. 4-7d), but exhibits sharp fluctuations in time (Fig. 4-7a). The flow field is highly intermittent (Fig. 4-7e), with only a small fraction of pores active at any given moment (Fig. 4-7b). This intermittency results in asymmetric and patch-like growth of the displacement pattern (Fig. 4-7c). Unlike invasion percolation, cooperative pore filling produces compact displacement patterns with no trapped patches of defending fluid. The difference stems from the nature of pore-scale invasion events: invasion percolation is dominated by *burst* events while cooperative pore filling is dominated by *overlap* and *touch* events (Cieplak & Robbins, 1988, 1990; Holtzman & Segre, 2015; Primkulov *et al.*, 2018).

4.3.5 Corner flow ($D_f = 1.54$, $w/a = 0.8$, $\text{Ca}^* < 1$)

In strong imbibition, the invading fluid no longer advances by filling the pores completely—instead, the invading fluid advances mainly through *corner-flow* events where it coats the corners at the intersection of posts with the top and bottom plates of the Hele-Shaw cell (Fig. 4-2c).

Fig. 4-8 explores corner flow through simulations at $\text{Ca} = 5 \cdot 10^{-7}$, $M = 0.1$, and $\theta = 4^\circ$ on the benchmark pore geometry. Corner flow shares many similarities with other capillary-dominated regimes. The spatial distribution of pressure is uniform within each fluid (Fig. 4-8d), while the injection pressure shows intermittency characteristic of capillary-dominated displacements (Fig. 4-8a). Only a small fraction of the pore space has appreciable flow (Fig. 4-8b), and flow changes direction frequently (Fig. 4-8e). The resulting pattern grows asymmetrically throughout the displacement

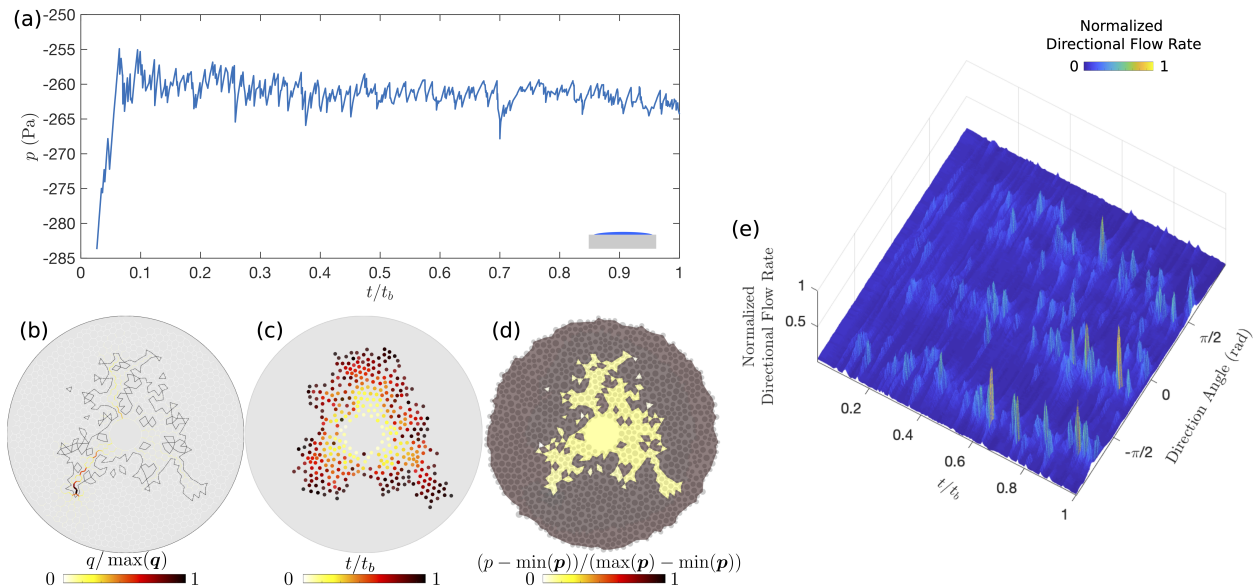


Figure 4-8: Corner flow in the benchmark geometry for $Ca = 5 \cdot 10^{-7}$, $M = 0.1$, and $\theta = 4^\circ$; (a) the injection pressure is highly intermittent (t_b is the breakthrough time); (b) flowrates within the network are localized, and only a small fraction of them have appreciable flow ($\max(\mathbf{q})$ is the largest local flowrate at given t); (c) pore-invasion times show radial asymmetry; (d) the pore-pressure distribution is uniform within each fluid phase ($\max(\mathbf{p})$ is the largest local pressure at given t); (e) the evolution of the directional flow rate shows a high degree of intermittency in the flow direction.

(Fig. 4-8c).

4.4 Crossover from viscous-dominated to capillary-dominated flow

We examine the difference in the invasion dynamics between high and low Ca through the spatial and temporal distributions of pore-invasion events. In this section, we focus on unfavorable viscosity contrast displacement, $M = 1/340$ (Zhao *et al.*, 2016, 2019). The effective ratio of viscous to capillary forces is therefore Ca/M , which we use in this section. Fig. 4-9a shows histograms of the Euclidean distance Δs between consecutive pore-invasion events. The distribution of Δs indicates that consecutive pore-invasion events are significantly more likely to take place near each other for low Ca/M than for high Ca/M . Furthermore, the time Δt_{inv} between consecutive pore-invasion events at $Ca/M = 10^{-7}$ shows that the median Δt_{inv} increases as $\theta \rightarrow 46^\circ$ (Fig. 4-9b). As the wettability of the substrate changes from strong drainage to weak imbibition, the relative frequency of cooperative pore-filling events increases (Cieplak & Robbins, 1990, 1988; Primkulov *et al.*, 2018). The increase in Δt_{inv} is chiefly due to the increase in relative frequency of *overlap* events, which result in rapid invasion of several neighboring pores. This in turn leads to significant retraction of the invading fluid from all of the throats at the displacement front. Thus, more time is needed to refill the pores at the displacement front, which results in the steady increase in Δt_{inv} as θ decreases (Fig. 4-9b).

The velocity distribution within the porous medium is also strikingly different at low and high Ca/M . We plot the temporal evolution of the directional flow rate for $\theta = 46^\circ$ in Fig. 4-9(d-f). At $Ca/M = 10^{-3}$, the invading fluid forms high velocity flow channels that persist until breakthrough

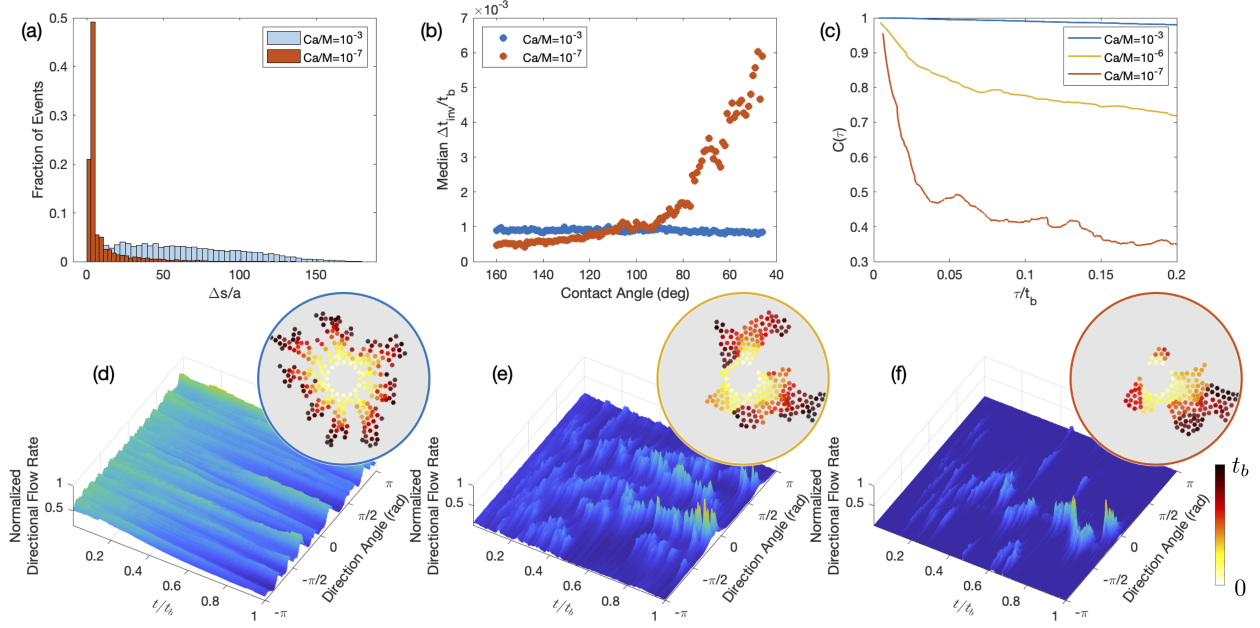


Figure 4-9: (a) Histogram of the distance (Δs) between consecutive pore-invasion events. (b) Median time (Δt_{inv}) between consecutive pore-invasion events as a function of θ . (c) Spatiotemporal autocorrelation of the normalized directional flow rate fields for $\theta = 46^\circ$. (d-f) Temporal evolution of the normalized directional-flow-rate fields for $\theta = 46^\circ$ and (d) $Ca/M = 10^{-3}$, (e) $Ca/M = 10^{-6}$, (f) $Ca/M = 10^{-7}$. The plots are complemented with the pore invasion time diagrams (insets).

(Fig. 4-9d). The pressure gradients in the defending fluid dominate the dynamics, and the invading fluid flows through growing viscous fingers. The displacement front advances with strong radial symmetry (Fig. 4-9d and video S3), as observed experimentally (Måløy *et al.*, 1985; Løvøll *et al.*, 2004; Holtzman *et al.*, 2012). As Ca/M decreases (Fig. 4-9e-f), the front velocity becomes increasingly intermittent. The pressure gradients within the fluids are negligible, and the pressure changes in the network are due almost exclusively to the Laplace pressure at the displacement front. Only portions of the displacement front are active at any given time (Holtzman *et al.*, 2012; Ferer *et al.*, 2004), and the front advances in asymmetric patches (Fig. 4-9e-f and video S1).

This transition from viscous-dominated to capillary-dominated flow can be quantified through the spatiotemporal autocorrelation of the normalized directional flow rate (Fig. 4-9c). The autocorrelation is calculated as $C(\alpha, \tau) = \frac{\langle q(\alpha, t)q(\alpha, t+\tau) \rangle}{\langle q(\alpha, t)q(\alpha, t) \rangle}$, where $\langle \cdot \rangle$ indicates the ensemble average over time, α is the direction, and τ is the time separation between the directional flow rate profiles. The average of $C(\alpha, \tau)$ over all α is shown in Fig. 4-9c for $\theta = 46^\circ$. The flow field becomes increasingly uncorrelated at low Ca/M , with a qualitative transition taking place below $Ca/M = 10^{-5}$.

4.5 Extending Lenormand's phase diagram

We extend Lenormand's diagram by simulating fluid-fluid displacement over a wide range of θ , Ca , M on the benchmark pore geometry (7560 simulations in total). This thorough sweep of the parameter space is possible due to the relatively low computational cost of our model. For each simulation, we measure D_f , w/a , and Ca^* at the moment of breakthrough. We use these variables to delineate regions corresponding to the different principal flow regimes.

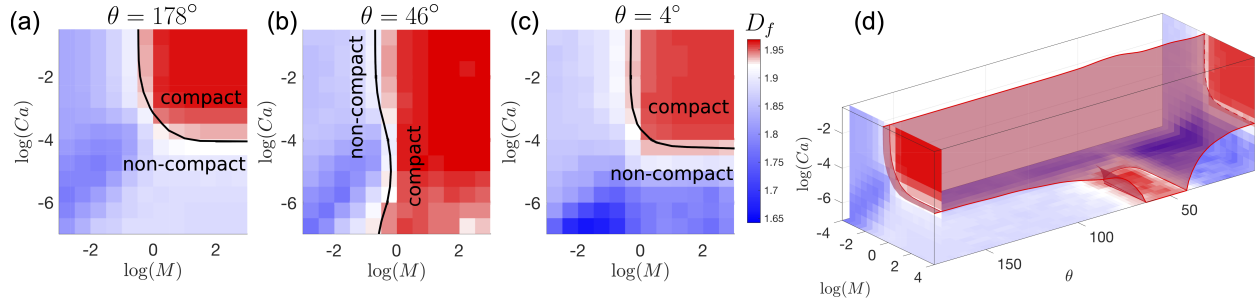


Figure 4-10: Evolution of D_f in M - Ca - θ space. Slices of the simulation data in (a) drainage, (b) weak imbibition, and (c) strong imbibition. (d) The maroon isosurface corresponding to $D_f = 1.92$ is used to draw the boundary between compact and non-compact displacement patterns. The black lines are the intersections of the isosurface with the cross-sections.

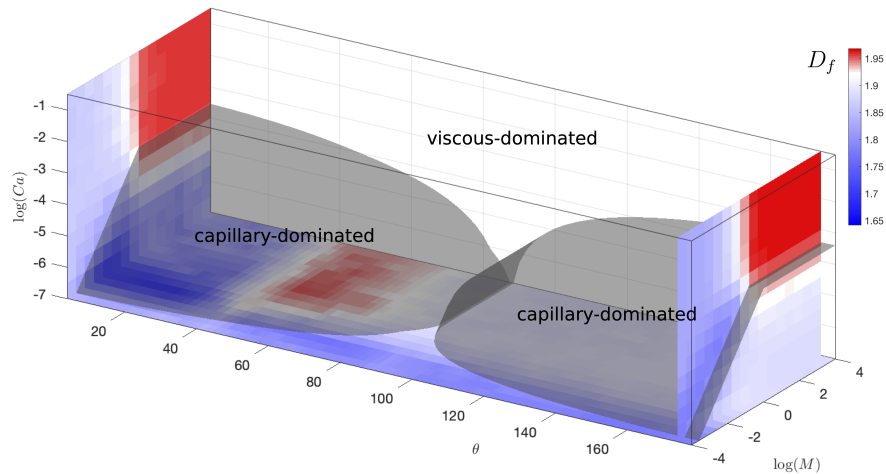


Figure 4-11: Viscous-dominated and capillary-dominated regions of M - Ca - θ space are separated by setting $Ca^* = 1$ in equation (4.7). This is depicted with a dark grey surface in this figure.

First, we use the fractal dimension D_f to separate compact patterns from non-compact patterns. Compact patterns include stable displacement and cooperative pore filling, both of which have $D_f > 1.92$ (maroon isosurface in Fig. 4-10d). A threshold based on w/a provides similar results (not shown).

Next, we use Ca^* to separate viscous-dominated flow regions (stable displacement and viscous fingering) from capillary-dominated flow regions (cooperative pore filling, invasion percolation, and corner flow). The surface resulting from $Ca^* = 1$ in Eq. (4.7) is depicted in Figure 4-11 in dark grey: the space above this surface is viscous-dominated, the space below it is capillary-dominated. The crease on the $Ca^* = 1$ surface originates from vanishing out-of-plane contribution to Laplace pressure near $\theta = 90^\circ$.

The combination of the maroon and gray isosurfaces from Figs. 4-10-4-11 is sufficient for delineating the principal flow regimes:

- invasion percolation is capillary dominated ($Ca^* < 1$) and non-compact ($D_f < 1.92$);
- cooperative pore filling is capillary dominated ($Ca^* < 1$) and compact ($D_f > 1.92$);
- corner flow is capillary dominated ($Ca^* < 1$) and non-compact ($D_f < 1.92$);

- viscous fingering is viscous dominated ($Ca^* > 1$) and non-compact ($D_f < 1.92$);
- stable displacement is viscous dominated ($Ca^* > 1$) and compact ($D_f > 1.92$).

Although we use sharp boundaries to outline regions that belong to different flow regimes, the transitions from one regime to another are smooth, as is evident from the cross-section images in Figs. 4-10–4-11.

Our extension of Lenormand’s diagram with added wettability axis is presented in Fig. 4-12. Our model faithfully reproduces the original diagram in drainage (cross-section $\theta = 180^\circ$ in Fig. 4-12), but reveals a more complete picture of the fluid-fluid displacement in porous media by augmenting the phase diagram with a wettability (θ) axis.

To assess the influence of pore-scale disorder on the displacement pattern, we run simulations on a pore geometry in which we can precisely define, and tune, the degree of geometric variability among realizations. To do so, we generate a regular triangular lattice with 2.8 mm spacing between vertices and place posts on its vertices. The radii of the posts are drawn from a uniform distribution ($r_0 - \xi r_v, r_0 + \xi r_v$), where $r_0 = 1100 \mu\text{m}$ and $r_v = 300 \mu\text{m}$ are selected to match the mean post size of the benchmark geometry and $\xi \in [0, 1]$ is the index of disorder. When $\xi = 0$, the medium is ordered and anisotropic; when $\xi = 1$, the medium is disordered and isotropic. As demonstrated in Appendix B.2, the values of D_f and w/a do not change significantly with the degree of disorder ξ . Therefore, although the data in Fig. 4-12 were collected from simulations on a single benchmark pore geometry, the results apply generally to porous media with varying degree of disorder. The capillary-dominated region of the phase diagram ($Ca^* < 1$) is divided into invasion percolation, cooperative pore filling, and corner flow. The boundary between compact and non-compact flow in the capillary-dominated region of Fig. 4-12 changes significantly with Ca : the upper and lower bounds (in θ) of the cooperative pore filling region move apart as Ca approaches the grey surface. When $M > 1$, viscous forces stabilize the displacement front and aid cooperative pore filling events in making the patterns more compact (Hu *et al.*, 2018).

The shape of the extended Lenormand diagram can be inferred outside the M – Ca – θ parameter space probed with the “moving-capacitor” model in Fig. 4-12. In particular, the cooperative pore filling region extends further into the $M < 1$ region as Ca decreases. This is evident from the quasi-static limit of the model, where cooperative pore filling boundaries are independent of M .

The extended Lenormand diagram in Fig. 4-12 is generated for a single pore geometry. While the overall shape of the diagram is expected to hold across different micromodels with a wide range of pore-scale disorder, spacing between the posts, and gap thickness h , the boundaries between the principal flow regimes are likely to shift depending on the pore structure. For example, increasing the spacing between the post centers would bring the onset of cooperative pore filling to higher θ (Prinkulov *et al.*, 2018). Larger spacing between the posts would also make corner flow less dominant in strong imbibition, as higher critical pressures would be needed to coat post corners. Therefore, compact displacement would occupy a greater proportion of the overall space in Fig. 4-12. The degree of disorder is also known to roughen the displacement front and shift the boundary between invasion percolation and viscous fingering (Holtzman & Juanes, 2010; Holtzman, 2016; Hu *et al.*, 2019). Given that the pore geometry used in Figure 4-12 is similar to one with $\xi = 0.99$ in Appendix B.2, a pore space with smaller degree of disorder would make compact displacement more favorable, which in turn would enlarge the compact displacement region in Fig. 4-12 (stable displacement and cooperative pore filling).

One should not think of the boundaries between the principal flow regimes in Fig. 4-12 as sharp, because transitions from one regime to another are gradual. Regions of the M – θ – Ca space near the maroon and grey boundaries correspond to crossover zones between principal flow regimes.

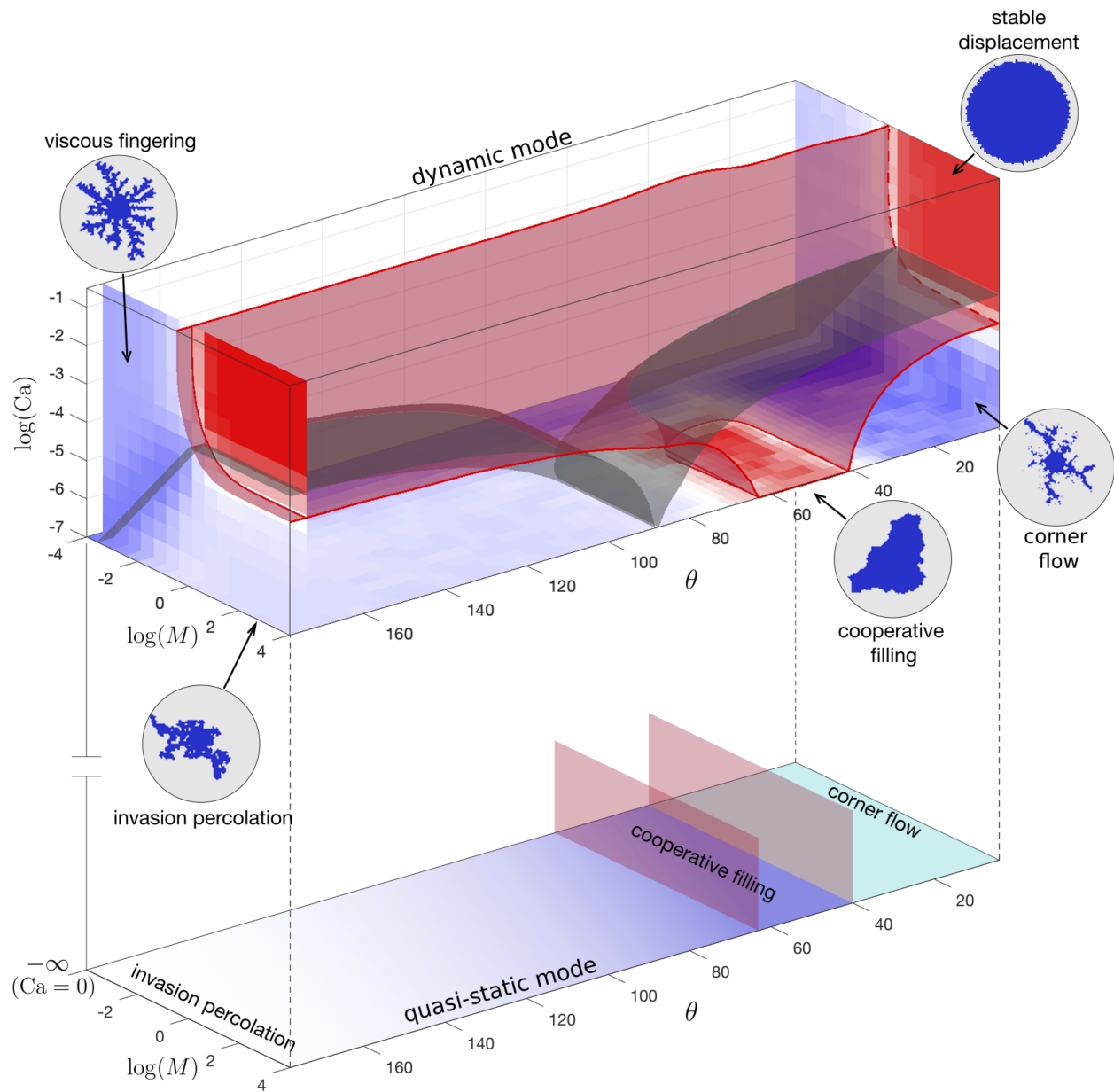


Figure 4-12: Extended Lenormand diagram constructed using Ca^* and D_f phase boundaries from Figs. 4-10-4-11 to separate the five principal flow regimes within the M - Ca - θ parameter space: viscous fingering, stable displacement, invasion percolation, and cooperative pore filling. Results from the “moving-capacitor” model are complemented with results from the quasi-static model that allows inferring the extent of cooperative pore filling in the limit $Ca \rightarrow 0$.

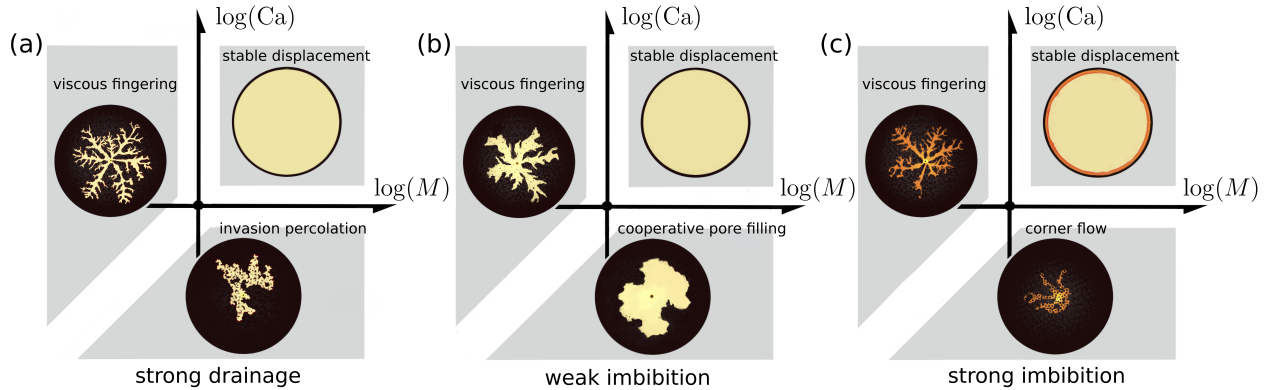


Figure 4-13: A sketch of Lenormand’s phase diagram in (a) strong drainage, (b) weak imbibition and (c) strong imbibition. The darker shades in strong imbibition represent partial pore-scale displacement [art credit: Kamilla Omarova].

We summarize the findings from our comprehensive study with a schematic (Fig. 4-13). The classic phase diagram of Lenormand was developed for strong drainage (Fig. 4-13a), where displacement patterns advance through either viscous fingering, stable displacement, or invasion percolation. This diagram undergoes a qualitative change when the system moves to weak imbibition (Fig. 4-13b), in which viscous fingers become significantly wider and invasion percolation is replaced by cooperative pore filling. Therefore, the majority of the M – Ca space leads to compact displacement patterns. Strong imbibition has only been sparsely studied (Zhao *et al.*, 2016; Odier *et al.*, 2017; Primkulov *et al.*, 2018), but enough is known to outline the main modes of displacement (Fig. 4-13c). The displacement patterns advance through corner flow at low Ca , where the injected fluid occupies only a fraction of the pore space (denoted by darker shades in Fig. 4-13c). This mode of displacement has been explored experimentally by Zhao *et al.* (2016) and Odier *et al.* (2017), and numerically in the quasi-static limit (Primkulov *et al.*, 2018). The invasion pattern advances through thin films on the solid surface for high Ca and $M < 1$ (Levaché & Bartolo, 2014), while maintaining the viscous fingering morphology (Zhao *et al.*, 2016).

The simulations in Fig. 4-12 reproduce many experimental observations. First, as θ changes from 180° to 46° , displacement patterns change from invasion percolation to cooperative pore filling (Trojer *et al.*, 2015; Zhao *et al.*, 2016), and finger width increases in the viscous-fingering region of the diagram (Stokes *et al.*, 1986; Trojer *et al.*, 2015; Zhao *et al.*, 2016). Second, the injection pressure fluctuates sharply in capillary-dominated regimes (Måløy *et al.*, 1992; Furuberg *et al.*, 1996), but instead varies monotonically with time in viscous-dominated regimes. Third, the model naturally reproduces the intermittent flow that is modulated by pore disorder in capillary-dominated flow. Finally, the model reproduces the interplay between imposed ordered post lattice and the flow morphology: snow flake patterns in viscous fingering (Chen & Wilkinson, 1985; Chen, 1987), regular crystal-growth morphology in cooperative pore filling regime (Lenormand, 1990), perfect circles in stable displacement, and disordered morphology in invasion percolation (Lenormand & Zarcone, 1985; Wilkinson & Willemsen, 1983; Måløy *et al.*, 1992).

While our “moving-capacitor” model is successful in reproducing the dynamics of the principal flow regimes (Fig. 4-13), it assumes piston-like displacement for *burst*, *touch*, and *overlap* events. As a result, the model overestimates the invading fluid saturation at high Ca , as pointed out by Zhao *et al.* (2019). Strong drainage and high Ca features residual films of defending fluid (Bretherton, 1961; Zhao *et al.*, 2016). In strong imbibition, invading fluid films dominate the displacement patterns in viscous fingering and corner flow regimes (Levaché & Bartolo, 2014; Zhao *et al.*, 2016;

Odier *et al.*, 2017). These regimes are captured more naturally through pore-scale 3D continuum models (Zhao *et al.*, 2019), which are unfortunately still prohibitively expensive for populating significant portions of the M - Ca - θ parameter space in Lenormand’s diagram (Fig. 4-12).

4.6 Conclusion

We have presented the results of a “moving-capacitor” dynamic pore-network model that is able to reproduce the full M - Ca space of Lenormand’s phase diagram and extend it with a third dimension θ , thus accounting for the system’s wettability. The model captures the pressure and flow within the porous medium, and our analysis of the model results shows the contrast in pore-scale dynamics between viscous-dominated and capillary-dominated flow through pore-invasion-event statistics and autocorrelation of the velocity field. The “moving-capacitor” model provides a single framework that captures the dynamics of fluid-fluid displacement in micromodels across an unprecedented span of M - Ca - θ parameters. The model cannot be directly applied to generic porous materials with complex shapes or hierarchical geometries. However, in the spirit of Lenormand *et al.* (1988) and Cieplak & Robbins (1988), here we studied a simpler pore geometry in order to learn something general about two-phase displacement in more complex porous media. We use our model to build the first three-dimensional version of Lenormand’s phase diagram with wettability as the third axis, whose general shape we expect to hold for more complex three-dimensional porous materials. We demonstrate that cooperative pore filling can occupy a significant portion of M - Ca - θ space, and that two metrics—the classical fractal dimension and modified capillary number Ca^* —are sufficient for delineating the five principal displacement regimes. One can use the diagram to design efficient fluid-fluid displacement in disordered porous media. Furthermore, the “moving-capacitor” model used in this work enables modeling multiphase flow in deformable granular media (movable posts) (Jain & Juanes, 2009; Sandnes *et al.*, 2011; Lee *et al.*, 2020), while accounting for the wettability effects, when combined with discrete element method (DEM) models (Meng *et al.*, 2020).

Chapter 5

Avalanches in strong imbibition

This chapter has been published in [Primkulov et al. \(2022\)](#)

5.1 Introduction

The complexity of the world around us—in rivers, climate patterns, landslides, and earthquakes—is often attributed to the prevalence of self-organized criticality (SOC), where systems naturally evolve toward a state in which small perturbations have scale-free consequences ([Bak, 2013](#)). Slow injection of a non-wetting fluid (i.e. slow drainage) into a porous medium is arguably one of the most accessible examples of SOC ([Bak et al., 1987, 1988](#); [Bak & Chen, 1989](#); [Martys et al., 1991](#); [Moura et al., 2017b,a](#)). It can be studied in great detail with benchtop experiments and simple pore-network models ([Furuberg et al., 1988](#); [Moura et al., 2017b,a](#)), and the universality of observed trends can be tested by changing the properties of the fluids and the porous medium ([Biswas et al., 2018](#)).

In drainage, constant-rate displacement is achieved by forcing the invading fluid into the porous medium. In slow drainage, when viscous forces are negligible, the invading fluid advances into clusters of pore bodies via intermittent avalanches ([Lenormand et al., 1983](#); [Måløy et al., 1992](#)), with waiting times between events and sizes of invasion clusters exhibiting scale-free behavior ([Moura et al., 2017b](#)). These scale-free features are the hallmarks of SOC.

Wetting conditions have a pronounced influence on invasion mechanisms and patterns in porous media ([Lenormand et al., 1983](#); [Blunt & Scher, 1995](#); [Zhao et al., 2016](#); [Odier et al., 2017](#)). During the injection of a strongly wetting fluid (i.e. strong imbibition), the invading fluid advances by coating crevices and corners within the pore space (Fig. 5-1). Slow, constant-rate displacement is achieved by resisting spontaneous imbibition, producing invasion patterns distinct from drainage ([Zhao et al., 2016](#)). However, much like slow drainage, slow strong imbibition evolves via intermittent avalanches ([Zhao et al., 2016](#)). Given the disparity in both pore-scale mechanisms and macroscopic patterns, it is not obvious that the scale-free features associated with drainage would translate to strong imbibition.

In this letter, we use experiments and simulations to show that slow strong imbibition in porous media exhibits all of the same scale-free features of SOC documented for drainage. In particular, we demonstrate that strong imbibition joins drainage as a second known example to follow the remarkable correlation scaling of [Furuberg et al. \(1988\)](#) describing the space-time statistics of invasion at the pore scale.

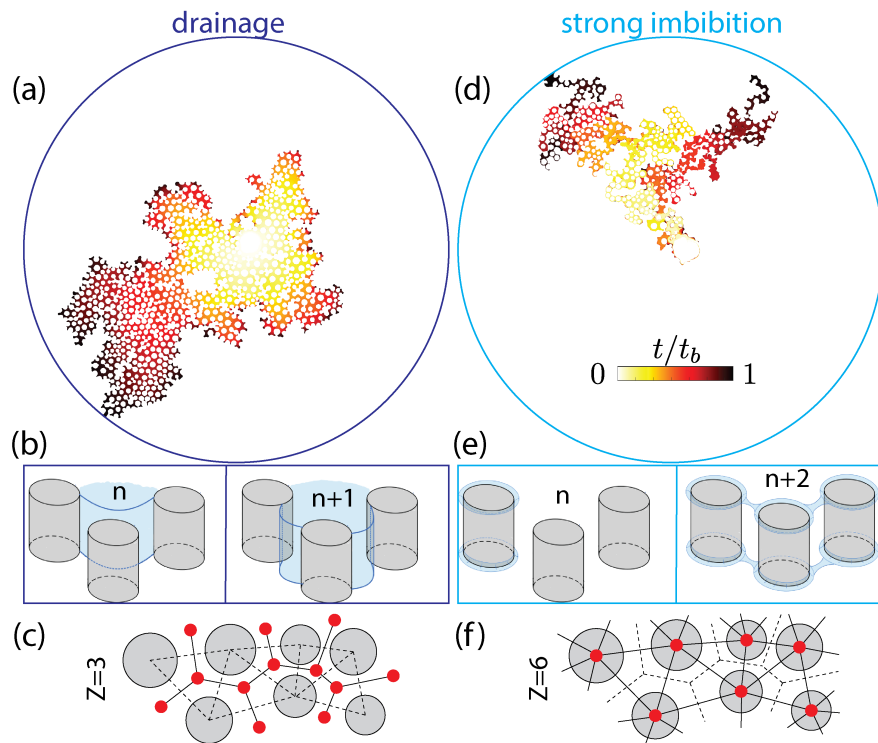


Figure 5-1: Temporal evolution of slow fluid-fluid displacement in (a) drainage and (d) strong imbibition from experiments in a micromodel patterned with cylindrical posts, where events are colored according to invasion time with t_b the breakthrough time. Invasion events are intermittent in both cases. (b) In drainage, the invading fluid enters throats with lowest entry pressures and occupies pore bodies. (c) In the quasi-static limit, this process is equivalent to invasion percolation on a hexagonal lattice (coordination number $Z = 3$). (e) In strong imbibition, the invading fluid advances by coating corners between posts and top/bottom plates, leaving pore bodies filled with defending fluid. (f) In the quasi-static limit, this process is equivalent to invasion percolation on a triangular lattice ($Z = 6$).

5.2 Pore-scale physics and intermittency

Experimentally, we examine fluid-fluid displacement in a micromodel, where cylindrical posts are placed at nodes of an irregular triangular mesh and confined between two transparent disks. Both node locations and post sizes are disordered. The micromodel is fabricated via soft lithography from a photocurable polymer (NOA81, Norland Optical Adhesives) (Denis Bartolo *et al.*, 2008; Levaché *et al.*, 2012), which allows precise control of wettability conditions. We refer to this micromodel design as the benchmark geometry; micromodel characteristics and fabrication details can be found in Zhao *et al.* (2016). We use fixed contact angles of $150^\circ \pm 5^\circ$ for drainage and $7^\circ \pm 3^\circ$ for strong imbibition (Fig. 5-1), as measured through the invading phase. In both cases, we inject the invading fluid from the center of the micromodel at $0.4 \mu\text{L}/\text{min}$ while maintaining a constant pressure at the outer perimeter. This slow injection rate provides capillary-dominated flow with negligible viscous effects ($\text{Ca} = 5.8 \times 10^{-3}$, see appendix for details).

Slow fluid-fluid displacement in micromodels can be modelled quasi-statically by incorporating the pore-invasion events of Cieplak & Robbins (1988, 1990) and corner-flow events, as described in detail in Primkulov *et al.* (2018), and compared against experiments in (Zhao *et al.*, 2019). In the model, pore-invasion pressures p are determined from local post geometry and wettability: (i) in slow drainage (Fig. 5-1b), invasion fills pore bodies in sequence according to the widest available pore throats; (ii) in slow strong imbibition (Fig. 5-1e), invasion proceeds by sequential post coating. We ran this model in strong imbibition on the benchmark geometry.

In both drainage and strong imbibition, intermittency emerges from capillary-dominated interactions of the fluid-fluid interfaces with the quenched disorder of the pore geometry. In slow drainage, the invading fluid advances by progressively occupying new pore bodies. Posts act as local pinning sites of the displacement front (Fig. 5-1). Since viscous forces are negligible, the pressure difference between the two fluids across the interfaces (the Laplace pressure) must be the same for all menisci (Primkulov *et al.*, 2018). As the invading fluid is injected, Laplace pressure builds uniformly across the micromodel until it matches the lowest capillary-entry pressure at the displacement front, at which point the associated meniscus becomes unstable. This meniscus then rapidly advances while all other menisci retract, a process known as a burst event (Cieplak & Robbins, 1988, 1990) or Haines jump (Haines, 1930; Berg *et al.*, 2013). These events often occur in rapid successions or avalanches, the sizes of which are scale-free (Moura *et al.*, 2017b). The repetition of this process generates the marked intermittency of slow drainage, where rapid invasion events are punctuated by periods of apparent inactivity. Since clusters of defending fluid occasionally get surrounded and disconnected (i.e, trapped) during the displacement, the quasi-static invasion process is analogous to invasion percolation with trapping (see Fig. 5-1 and Table 5.1).

We find that intermittent pore-scale invasion persists in slow strong imbibition, despite the substantial differences in the pore-scale displacement mechanisms (Fig. 5-1). In strong imbibition, the invading fluid advances by preferentially coating the corners between posts and top/bottom plates (Zhao *et al.*, 2016; Primkulov *et al.*, 2018). After a particular post-coating event, the corner menisci swell as the Laplace pressure increases uniformly across the micromodel until the displacement front touches an uncoated post, triggering rapid coating of the new post (Ponomarenko *et al.*, 2011). The repetition of this process generates the marked intermittency apparent in experiments (see supplemental video). As in drainage, the spatiotemporal evolution of the invasion front displays irregular changes in flow direction and the formation of invasion clusters—a signature of capillary-dominated flow in disordered porous media (Primkulov *et al.*, 2021). Clusters of defending fluid occasionally get surrounded by chains of coated posts, but it remains unclear whether these clusters become disconnected and trapped. Our experimental observations are ambiguous but suggestive of trapping [supplemental video], but our simulations do not include trapping because our model

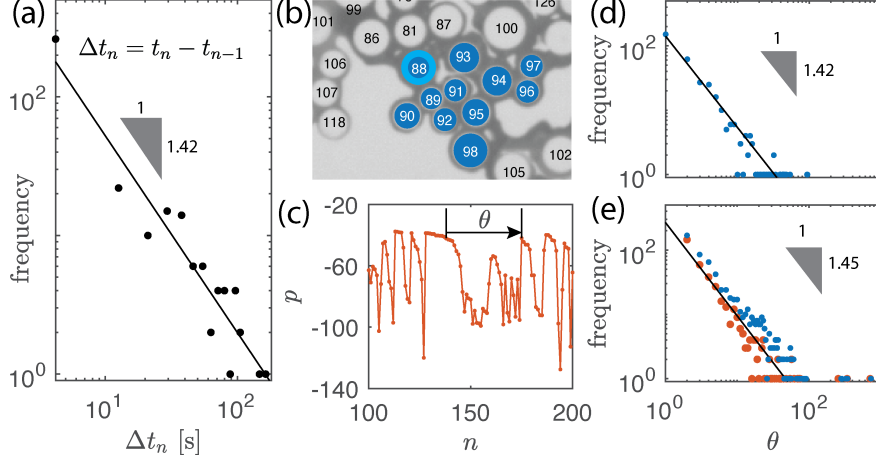


Figure 5-2: (a) Scale-free distribution of waiting times between consecutive post-coating events from the strong imbibition experiment (see supplemental video). We calculate avalanche size θ as (b) the cluster size of consecutive events connected to a reference post (e.g. sequence of posts 88-98), or as (c) the number of events found by traversing the pressure signal p from numerical simulations until a value higher than the reference value is reached. Here, avalanches originate from all data points with negative slope. The distribution of θ is scale-free in (d) experiments and (e) simulations, where the colors correspond to θ -counting methods in (b) and (c).

does not allow for trapping in strong imbibition (Primkulov *et al.*, 2018). We therefore assume that the quasi-static invasion process is analogous to invasion percolation without trapping (Fig. 5-1 and Table 5.1). In the Supplemental Materials, we use a simplified model to show that the presence or absence of trapping does not have significant influence on the invasion statistics.

5.3 SOC signature in waiting time

Scale-free waiting times between events are a signature of SOC. As a result, the timing of pore-invasion events in drainage is fundamentally unpredictable. To show that post-coating events in strong imbibition also behave in this way, we measure the waiting times between consecutive post-coating events in our experiments. We find that the histogram of waiting times follows a power-law scaling, similar to drainage (Moura *et al.*, 2017b). The slope of the power-law fit to the experimental data is smaller than 2 (Fig. 5-2a), confirming that the distribution is scale-free.

5.4 SOC signature in avalanche size

An avalanche in strong imbibition is a cluster of consecutive post-coating events that originate from the same reference post (e.g. the sequence 88-98 in Fig. 5-2b). Avalanche size θ can be characterized by counting the number of events before encountering a post-coating event disconnected from the cluster (e.g. event 99 in Fig. 5-2b). For quasi-static invasion, a nearly equivalent definition of θ relies on the pressure signal (Roux & Guyon, 1989; Moura *et al.*, 2017a; Maslov, 1995). Given the lowest capillary entry pressure p_0 at the displacement front at some reference time, θ can be defined as the number of pore-invasion events that occur before p_0 is next exceeded (Fig. 5-2c and (Roux & Guyon, 1989)).

As in drainage (Moura *et al.*, 2017b), avalanches in strong imbibition retrieved by the counting method detailed in Fig. 5-2b reveal power-law distributions in both experiments and simulations (Fig. 5-2d-e). We obtain a similar power-law distribution from the quasi-static pressure signal, a portion of which is illustrated in Fig. 5-2c. Again, the slope of these power-law distributions is less than 2, indicating that avalanche sizes are scale free. For both drainage and strong imbibition, the scale-free distribution of avalanches is responsible for the fractal nature of the displacement patterns, which are aggregates of scale-free avalanche clusters. Therefore, slow strong imbibition, despite its distinct invasion mechanism, exhibits all the characteristics of SOC—scale-free waiting times between events, scale-free avalanches, and fractal displacement patterns—that have been documented in slow drainage (Moura *et al.*, 2017b).

5.5 Furuberg scaling

The above findings raise the question of whether the correlation scaling of Furuberg *et al.* (1988), originally proposed for drainage, also holds in strong imbibition. The correlation function $N(r, n)$ measures the probability of pore invasion at distance r in space and a number of events n in time away from a reference event. Here, we measure r as the Euclidean distance normalized by the characteristic distance between posts, and n as consecutive pore-scale event number. Furuberg *et al.* (1988) found that in drainage,

$$N(r, n) = r^{-1} f(r^D/n), \quad f(x) \sim \begin{cases} x^a, & x \ll 1 \\ x^{-b}, & x \gg 1 \end{cases} \quad (5.1)$$

where D is the fractal dimension of the displacement pattern. For slow drainage, Furuberg *et al.* (1988) obtained exponents $a \approx 1.4$ and $b \approx 0.6$ by fitting the results of an invasion-percolation model. Roux & Guyon (1989) argued that a and b are linked to exponents of ordinary percolation theory, and Maslov (1995) subsequently showed that, under that ansatz,

$$b = 1 - (D_e - 1/\nu)/D, \quad (5.2)$$

where D_e is the fractal dimension of the fluid-fluid interface and ν is the correlation-length-divergence exponent from ordinary percolation. Roux & Guyon (1989) argued that $a \geq 1$, while Moura *et al.* (2017a) showed that $a = 1 + D_e/D$ when $n \gg 1$, so we should expect

$$1 \leq a \leq 1 + D_e/D. \quad (5.3)$$

Expected values of exponents a and b from Eqs. (5.2) and (5.3) are reported in Table 5.1. Equation (5.1) was only recently verified experimentally in drainage by Moura *et al.* (2017a).

5.6 Furuberg scaling in strong imbibition

Both model and experiment allow us to test the validity of Eq. (5.1) in strong imbibition. For a fixed value of n , $N(r, n)$ is the histogram of distances r between pore-scale events separated in time by n events (Fig. 5-3b). The data from our model and experiments resemble those reported for strong drainage (Furuberg *et al.*, 1988; Moura *et al.*, 2017a), with peaks in $N(r, n)$ moving to larger r as n increases. These data collapse for both model and experiment when we plot $rN(r, n)$ against r^D/n (Fig. 5-3c), with a peak near $r^D/n = 1$ and power-law behavior on either side of the peak signifying the validity of Eq. (5.1) in strong imbibition.

Table 5.1: Critical exponents for invasion percolation for lattice configurations relevant to our study, with values of D , D_e , and ν taken from [Stauffer & Aharony \(1985\)](#); [Wilkinson & Willemsen \(1983\)](#); [Knackstedt *et al.* \(2002\)](#). Values of a and b are calculated from Eqs. (5.2)-(5.3).

lattice	square	hexagonal	triangular
D_e	1.22	1.21	1.62
D	1.82	1.83	1.89
ν	4/3	4/3	4/3
trapping	yes	yes	no
a	[1,1.67]	[1,1.66]	[1,1.86]
b	0.74	0.75	0.54

Table 5.2: Result of data collapse analogous to Fig. 5-3c for simulations on the benchmark geometry, and also on a set of regular lattices with post radii assigned from a uniform distribution. We report the mean and the standard deviation from 40 realizations.

	exponents	drainage $\theta = 150^\circ$	strong imbibition $\theta = 7^\circ$
benchmark geometry	a	1.21	1.05
	b	0.58	0.72
regular lattice, random radii	a	1.41 ± 0.08	1.11 ± 0.06
	b	0.72 ± 0.15	0.76 ± 0.13

We confirm the robustness of this collapse by running a set of additional simulations for both drainage and strong imbibition in which we place posts on a regular triangular lattice and draw post radii from a uniform distribution; the resulting data also collapses, as in Fig. 5-3, with values of exponents a and b reported in Table 5.2.

[Roux & Guyon \(1989\)](#) demonstrated that the robustness of the collapse suggested by Eq. (5.1) relies on the power-law distributions of avalanches ($P_n(\theta) \sim \theta^{-\tau_b}$) and distances between active pores at the displacement front ($Q_\theta(r) \sim r^\alpha$). These conditions are satisfied in both drainage and strong imbibition, where fluid displacement exhibits features of SOC. However, the predictions of Eqs. (5.2) and (5.3) for the slopes a and b appear not to hold in strong imbibition, with the expected value of b (Table 5.1) significantly different from the value in the experiment (Fig. 5-3c) and almost two standard deviations away from the mean value in simulations (Table 5.2). In fact, [Biswas *et al.* \(2018\)](#) showed that τ_b is sensitive to the details of the pore structure and the presence of spatial correlation, something that the relatively wide standard deviation across our simulations also shows. This dependence is absent from Eq. (5.2), where b (which is a function of τ_b ([Roux & Guyon, 1989](#))) depends only on ν and fractal dimensions.

5.7 Discussion and conclusion

We have demonstrated that slow fluid-fluid displacement in strong imbibition exhibits features of SOC previously documented for drainage. The invading fluid advances intermittently, and scale-free distributions emerge for waiting times and avalanche sizes. Both our model and our experiment also show that avalanches in strong imbibition robustly follow the pore-scale event correlation of [Furuberg *et al.* \(1988\)](#). Slow drainage and strong imbibition are thus the only two known examples of SOC that follow a definitive correlation of events in space and time [Eq. (5.1)]. It is remarkable that

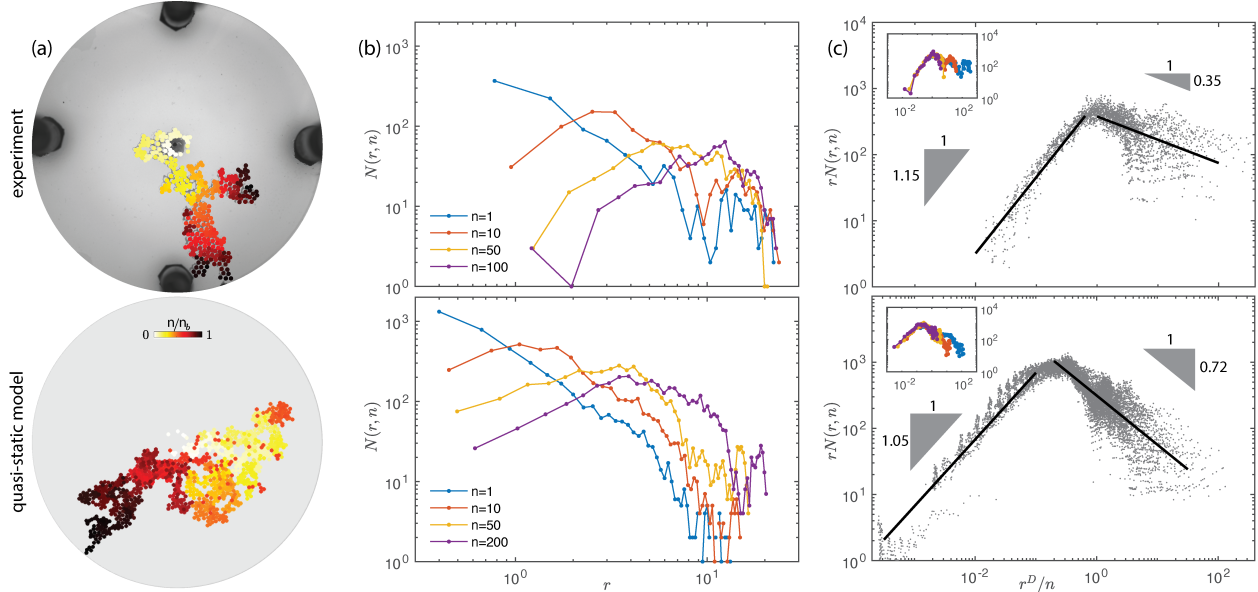


Figure 5-3: Verification of Eq. (5.1) in slow strong imbibition for our experiment (top row) and model (bottom row). (a) Invasion-event-number plot, where events are colored by event number n with n_b the number of events at breakthrough. (b) Plots of $N(r, n)$ vs. r for several values of n . (c) Collapse of $rN(r, n)$ vs. r^D/n points to the validity of the scaling in Eq. (5.1). Here, data points correspond to all different values of the time delay n , while the insets show the collapse for a selection of n from (b).

these two phenomena—governed by entirely distinct pore-level mechanisms—both exhibit collapse in the correlated nature of invasion percolation.

Furthermore, we anticipate that the correlation scaling of [Furuberg *et al.* \(1988\)](#) would still be valid in 3D, as long as the two assumptions of [Roux & Guyon \(1989\)](#) (power-law scaling of avalanche sizes and distance between active pores) still hold. Validating this correlation scaling in 3D with either simulations or experiments would be an intriguing next step. Additionally, we found that increasingly strong spatial correlation in wettability or pore-sizes eventually breaks the collapse of the correlation data (Fig. 3c). This is especially true in weak imbibition, where the invasion dynamics on a highly correlated regular lattice resembles the growth of a crystal ([Lenormand, 1990](#)). While this discussion falls outside the scope of this letter, it is another great direction for follow-up studies.

Scientific understanding of SOC is still at a relatively early stage ([Yang *et al.*, 2004](#); [Bak, 2013](#); [Marković & Gros, 2014](#)), and much of the progress in the field is made by studying one example of SOC and trying to extrapolate to others ([Goldenfeld & Kadanoff, 1999](#)). Many other natural examples of SOC, like landslides, snow avalanches, and earthquakes, share features similar to avalanches in drainage and strong imbibition ([Bak, 2013](#)). For instance, in earthquakes: (i) the sliding of geologic faults occurs by means of intermittent stick-slip motion; (ii) magnitudes and waiting times between consecutive earthquakes are scale-free ([Bak, 2013](#)), and (iii) earthquake locations within slip planes have been speculated to form fractal patterns ([Bak & Chen, 1989](#)). An intriguing follow-up to this work would be to investigate whether the scaling in Eq. (5.1) holds for earthquakes, given the density and precision of modern earthquake catalogs ([DeVries *et al.*, 2018](#); [Ross *et al.*, 2019](#)).

Part II

Moving fluid interfaces and contact lines

Chapter 6

Spin coating of capillary tubes

This chapter has been published in [Primkulov et al. \(2020b\)](#).

6.1 Introduction

Use of capillary tubes is widespread in a range of health and industrial applications, for example, in the studies of film instability ([Goren, 1962](#); [Rossen, 2000](#); [Duclaux et al., 2006](#)), wetting ([Washburn, 1921](#); [Hoffman, 1975](#); [Walls et al., 2016](#); [Zhao et al., 2018](#)), blood flow ([Goldsmith & Spain, 1984](#); [Pries et al., 1992](#)), and oil recovery ([Morrow & Mason, 2001](#); [Patzek & Kristensen, 2001](#); [Blunt, 2001](#)). In many of these applications, precise control of the surface properties of the capillary tubes is critical. Here, we demonstrate that such control is possible through the deposition of thin layers of functional polymers via spin-coating ([Emslie et al., 1958](#); [Scriven, 1988](#)), a technique that has not previously been explored for coating capillary tubes.

The prevalent approach to coating the inner wall of a capillary tube dates back to G.I. Taylor ([Taylor, 1961](#)). A tube is filled with viscous liquid, which is subsequently expelled by air at a prescribed flow rate. As the air bubble propagates through the tube, a liquid film of uniform thickness is left on the wall of the tube. When $Ca \ll 1$, the thickness h can be estimated from Bretherton's law ([Bretherton, 1961](#)) as $h \sim RCa^{2/3}$, where $Ca = \frac{\mu u}{\sigma}$ is the capillary number, μ the liquid viscosity, u the bubble velocity, σ the surface tension and R the tube radius. This method has been used extensively to generate annular films of controlled thickness ([Goren, 1962](#); [Aussillous & Quéré, 2000](#); [Duclaux et al., 2006](#)). While it is well suited to generating relatively thick films at moderate bubble speeds, practical difficulties in maintaining very low gas flow rates may preclude the deposition of films of uniform thickness at very low displacement rates. In particular, syringe pumps operating at low constant injection rates are known to have stepper-motor-induced pressure fluctuations ([Li et al., 2014](#); [Zeng et al., 2015](#)).

Here, we explore centrifugally-forced deposition of viscous liquids in capillary tubes, which offers an easily accessible alternative to Taylor's method that is particularly advantageous for micron-scale films. In §6.2, we describe the details of the experimental setup. We present theoretical arguments for the early and late-time flow dynamics in §6.3. Control over the film thickness allows for manipulation of the timescale of the subsequent Rayleigh-Plateau instability described in §6.5. We thus present methods for generating both cylindrical and corrugated coatings on capillary tubes with a curable polymer, and point to potential applications in §6.6.

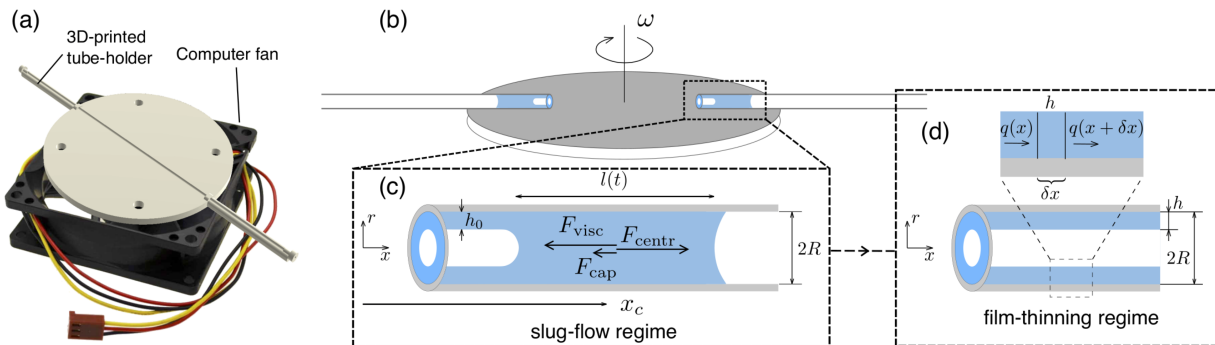


Figure 6-1: (a) Diagram of the computer fan repurposed as a spin-coater. (b) Schematic of the capillary tubes filled with liquid slugs, spun at angular velocity ω . (c) Schematic of the slug-flow regime. (d) Schematic of the film-thinning regime.

6.2 Experimental method

We repurpose a computer fan as a spin-coater: the blades of the fan are removed and a 3D-printed platform for holding capillary tubes is attached, centered at the spin axis (fig. 6-1a). The fan is connected through an Arduino board to MATLAB, where we fix the angular velocity at 854 ± 10 rpm for all of the experiments presented below.

First, we explore how liquid slugs move within the spinning capillary tubes with high speed imaging (see Supplemental Materials, video V1). We introduce 20 mm-long liquid slugs into the capillary tubes (Hilgenberg borosilicate glass, 75 mm in length, $290 \mu\text{m}$ inner radius), place them onto the spin-coating platform as shown in fig. 6-1b, and spin. We track the slug length $l(t)$ and slug-center distance $x_c(t)$ from the spin-axis (fig. 6-2a-b). As the slug moves outwards, it leaves a film of liquid behind, reducing the slug length l as x_c increases. Notably, the evolution of l with x_c is nearly independent of the liquid viscosity (fig. 6-2b), which means that the film thickness profile deposited by the slug is also independent of viscosity. Furthermore, x_c grows exponentially with time (fig. 6-2a), which makes the slug flow regime very brief. Both of these observations are to be rationalized in §6.3.2.

In the second set of experiments, we explore the thinning dynamics of the liquid films on the capillary tube walls arising after the slug has exited the tube. We introduce a sufficient volume of liquid into the capillary tubes such that the film is deposited throughout the tube. The excess liquid is allowed to escape from the outer end of the tube. The thickness of the liquid film left on the walls is estimated from the weight difference of the dry and coated tubes. This is done in groups of ten capillary tubes—weights are measured with an Ohaus Explorer EX225D scale, which allows 0.1 mg precision, corresponding to sub-micrometer precision in the final film thickness.

When capillary tubes are spun at sufficiently high angular speed, the amount of liquid within the tubes drops sharply at first, then slowly approaches its long-time limit. The experimental results of spin-coating capillary tubes with different liquids (50-1000 cSt silicone oils and NOA81) are reported in fig. 6-3a. Silicone oils and NOA81 show similar trends, with the value of the final thickness increasing with viscosity.

We rationalize these observations with theoretical models developed in the next section, where we distinguish two flow modes: slug motion and film thinning. We find the characteristic timescales of these two modes and show that the temporal evolution evident in fig. 6-3 is largely associated with the slow thinning of the viscous films. Note that we do not attempt to model the film thinning of NOA81, as its rheology is yet to be fully characterized. We found that its viscosity (~ 240 cSt)

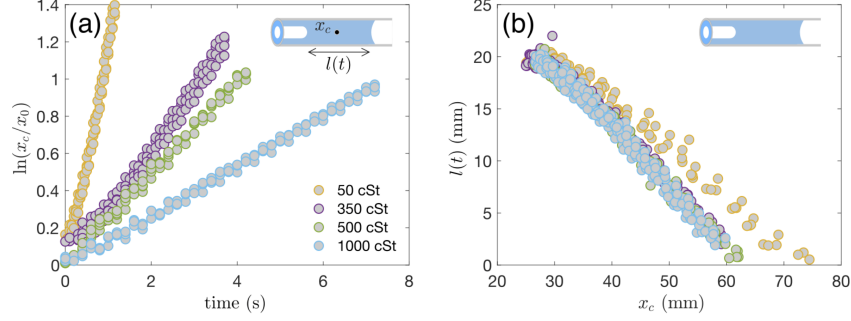


Figure 6-2: (a) Exponential change in the slug-center position x_c with time, where the timescales (inverse of the slope) are [0.9, 3.2, 4.0, 7.5] s for [50, 350, 500, 1000] cSt, respectively. Here x_0 is the initial coordinate of the slug-center. (b) Measurements of the slug length l with x_c suggest viscosity-independent film-deposition profiles (see Appendix D.1 for a discussion of the deviation of the 50 cSt oil curve).

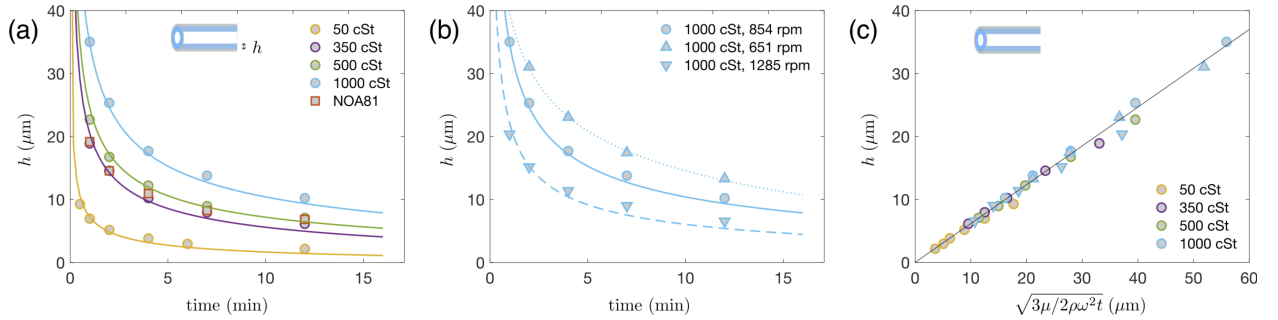


Figure 6-3: (a) Temporal evolution of the deposited film thickness long after the slug-motion: measurements are denoted with circles (and squares), theory with solid lines. (b) Film thickness evolution of 1000 cSt silicone oil spun at 651, 854, and 1285 rpm. (c) Collapse of the data from fig. 6-3a and fig. 6-3b using (6.11). Each point corresponds to 10 spin-coating experiments, with over 350 total coated tubes.

increases with shelf-life and that it exhibits non-Newtonian behavior at low film heights. As a result, the polymer is primarily used here to illustrate the possibility of making channels with wavy walls in §6.6.

6.3 Theory

Consider a capillary tube, containing a liquid slug of density ρ and dynamic viscosity μ , that is spun at a prescribed angular speed ω (fig. 6-1c). As the slug moves outwards, it deposits a liquid film on the tube walls. We consider the control region containing the slug only. Three forces may be significant in this configuration: the capillary (F_{cap}), viscous (F_{visc}), and centrifugal (F_{centr}) forces. The capillary force can be estimated from the different end-curvatures of the liquid slug; the Laplace pressure difference on its ends opposes the outward motion (Bico & Quéré, 2001):

$$F_{\text{cap}} = -\pi R^2 \frac{2\sigma}{R} + \pi(R - h_0)^2 \frac{2\sigma}{R - h_0} = -2\pi\sigma h_0,$$

where h_0 is the characteristic thickness of the film deposited by the slug motion, and we assume a completely wetting liquid. The viscous force associated with Poiseuille flow can be estimated from the drag on the tube walls:

$$F_{\text{visc}} = -2\pi Rl(t) \frac{4\mu}{R} \dot{x}_c = -8\pi\mu l(t) \dot{x}_c,$$

where $l(t)$ is the liquid slug length, x_c the position of the slug center, and \dot{x}_c its velocity. Finally, the centrifugal force acting at the slug can be expressed as:

$$F_{\text{centr}} = \int_{x_c-l/2}^{x_c+l/2} \rho\pi R^2 \omega^2 x dx = \rho\pi R^2 \omega^2 l(t) x_c.$$

Therefore, the motion of the slug is governed by $\frac{d(m\dot{x}_c)}{dt} = F_{\text{cap}} + F_{\text{visc}} + F_{\text{centr}}$, from which it follows that

$$\frac{m\dot{x}_c}{m} + \ddot{x}_c = -\frac{2\sigma h_0}{\rho l(t) R^2} - \frac{8\mu\dot{x}_c}{\rho R^2} + \omega^2 x_c.$$

We neglect $m\dot{x}_c$ since $\frac{m\dot{x}_c}{m\ddot{x}_c} = \frac{\rho 2\pi R h_i \dot{x}_c^2}{\rho \pi R^2 l \ddot{x}_c} = \frac{h_i}{R} \frac{2\dot{x}_c^2}{\ddot{x}_c l} \sim \frac{h_i}{R} \frac{l^2 / \tau_{\text{inert}}^2}{l^2 / \tau_{\text{inert}}^2} = \frac{h_i}{R} \ll 1$, where h_i is the film thickness deposited in the inertial regime and τ_{inert} the inertial timescale (see §6.3.1). Furthermore, $\frac{F_{\text{cap}}}{F_{\text{centr}}} = \frac{h}{R} \frac{2\sigma}{\rho l x_c R \omega^2} \sim 10^{-2} \frac{h}{R} \ll 1$; hence, we may safely neglect the contribution of the capillary force from this point on. The force balance then reduces to:

$$\ddot{x}_c = -\frac{8\mu\dot{x}_c}{\rho R^2} + \omega^2 x_c. \quad (6.1)$$

We proceed by separating the slug dynamics (fig. 6-1c) into early inertial (§6.3.1) and late viscous (§6.3.2) regimes. The subsequent thinning of the film on the tube walls (fig. 6-1d) is described thereafter.

6.3.1 Inertial slug-flow ($t < \frac{\rho R^2}{8\mu}$)

When the flow is dominated by inertia, the viscous term in (6.1) can be neglected and the motion of the slug is governed by

$$\ddot{x}_c = \omega^2 x_c. \quad (6.2)$$

The position of the slug can be expressed as $x_c(t) = x_0 \cosh(\omega t)$, where x_0 is the initial coordinate of the slug-center.

The inertial flow persists until the boundary effects diffuse across the tube and motion becomes viscosity-dominated. The crossover between the two regimes occurs when the viscous term becomes comparable to inertia and $\ddot{x}_c \sim \frac{8\mu\dot{x}_c}{\rho R^2}$, which allows us to establish the characteristic time for the inertial flow as $\tau_{\text{inert}} \equiv \frac{\rho R^2}{8\mu}$. The characteristic timescale of inertial slug-flow ranges between 10^{-5} and $2 \cdot 10^{-4}$ s for the silicone oils used in our study. Notably, these times correspond to the oil

slug displacements between 8 nm and 3 μm (for 1000 cSt and 50 cSt oils, respectively): in our experiments, the system quickly switches to the viscosity-dominated regime.

6.3.2 Viscous slug-flow ($\frac{\rho R^2}{8\mu} < t < \frac{8\mu}{\rho\omega^2 R^2}$)

In the viscosity-dominated slug regime, we neglect the inertial terms so that (6.1) reduces to

$$\frac{8\mu\dot{x}_c}{\rho R^2} = \omega^2 x_c, \quad (6.3)$$

and the slug position can be expressed as $x_c = x_0 e^{\frac{\rho\omega^2 R^2}{8\mu}t}$. The characteristic time for the slug flow is $\tau_{\text{slug}} \equiv \frac{8\mu}{\rho\omega^2 R^2}$, which corresponds to 0.6 and 11.7 s for 50 and 1000 cSt silicone oils, respectively. These times are in close agreement with the experimental measurements of the slug-flow timescale reported in fig. 6-2a.

As the liquid slug moves through the tube, it deposits a film on the wall. This film is also subject to centrifugal forces; however, we neglect its thinning within the relatively brief time frame of the viscous slug-flow (an approximation to be justified a posteriori by comparison with the thinning timescale). Then, the thickness of the deposited film can be estimated from Bretherton's scaling (Bretherton, 1961) as:

$$h_0(x) \sim RCa^{2/3} = R \left(\frac{\mu\dot{x}}{\sigma} \right)^{2/3} = R \left(\frac{\rho\omega^2 R^2}{8\sigma} x \right)^{2/3}. \quad (6.4)$$

Notably, this thickness is independent of the liquid viscosity, in agreement with the experimental data in fig. 6-2b.

As the slug speed increases, the Ca increases from 0 to about 0.8 in our experiments. Therefore, the Bretherton's scaling (6.4) is only applicable while the slug is near the inner end of the tube, where $Ca \ll 1$. While a more accurate scaling of $h_o(x) \sim R \frac{Ca^{2/3}}{1+Ca^{2/3}}$ can be used for Ca between 0.01 and 1 (Aussillous & Quéré, 2000), we demonstrate in §6.4 that the late-time thinning profile is not sensitive to the film thickness profile left after the viscous slug-flow regime. This is consistent with the work of Emslie *et al.* (1958). Therefore, we use the expression (6.4) as a leading order approximation for simplicity in this work.

6.3.3 Film thinning ($t > \frac{8\mu}{\rho\omega^2 R^2}$)

In the late-time flow regime, we start with the film thickness profiles from (6.4). Subsequent thinning of the film is resisted predominantly by the viscosity of the liquid. As the liquid film thins, viscous resistance balances the centrifugal force, $F_{\text{visc}} \sim F_{\text{centr}}$, as is the case in the spin-coating of flat surfaces (Emslie *et al.*, 1958). Then, in the absence of inertia and provided that $h \ll R$, we can invoke the lubrication approximation, according to which

$$0 = \mu \frac{\partial^2 u}{\partial r^2} + \rho\omega^2 x. \quad (6.5)$$

By imposing the no-slip boundary condition at the wall and zero shear stress at the liquid surface, we obtain from direct integration of (6.5) the velocity field: $u(x, r) = \frac{\rho\omega^2 x}{\mu} (-r^2/2 + r(R - h(x)) +$

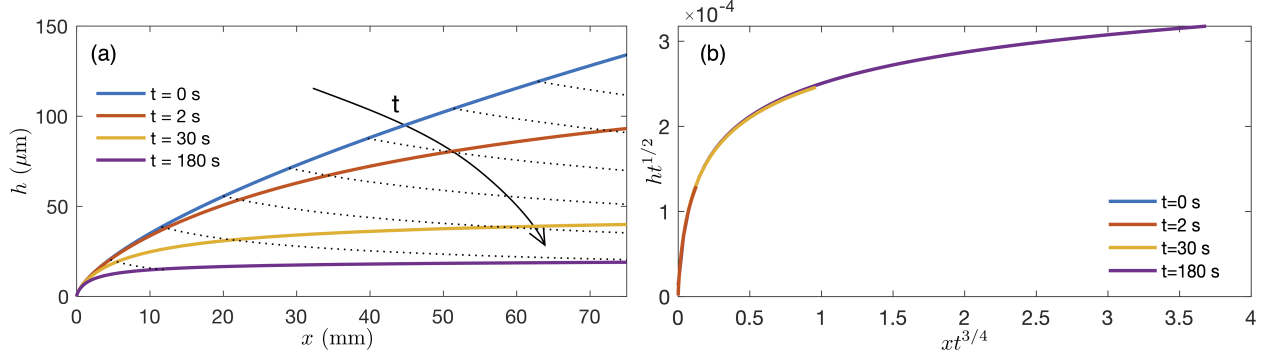


Figure 6-4: (a) Silicon oil (500 cSt) film thickness profiles at various times, where the initial profile (blue) is estimated with (6.4). Subsequent thickness profiles are obtained by evolving the surface coordinates with the system (6.9). Dotted lines represent the material point trajectories. (b) Collapse of the film thinning profiles onto a single curve via the similarity transformation developed in §6.4.

$R(h(x) - R/2)$). Thus, we estimate the volume flow rate as:

$$q(x) = \int_{R-h(x)}^R 2\pi r u(x, r) dr = \frac{\pi \rho h(x)^3 \omega^2 x}{12\mu} (8R - 5h(x)). \quad (6.6)$$

Conservation of mass in a representative section of the liquid film (see fig. 6-1d) yields $q(x) - q(x + \delta x) = \frac{2\pi(R-h(x))\delta h \delta x}{\delta t}$, which can be re-written as

$$\frac{dh}{dt} = -\frac{1}{2\pi(R-h(x))} \frac{dq(x)}{dx}. \quad (6.7)$$

This is a first-order partial differential equation for $h(t, x)$, equivalent to

$$\frac{24\mu(R-h)}{\rho\omega^2} \frac{dh}{dt} + 4xh^2(6R-5h) \frac{dh}{dx} = -h^3(8R-5h). \quad (6.8)$$

If we define $dn \equiv \frac{\rho\omega^2 dt}{24\mu(R-h)} = \frac{dx}{4xh^2(6R-5h)} = -\frac{dh}{h^3(8R-5h)}$, then the solution of (6.8) can be written as (Cheng, 2007):

$$\frac{dt}{dn} = \frac{24\mu(R-h)}{\rho\omega^2}, \quad \frac{dx}{dn} = 4xh^2(6R-5h), \quad \frac{dh}{dn} = -h^3(8R-5h). \quad (6.9)$$

Evolution of the film thickness can be resolved by taking the (x, h) coordinates of the Bretherton's film from (6.4), and solving the system (6.9). We do so for all silicone oils used in our experiments and plot the theoretical film thicknesses in fig. 6-3a and fig. 6-3b, where the theory closely matches the experimental measurements. The typical temporal evolution of the liquid thickness profiles is reported in fig. 6-4a. Noting that the scales of the vertical and horizontal axes are very different in fig. 6-4a, we see that when capillary tubes are spun at high ω , the film thickness very quickly becomes nearly uniform. In that case, $\frac{dh}{dx} \ll 1$ and (6.7) yields $\frac{dh}{dt} = -\frac{\rho\omega^2 h^3}{24\mu} \frac{8R-5h}{R-h} [1 + \frac{3x}{h} (1 - \frac{5}{24} \frac{h}{R}) \frac{dh}{dx}]$ which reduces to:

$$\frac{dh}{dt} = -\frac{\rho\omega^2 h^3}{24\mu} \frac{8R-5h}{R-h}. \quad (6.10)$$

We note that in the above approximation, the rate of thinning is independent of x . This feature is consistent with numerous spin-coating applications in which the film thickness is known to be nearly uniform and insensitive to the initial shape of the liquid bulk (Emslie *et al.*, 1958; Scriven, 1988).

Since $h \ll R$, the expression (6.10) reduces to $\frac{dh}{dt} = -\frac{\rho\omega^2 h^3}{3\mu}$. Then, the evolution of the film thickness is independent of the tube radius, and integration yields

$$h_0^{-2} - h^{-2} = -\frac{2\rho\omega^2}{3\mu}t. \quad (6.11)$$

This suggests that if we plot the data in figs. 6-2a-b as h against $\sqrt{\frac{3\mu}{2\rho\omega^2 t}}$, when $h \ll h_0$ the data should collapse onto a straight line, as is indeed evident in fig. 6-3c. The characteristic timescale of the film thinning changes with the film thickness as $\tau_{\text{thinning}} \equiv \frac{3\mu}{2\rho\omega^2 h^2}$, which is significantly larger than the timescale of the viscous slug motion: $\frac{\tau_{\text{slug}}}{\tau_{\text{thinning}}} = \frac{h^2}{R^2} \ll 1$. This disparity in the timescales justifies our neglecting the film thinning in §6.3.2.

6.4 Self-similar solution of film thinning

We proceed by developing a similarity solution suggested by our governing equations. The film thinning in capillary tubes is governed by (6.8), which can be rewritten as

$$k_2(R-h)\frac{dh}{dt} + 4xh^2(6R-5h)\frac{dh}{dx} = -h^3(8R-5h), \quad (6.12)$$

where $k_2 = \frac{24\mu}{\rho\omega^2}$. The initial conditions are set by:

$$h(0, x) = k_1 x^{2/3}, \quad (6.13)$$

where $k_1 = R \left(\frac{\rho\omega^2 R^2}{8\sigma} \right)^{2/3}$.

The equations of characteristics for (6.12) yield (Cheng, 2007):

$$\frac{dt}{k_2(R-h)} = \frac{dx}{4xh^2(6R-5h)} = -\frac{dh}{h^3(8R-5h)}. \quad (6.14)$$

Resolving the first and second equalities in (6.14) results in the following equations:

$$\ln x = \frac{4h^2(6R-5h)}{k_2(R-h)}t + \ln c_1 \quad \text{and} \quad \ln x = -3 \ln h - \ln(h - 8R/5) + \ln c_2,$$

which simplify to

$$x = c_1 e^{\frac{4h^2(6R-5h)}{k_2(R-h)}t} \quad \text{and} \quad x = \frac{c_2}{h^3(h - 8R/5)},$$

respectively, with:

$$c_1 = x e^{-\frac{4h^2(6R-5h)}{k_2(R-h)}t} \equiv f(t, x, h) \quad \text{and} \quad c_2 = x h^3(h - 8R/5) \equiv g(t, x, h). \quad (6.15)$$

With given values of c_1 and c_2 , (6.15) describes two-dimensional surfaces in (t, x, h) space. The intersection of these two surfaces is a characteristic curve, and one obtains the characteristic curves of (6.12) by spanning all possible combinations of c_1 and c_2 . The solution that satisfies the initial condition (6.13) can be found graphically (Cheng, 2007). We choose characteristic curves that pass through points $(0, x, h(0, x))$, and the aggregate of these curves forms a solution surface in the (t, x, h) space.

Alternatively, one can find the analytical solution by finding the curves that satisfy the relation:

$$c_1 = F(c_2) \quad \text{or} \quad g(t, x, h) = F(f(t, x, h)), \quad (6.16)$$

where F is an arbitrary function. Here, (6.16) is the general solution of (6.12), and the function F can be determined from the initial condition $g(0, x, h(0, x)) = F(f(0, x, h(0, x)))$, which using $h(0, x)$ from (6.13) yields

$$F(x) = k_1^3 x^3 (k_1 x^{2/3} - 8R/5). \quad (6.17)$$

Finally, the general solution of (6.12) with initial condition (6.13) is $g(t, x, h) = F(f(t, x, h))$, which can be rewritten as $g = k_1^3 f^3 (k_1 f^{2/3} - 8R/5)$ or

$$xh^3(h - 8R/5) = k_1^3 \left[x e^{-\frac{4h^2(6R-5h)}{k_2(R-h)}t} \right]^3 \left(k_1 \left[x e^{-\frac{4h^2(6R-5h)}{k_2(R-h)}t} \right]^{2/3} - 8R/5 \right). \quad (6.18)$$

Here, (6.18) can be solved implicitly for h given a combination of t and x . When solved for 500 cSt silicone oil spun at 854 rpm, (6.18) produces the curves in fig. 6-4a.

The solution (6.18) at later times, when $h \ll R$ and $t \gg 1$, reduces to:

$$xh^3 = k_1^3 x^3 e^{-\frac{24h^2}{k_2}t}. \quad (6.19)$$

We substitute $h = t^\alpha H$ and $x = t^\beta \xi$ into (6.19) to obtain:

$$t^{3\alpha-2\beta} \frac{H^3}{\xi^2} = k_1^3 e^{-\frac{24H^2}{k_2}t^{2\alpha+1}}. \quad (6.20)$$

The profile $H(\xi)$ is self-similar when (6.20) is independent of t . This happens when:

$$3\alpha - 2\beta = 0 \quad \text{and} \quad 2\alpha + 1 = 0, \quad \text{or equivalently} \quad \alpha = -1/2, \quad \beta = -3/4.$$

Plotting $ht^{1/2}$ versus $xt^{3/4}$ collapses all curves from fig. 6-4a onto the self-similar profile shown in fig. 6-4b.

6.5 Rayleigh-Plateau instability

Having produced nearly uniform micrometer-scale films on the inner walls of the capillary tubes by spin-coating over the timescales reported in fig. 6-3a, we stop the spinning, making F_{centr} vanish. In this setting, the ratio of gravitational to capillary forces is relatively low, so that $\text{Bo} \equiv \frac{(R-h_0)^2}{\ell_{\text{cap}}^2} \approx 0.04$, where $\ell_{\text{cap}} \equiv \sqrt{\frac{\sigma}{\rho g}}$ is the capillary length. Therefore, these thin films are subject to Rayleigh-Plateau instability (fig. 6-5a), with the fastest growing wavelength and timescale of the instability depending on the film thickness h_0 after spin-coating (Goren, 1962; Duclaux *et al.*, 2006; Eggers & Villermaux, 2008). Consequently, one should be able to control these parameters by tuning the

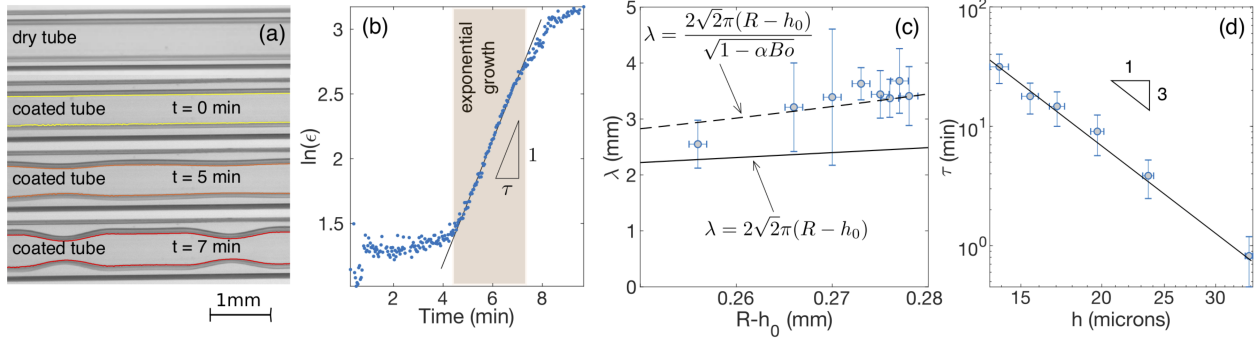


Figure 6-5: Rayleigh-Plateau instability of 500 cSt silicone oil films. (a) Typical temporal evolution of liquid film instability. Note that the liquid-solid boundary is not visible because the refractive indices of the oil ($n = 1.41$) and glass ($n = 1.51$) are very similar. (b) Evolution of the Rayleigh-Plateau crest thickness ϵ . The instability timescale τ is the inverse of the slope. Such plots are used to measure τ values in fig. 6-5d. (c) Measurements of instability wavelengths. (d) The timescale of the Rayleigh-Plateau instability, as estimated from the slope of the linear portion of $\ln(\epsilon(t))$ in fig. 6-5b. The film thickness is estimated from (6.10). A conservative estimate of the error is taken as the largest difference between the experimental and theoretical film thicknesses in fig. 6-3a. Vertical error bars represent standard deviations in both (c) and (d).

spinning and curing times of the polymer film, thereby generating either flat or wavy surfaces inside the capillary tubes.

We track the temporal progression of the film instability by detecting inner boundaries of the liquid from the top-view images of the experiment (fig. 6-5a). The wavelength of instability λ is measured as the distance between the crests on the liquid surface. Depending on h_0 , the mean experimental values of λ range between 2.5 and 3.5 mm (fig. 6-5c), which are about 32% higher than the expected wavelength of $\lambda \sim 2\sqrt{2}\pi(R-h_0)$ for viscous annular films (Goren, 1962). This discrepancy has been attributed to gravity effects by Duclaux *et al.* (2006), who suggested a corrected expression for the wavelength of $\lambda \sim 2\sqrt{2}\pi(R-h_0)/\sqrt{1-\alpha Bo}$, where α is an empirical coefficient. Adapting this expression would require $\alpha \approx 12$ to fit our data. Duclaux *et al.* (2006) outline three distinct regimes of film instability in terms of two parameters: \sqrt{Bo} and $Bo(R-h_0)/h_0$. When $\sqrt{Bo} \ll 1$ and $Bo(R-h_0)/h_0 \ll 1$, the effects of gravity are negligible and the classical wavelength of $\lambda \sim 2\sqrt{2}\pi(R-h_0)$ is recovered (Goren, 1962). When $\sqrt{Bo} \ll 1$ and $Bo(R-h_0)/h_0 = O(1)$, the wavelength is unaffected, but the instability grows faster on the lower side of the horizontal tube. Finally, as \sqrt{Bo} approaches $O(1)$, the wavelength increases as compared to the classical scaling. In our experiments $\sqrt{Bo} \approx 0.2$, hence the wavelength λ is quite possibly being affected by gravitational effects.

Despite the discrepancy in the observed wavelength, our measurements of the instability timescale closely match the theory. The growth rate is expected to follow an exponential law $\frac{d\epsilon}{dt} \sim \tau^{-1}\epsilon$, where τ is the characteristic timescale (Plateau, 1873; Rayleigh, 1892). Indeed, significant portions of the $h(t)$ are linear on a semi-logarithmic plot (fig. 6-5b). The timescales τ for different h_0 are estimated from the slopes of these linear sections. The experimental data follows the theoretically expected scaling of $\tau \sim \frac{\mu(R-h_0)^4}{\sigma h_0^3}$ (Goren, 1962; Johnson *et al.*, 1991), which reduces to $\tau \sim \frac{\mu R^4}{\sigma h_0^3}$ for thin films (see fig. 6-5d).

We observe that Rayleigh-Plateau instabilities grow nearly simultaneously throughout the capillary tubes in all of our experiments (see Supplemental Materials, video V2). Therefore, the data in

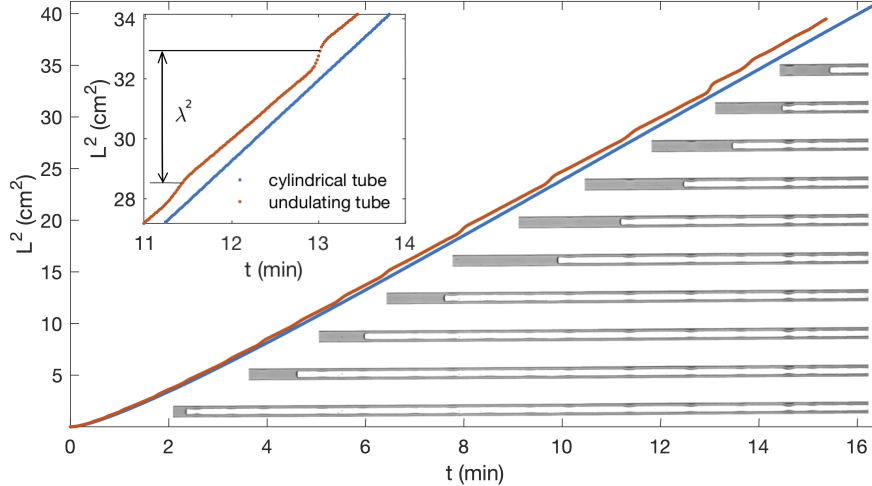


Figure 6-6: Capillary imbibition of silicone oil in two horizontal capillary tubes coated with NOA81: one with a flat, another with a corrugated inner channel. The inset shows the temporary acceleration of the liquid interface arising at the narrowest parts of the channel.

fig. 6-5d provide further confirmation that centrifugal spin coating produces films of nearly uniform thickness on the tube wall. Note that as the film thickness changes from $20 \mu\text{m}$ to $13 \mu\text{m}$, the characteristic timescale of instability changes from a minute to more than an hour (fig. 6-5d). If the film thickness were to change appreciably from one end of the tube to the other, we would thus expect to see significant variations in the timescale of the Rayleigh-Plateau instability along the tube, which is not the case in our experiments.

6.6 Coating with curable polymers

Having explored the coating of the capillary tubes with 500 cSt silicone oil and the subsequent instability of the resulting films, we illustrate one particularly interesting application of the spin-coating method. We coat the inner walls of two capillary tubes with a $13 \mu\text{m}$ film of NOA81. We cure one tube with UV light immediately after depositing the film, and let the other form Rayleigh-Plateau instabilities for one hour prior to curing. By doing so, we fabricate two capillary tubes: one with straight and the other with wavy inner walls. Since these surfaces are generated by curing liquid polymers, one may obtain surfaces that are smooth down to a molecular scale (de Gennes *et al.*, 2004).

Capillary tubes are often used in flow experiments as analogs of porous media. The two tubes we generated here represent two types of pore channels. Liquid should spontaneously imbibe into them following the Washburn law (Washburn, 1921) $L \sim (\frac{(R-h_0)\sigma}{2\mu}t)^{1/2}$, where L is the axial distance of the liquid penetration. Since both tubes have nearly identical mean inner radii, we expect that their experimental $L(t)$ curves would be nearly identical, with both following $L(t) \sim t^{1/2}$. This is indeed the case (fig. 6-6), with an important distinction between the two: the liquid in a wavy tube gets intermittent boosts in the capillary driving force whenever the liquid front passes through constrictions in the film's wavy pattern. This effect results in a distinct temporal profile of the liquid in a wavy tube compared to that in a flat one (fig. 6-6).

6.7 Conclusion

We have proposed and realized experimentally a robust and practical method of spin-coating the inner wall of capillary tubes with viscous liquids. We first demonstrated the dynamics of centrifugally-driven slug motion within the tubes. We then showed that the dynamics of the film thinning is governed by the balance of viscous and centrifugal forces, and that the thickness of the film can be anticipated through theoretical arguments. The method of coating presented here is an alternative to that of [Taylor \(1961\)](#), and is well suited to generating micron-scale liquid films.

The ability to produce both cylindrical and undulatory inner surfaces may be useful in many practical applications. For instance, coating capillary tubes with NOA81 would allow for careful control of the substrate wettability ([Zhao *et al.*, 2016](#); [Otier *et al.*, 2017](#)), while having wavy inner surfaces may prove useful in studying the pinch-off and trapping of the resident liquid in porous media. Finally, the inner wall of the tubes can be coated *sequentially* with polymers with different electric conductivity, which would allow for the generation of electrowetting ([Mugele & Baret, 2005](#)), where wettability may be modulated by a time-varying electric current. This may ultimately enable the manufacturing of capillary tubes that act like pressure oscillators in microfluidic devices.

Chapter 7

Characterizing dissipation in fluid–fluid displacement using constant-rate spontaneous imbibition

This chapter has been published in [Primkulov et al. \(2020a\)](#).

7.1 Introduction

Many of our daily experiences involve one fluid displacing another on a solid surface: from cooking oil spreading on a frying pan to paper absorbing ink ([Alava et al., 2004](#); [Kim et al., 2011](#)) and tea flowing up a biscuit ([Fisher, 1999](#)). In all of these examples, capillarity drives the flow as energy dissipates within the fluid bulk and near the contact line (the intersection of the fluid–fluid interface with the solid surface). While dissipation in the fluid bulk is purely viscous, dissipation near the contact line is not yet fully understood ([de Gennes, 1985](#); [Snoeijer & Andreotti, 2013](#); [Brochard-Wyart & de Gennes, 1992](#); [Joanny & Robbins, 1990](#); [Raphaël & De Gennes, 1989](#); [Sheng & Zhou, 1992](#); [De Coninck & Blake, 2008](#); [Pahlavan et al., 2015](#); [Levaché & Bartolo, 2014](#); [Eggers & Stone, 2004](#); [Bird et al., 2008](#)). Characterizing what fraction of energy is lost in each region is a nontrivial task; the contact-line dynamics remains in many respects unresolved and continues to challenge our descriptions of multiphase flow ([de Gennes, 1985](#); [De Coninck & Blake, 2008](#); [Bonn et al., 2009](#); [Snoeijer & Andreotti, 2013](#)).

In this work, we unambiguously separate contact-line and bulk dissipation and map out their relative importance within a simple fluid–fluid displacement system. This is challenging since the dynamics of moving contact lines is nonlinear and rate-dependent: the macroscopic contact angle θ at which the fluid–fluid interface meets the solid surface changes with the rate of displacement, and dissipation at the contact line, in turn, changes with θ ([Huh & Scriven, 1971](#)). The dynamics of moving contact lines has traditionally been studied through two classes of experiments: (i) constant-rate displacement under an external force (e.g., dip-coating ([Moulinet et al., 2004](#); [Perrin et al., 2016](#)), forced displacement in capillary tubes ([Hoffman, 1975](#); [Fermigier & Jenffer, 1991](#))) and (ii) spontaneous, variable-rate displacement (e.g., spreading of a droplet on a solid surface ([Seaver & Berg, 1994](#); [Tanner, 1979](#)), imbibition of a liquid into a capillary tube ([Mumley et al., 1986](#); [Hilpert, 2009, 2010](#); [Schäffer & Wong, 1998, 2000](#); [Walls et al., 2016](#))).

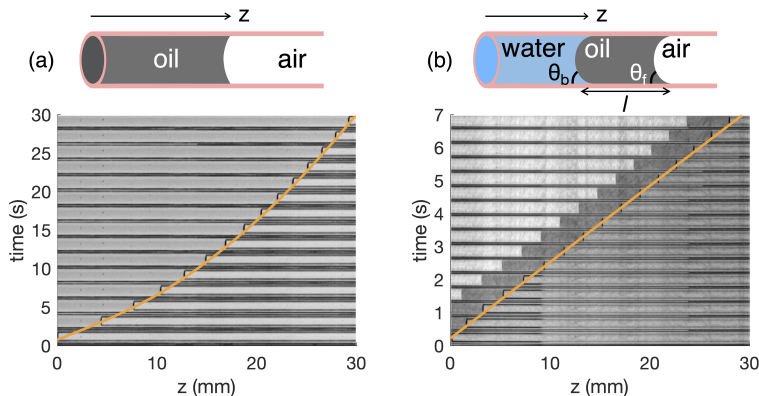


Figure 7-1: Experimental snapshots of (a) the classical spontaneous imbibition ($z \sim t^{1/2}$) of 50 cSt silicone oil in a capillary tube and (b) constant-rate spontaneous imbibition ($z \sim t$) of water with a 50 cSt silicone oil slug precursor.

7.2 Experimental method

Here, we present an alternative experimental setup whose novelty is the result of combining, for the first time, three key ingredients: (i) moving contact line dynamics, (ii) confined geometries, and (iii) spontaneous, constant-rate interfacial motion. Although the dynamics of the moving contact lines was first properly described by Voinov (Voinov, 1977) and Cox (Cox, 1986), most studies have focused on unconfined configurations such as spreading of liquid drops on solid surfaces (Oron *et al.*, 1997; Bonn *et al.*, 2009; Snoeijer & Andreotti, 2013). Confinement increases the ratio of interfacial area (solid-fluid and fluid-fluid) to bulk volume, often by orders of magnitude, which raises a fundamental question about the balance among different dissipation sources. While many studies have analyzed the importance of the different contributions to energy dissipation in the context of spontaneous imbibition of a liquid displacing air, as described by the Lucas–Washburn law (Washburn, 1921; Alava *et al.*, 2004), bulk viscous dissipation is the dominant dissipation contribution at all times, except for the early onset of the flow (Delannoy *et al.*, 2019). What sets our experimental setup apart from previous studies is that it allows us to achieve *constant-rate* imbibition, and therefore keep the ratio of the different dissipation contributions fixed throughout each experiment. This allows us to unambiguously extract the sources of dissipation in the different regimes and construct a phase diagram describing the ratio of the energy that is dissipated at the contact line.

Our experimental setup is built upon the classical case of spontaneous imbibition into a capillary tube. By exposing one end of a horizontal capillary tube to a silicone oil reservoir, oil spontaneously wets the capillary (“classical imbibition”, FIG. 7-1a). The position of the oil front (z) mostly follows Washburn’s scaling ($z \sim t^{1/2}$) (Washburn, 1921). The mechanism behind the slowing of the liquid front is well understood: the capillary driving force remains nearly constant, while viscous resistance increases in proportion to z . We modify this setup to achieve constant-rate spontaneous imbibition by restricting the viscous resistance to an oil slug of fixed length (“constant-rate imbibition”, FIG. 7-1b). We place a silicone oil (Sigma-Aldrich) slug of viscosity μ_o and length l into a hydrophilic glass tube (untreated Hilgenberg GmbH borosilicate glass 3.3), and then expose the end with the slug to a reservoir of water with viscosity μ_w . The bulk viscous resistance is then proportional to $\mu_o l + \mu_w z$; when $\mu_o l \gg \mu_w z$, the slug moves at a constant rate that can be controlled by tuning l and/or μ_o . In our experiments, the length of the oil slug does not change as water penetrates the tubes, which implies that the oil slug does not leave a film of oil behind (Bico & Quéré, 2002, 2001; Zhao *et al.*,

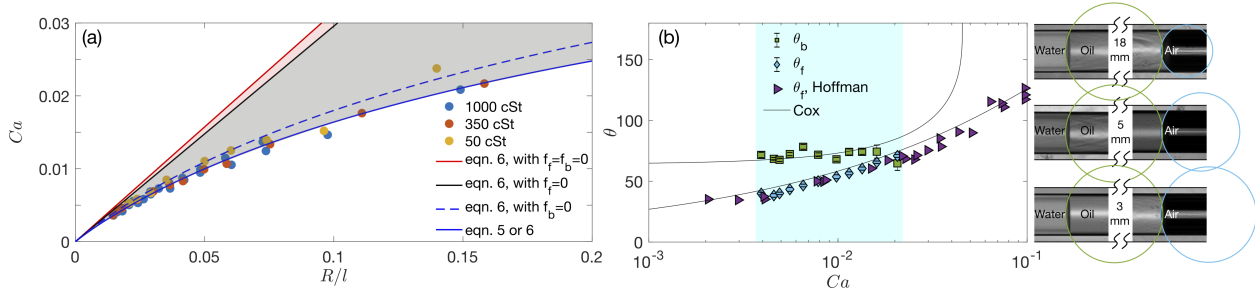


Figure 7-2: (a) Constant-rate imbibition experiments for $\mu_o \in \{48, 485, 970\}$ mPa·s and $l \in [2, 14]$ mm. Solid lines represent theoretical predictions of constant-rate imbibition after accounting for dissipation sources within the oil slug. The experimental data is captured accurately by equation (7.5) (or equivalently equation (7.6)). (b) Measurements of θ_f (blue diamonds) and θ_b (green squares) during constant-rate imbibition were taken under a microscope, with typical snapshots for slugs of different lengths (and thus Ca) displayed beside the figure. The solid lines show the generalized Cox relation (Cox, 1986) with $\Gamma = 6.9$, and purple triangles indicate the data from Hoffman (Hoffman, 1975). The blue shaded region indicates the range of Ca in our constant-rate imbibition experiments.

2018). We include further experimental details in the supplemental materials E.

In contrast with classical imbibition, the oil slug in our experiments has two menisci: one at the front (oil–air) and one at the back (water–oil) (FIG. 7-1b). The contact angles of these two menisci are expected to change with the contact-line speed, and we use the term “dynamic contact angle” for angles at nonzero speeds. We denote the dynamic contact angles of the back and front menisci as θ_b and θ_f , and their respective static-advancing values as $\theta_{b,a}$ and $\theta_{f,a}$. Each individual experiment has a fixed speed and thus fixed dynamic contact angles. To probe the dynamics of the system at different spontaneous contact-line speeds, we span a wide range of slug viscosities and lengths, with $\mu_o \in \{48, 485, 970\}$ mPa·s and $l \in [2, 14]$ mm. We characterize the nominal ratio of viscous to capillary forces in each experiment through the capillary number $Ca \equiv \frac{\mu_o \dot{z}}{\gamma_o}$, where \dot{z} is the slug speed and γ_o the surface tension of the oil. We plot Ca against the ratio of tube radius R to slug length l in FIG. 7-2a, where 44 constant-rate imbibition experiments collapse onto a single curve. While each individual experiment is constant-rate, the nonlinear global trend emerges from the dynamics near the contact lines. We begin to rationalize this trend through force balance.

7.3 Theory

Constant-rate imbibition is governed by the balance of bulk viscous resisting force (F_{bulk}) and capillary driving force (F_{cap}). The bulk viscous force can be calculated from the drag on the tube walls by assuming classical Poiseuille flow (see supplemental materials E) as $F_{\text{bulk}} = 2\pi R(l \frac{4\mu_o}{R} + z \frac{4\mu_w}{R})\dot{z}$. Since $\frac{\mu_w z}{\mu_o l} \in [0.001, 0.2]$ in our experiments, we neglect the viscous pressure drop within the water phase and the expression for F_{bulk} reduces to

$$F_{\text{bulk}} = 8\pi\mu_o l \dot{z}. \quad (7.1)$$

The capillary driving force can be expressed through the dynamic contact angles of the back and front menisci:

$$F_{\text{cap}} = 2\pi R(\gamma_{ow} \cos \theta_b + \gamma_o \cos \theta_f), \quad (7.2)$$

where γ_{ow} is the oil–water interfacial tension. For quasi-static displacement in the absence of gravity, F_{cap} and F_{bulk} must balance to yield the speed of the oil slug, $\dot{z} = \frac{R}{4\mu_o l}(\gamma_{ow} \cos \theta_b + \gamma_o \cos \theta_f)$, which in dimensionless form reads:

$$\text{Ca} = \left(\frac{\gamma_{ow}}{\gamma_o} \cos \theta_b + \cos \theta_f \right) \frac{R}{4l}. \quad (7.3)$$

To fully resolve equation (7.3), we need to know how θ_b and θ_f evolve with Ca (de Gennes, 1985; Bonn *et al.*, 2009; Snoeijer & Andreotti, 2013). When the solid surface is perfectly smooth and homogeneous, both angles are expected to follow the generalized Cox equation (Cox, 1986), which can be written as

$$g(\theta, M) - g(\theta_a, M) = \text{Ca} \Gamma, \quad (7.4)$$

where $\Gamma = \ln(R/h_{\text{micro}})$, h_{micro} is the microscopic cut-off-length near the contact line, M is the ratio of the defending to invading fluid viscosities, and the function $g(\theta, M)$ is defined in the supplemental materials E. Indeed, when using $M = 0$ for the oil–air interface, $M = 1000$ for the water–oil interface, and $h_{\text{micro}}/R = 10^{-3}$ ($\Gamma = 6.9$) for both (Cox, 1986), the generalized Cox equation produces good agreement with the experimental measurements of θ_f and θ_b (FIG. 7-2b). Although equations (7.3) and (7.4) can be used to reproduce the constant-rate imbibition trend in FIG. 7-2a, we seek further simplifications of equation (7.4) for the two menisci. First, we take $\theta_b = 72^\circ$. This is justified since both θ_b measurements and the generalized Cox trend in FIG. 7-2b appear to be approximately constant within the Ca range of our constant-rate imbibition experiments. Second, we note that equation (7.4) simplifies greatly for the oil–air meniscus: when $M \ll 1$, it reduces to the commonly-used Cox–Voinov relation $\theta_f^3 = \theta_{f,a}^3 + 9\Gamma\text{Ca}$ (Cox, 1986; Voinov, 1977). This further reduces to $\theta_f = (9\Gamma\text{Ca})^{1/3}$ since silicone oil wets the glass surface completely ($\theta_{f,a} = 0^\circ$). Therefore, after using the expansion $\cos \theta_f = 1 - \theta_f^2/2 + O(\theta_f^4)$ and the Cox–Voinov expression, equation (7.3) yields:

$$\text{Ca} = \left[\frac{\gamma_{ow}}{\gamma_o} \cos \theta_b + 1 - \frac{1}{2}(9\Gamma\text{Ca})^{2/3} \right] \frac{R}{4l}, \quad (7.5)$$

which accurately reproduces the experimental trend (FIG. 7-2a). Note that the generalized Cox relation predicts approximately constant θ_b within the Ca of our experiments for any liquid pair as long as $M \ll 1$ and $\theta_{b,a}$ is not much greater than the value in our experiments ($\theta_{b,a} = 64^\circ$).

7.4 Contact-line dissipation

We can now use this theoretical description of constant-rate imbibition [Eq. (7.5)] to evaluate the contributions of the two moving contact lines to the macroscopic trend in FIG. 7-2a. It is important to make a distinction between the two menisci in FIG. 7-1b, because wettability plays a key role in how they interact with surface defects. The water–oil interface is in partial wetting, and can experience pinning at surface defects (Joanny & Robbins, 1990); whenever $\theta_b < \theta_{b,a}$, surface tensions at the contact line are in static balance. This balance no longer holds when $\theta_b > \theta_{b,a}$, and the contact line sets in motion. We define the dynamic contact-line force at the back meniscus as $f_b = \gamma_{ow}(\cos \theta_{b,a} - \cos \theta_b)$. We measure $\theta_{b,a} \approx 64^\circ$, and thus $f_b \approx 0.13\gamma_{ow}$. In contrast, the oil–air interface is in complete wetting, and is not sensitive to most surface defects (Joanny & Robbins, 1990). We define $f_f = \gamma_o(\cos \theta_{f,a} - \cos \theta_f)$ in analogy to the water–oil meniscus. Recall that $\theta_{f,a} = 0^\circ$. Then, the force at the front meniscus reduces to $f_f = \frac{\gamma_o}{2}(9\Gamma\text{Ca})^{2/3}$. We can then rewrite equation (7.5) through the dynamic contact-line forces,

$$\frac{4l}{R}\text{Ca} + \frac{f_b}{\gamma_o} + \frac{f_f(\text{Ca})}{\gamma_o} = 1 + \frac{\gamma_{ow}}{\gamma_o} \cos \theta_{b,a}, \quad (7.6)$$

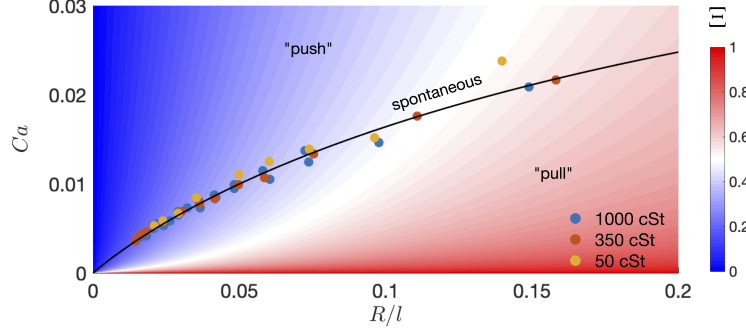


Figure 7-3: Phase diagram of forced, rate-controlled imbibition of viscous oil slugs. An external force is needed to move the slug at higher Ca (“push”) or lower Ca (“pull”) than the spontaneous rate predicted by equation (7.6) (black solid line). The color of the $R/l - Ca$ space represents the ratios of contact-line to total dissipation in such moving slugs, $\Xi = \Phi_{cl}/(\Phi_{cl} + \Phi_{bulk})$.

where “driving” terms are grouped on the right-hand-side, and “resisting” terms are grouped on the left-hand-side. Equation (7.6) is equivalent to equation (7.5), but its form is convenient for inferring the relative importance of f_b and f_f to the overall trend in FIG. 7-2a. If there were no dynamic contact-line forces at the two menisci ($f_f = f_b = 0$), the equation of motion would reduce to equation (7.3) with $\theta_b = \theta_{b,a}$ and $\theta_f = \theta_{f,a}$. This scenario corresponds to the red line in FIG. 7-2a. If we now remove the dynamic contact-line force at the front meniscus only, equation (7.6) would reduce to equation (7.5) with term $\frac{\gamma}{2}(9\Gamma Ca)^{2/3} = 0$, corresponding to the black line in FIG. 7-2a. This allows making several conclusions: (i) neglecting the dynamic contact-line forces produces a trend with a significant qualitative and quantitative disagreement with the experiments in FIG. 7-2a, (ii) non-linearity in constant-rate imbibition comes from the dynamic contact-line force at the front meniscus, (iii) the contribution of f_b to the overall trend in FIG. 7-2a is relatively small (see Eq. (7.6) with $f_b = 0$ in FIG. 2a), with $2 < f_f/f_b < 8$ within the experimental range of constant-rate imbibition.

Although our experiments are in spontaneous imbibition, our results are also relevant to forced imbibition. Addition of an external force would not change the sources of dissipation within the moving slug. There are only three dissipative forces in our system: bulk viscous force, and contact line forces at the two menisci. The energy dissipation in the bulk is $\Phi_{bulk} = 8\pi\mu_{ol}\dot{z}^2$, again assuming Poiseuille flow and $\mu_{ol} \gg \mu_w z$. The dissipation due to dynamic contact-line forces is $\Phi_{cl} = 2\pi R(f_f + f_b)\dot{z}$. We can map the relative magnitudes of Φ_{bulk} and Φ_{cl} during arbitrary motion of the oil slug. FIG. 7-3 shows a phase diagram where spontaneous imbibition [Eq. (7.5)] separates regions where an external force either “pushes” the slug to move faster or “pulls” it to move slower than the spontaneous rate. The ratio of contact-line to total dissipation within the moving slug is $\Xi = \Phi_{cl}/(\Phi_{cl} + \Phi_{bulk})$, which is equivalent to

$$\Xi = \frac{f_b + f_f}{f_b + f_f + \frac{4l}{R}Ca\gamma_o}, \quad (7.7)$$

and can be alternatively derived by considering dissipative forces within the system (contact line vs. total). The black lines in FIG. 7-3 represent isolines corresponding to different values of Ξ in equation (7.7). A surprisingly large fraction of the dissipation (between 20% for 14 mm slugs and 50% for 2 mm slugs) occurs in the vicinity of the contact line during our constant-rate imbibition experiments. Dissipation isolines in FIG. 7-3 are valid within the Ca range of our experiments. However, it is important to note what would happen in the upper and lower bounds of Ca in

FIG. 7-3. In the upper bound ($Ca > 0.02$), our approximation of constant θ_b would no longer hold (see FIG. 7-2b). Thus, the isolines in FIG. 7-3 likely underestimate the true dissipation ratio when $Ca > 0.02$. In the lower bound ($Ca \rightarrow 0$), the system would approach a depinning threshold, where the water–oil contact line would move by hopping between surface defects, resulting in $\theta_b(Ca)$ relation that is very different from the generalized Cox equation (Joanny & Robbins, 1990; Raphaël & De Gennes, 1989; Sheng & Zhou, 1992). The fact that the motion of the water–oil meniscus in our experiments appears to be smooth and θ_b is in good agreement with the generalized Cox equation suggests that we are either sufficiently far from the depinning threshold or that the strength of the surface defects on our glass surface is too small to have appreciable influence on the overall trend in FIG. 7-3.

The ratio of contact-line to bulk dissipation in FIG. 7-3 has important macroscopic implications for problems beyond the constant-rate imbibition we present in this work. Neglecting dissipation near the contact lines would lead to erroneous (linear) relation between dissipation and Ca ; FIG. 7-3 demonstrates that this relation is nonlinear and is a function of the slug dimensions. One example where this may be significant is the flow of foam or ganglia in porous media (Tallakstad *et al.*, 2009a,b), a system that has an inherently large number of (potentially very short) viscous slugs and thus might be expected to have significant energy dissipation associated with dynamic contact angle effects. Another example is classical imbibition in capillary tubes. It has been recently demonstrated that early-time viscous effects near the contact line move the system away from the commonly known form of the Washburn equation ($z \sim t^{1/2}$), towards $z \sim t$ (Delannoy *et al.*, 2019). This is when Φ_{bulk} and Φ_{cl} are comparable. However, this flow regime is rather brief in classical imbibition (see supplemental materials E, which includes (Bico & Quéré, 2002; Delannoy *et al.*, 2019; Hilpert, 2009, 2010; Heshmati & Piri, 2014; Hoffman, 1975; Thielicke & Stamhuis, 2014; Cox, 1986)). Alternatively, one can readily access the flow regime with significant Φ_{cl} contribution through constant-rate imbibition, as we demonstrate in FIG. 7-3.

7.5 Conclusion

In summary, we have mapped out the contributions of contact-line and bulk dissipation during fluid–fluid displacement, and we have shown that a large portion of the dissipation takes place in the vicinity of the contact line. We did so using constant-rate spontaneous imbibition, achieved by introducing a viscous oil slug in front of the invading fluid inside a capillary tube. The rate of imbibition in such experiments can be precisely controlled through the viscosity and length of the oil slug. This setup allows probing flow regimes that would otherwise be accessible only during the early-time spontaneous flow—a novel feature of our experimental setup that has significant utility in the study of moving contact line problems. Alternatively, one can ensure that dynamic contact line effects are negligible by making the oil slugs sufficiently long ($\Xi \rightarrow 0$ when $l/R \gg 1$). For example, in order for contact-line dissipation to account for less than 5% of total dissipation, a slug must be longer than $l/R = 155$ at $Ca = 0.02$ and longer than $l/R = 65$ at $Ca = 0.2$.

The system we present in this work could be utilized for fabrication of precise micro- and nano-pumps. The ability to precisely control the flowrate without external forces would be useful in designing passive microfluidic devices (Zimmermann *et al.*, 2007), which have applications in miniature heat pipes for cooling of electronic components (Vasiliev, 2008), patterning biomolecules in microchannels (Delamarche *et al.*, 2005), and clinical diagnostics (Ahn *et al.*, 2004). Indeed, a known method of maintaining a fixed flowrate in such devices is by having a constriction ahead of the flow channel that is about an order of magnitude smaller than the rest of the channel (Guo *et al.*, 2018). However, it can be technically challenging to scale down this technique to sizes below

a micron, where one would need to precisely fabricate nanometer-scale constrictions. The constant-rate imbibition depicted in FIG. 7-1b does not have such scaling limitations, and it is a cheap technique that can be used for passive control of flowrates in microfluidic devices.

Chapter 8

Moving contact lines over heterogeneous surfaces: from stick–slip to steady sliding

8.1 Introduction

The vast majority of solid surfaces exhibit physical and chemical defects. For instance, surface heterogeneity of window glass is apparent in how it interacts with rain—here, larger raindrops slide smoothly down the slope, smaller ones remain pinned, and droplets of intermediate size undergo macroscopic stick–slip motion. The complex behavior of fluid–fluid interfaces moving over heterogeneous solid surfaces has captivated the fluid–mechanics community over the past several decades (de Gennes, 1985; Bonn *et al.*, 2009; Snoeijer & Andreotti, 2013), driven by elegant physics of the problem and the multitude of relevant practical applications, such as CO₂ sequestration (MacMinn *et al.*, 2010, 2011; Szulcowski *et al.*, 2012), geologic storage of hydrogen, and design of electrolyzers (Lee *et al.*, 2019).

At the same time, experiments exhibiting intermittent motion of fluid–fluid–solid contact lines have been often dismissed whenever the surfaces were considered not sufficiently smooth and clean, with researchers developing widely-adopted surface-cleaning protocols (de Gennes *et al.*, 2004). This introduced a historical bias, and most of the experimental and, therefore, theoretical progress in the physics of moving contact lines was made for surfaces with the highest practically-attainable degree of homogeneity.

As a result, many previous studies have examined the motion of contact lines over solid surfaces with nanometer-scale heterogeneity. Here, fluid–fluid interfaces appear to move smoothly, and interface distortions due to defects are not directly observable. Even on those surfaces, defects at the nanometer scale can impact the macroscopic motion of contact lines. Perrin *et al.* (Perrin *et al.*, 2016, 2018*a,b*) demonstrated that while the balance of viscous and capillary forces governs the interface shape at high velocities (Voinov, 1977; Cox, 1986), macroscopic dynamics is dominated by thermally-activated interactions of the interface with nano-scale defects at slow displacement rates.

A much less theoretically explored physical situation arises when surface defects are on the micrometer scale, where distinct stick–slip motion of the fluid–fluid interface can emerge. Thiele and Knobloch (Thiele & Knobloch, 2006*a,b*) developed a thin-film model that captures how droplets transition from a pinned state to intermittent motion on surfaces with pre-wetting films. In that model, a constant body force drives the droplet, while hydrophobic defects pin the drop at the front, and hydrophilic defects stretch it at the back. A similar system was realized experimentally by fabricating hydrophilic/hydrophobic stripes on glass, where stick–slip dynamics resulted in slowing of droplets by an order of magnitude (Varagnolo *et al.*, 2013). Equally intriguing experiments have

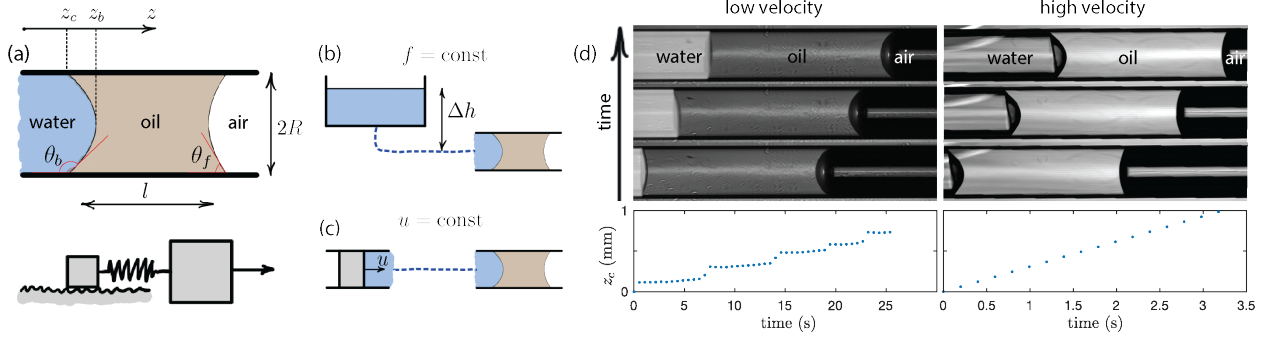


Figure 8-1: (a) Viscous slug schematic, where only the back meniscus is in partial wetting and therefore interacts with surface defects. (b) Constant-force experiment can be realized by imposing a fixed pressure difference across the viscous slug (neglecting the pressure gradient in water) by controlling the reservoir height Δh . (c) Constant-rate experiment can be realized by supplying water through a syringe at a prescribed flowrate. (d) A slug of viscous oil displaced by water inside NOA81-coated capillary tube crosses over from stick-slip motion (left) to steady sliding (right) as the displacement rate increases.

been reported for systems driven at a constant rate. Zuo et al. (Zuo *et al.*, 2012) reported stick-slip droplet motion during advancing contact angle measurements. In these experiments, the amplitude of contact-line oscillations decreased on surfaces with higher concentration and, therefore, spacing of impurities on the surface. Finally, we show in this study that the stick-slip motion crosses over to steady sliding with increasing displacement rates (Fig. 8-1). No model exists to date able to delineate the link between the amplitude of stick-slip cycles and the spacing of surface defects, let alone predict the rate-dependent transition from stick-slip to steady sliding shown in Fig. 8-1.

Here, we build on the work of Raphaël-de Gennes and Joanny-Robbins (Raphaël & De Gennes, 1989; Joanny & Robbins, 1990) by reducing the dynamics of fluid-fluid displacement in partial wetting to a system of coupled ordinary differential equations. We take a step further and connect these equations to a mechanical analog (Adler, 1946) that allows reducing the complexity of stick-slip dynamics to a few key parameters, elucidating both constant-force and constant-rate displacement regimes. While the work of Raphaël-de Gennes and Joanny-Robbins (Raphaël & De Gennes, 1989; Joanny & Robbins, 1990) focused on the force-velocity scaling at diminishing displacement rates, ours provides a rationale for the crossover between stick-slip and steady sliding motion at high displacement rates. This transition is characterized by a simple scaling relation between the spacing of the defects, the characteristic size of the fluid-fluid interface, and the capillary number—a scaling relation that can help explain disparate stick-slip phenomenology from recent experimental studies.

8.2 Physical setup and governing equations

Consider a viscous silicone oil slug of length l being displaced by water inside a capillary tube with an inner radius R , whose surface is not perfectly smooth or homogeneous (Fig. 8-1a). Here, θ_b and θ_f are water-oil and oil-air contact angles; z_b and z_c are positions of water-oil meniscus center and contact line along the tube. We chose a silicone oil with viscosity much greater than the viscosity of water ($\mu_o \gg \mu_w$), which allows neglecting pressure gradients outside the slug. Furthermore, only the partially wetting water-oil interface interacts with the surface imperfections; the oil-air interface is in complete wetting, where a precursor film (or hemi-wicking front) masks surface defects (Joanny

& Robbins, 1990). One can drive the viscous slug at either constant force (Fig. 8-1b) or constant rate (Fig. 8-1c). At low displacement rates the slug moves through stick–slip motion, while at high velocity it experiences steady sliding (Fig. 8-1d). This is reminiscent of a solid block being pulled through a spring (a spring–slider model (Brace & Byerlee, 1966), Fig. 8-1a). However, while the transition from stick–slip to steady sliding is controlled by the stiffness of the spring in the spring slider, the analogous transition in viscous slugs seems to be also controlled by the displacement rate.

To rationalize the transition from stick–slip to steady sliding, we simplify the system in Fig. 8-1a, producing governing equations identical to the ones in the depinning dynamics framework by Raphaël-de Gennes and Joanny-Robbins (Raphaël & De Gennes, 1989; Joanny & Robbins, 1990). In fact, by forcing the viscous slug at either constant force (Fig. 8-1b) or constant rate (Fig. 8-1c) one can experimentally probe the seminal force-velocity scaling relations proposed in (Raphaël & De Gennes, 1989; Joanny & Robbins, 1990) (see force-velocity arguments in section F.2). Here, we examine how the governing equations behave *away from the depinning limit* and rationalize the transition from stick–slip to steady motion for both constant-rate and constant-force settings.

The overall motion can be described by several forces. We can express the externally applied force through the pressure difference Δp at the two ends of the slug as

$$F_{\text{ext}} = \Delta p \pi R^2. \quad (8.1)$$

The bulk viscous force of the slug due to Poiseuille flow is

$$F_{\text{v,bulk}} = 8\pi\mu_o l \dot{z}_b. \quad (8.2)$$

Since the front meniscus is completely wetting, its capillary force can be approximated with

$$F_f \approx 2\pi R \gamma_o, \quad (8.3)$$

where we neglected the dynamic contribution of F_f , assuming a sufficiently long slug (Primkulov *et al.*, 2020a). We model the chemical heterogeneity of the solid surface by a spatially-periodic perturbation $h(z_c)$ to a spreading coefficient (Joanny & Robbins, 1990; Raphaël & De Gennes, 1989), which is equivalent to

$$\cos \theta_b = \cos \theta_{b0} + h(z_c)/\gamma_{ow}, \quad (8.4)$$

where θ_{b0} is the contact angle on an ideally smooth and homogeneous surface. For simplicity, we assume $\theta_{b0} = \pi/2$ and neglect the viscous bending of the interface in both the front and back menisci. We can then treat the water-oil interface as a linear spring, where

$$F_{\text{spring}} = 2\pi R k (z_b - z_c), \quad (8.5)$$

and the spring constant can be approximated as $k = \gamma_{ow}/R$. Finally, we approximate the local viscous force of the back meniscus as a cumulative force of moving wedge-shaped fluid slices with contact angle θ_{b0} (de Gennes, 1985; Joanny & Robbins, 1990; Golestanian, 2004)

$$F_{\text{v,b}} \approx 2\pi R \frac{3\Gamma\mu_o}{\pi - \theta_{b0}} \dot{z}_c \approx 2\pi R \frac{6\Gamma\mu_o}{\pi} \dot{z}_c, \quad (8.6)$$

where Γ is the logarithmic factor of order one (de Gennes, 1985). $F_{\text{v,b}} \sim \dot{z}_c$ in Eq. 8.6 means that the water-oil contact line acts similarly to a viscous dashpot in the classic spring–slider model. We

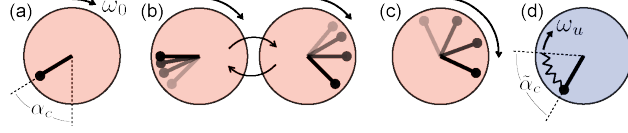


Figure 8-2: Mechanical analog of the spring oscillator model in a constant-force regime (a) moves through either stick–slip (b) or steady motion (c). This analog can be extended to a constant displacement regime by introducing a spring that is pulled at constant ω_u (d).

can then write down the coupled dynamics of the back contact line and the slug as

$$F_{v.\text{bulk}} = F_f + F_{\text{ext}} - F_{\text{spring}}, \quad (8.7)$$

$$F_{v.b} = F_{\text{spring}} + 2\pi R h(z_c). \quad (8.8)$$

Equations 8.7-8.8 reduce to

$$\underbrace{b_b \dot{z}_b}_{\text{slug dashpot}} = \underbrace{f}_{\text{applied force}} - \underbrace{k(z_b - z_c)}_{\text{coupling spring}}, \quad (8.9)$$

$$\underbrace{b_c \dot{z}_c}_{\text{contact-line dashpot}} = k(z_b - z_c) + \underbrace{h(z_c)}_{\text{pinning force}}, \quad (8.10)$$

where $b_b = 4\mu_o l/R$, $b_c = 6\Gamma\mu_o/\pi$, and $f = \gamma_o + \Delta p R/2$.

Following (Joanny & Robbins, 1990) we model heterogeneity in the spreading coefficient with a sine function as this minimal model still allows to capture the essential physics of interest here. Therefore,

$$h(z_c) = -\epsilon\gamma_{ow} \sin(2\pi z_c/q), \quad (8.11)$$

where $\epsilon < 1$ and q is the distance between the consecutive peaks of the sine function. We write down the system of Eqs. 8.9-8.10 in a reduced form by defining $\alpha = 2\pi z/q$ as

$$\dot{\alpha}_b = \underbrace{\omega_0}_{\text{force term}} - \underbrace{K(\alpha_b - \alpha_c)}_{\text{spring term}}, \quad (8.12)$$

$$\lambda \dot{\alpha}_c = K(\alpha_b - \alpha_c) - \underbrace{B \sin \alpha_c}_{\text{pinning term}}, \quad (8.13)$$

where $\lambda = b_c/b_b$, $\omega_0 = 2\pi f/b_b q$, $K = k/b_b$, and $B = 2\pi\gamma_{ow}\epsilon/b_b q$. This dynamical system has two interacting parts: bulk motion of the slug and the local motion of the water-oil contact line. These two parts interact through a spring (water-oil interface). One can either drive this system at a constant force (by fixing ω_0) or at a constant rate (by imposing $\dot{\alpha}_b = \omega_u$).

8.3 Results and Discussion

8.3.1 Constant-force analog

When the system is driven at a constant force, ω_0 is constant in equation 8.12. We can neglect $\lambda\dot{\alpha}_c$ assuming $\lambda = b_c/b_b \ll 1$, so Eqs. 8.12-8.13 reduce to $\dot{\alpha}_c = \omega_0 - B \sin \alpha_c$ or

$$\underbrace{\dot{\alpha}_c}_{\text{pendulum velocity}} = \underbrace{\omega_0}_{\text{drum velocity}} - \underbrace{B \sin \alpha_c}_{\text{gravity term}}, \quad (8.14)$$

if we assume that $\frac{d}{dt}(\alpha_b - \alpha_c) \approx 0$, which is in agreement with numerical solution of Eqs. 8.12-8.13 at nearly all times during slow displacement (see section F.2). This corresponds to the adiabatic approximation of Raphaël-de Gennes and Joanny-Robbins (Raphaël & De Gennes, 1989; Joanny & Robbins, 1990). Eq. 8.14 has been examined in the context of locking phenomena in electric oscillators by Adler (Adler, 1946), who proposed a mechanical analog that we will use to understand our system.

Eq. 8.14 describes the dynamics of a pendulum inside a drum filled with viscous fluid, where the drum is rotated at a fixed angular velocity ω_0 , and $-B \sin \alpha_c$ is the gravity term acting on the pendulum (Fig. 8-2a). The pendulum acquires a static angle α_c when the applied force is insufficient for overcoming gravity ($\omega_0 < B$). This represents a pinned state of the viscous slug. When ω_0 is infinitesimally greater than B , the pendulum goes through distinct stick-slip motion; it is slower when moving against gravity and faster when moving in the direction of gravity (Fig. 8-2b). The pendulum spends most of its period near the value of α_c corresponding to the maximum of the gravity term. This regime corresponds to the stick-slip motion of the viscous slug near the depinning limit. Adler (Adler, 1946) demonstrated that the pendulum's mean angular velocity is $\bar{\omega} = \sqrt{\omega_0^2 - B^2}$, whenever $\omega_0 > B$ (see section F.2).

When $\omega_0 \gg B$, the viscous fluid within the drum sweeps up the pendulum (Fig. 8-2c) and its mean angular velocity $\bar{\omega}$ approaches ω_0 . This means that the amplitude of pendulum oscillations about $\bar{\omega}t$ diminishes at large ω_0 . In fact, if we take $\tilde{\alpha}_c = \alpha_c - \bar{\omega}t$, we can rewrite Eq. 8.14 in this moving frame as $\frac{d\tilde{\alpha}_c}{dt} = \omega_0 - \bar{\omega} - B \sin(\tilde{\alpha}_c + \bar{\omega}t) \approx -B \sin(\omega_0 t)$, where we assumed $\tilde{\alpha}_c \ll \bar{\omega}t$. This allows approximating the oscillations about the moving frame as

$$\tilde{\alpha}_c(t) \approx \underbrace{\frac{B}{\omega_0}}_{\text{amplitude}} \cos(\omega_0 t) + C. \quad (8.15)$$

In other words, we expect the amplitude of oscillations to decay with increasing ω_0 , following B/ω_0 scaling, which is indeed what we observe in the numerical solution to Eq. 8.14 (see Fig. F-4).

8.3.2 Constant-rate analog

When the viscous slug is driven at a constant rate $\dot{\alpha}_b = \omega_u$, a modified version of the drum analog still holds. In the constant-rate analog, the drum is free, while the pendulum is pulled at a fixed angular velocity ω_u through a spring (Fig. 8-2d). It is useful to switch to a frame moving with the viscous slug. In this coordinate system, $\frac{d\tilde{\alpha}_b}{dt} = 0$ and we can choose the frame in a way that $\tilde{\alpha}_b = 0$,

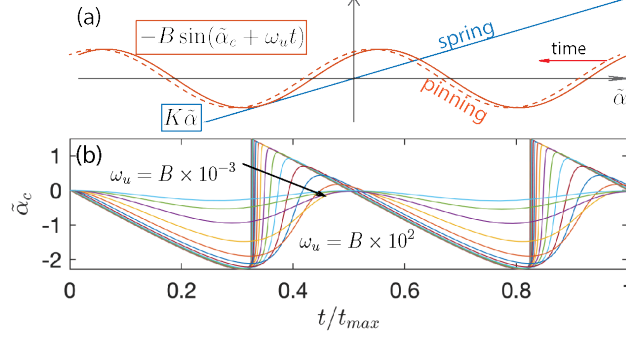


Figure 8-3: (a) Quasi-static motion of the pendulum in the constant-rate displacement is governed by the balance between spring and gravity terms, where latter shifts left with time. When $K < B$, two lines occasionally intersect more than once, which results in disanchoring events depicted here. (b) Evolution of $\tilde{\alpha}_c$ from numerical solution of Eq. 8.17 for $\omega_u/B \in [10^{-3}, 10^2]$ shows that amplitude of $\tilde{\alpha}_c$ vanishes at increasing rate ω_u .

so Eqs. 8.12-8.13 transform to

$$\omega_0 - \omega_u = -K\tilde{\alpha}_c, \quad (8.16)$$

$$\underbrace{\lambda \frac{d\tilde{\alpha}_c}{dt}}_{\text{dynamic term}} + \underbrace{K\tilde{\alpha}_c}_{\text{spring}} = -\underbrace{B\sin(\tilde{\alpha}_c + \omega_u t)}_{\text{gravity (pinning)}}, \quad (8.17)$$

where $\omega_0 - \omega_u$ is the force term due to loading of the spring, and the pendulum motion is governed by Eq. 8.17.

In the quasi-static limit we can neglect $\lambda \frac{d\tilde{\alpha}_c}{dt}$, and Eq. 8.17 reduces to $K\tilde{\alpha}_c = -B\sin(\tilde{\alpha}_c + \omega_u t)$. Therefore, the position of the pendulum is determined by the balance of a linear spring and a sinusoidal gravity term, where the graphical solution for $\tilde{\alpha}_c$ is the intersection of the respective functions (Raphaël & De Gennes, 1989) (see Fig. 8-3a). If the slope of $K\tilde{\alpha}_c$ is greater than the maximal slope of $-B\sin(\tilde{\alpha}_c + \omega_u t)$ (or $K > B$), the red line (which shifts to the left with time) and the blue line in Fig. 8-3a intersect only once at any given time. This results in relatively smooth motion of the pendulum. If $K < B$, the two functions intersect more than once. An abrupt change in $\tilde{\alpha}_c$ takes place whenever the system moves past the point where spring and pinning functions are tangent to each other (i.e. disanchoring configuration depicted in Fig. 8-3a). This is when the term $\lambda \frac{d\tilde{\alpha}_c}{dt}$ becomes important, and quasi-static assumption breaks down.

The term $\lambda \frac{d\tilde{\alpha}_c}{dt}$ regularizes the quasi-static jump discontinuity until the spring and gravity terms are balanced again. As a result, periods of relatively gradual motion of the pendulum are punctuated by rapid disanchoring events. This corresponds to the stick-slip motion of the water-oil interface at low displacement rates in Fig. 8-1d.

Numerical solution of Eq. 8.17 shows that the amplitude of pendulum oscillations $\tilde{\alpha}_c(t)$ diminishes with increasing angular velocity ω_u (Fig. 8-3b). In fact, when ω_u is sufficiently high, so that $\tilde{\alpha}_c \ll \omega_u t$, we can approximate Eq. 8.17 as $\lambda \frac{d\tilde{\alpha}_c}{dt} + K\tilde{\alpha}_c = -B\sin(\omega_u t)$, whose solution can be written as

$$\tilde{\alpha}_c(t) = -\frac{\overbrace{B}^{\text{amplitude}}}{\sqrt{K^2 + \lambda^2 \omega_u^2}} \sin(\omega_u t - \phi) + \overbrace{C e^{-Kt/\lambda}}^{\text{transient solution}}, \quad (8.18)$$

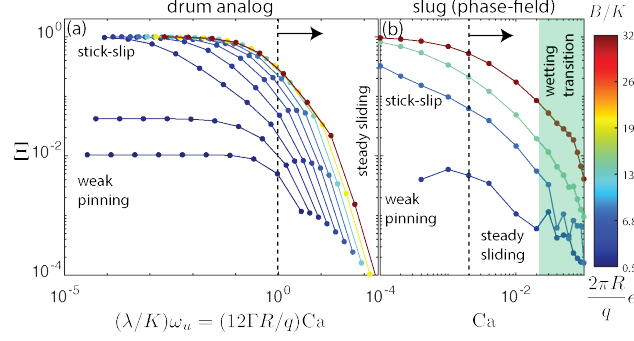


Figure 8-4: (a) Fraction of the total dissipation Ξ due to stick-slip motion of the contact line. The dashed line represents inequality 8.19. (b) Phase-field simulations reveal a similar Ξ trend, where dashed line represents inequality 8.22.

where $\frac{B}{\sqrt{K^2 + \lambda^2 \omega_u^2}}$ is the amplitude of oscillations, $\phi = \text{Arg}(K + i\lambda\omega_u)$, and the transient solution constant C is determined by the initial conditions. This solution reveals two characteristic timescales of our system: $1/\omega_u$ is the time interval between disanchoring events, λ/K is the timescale for relaxation of the contact line. When

$$\omega_u \gg K/\lambda, \quad (8.19)$$

the contact line is unable to keep up with the local changes in the forcing by surface imperfections, so the amplitude of oscillations diminishes. This corresponds to the steady sliding of the water-oil contact line at high displacement rates in Fig. 8-1. Here, the amplitude of oscillations scales as B/ω_u , which is consistent with the simulation results (see Fig. F-10).

8.3.3 Energy dissipation

The transition from stick-slip to steady sliding also signifies a change in the dominant dissipation mechanisms. The fraction of the total dissipation due to stick-slip motion of the contact line reads as

$$\Xi = \frac{\langle -K\tilde{\alpha}_c \rangle}{\langle -K\tilde{\alpha}_c \rangle + \omega_u}, \quad (8.20)$$

in a drum analog. This is equivalent to

$$\Xi = \frac{\langle k(z_b - z_c) \rangle}{\langle k(z_b - z_c) \rangle + b_b \dot{z}_b} = \frac{\langle k(z_b - z_c) \rangle}{\langle f \rangle}, \quad (8.21)$$

where numerator is the mean spring force, and $\langle f \rangle$ is the mean total driving force in the spring-dashpot analog in Eq. 8.9. Multiplying both numerator and denominator by the prescribed displacement rate of the slug \dot{z}_b converts this force fraction to an estimate of dissipation fraction.

Fig. 8-4a shows that the contribution to the total energy dissipation due to contact-line oscillations depends on both the displacement rate and the relative magnitudes of K and B . When $B > K$, most of the energy dissipation can take place near the oscillating contact line. This state can be achieved on dirty surfaces (large B) or with fluids with low surface tension (small spring-stiffness parameter K). In contrast, systems with clean surfaces (small B) or with high surface energy liquids (small spring-stiffness parameter K) would dissipate most of the energy away from the contact line. Another practical way of reducing contact-line oscillations and dissipation is reducing the radius R

of the tube in Fig. 8-1, which would result in a higher stiffness parameter K . Ultimately, the fraction of contact-line dissipation diminishes for all B/K at high displacement rates, where inequality 8.19 is satisfied (to the right of the dashed line in Fig. 8-4a).

8.3.4 Phase-field simulations

Our drum analog system accurately predicts the main displacement regimes on heterogeneous surfaces: smooth displacement in weakly pinning settings, stick–slip motion in strong pinning, and steady sliding at high displacement rates. We verify this by means of 2D phase-field simulations, where -1 and 1 values of the phase-field parameter ϕ mark two fluids, and their diffuse interface is the region where $\nabla\phi \neq 0$. The evolution of ϕ in space and time is resolved through coupled Cahn-Hilliard and creeping flow equations (Eqs. F.24-F.25), where position-dependent contact angle is prescribed by imposing the angle between $\nabla\phi$ and the normal vector at the solid surface through Eq. F.26.

We restrict our phase-field simulations to a single meniscus moving inside a channel with constant-flowrate and constant-pressure boundaries imposed at its two ends. We assign equal viscosities to the invading and the defending fluids, so that the bulk viscous resistance due to Poiseuille flow is fixed in a single simulation. This allows isolating the pressure fluctuations across the channel due to stick–slip motion of the contact line and allows finding its respective contribution to total dissipation (see section F.3).

Phase-field simulations qualitatively reproduce the transition from stick–slip motion at low flow rates to steady sliding at high flow rates. The condition for the dynamic transition from stick–slip to steady sliding in inequality 8.19 is equivalent to

$$\text{Ca} \gg \frac{q}{R} \frac{1}{12\Gamma}. \quad (8.22)$$

In fact, after running a sweep of phase-field simulations for a range of pinning force strengths (controlled through ϵ) and Ca , we can characterize the contribution of contact line oscillations to the overall dynamics. We do so by tracking Ξ through phase-field pressure measurements (Eq. F.28), which essentially reproduces the trends from the drum analog (Fig. 8-4b).

8.4 Conclusions

Our model provides a rationale to many recent experimental observations related to stick–slip dynamics of moving contact lines. For example, Fig. 8-4 shows that stick–slip dynamics accounts for nearly all of the dissipation under strong pinning. This is in agreement with experiments of Varagnolo et al. (Varagnolo *et al.*, 2013) (see Fig. F-1a), where droplets move an order of magnitude more slowly on surfaces with hydrophilic/hydrophobic stripes. Additionally, our approximation leading up to Eq. 8.18 is consistent with temporal modulation of the contact angle on electrowetting surfaces. Therefore, ω_u in Eq. 8.18 can represent the frequency of ac signal. Eq. 8.18 shows that the amplitude of oscillations decays with ω_u , which is indeed what has been reported in experiments of Mannetje et al. (Mannetje *et al.*, 2013) (Fig. F-1b). Finally, inequality 8.22 suggests that by decreasing the spacing between defects on a solid surface, one can trigger the transition from stick–slip to steady sliding at lower Ca . This appears to be happening in experiments of Zuo et al. (Zuo *et al.*, 2012), where by increasing the concentration of impurities in a polymer substrate, authors generate surfaces with varying spatial correlation lengths of defects. Closer spacing of defects corresponds to decreased amplitude of stick–slip in their experiments (Fig. F-1c), which is consistent

with the expectations from our model. If we allow stretching this trend to a nanometer scale q (nanoscale spacing of defects), inequality 8.22 predicts steady sliding for most experimentally attainable Ca.

At last, since Eq. 8.18 is the solution to a linear equation, our analysis extends to arbitrary pinning landscapes (Savva *et al.*, 2011), where Eq. 8.18 would still hold for each Fourier mode of an arbitrary pinning function. In fact, natural surfaces are known to exhibit fractal features, from nanometer to geologic scales (Chiarello *et al.*, 1991; Sparrow & Mandelbrot, 1984). This means that the roughness profile power spectrum has a power-law distribution (Majumdar & Tien, 1990). This suggests that in contact-line experiments on natural rough surfaces, shorter wavelength modes are often in either weak pinning or steady sliding regime of the phase diagram in Fig. 8-4. In other words, on natural surfaces the longer wavelength modes exhibit strongest effective pinning and, therefore, dictate when a fluid-fluid interface crosses over from stick-slip to steady sliding dynamics, much like the experimental example in Fig. F-1c.

Overall, we capture the complex motion of partially-wetting contact lines over heterogeneous surfaces with a system of ordinary differential equations and connect these equations to a mechanical analog in Fig. 8-2. This allows reducing the complexity of the motion to a few key parameters. We present a simple model that connects the stick-slip amplitudes of contact-line motion with the strength and spacing of surface defects, explaining the rate-dependent transition from stick-slip to steady sliding shown in Fig. 8-1.

Chapter 9

Summary

This thesis examined a range of interfacial fluid dynamics problems in porous media. Part I focused on the dynamics of fluid-fluid displacement at the scale of hundreds to thousands of pores.

- In Chapter 2, we extended the classical invasion-percolation model to account for wettability conditions. Using this model alongside microfluidics can help improve applications like CO₂ storage, reinforcement of ceramics, and soil remediation.
- In Chapter 3, we developed a “moving-capacitor” pore-network model. We did so by extending our quasi-static model from chapter 2 to account for viscous forces by drawing an analogy between fluid-fluid displacement in porous media and currents in electrical circuits. This simple model reproduces a wide range of experimentally documented patterns and helps predict changes with increasing displacement rates.
- Our modeling efforts allowed completing Lenormand’s seminal diagram with a missing wettability axis in Chapter 4. This study may be particularly impactful since it synthesized decades’ worth of experimental observation within a single pore-network model, highlighting a subtle interplay of viscous and capillary forces with wettability.
- Finally, in Chapter 5, we characterized avalanches in strong imbibition. We demonstrated that strong imbibition shares all features of self-organized criticality, previously thought to be exclusive to drainage.

Part II of this thesis zoomed into the fluid displacement at the scale of a single capillary.

- In Chapter 6, we developed a spin-coating technique, alongside its accurate mathematical model, that allows coating capillary ducts with viscous fluids. This method may be very impactful in fabricating microelectromechanical systems and micro-channels with functional surfaces.
- In Chapter 7, we developed a fluid-fluid displacement system to tune the ratio of contact-line to bulk viscous dissipation experimentally. While this constant-rate imbibition setup may prove helpful in practical applications like miniature pumps and cooling pipes for electronics, it enables controlled studies of wetting on heterogeneous surfaces.
- Finally, in Chapter 8, we theoretically examined the contact-line motion over heterogeneous surfaces. We rationalized the transition of moving contact lines from stick-slip to steady sliding at increasing displacement rates.

Appendix A

Corner meniscus and characteristics of displacement patterns

A.1 Corner meniscus

In this appendix we examine the shape of the corner meniscus around a typical post. We follow a similar derivation to that of the droplet shape on a fiber (de Gennes *et al.*, 2004). We treat our post as a fiber and impose desired contact angles as boundary conditions at the interface ends, imposing that contact angles of θ are maintained at both post and plate contacts. Finally, we examine the growth and potential mid-post coalescence of the top/bottom menisci.

A.1.1 Corner meniscus shape

Here we determine how far the meniscus extends in the horizontal and vertical directions for a given Laplace pressure, and check whether the force balance equation suggested in this work adequately captures the horizontal extent of the meniscus.

FIG. A-1 shows a cross section of the corner meniscus around a post with radius r_1 . By developing an argument very similar to the formulation of the droplet shape on a fiber of de Gennes *et al.* (2004), we can find the meniscus shape equation. We start with the Young-Laplace equation for an arbitrary point A on the liquid interface:

$$\frac{1}{AN} - \frac{1}{AM} = \frac{\Delta p}{\gamma}. \quad (\text{A.1})$$

Noting that $r = AN \cdot \cos \alpha$ and $ds = AM \cdot d\alpha$, Equation (A.1) can be written as:

$$\frac{\cos \alpha}{r} - \frac{d\alpha}{ds} = \frac{\cos \alpha}{r} - \frac{d\alpha}{dr} \frac{dr}{ds} = \frac{\Delta p}{\gamma}. \quad (\text{A.2})$$

Furthermore, $dr = \sin \alpha ds$, so the Young-Laplace equation takes the following form:

$$\frac{\cos \alpha}{r} - \frac{d\alpha}{dr} \sin \alpha = \frac{\Delta p}{\gamma}. \quad (\text{A.3})$$

Noting that $dr = \sin \alpha ds$ and $dx = \cos \alpha ds$,

$$\frac{dx}{dr} = \dot{x} = \cot \alpha. \quad (\text{A.4})$$

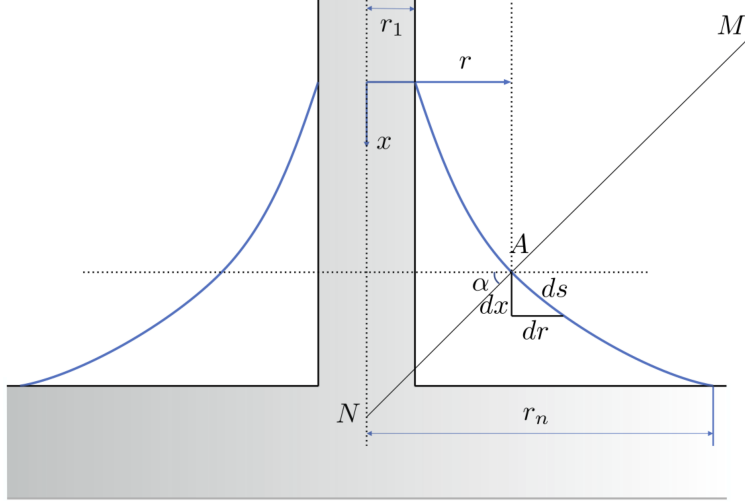


Figure A-1: Shape of the corner meniscus around the post with radius r_1 . AM and AN are the principal radii of curvature at point A, where AM is in plane and AN is perpendicular to the plane.

Squaring both sides of Equation (A.4) leads to the following equations:

$$\sin \alpha = \frac{1}{(1 + \dot{x}^2)^{1/2}}, \quad (\text{A.5a})$$

$$\cos \alpha = \frac{\dot{x}}{(1 + \dot{x}^2)^{1/2}}. \quad (\text{A.5b})$$

Differentiating Equation (A.4) with respect to r , yields:

$$\ddot{x} = -\frac{1}{\sin^2 \alpha} \frac{d\alpha}{dr}. \quad (\text{A.6})$$

Finally, substituting Equations (A.5) and (A.6) into Equation (A.3), we obtain the final equation for the liquid interface:

$$\frac{\dot{x}}{r(1 + \dot{x}^2)^{1/2}} + \frac{\ddot{x}}{(1 + \dot{x}^2)^{3/2}} = \frac{\Delta p}{\gamma}. \quad (\text{A.7})$$

Now, Equation (A.7) with $\dot{x}(r_1) = \cot \theta_1$ and $x(r_1) = 0$ can be used to find the corner meniscus profile. FIG. A-2 shows the solution of Equation (A.7) for $r = (r_1, r_n)$ with a typical geometry and contact angle used in this study.

The pressure drop across the interface should be such that $\dot{x}(r_n) = \tan \theta_1$. It turns out that this condition is exactly satisfied when Δp is calculated from the force balance equation (2.7). This verifies the validity of the force balance approach in finding critical values of Δp for *corner flow*.

At the same time, FIG. A-2 shows that the extent of the corner meniscus is of comparable size in horizontal and vertical directions. Since the height of the posts in Zhao *et al.* (2016) experiments is $100 \mu m$, we need to consider two cases: (1) corner menisci at the top and bottom which do not touch; and (2) corner menisci that meet and merge at the mid-height of the cell. When the liquid menisci do not meet in the middle of the post, the critical Δp for *corner flow* can be estimated from the force balance equation (2.7). However, when corner liquids meet, the shape of the interface can be estimated as a *capillary bridge* between two flat plates, described by the equation (de Gennes *et al.*, 2004):

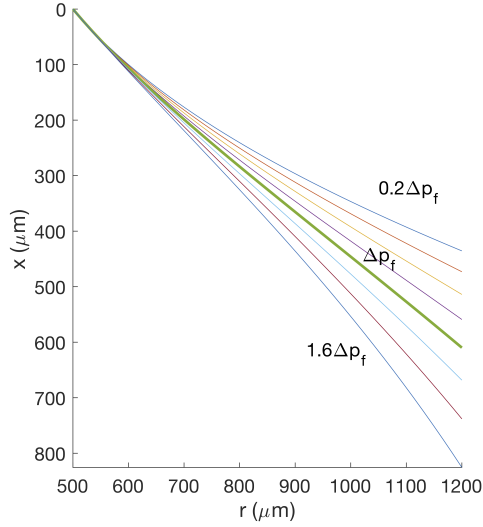


Figure A-2: Interface shape of a corner meniscus outside a post. Equation (A.7) solved with $\theta = 40^\circ$, $r_1 = 500\mu m$, $r_n = 1200\mu m$. Here, Δp_f represents the Laplace pressure obtained from the force balance Equation (2.7). Condition $\dot{x}(r_n) = \tan \theta_1$ is exactly satisfied when $\Delta p = \Delta p_f$.

$$\frac{1}{r_n - \frac{h}{2\cos\theta_1}(1 - \sin\theta_1)} - \frac{2\cos\theta_1}{h} = \frac{\Delta p}{\gamma} \quad (\text{A.8})$$

A.1.2 Corner meniscus growth

We now consider the growth of the corner meniscus on a post with height of $100\mu m$ (FIG. A-3(a)). At first, the invading liquid is confined to the top and bottom corners of the post—growth of the meniscus in the horizontal direction increases the Laplace pressure requirement. Top and bottom menisci grow to the point that they touch at mid-height of the post. At this point, the shape of the corner liquid changes into a capillary bridge.

We make the following observations. Firstly, before the menisci merge, the Laplace pressure increases with growing r_n . After they merge, the shape turns into a capillary bridge, and the Laplace pressure decreases with growing r_n . This means that if the liquid invasion was stimulated with small pressure increments, the corner liquid would grow gradually with increasing Δp , and then grow spontaneously after assuming a capillary bridge shape.

Secondly, the magnitude of the discontinuity in Δp at the corner liquid *merger* point is smaller at low contact angles (FIG. A-3(a)). This can be explained intuitively by visualizing the corner merging instant at contact angles of 0° and 45° . For $\theta = 0^\circ$, when two corner liquids meet at the mid-height of the post, $\frac{dr}{dx}|_{x=h/2} = 0$ both before and after the merger. However, for $\theta = 45^\circ$, $\frac{dr}{dx}|_{x=h/2} = 1$ before and $\frac{dr}{dx}|_{x=h/2} = 0$ after the merger. This means that at 45° the invading liquid needs to “snap” from the *corner* to *bridge* shape. The magnitude of this “snap” is small at contact angles near 0° .

Finally, FIG. A-3(b) shows that the Laplace pressure is smaller for larger posts. The out-of-plane radius of curvature (AN in FIG. A-1) is always greater than the radius of the post, and hence posts with greater radius correspond to lower Laplace pressures (Equation (A.1)). In other words, it is easier to grow the corner menisci around the posts with larger radius.

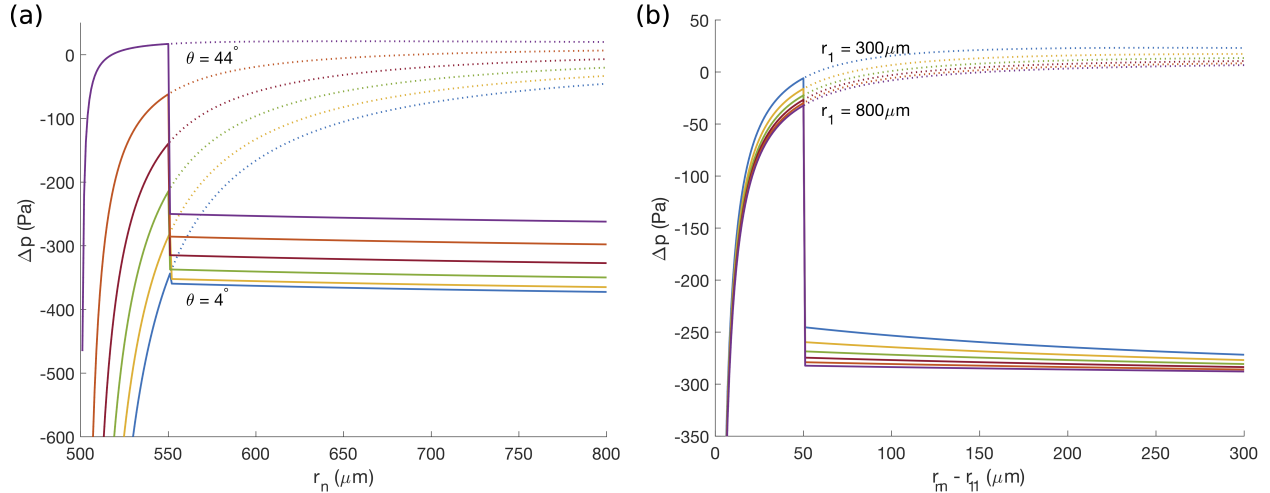


Figure A-3: Laplace pressure for a growing corner meniscus. Initially, the invading liquid is confined to the corners. As the horizontal extent of the liquid grows, the top and bottom corners meet at the mid-height of the post, and the shape changes into a capillary bridge. This transition point corresponds to the negative jump in Laplace pressure. (a) Evolution of the corner menisci for contact angles between 4° and 44° and $r_1 = 500 \mu\text{m}$. (b) Evolution of the corner menisci for post radii between $300 \mu\text{m}$ and $800 \mu\text{m}$ and contact angle of 40° .

A.2 Measuring fractal dimension

The morphology of the invading fluid phase can be complex (FIG. 2-4), and fractal dimension can be an intuitive way to capture this complexity. Fractal dimension can be thought of as an “index of the scale-dependency of a pattern” (Kenkel & Walker, 1996). In this work, we utilize the box-counting method (Kenkel & Walker, 1996; Iannaccone & Khokha, 1996) to estimate the fractal dimension of the invading fluid patterns.

The box counting method iteratively tiles the image containing the flow pattern with boxes of size ϵ . Each iteration uses increasingly greater value of ϵ and measures the number N of boxes that contain (or “directly cover”) the flow pattern. The magnitude of the slope of N against ϵ on a log-log plot defines the box-counting fractal dimension (Iannaccone & Khokha, 1996).

To estimate the fractal dimension of the invading fluid we took the following steps: (1) obtain the invasion pattern image from the simulation, with fully surrounded posts treated as part of the invading phase (FIG. A-4(a)); this step typically produced images of 1200×1200 pixels in size; (2) convert image to black and white (FIG. A-4(b)); (3) grid the image with boxes of size ϵ between 1 and the number of pixels in each direction of the image (n_{pix}) (FIG. A-4(c)-(d)); (4) record the number N of boxes required to fill the pattern for each ϵ ; (5) calculate the fractal dimension as an absolute value of the slope of N against ϵ on a log-log plot (FIG. A-4(e)).

When calculating the slope of N against ϵ on the log-log plot, we imposed user-defined expectations on the bounds of the fractal behavior. We exclude the boxes close to the image size, so we set $\epsilon < \frac{n_{\text{pix}}}{8}$.

A.3 Measuring finger width

In order to estimate the invading fluid finger width (w), Cieplak and Robbins (Cieplak & Robbins, 1988, 1990) put forward the following method. First, they slice the invasion pattern along the nodes

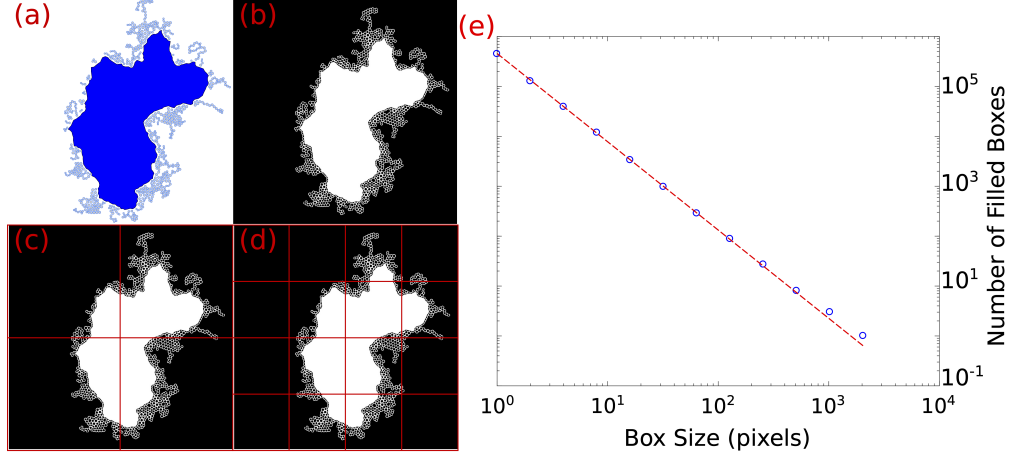


Figure A-4: Fractal dimensions calculated with the box-counting method. (a) color image (1500×1500 pixels) produced by the invasion algorithm for $\theta = 40^\circ$; (b)-(d) black and white versions of the invasion pattern placed on a grid of size $\epsilon = [1, n_{\text{pix}}]$; (e) fractal dimension measured as a slope of number N of filled boxes against ϵ on a log-log plot, slope was calculated from points with $\epsilon = [1, \frac{n_{\text{pix}}}{8}]$.

of their regular lattice. Then, they measure the size of the invaded region clusters along each 1D slice. The mean size of the clusters was taken as an estimate of w , which was then divided by the lattice length a .

We cannot follow the method of Cieplak and Robbins (Cieplak & Robbins, 1988, 1990) precisely since our post geometry was built on an irregular lattice. We use a close equivalent estimate of w instead. We start with black and white images used to measure box-counting fractal dimension and slice it into separate rows. We collect the statistic of the invading clusters in resulting slices using MATLAB's `bwconncomp` function, where mean size of the clusters estimates w in pixels. We repeat the same procedure on an image where pore spaces and posts have white and black colors respectively. This allows estimating a as an average pore size in pixels. Thus, we recover the w/a used by Cieplak and Robbins. The above procedure was repeated for vertical slices as well.

FIG. A-5 shows that the finger width spans several pores in the invasion-percolation regime, and starts diverging at contact angles below 60° . This growth of finger width is abruptly interrupted below 40° , where fluid invasion is dominated by corner flow and w is only a fraction of the mean pore size a .

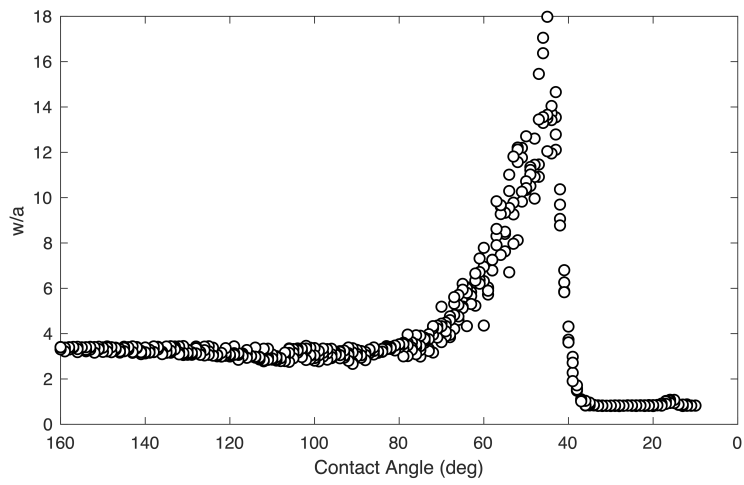


Figure A-5: Ratio of the invading pattern finger width to mean pore size, estimated in analogy to the work of Cieplak and Robbins (Cieplak & Robbins, 1988, 1990).

Appendix B

Corner-flow parameter and pore-scale disorder

B.1 Fitting parameter for corner flow

Ideal system. We first highlight how changes in h —the height of posts within our micromodel—impact the onset of corner flow. This has been explored in earlier work (Primkulov *et al.*, 2018), but we include it here for completeness. We examine the transition to corner flow in the quasi-static limit, where we set the outer radius of the micromodel to 15 cm.

The out-of-plane contribution to Laplace pressure for *burst*, *touch*, and *overlap* events is a function of h and reads as $-\frac{\gamma \cos \theta}{h/2}$. Therefore, the total Laplace pressure of *burst*, *touch*, and *overlap* decreases with decreasing h . In contrast, the critical Laplace pressure of *corner-flow* event is independent of h (Primkulov *et al.*, 2018). In capillary-dominated displacement, events with lowest critical Laplace pressure take precedence. Therefore, the onset of corner flow depends on h . The impact of h on the onset of corner flow at $\text{Ca} = 0$ is summarized in Figure B-1. When the posts are infinitely tall ($h \rightarrow \infty$), the mode of fluid-fluid displacement changes smoothly from invasion percolation to cooperative pore filling and then sharply to corner flow as wettability conditions change from drainage to weak and then strong imbibition. For $h \rightarrow \infty$, $\theta = 39^\circ$ marks the onset of corner flow. Decreasing the value of h moves the onset of corner flow towards lower θ , until corner flow disappears altogether. Corner flow does not take place when $h = 100 \mu\text{m}$ in our micromodel.

Alternatively, one can shift the onset of corner flow by changing the spacing between the posts: narrower spacing would trigger corner flow at higher θ . The Laplace pressure of a corner meniscus is a monotonically increasing function of its size: it increases from $-\infty$ to Δp_{crit} as the meniscus volume increases from zero to its critical volume (Fig. 4-3d). Therefore, smaller spacing between the posts lowers critical Laplace pressures for *corner-flow* events and shifts the onset of corner flow to higher θ . The changes in the spacing between the posts would also shift the transition from invasion percolation to cooperative filling (Primkulov *et al.*, 2018), where wider spacing extends the cooperative pore filling regime to higher θ .

Real system. We now compare the model outcomes to experimental data from Zhao *et al.* (2016). The major difference between the model and experiments is in the onset of corner flow: corner flow is the primary mode of capillary-dominated displacement in experiments with $h = 100 \mu\text{m}$ and $\theta = 7^\circ$, while our model anticipates no corner flow for $h = 100 \mu\text{m}$ (Fig. 4-3d). In our model, corner flow is triggered when the horizontal radius of a corner meniscus reaches a neighboring uncoated post; this radius is marked r_n in Fig. 4-3d. In the experiments, in contrast, neighboring posts are frequently coated well before the corner meniscus swells to the radius r_n (Fig. 4-3d).

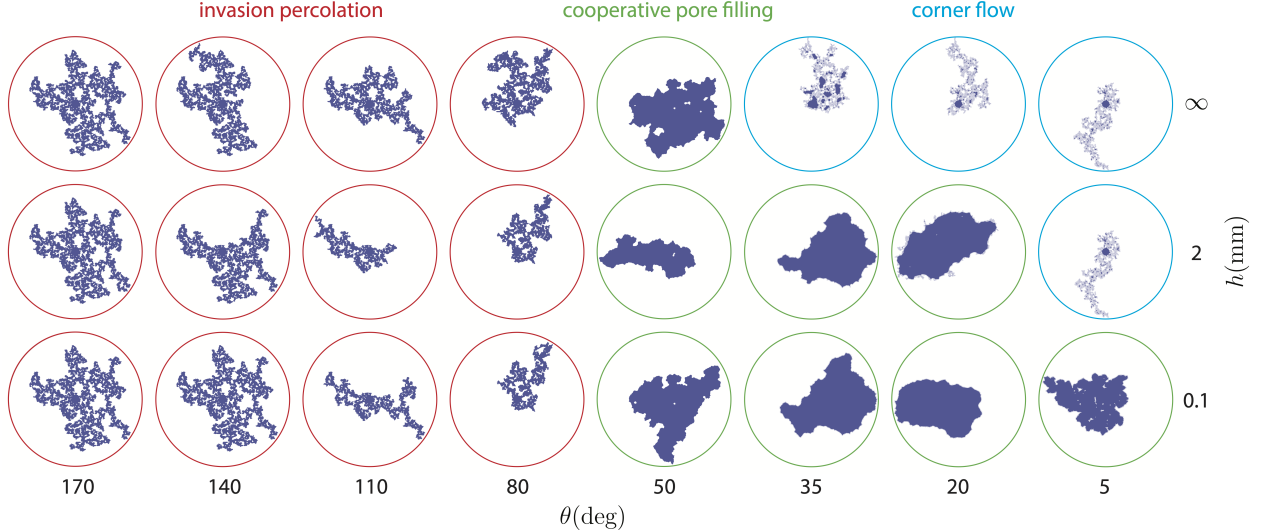


Figure B-1: Transition to corner-flow regime as a function of post height h . Decreasing h narrows the range of θ where corner flow dominates.

Experiments suggest that more complex dynamics at the scale of the contact line can trigger the transition to corner flow.

While our model is strictly applicable for micromodels with ideal surfaces, the model can be tuned to match the experimentally observed onset of corner flow at $h = 100 \mu\text{m}$ by introducing a fitting parameter. Motivated by the observations in Fig. B-2a, we can either trigger corner flow before the horizontal radius of a corner meniscus reaches r_n or lower the critical Laplace pressure of corner flow events by out-of-plane curvature multiplied by coefficient c_{parm} . We chose the latter approach in this study. Setting $c_{\text{parm}} > 0$ triggers earlier coating of the nearest posts through corner flow. We explore the sensitivity of our model to c_{parm} in Fig. B-2b by reporting the fraction of corner-flow events as a function of θ and c_{parm} . We set $c_{\text{parm}} = 1$ for the remainder of the discussion, which corresponds to a transition from cooperative pore filling to corner flow at $\theta = 39^\circ$, in agreement with known experimental data (Zhao *et al.*, 2016), where the transition from cooperative pore filling to corner flow takes place somewhere between 7° and 60° .

The physical mechanisms behind the earlier onset of corner flow are not yet known. We speculate that since UV-treated NOA81 surfaces are highly hydrophilic (Levaché *et al.*, 2012) and not ideally smooth, micron-scale water films may be present throughout the micromodel—between oil and the solid. This is in line with postulated film flow through micro-roughness by Vizika *et al.* (1994); Tzimas *et al.* (1997); Constantinides & Payatakes (2000). However, since water saturation was tracked through concentration of the dye within the injected water phase in experiments of Zhao *et al.* (2016), detecting such films was not trivial. More detailed pore-scale studies are needed to fill this gap, where either water-sensitive dye is added to NOA81 or electric conductivity is utilized to sense pre-existing water films.

B.2 Impact of pore-scale disorder on displacement patterns

Displacement patterns in each principal flow regime outlined in §4.3 interact with pore-scale disorder. We document this dependence briefly below.

Stable displacement. When Ca is sufficiently high and $M \gg 1$, the displacement pattern

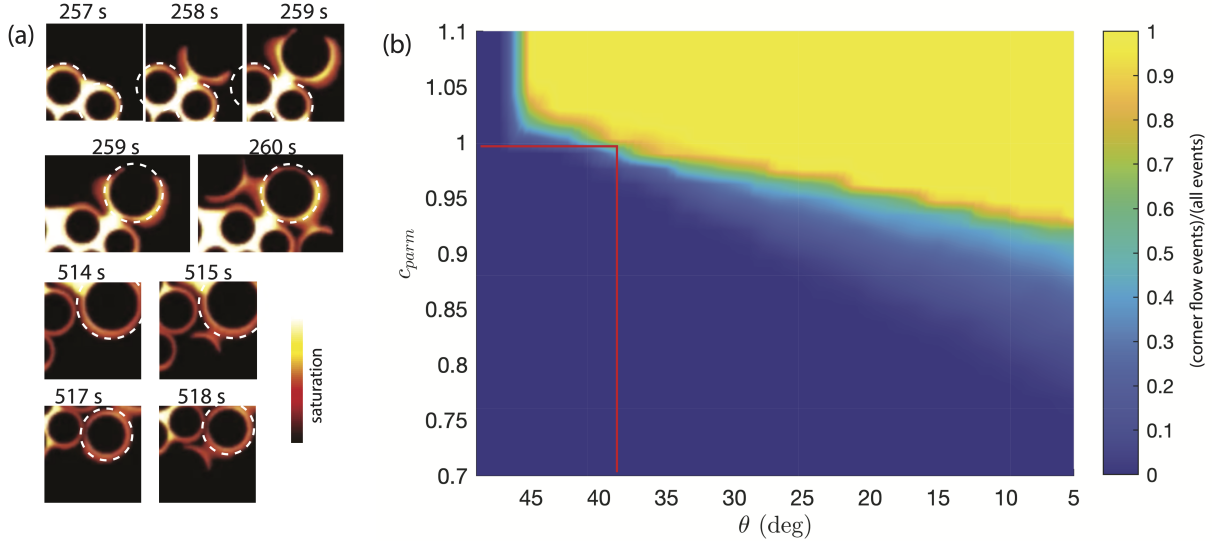


Figure B-2: (a) Experimental image sequences of corner flow taken from [Zhao *et al.* \(2016\)](#) demonstrate instances where post-coating events take place before a circular portion of the corner meniscus swells to the extent of the nearby post; (b) changes in the fraction of corner flow events as a function of θ and the fitting parameter c_{parm} are explored through the sweep of quasi-static simulations. The value of c_{parm} used in this work and corresponding transition to corner flow are highlighted in red.

becomes insensitive to both wettability (given $\theta > 45^\circ$) and disorder. The pattern is insensitive to wettability because viscosity dominates capillarity at high Ca , and the pattern is insensitive to disorder because viscosity stabilizes the small perturbations from disorder.

Viscous fingering. In a circular Hele-Shaw cell without obstacles, the most unstable wavelength λ of the instability follows ([Saffman & Taylor, 1958](#))

$$\frac{\lambda}{h} = \pi \sqrt{\frac{M}{Ca(1-M)}}, \quad (\text{B.1})$$

where h is the spacing between the plates. In a radial Hele-Shaw cell, the number of viscous fingers with thickness $\lambda/2$ increases with the radial distance from the center as the displacement evolves ([Chen, 1987, 1989](#)).

Heterogeneity and anisotropy in the pore geometry can control the number of viscous fingers. In general, the degree of rotational symmetry of viscous fingers in ordered anisotropic media can be controlled by changing the post pattern. For instance, setting a rectangular lattice pattern on one plate of a circular Hele-Shaw cell promotes four-fold symmetry in finger growth ([Chen, 1987](#)). A similar pattern occurs when posts are arranged on a rectangular lattice ([Chen & Wilkinson, 1985](#)). The simulations in Fig. B-3 reproduce the results of the seminal work of [Chen & Wilkinson \(1985\)](#), but on a triangular lattice. As ξ increases from 0 to 1, the invasion pattern moves away from the six-fold symmetry imposed by the lattice (Fig. B-3a) ([Holtzman, 2016](#)). The fractal dimension remains within the range $1.61 < D_f < 1.73$, consistent with experiments ([Chen & Wilkinson, 1985](#); [Måløy *et al.*, 1985](#)), while the finger width ranges from two to five pores ($2 < w/a < 5$).

Whether the flow cell is ordered or disordered, wettability strongly influences the invasion patterns. [Stokes *et al.* \(1986\)](#) were the first to report that viscous fingers in imbibition are wider than in drainage. This observation has been confirmed in subsequent experimental studies ([Trojer *et al.*,](#)

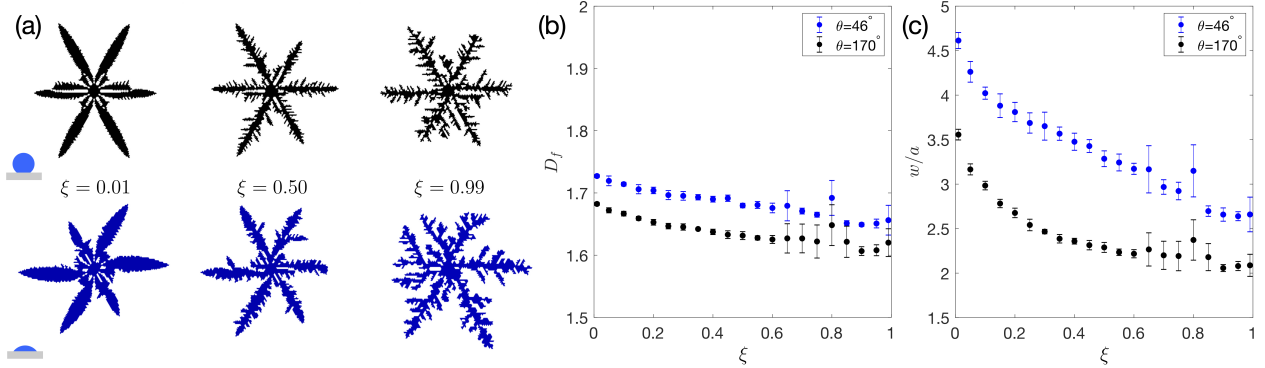


Figure B-3: Viscous-fingering simulations ($Ca = 10^{-1}$ and $M = 10^{-3}$) conducted on a regular triangular lattice with varying degree of disorder ξ . (a) Black invasion patterns are in drainage ($\theta = 170^\circ$), blue patterns are in imbibition ($\theta = 46^\circ$). (b) Fractal dimension D_f and (c) finger width w/a are higher in imbibition across all degrees of disorder ξ . The error bars in (b-c) represent standard deviation of nine realizations.

2015; Zhao *et al.*, 2016; Lan *et al.*, 2020). We observe the same trend for all degrees of disorder: both the finger width and the fractal dimension are consistently higher in imbibition than in drainage (Fig. B-3b-c).

Invasion percolation. In this regime, the invading fluid preferentially enters pores with the lowest capillary entry pressures, one at a time. This process results in incomplete displacement of the defending fluid, which becomes trapped in clusters (Fig. B-4, black). Both D_f and w/a of the resulting patterns remain nearly unaffected by the degree of disorder, with $1.61 < D_f < 1.79$ and $w/a \approx 3$ (Fig. B-4b-c). Invasion percolation requires disorder in the throat sizes, but the actual degree of disorder does not matter when viscous forces are negligible ($Ca \rightarrow 0$). The lack of sensitivity of such invasion-percolation patterns to disorder is intuitive, as the pattern is ultimately determined only by the sequence in which pores are invaded. Therefore, a porous medium with small variations in throat size is equivalent to a porous medium with large variations in throat size—only the relative order of the throat sizes and their locations matter in shaping the invasion-percolation fronts. Therefore, unlike most fluid-fluid displacement regimes, it is very difficult to alter invasion-percolation patterns by imposing the order in the post lattice (see Fig. B-4, black). This lack of sensitivity to disorder is likely responsible for the robustness and universality of the resulting patterns across different kinds of disordered media (Wilkinson & Willemsen, 1983; Cieplak *et al.*, 1996; Sheppard *et al.*, 1999).

Cooperative pore filling. Cooperative pore-filling events, which tend to smooth local concavities of the displacement front, allows patterns to be controlled by the post configuration. Slow injection of a wetting fluid into a porous medium with a regular triangular lattice results in a hexagonal invasion pattern (Fig. B-4, blue). In fact, equivalents to our crystal-like patterns in imbibition and $\xi = 0.01$ have been observed experimentally by Lenormand (1990). One can tune the displacement patterns to be squares, triangles (Lenormand, 1990), and hexagons (Fig. B-4, blue), via the lattice structure. Increasing ξ makes the regular structure of the invading fluid become distorted.

Corner flow. Corner flow is remarkably similar to invasion percolation in how it interacts with disorder. While corner flow is sensitive to even mild disorder, it does not distinguish between different degrees of disorder, much like invasion percolation. Therefore corner flow is, in a sense, an analogue of invasion percolation for strong imbibition and may therefore possess universal features—producing robustly similar invasion pattern across different kinds of disordered media (Fig. B-5).

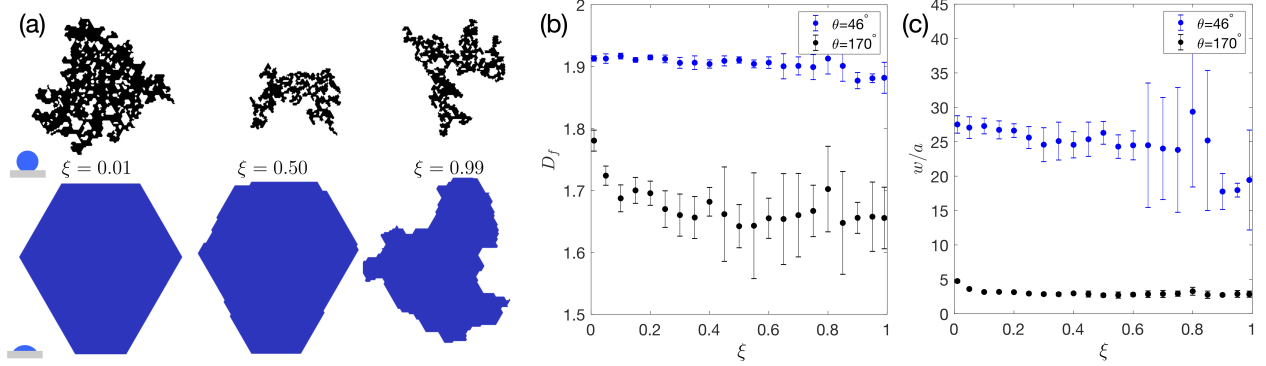


Figure B-4: Capillary-dominated simulations ($Ca = 10^{-7}$ and $M = 1$) conducted on a regular triangular lattice with varying degree of disorder ξ . (a) Black invasion patterns are in drainage ($\theta = 170^\circ$) and correspond to invasion percolation, blue patterns are in imbibition ($\theta = 46^\circ$) and correspond to cooperative pore filling. (b) Fractal dimension D_f and (c) finger width w/a are higher in imbibition across all degrees of disorder ξ . The error bars in (b-c) represent standard the deviation of nine realizations.

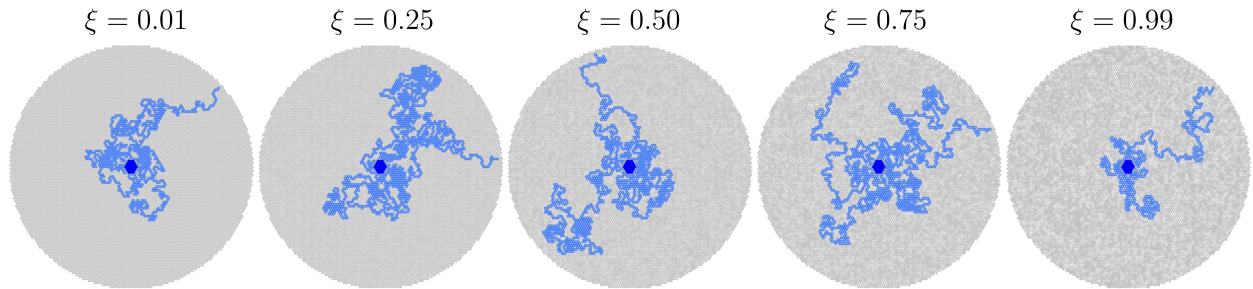


Figure B-5: Quasi-static simulations in strong imbibition ($\theta = 10^\circ$) in a flow cell with a triangular post lattice and different degrees of disorder ξ . Dark blue regions represent fully invaded pores; light blue regions represent partially invaded pores with coated post corners.

Appendix C

Experimental and computational protocols for strong imbibition

C.1 Experimental details

For our experiments, we used the same micromodel geometry (benchmark geometry) as in our previous work (Zhao *et al.*, 2016), where disordered placement of cylindrical posts was generated using MATLAB’s *pdemesh* tool. The micromodel was fabricated via multi-step soft lithography process (Zhao *et al.*, 2016) with a photocurable polymer (NOA81, Norland Optical Adhesives) (Denis Bartolo *et al.*, 2008; Levaché *et al.*, 2012). NOA81 surface was coated with trimethoxysilane through the chemical vapor deposition process (30 min in a desiccator) in order to obtain the contact angles of $150^\circ \pm 5^\circ$. In order to obtain the contact angle of $7^\circ \pm 3^\circ$, we exposed NOA81 surfaces to high-intensity UV light for 30 min in Samco’s UV Ozone Cleaner UV-1. These contact angles were measured using Ramé-Hart goniometer (Model 590) by placing water droplets on flat, treated substrates submerged in silicone oil; these substrates were fabricated via the same protocol as our micromodels.

We first saturated our micromodel with silicone oil ($\mu_o = 0.34$ Pa·s; 350 cSt, Sigma-Aldrich), and then injected DI water at $Q = 0.4$ $\mu\text{L}/\text{min}$. Given the oil-water interfacial tension of $\gamma = 13$ mN/m, the ratio of viscous to capillary forces (capillary number) in our experiments was $\text{Ca} = \frac{\mu_o u}{\sigma} = 5.8 \times 10^{-3}$, where $u = Q/(bd)$ is the characteristic displacement rate, $b = 100$ μm is the thickness of the gap between the top and bottom plates, and $d = 300$ μm is the characteristic pore-throat size.

Different definitions of the characteristic velocity would result in different values of Ca. For example, taking $u = Q/(2\pi R_{\min}b)$, where R_{\min} is the radial distance of the post closes to the

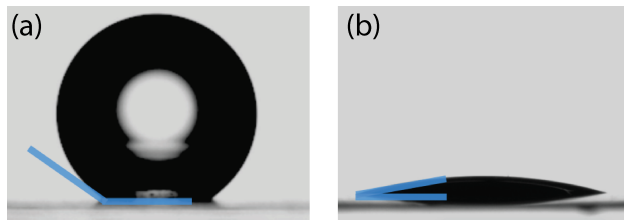


Figure C-1: Optical measurements of water-oil contact angle on flat substrates (a) NOA81 treated with chemical vapour deposition of trimethoxysilane ($\theta = 150^\circ \pm 5^\circ$) and (b) NOA81 treated with high-intensity UV-light ($\theta = 7^\circ \pm 3^\circ$). Reprinted from Zhao *et al.* (2016).

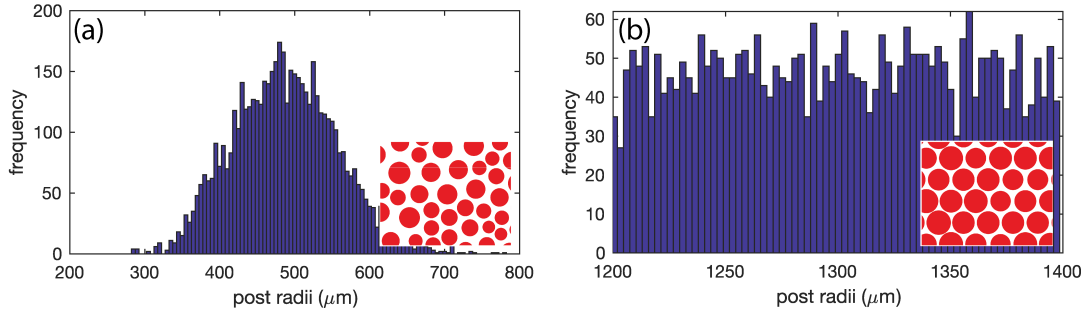


Figure C-2: Post-size distribution for (a) the benchmark geometry and (b) micromodel with regular triangular lattice and random post-size assignment.

injection port (2.8 mm) (Primkulov *et al.*, 2019) would lead to $Ca = 9.8 \times 10^{-5}$. Alternatively, taking $u = Q/(2\pi R_{\text{out}}b)$, where R_{out} is the radial distance to the edge of the cell (50 mm) would lead to $Ca = 5.5 \times 10^{-6}$.

C.2 Simulation protocol

Simulations in this manuscript were conducted on two micromodel geometries. The first one (the benchmark geometry) was generated using MATLAB’s *pdemesh* tool to create an irregular triangular mesh (Zhao *et al.*, 2016). Post centers were placed on the nodes of this mesh and post radii were taken to be 45% of the length of the shortest associated edge, resulting in a median pore-throat size of 300 μm and the post-size distribution reported in Fig. C-2a.

The second micromodel geometry was generated by placing posts on a regular triangular lattice with edge length 2.8 mm and then drawing random post radii from a uniform distribution between 1.2 mm and 1.4 mm (Fig. C-2b). This protocol produced a median pore-throat size of 280 μm , which is close to that of the benchmark geometry (300 μm). This second method allowed us to easily generate different realizations of the same pore geometry in order to obtain error bars for the exponents a and b (Table II).

C.3 Influence of trapping on the displacement statistics

Our experiments in strong imbibition are not definitive but suggest that trapping of the defending fluid may be taking place. The trapping can happen when the corner films swell and locally fill the entire gap between the top/bottom plates of the Hele-Shaw cell. However, our quasi-static model only accounts for trapping by pore bodies and not by corner films (Primkulov *et al.*, 2018, 2021). Therefore, here we use a simple invasion percolation model on a square lattice, where trapping is easily enabled/disabled, to examine the influence of trapping on the values of exponents a and b in the paper.

Fig. C-3 shows the results of invasion percolation simulations on a 200 by 200 square lattice. We assign capillary-entry pressures p from a uniform distribution between 0 and 1 and start the invasion process at the center of the domain. We use the same seed number to generate p in simulations with and without trapping, where the resulting differences in the values of exponents a and b are not significant. Here, we used the literature values of $D = 1.82$ and $D = 1.88$ for invasion percolation with and without trapping, respectively (Wilkinson & Willemsen, 1983).

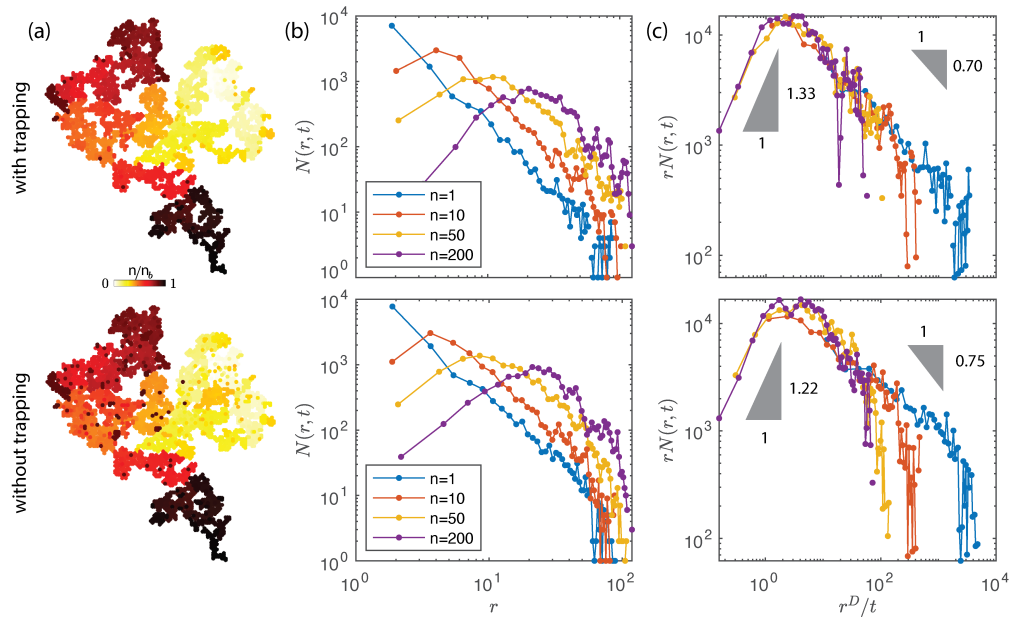


Figure C-3: Verification of Eq. (5.1) using invasion percolation model on a square lattice with (top row) and without trapping (bottom row). (a) Invasion-event-number plot, where events are colored by event number n with n_b the number of events at breakthrough. (b) The plots of $N(r, n)$ vs. r for several values of n . (c) Collapse of $rN(r, n)$ vs. r^D/n , where slopes a and b do not change significantly due to trapping.

Appendix D

Spin-coater speed and experimental details

D.1 Spin-coater speed and experimental data

In this section we assess two potential sources of error that come from the design of the spin-coater system. First, it takes about 1 s for our computer fan to reach its target speed. Second, the speed of the computer fan is found to fluctuate within a ± 10 rpm window, which has implications for the error in the film thickness. The size of the error window would depend on the details of the electric circuit and power source. We took steps to reduce the heating of the electric components and variations in the power supply from the building in order to minimize the error.

D.1.1 Deviation of 50 cSt oil from more viscous oils in figure 2b

The discrepancy between the 50 cSt silicone oil and more viscous oils stems from the fact that it takes ~ 1 s for the fan to reach the target speed of 854 rpm. Incidentally, the characteristic timescale for the slug flow of 50 cSt silicone oil is 0.9 s (figure 6-2a). As a result, the 50 cSt silicone oil slug flow regime effectively sets in at lower angular velocity, 673 rpm compared to 854 rpm for higher viscosity oils. This results in a thinner initial film coating, which explains the deviation in the $l(x_c)$ profile evident in figure 2b.

D.1.2 Estimating film thickness variation in comparison to Taylor’s coating method

Below, we briefly compare the expected variation in thickness of the deposited liquid films using Taylor’s method and our spin-coating method.

Imagine one wants to coat our tube with a 20 μm thick layer of 1000 cSt silicone oil. In Taylor’s method, the oil is removed from one end of the tube with the syringe pump while the other end is exposed to air. When the oil completely wets the glass, the thickness of the film left behind follows Bretherton’s scaling (Bretherton, 1961):

$$h \sim R \left(\frac{\mu u}{\sigma} \right)^{2/3}. \quad (\text{D.1})$$

One would need to draw out the silicone oil at $u = 0.36$ mm/s to leave a 20 μm film behind. Taking

the variation of h with respect to u yields

$$\delta h \sim \frac{2R}{3} \left(\frac{\mu u}{\sigma} \right)^{2/3} \frac{\delta u}{u}. \quad (\text{D.2})$$

The assumption of fully developed Poiseuille flow leads to $\delta u/u = \delta p/p$. If we take the characteristic value of normalized pressure fluctuations due to the syringe pump to be 1% as in [Zeng *et al.* \(2015\)](#), then (D.2) gives an estimate of thickness variation to be $\delta h \sim 0.13 \mu\text{m}$.

Similarly, estimating the variation in thickness induced by fluctuation of angular velocity during spin-coating, we use the results of figure 6-3c, where the film thickness at sufficiently long time follows:

$$h \sim \sqrt{\frac{3\mu}{2\rho\omega^2 t}}. \quad (\text{D.3})$$

We would then need to spin 1000 cSt silicone oil for about 4 min to obtain a film thickness of $20 \mu\text{m}$. Taking the variation of h with respect to ω :

$$\delta h \sim \sqrt{\frac{3\mu}{2\rho t}} \frac{\delta\omega}{\omega^2}. \quad (\text{D.4})$$

The variation of thickness in the film for the angular velocity of $854 \pm 10 \text{ rpm}$ yields $\delta h \sim 0.03 \mu\text{m}$, a variation about 4 times smaller than in Taylor's method.

Appendix E

Spontaneous imbibition experiments and classical imbibition

E.1 Details of the experimental setup

All of the experiments were conducted in Hilgenberg borosilicate glass tubes that are 75 mm in length and 290 μm in inner radius. The interfacial tensions of the oil–air and oil–water interfaces were $\gamma_o = 22 \text{ mN/m}$ and $\gamma_{ow} = 13 \text{ mN/m}$, respectively. The dynamic contact angles of the water–oil interface in glass capillaries were measured under a microscope. The tubes were submerged into glycerol, which has a matching refractive index with the borosilicate glass in use (1.473). Contact angles were measured from the curvature of the interface, with parallax correction applied as in (Hoffman, 1975).

Throughout this manuscript we assumed that Hagen–Poiseuille flow is maintained through the oil slug and that, therefore, the velocity profile is parabolic. This assumption was used to calculate the viscous drag and dissipation within the bulk of the oil slug. We confirmed the parabolic velocity profile within the oil slug through PIV tracing (Thielicke & Stamhuis, 2014). In FIG. E-1 we show that even for the shortest slug used in this study (2 mm), the majority of the bulk space maintains the parabolic velocity profile.

E.2 Generalized Cox equation

In the main body of the manuscript we use the generalized Cox equation Cox (1986)

$$g(\theta, M) - g(\theta_a, M) = \text{Ca} \Gamma, \quad (\text{E.1})$$

where M is the ratio of the defending to invading fluid viscosities, $\Gamma = \ln(R/h_{\text{micro}})$ is the cut-off-length parameter near the contact line, and function $g(\theta, M)$ is

$$g(\theta, M) = \int_0^\theta \frac{d\beta}{f(\beta, M)}, \quad (\text{E.2})$$

and

$$f(\beta, M) = \frac{2 \sin \beta [M^2(\beta^2 - \sin^2 \beta) + 2M(\beta(\pi - \beta) + \sin^2 \beta) + (\pi - \beta)^2 - \sin^2 \beta]}{M(\beta^2 - \sin^2 \beta)(\pi - \beta + \sin \beta \cos \beta) + ((\pi - \beta)^2 - \sin^2 \beta)(\beta - \sin \beta \cos \beta)}. \quad (\text{E.3})$$

E.3 Classical imbibition

FIG. 3 in the manuscript demonstrates that contact-line dissipation can be responsible for a significant portion of the energy loss in capillary-driven flow systems. To stress this point further, we return to the classical imbibition depicted in FIG. 1a of the manuscript. The need to account for contributions of the contact-line dynamics to the rate of classical imbibition has been the focus of a series of recent studies (Bico & Quéré, 2002; Delannoy *et al.*, 2019; Hilpert, 2009, 2010; Heshmati & Piri, 2014). We plot the evolution of the front position $z(t)$ for 50 cSt silicon oil in FIG. E-2. The classical Washburn scaling for $z(t)$ can be obtained by balancing $F_{\text{bulk}} = 8\pi\mu_o z\dot{z}$ with $F_{\text{cap}} = 2\pi R\gamma_o \cos\theta_o = 2\pi R\gamma_o(1 - \frac{1}{2}(9\Gamma\frac{\mu_o\dot{z}}{\gamma_o})^{2/3})$ and neglecting the dynamic contact angle. Then the force balance reduces to

$$\frac{4\mu_o}{R\gamma_o} z\dot{z} = 1. \quad (\text{E.4})$$

The solution to equation (E.4) is $z^2 = \frac{\gamma_o R}{2\mu_o} t$, which differs from the early-time experimental data in FIG. E-2. A more complete description emerges by considering the dynamic contact angle

$$\frac{4\mu_o}{R\gamma_o} z\dot{z} = 1 - \frac{1}{2}(9\Gamma\frac{\mu_o\dot{z}}{\gamma_o})^{2/3}. \quad (\text{E.5})$$

Equation (E.5) captures the dynamics of viscosity-dominated classical imbibition at both early- and late-times. At early times (when z is small), Φ_{bulk} and Φ_{cl} are comparable (see FIG. E-2) and therefore the dynamics is best described by including both dissipation sources. At late times, the liquid front slows and θ_o approaches $\theta_{o,a}$, making Φ_{cl} negligible. As a result, the experimental $z(t)$ approaches the $z \sim t^{1/2}$ scaling (FIG. E-2).

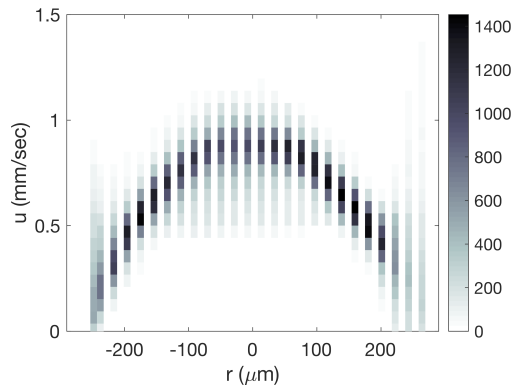


Figure E-1: PIV measurements of the velocity profile in spontaneously moving 2 mm slug with 1000 cSt viscosity. The plot is the 2D representation of a histogram, where color stands for the frequency. The data was collected over the entire length of the 2 mm slug, over all frames. The figure demonstrates that even in the shortest slug used in this study (2 mm), the majority of the bulk space maintains the parabolic velocity profile.

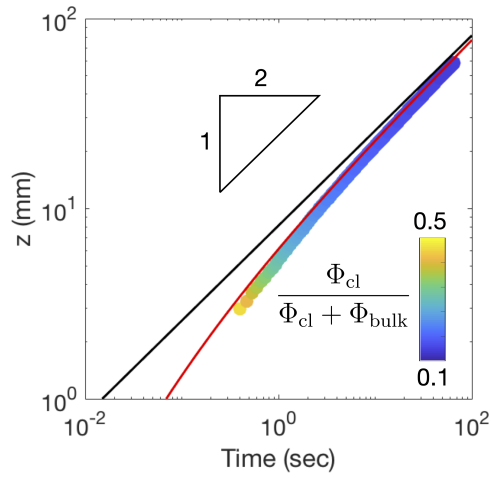


Figure E-2: Evolution of $z(t)$ during classical imbibition of 50 cSt silicon oil depicted in FIG. 1a of the manuscript. Here the black line represents the classical Washburn solution [Eq. (E.4)], the red line represents the solution corrected for dynamic contact angle [Eq. (E.5)]. The ratio of contact-line to total dissipation is denoted with a colormap.

Appendix F

Contact-line dynamics over imperfect surfaces

F.1 Experimental details

In this study we used capillary tubes with inner radius of $R = 290 \mu\text{m}$ (Hilgenberg GmbH borosilicate glass 3.3). We spin-coated the inner walls of the tubes with NOA81 photocurable polymer [Primkulov *et al.* \(2020b\)](#). While the surface properties of NOA81 polymer cured with high-intensity UV light have not yet been fully explored, we observed the growth of surface crystals (Fig. F-2). These crystals cover the cured polymer within several hours, generating a carpet of surface roughness.

F.2 Force-velocity relations

Here, we first revisit the force-velocity scaling of Raphaël-de Gennes and Joanny-Robbins [Raphaël & De Gennes \(1989\)](#); [Joanny & Robbins \(1990\)](#) in constant-force and constant-speed settings, and then examine how the system evolves away from the depinning limit. We are particularly interested in how the amplitude of oscillations evolves at higher forcing and velocities.

F.2.1 Constant-force displacement

Consider a pendulum inside a drum that is filled with viscous fluid and rotated at angular velocity ω_0 (Fig. 8-2). As one gradually increases ω_0 , the system undergoes several distinct regimes.

Static state. The system would be in a static state for a range of very small ω_0 . Here, left-hand side of Eq. 8.14 vanishes, and the equation reduces to

$$\omega_0 = B \sin \alpha_c.$$

The back meniscus and the slug get pinned where local imperfections match the driving force.

Depinning limit. When the driving force is marginally stronger than the peak pinning site, or $\omega_0 \rightarrow B^+$, the slug moves forward in a stick-slip manner (Fig. F-3). We can rearrange and integrate Eq. 8.14 to get

$$\int \frac{d\alpha_c}{\omega_0 - B \sin \alpha_c} = t + C, \tag{F.1}$$

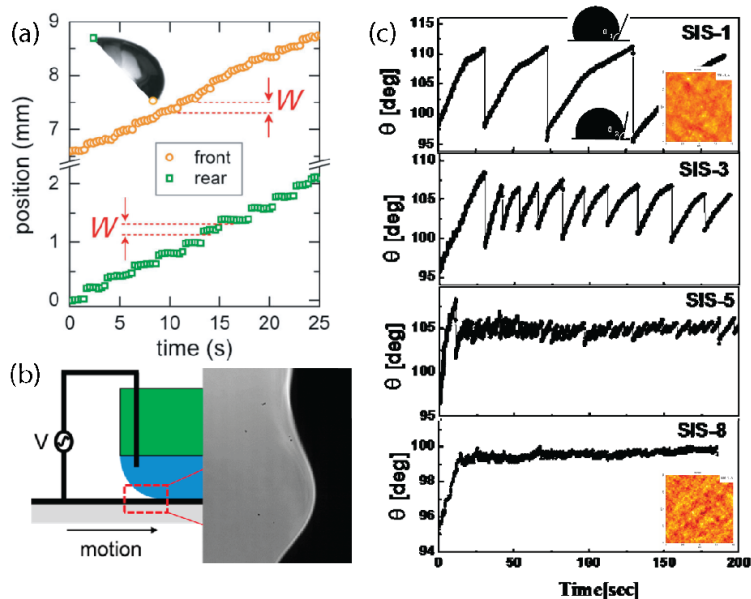


Figure F-1: Examples of stick-slip motion of contact lines. (a) stick-slip motion of a droplet sliding down a surface with hydrophobic-hydrophilic stripes. Reprinted from [Varagnolo *et al.* \(2013\)](#). (b) stick-slip dynamics can also emerge on electrowetting surfaces, where temporal changes in wettability are actuated through ac signal. Reprinted from [Mannetje *et al.* \(2013\)](#). (c) Amplitude of stick-slip oscillations are smaller on surfaces with more closely-spaced impurities. Adapted from [Zuo *et al.* \(2012\)](#).

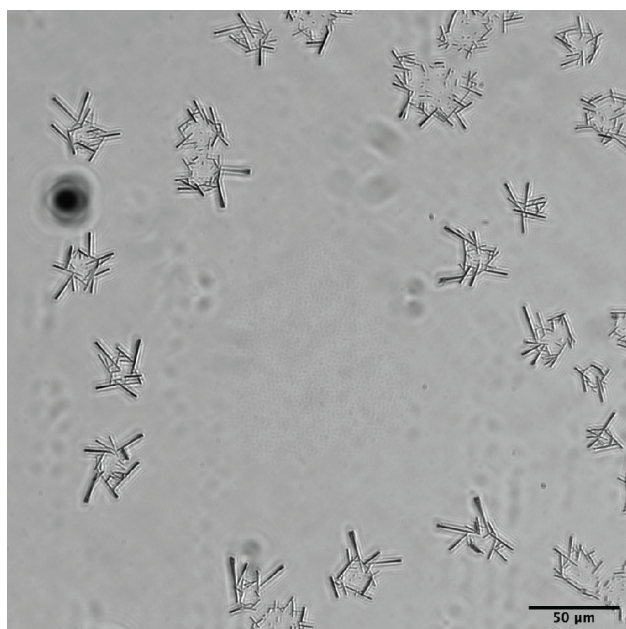


Figure F-2: Crystalline structures growing on cured NOA81 surfaces are reminiscent of the images obtained in the context of coarsening solidification via solvent-annealing in thin liquid films [Yu *et al.* \(2013\)](#). Liquid droplets, visible at the center of the image, are replaced by growing crystal structures as time advances.

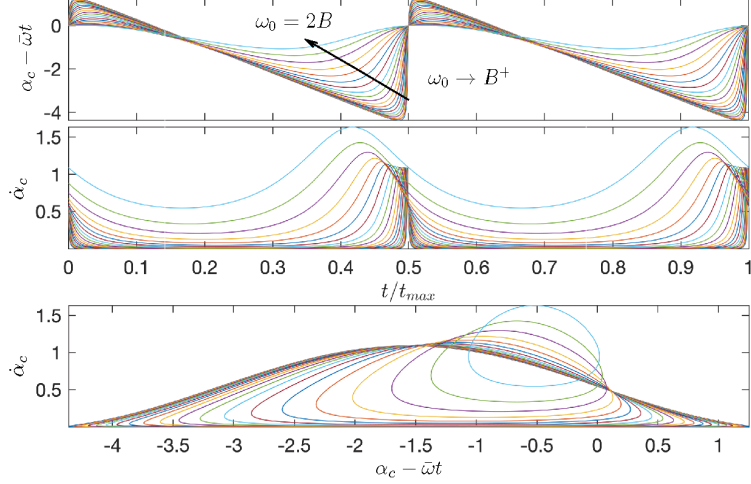


Figure F-3: Evolution of α_c in Eq. 8.14 for $\omega_0 \in (B, 2B]$.

or

$$\tan \frac{\alpha_c}{2} = \frac{B}{\omega_0} + \frac{\bar{\omega}}{\omega_0} \tan \frac{\bar{\omega}(t+C)}{2}, \quad (\text{F.2})$$

where the average frequency is [Adler \(1946\)](#)

$$\bar{\omega} = \sqrt{\omega_0^2 - B^2}. \quad (\text{F.3})$$

When $\omega_0 \rightarrow B^+$, $\bar{\omega} = \sqrt{[(\omega_0 - B) + B]^2 - B^2} = \sqrt{2B(\omega_0 - B) + (\omega_0 - B)^2} \approx \sqrt{2B(\omega_0 - B)}$. We can therefore write the force-velocity relation near the depinning limit as

$$\frac{\omega_0 - B}{B} = \frac{1}{2} \left(\frac{\bar{\omega}}{B} \right)^2, \quad (\text{F.4})$$

which is equivalent to the expressions obtained by Raphaël-de Gennes and Joanny-Robbins [Raphaël & De Gennes \(1989\)](#); [Joanny & Robbins \(1990\)](#). In fact, a relation equivalent to Eq. F.4 can be obtained from Eq. F.1 after realizing that when $\omega_0 \rightarrow B^+$, the dominant contribution to the integral comes from the neighborhood of the strongest pinning site.

Away from the depinning limit. When $\omega_0 \gg B$, Eq. F.3 simply reduces to $\bar{\omega} = \omega_0$, which we can rewrite in a form analogous to Eq. F.4

$$\frac{\omega_0 - B}{B} \approx \frac{\bar{\omega}}{B}. \quad (\text{F.5})$$

Away from the depinning limit force scales linearly with the speed.

Fig. F-3 shows that as one moves away from the depinning limit, the amplitude of oscillations diminishes in a frame moving at $\bar{\omega}$. In the limit where $\omega_0 \gg B$ and therefore $\bar{\omega} \rightarrow \omega_0$ (Eq. F.3). We can then rewrite Eq. 8.14 in this moving frame as

$$\frac{d\tilde{\alpha}_c}{dt} = \omega_0 - \bar{\omega} - B \sin(\tilde{\alpha}_c + \bar{\omega}t) \quad (\text{F.6})$$

$$\approx -B \sin(\omega_0 t), \quad (\text{F.7})$$

where we assumed $\tilde{\alpha}_c \ll \bar{\omega}t$. This allows to approximate the oscillations about the moving frame

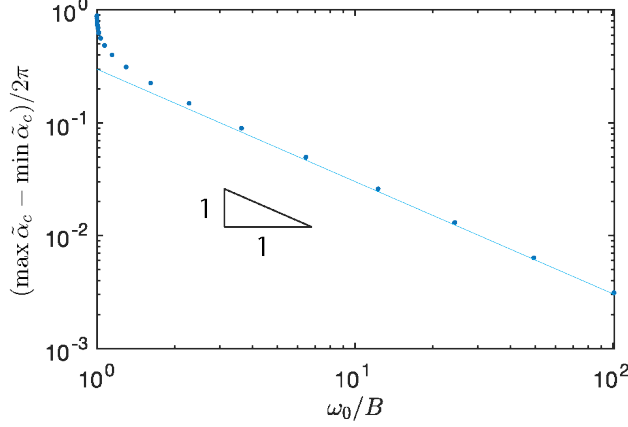


Figure F-4: Diminishing amplitude of oscillations with ω_0/B in constant force setting. Blue dots correspond to numerical solutions of Eq. 8.14 at varying ω_0/B .

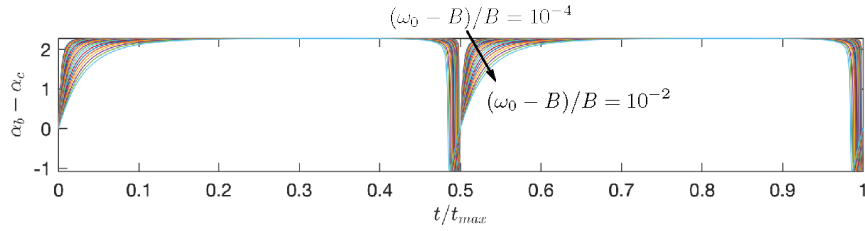


Figure F-5: Adiabatic approximation leading up to Eq. 8.14 assumes that $\alpha_b = \alpha_c + \Delta\alpha$, where $\Delta\alpha$ is constant. Numerical solution of Eqs. 8.12-8.13 shows that this is a good approximation near the depinning limit, where $\omega_0 - B \ll B$.

as

$$\tilde{\alpha}_c = \alpha_c - \bar{\omega}t \approx \frac{B}{\omega_0} \cos(\omega_0 t). \quad (\text{F.8})$$

In other words, when $\omega_0 \gg B$, we can expect the magnitude of oscillations decay following $(\omega_0/B)^{-1}$ scaling, which is indeed what we observe in the numerical solution to Eq. 8.14 (Fig. F-4).

Our assumption that $\alpha_b = \alpha_c + \Delta\alpha$, where $\Delta\alpha$ is constant holds up during slow displacement or when $\omega_0 - B \ll B$. Here, $\frac{d}{dt}(\alpha_b - \alpha_c) \approx 0$ at all times except near brief slip events (Fig. F-5).

F.2.2 Constant-rate displacement

Unlike the constant-force displacement, as long as the prescribed rate is not zero, pendulum does not have a static state.

Quasi-static state. However, at diminishing rates, we can take $\lambda \frac{d\tilde{\alpha}_c}{dt} \rightarrow 0$, which reduces Eq. 8.17 to

$$K\tilde{\alpha}_{c,qs} = -B \sin(\tilde{\alpha}_{c,qs} + \omega_u t). \quad (\text{F.9})$$

The balance of the spring and the pinning force can then be visually examined (Fig. F-6a), as suggested by Raphaël-de Gennes [Raphaël & De Gennes \(1989\)](#). Here, two distinct modes of motion emerge: (i) when $K \geq B$, a unique solution α_c exists at any given time; (ii) when $K < B$, or a slope of the spring term is smaller than the greatest slope of the pinning term, more than one solution α_c can emerge (Fig. F-6).

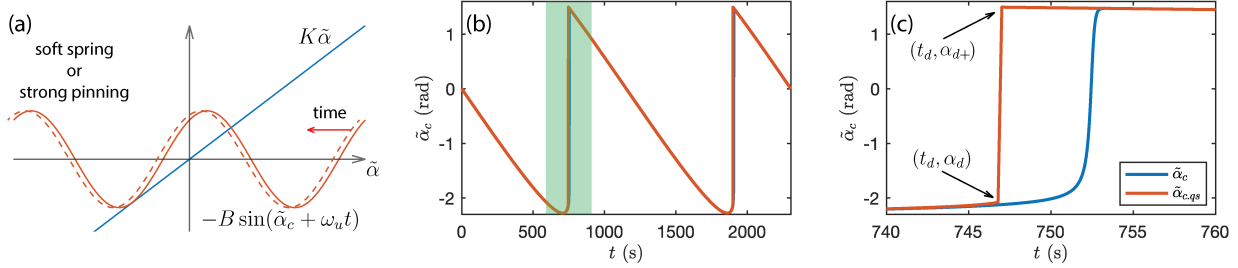


Figure F-6: (a) Quasi-static motion of the contact line is governed by the balance of the linear spring term $K\tilde{\alpha}_c$ and surface imperfection term $B \sin(\tilde{\alpha}_c + \omega_u t)$. Here, solution for $\tilde{\alpha}_c$ is non-unique for certain t when $K < B$. (b) Typical motion near depinning limit. A region highlighted in green corresponds to a disanchoring event, where quasi-static solution experiences jump-discontinuity in $\tilde{\alpha}_c$. This state is also depicted in (a). (c) Solution of Eq. 8.17 (blue curve) deviates from the quasi-static profile $\tilde{\alpha}_{c,qs}$ (red curve) only near disanchoring event.

We can calculate the average force term of the quasi-static displacement as

$$\bar{\omega}_{0,qs} = -\frac{1}{T} \int_0^T K \tilde{\alpha}_{c,qs}(t) dt, \quad (\text{F.10})$$

where T is the period of motion, and $\tilde{\alpha}_{c,qs}(t)$ is calculated from Eq. F.9.

Depinning limit. We now examine how the average force term evolves as we increase ω_u and therefore move away from the quasi-static approximation.

Fig. F-6b shows the typical $\tilde{\alpha}_c(t)$ profile obtained by solving Eq. 8.17. We are particularly interested in the dynamics near the disanchoring event highlighted in green. Here, in quasi-static limit, $\tilde{\alpha}_{c,qs}(t)$ experiences jump-discontinuity. In the dynamic model, this discontinuity is regularized by the viscous term in Eq. 8.17. In fact, the solution of Eq. 8.17 deviates from the quasi-static solution only immediately after these disanchoring events (see Fig. F-6c). This deviation is responsible for the force-velocity scaling near depinning limit of Raphaël-de Gennes and Joanny-Robbins [Raphaël & De Gennes \(1989\)](#); [Joanny & Robbins \(1990\)](#).

We can write the average force term from Eq. 8.16 as

$$\bar{\omega}_0 = -\frac{1}{T} \int_0^T K \tilde{\alpha}_c(t) dt, \quad (\text{F.11})$$

or alternatively we can use Eq. F.10 to rewrite the above equation as

$$\bar{\omega}_0 - \bar{\omega}_{0,qs} = -\frac{1}{T} \int_0^T K [\tilde{\alpha}_c(t) - \tilde{\alpha}_{c,qs}(t)] dt. \quad (\text{F.12})$$

The value of this integral can be approximated by treating the area between two curves in Fig. F-6c as a rectangle and finding its characteristic width in t . This is what we do next.

To understand how $\tilde{\alpha}_c$ evolves near the disanchoring point (t_d, α_d) , we substitute $t = t_d + t_\epsilon$ and $\tilde{\alpha}_c = \alpha_d + \alpha_\epsilon$ into Eq. 8.17 and obtain

$$\lambda \frac{d\alpha_\epsilon}{dt_\epsilon} + K(\alpha_d + \alpha_\epsilon) = -B \sin(\alpha_d + \omega_u t_d + \alpha_\epsilon + \omega_u t_\epsilon). \quad (\text{F.13})$$

We then note that $\sin(\alpha_d + \omega_u t_d + \alpha_\epsilon + \omega_u t_\epsilon) = \sin(\alpha_d + \omega_u t_d) \cos(\alpha_\epsilon + \omega_u t_\epsilon) + \cos(\alpha_d + \omega_u t_d) \sin(\alpha_\epsilon + \omega_u t_\epsilon) \approx \sin(\alpha_d + \omega_u t_d)(1 - (\alpha_\epsilon + \omega_u t_\epsilon)^2/2) + \cos(\alpha_d + \omega_u t_d)(\alpha_\epsilon + \omega_u t_\epsilon)$. We also note that at disanchoring point $-B \sin(\alpha_d + \omega_u t_d) = K\alpha_d$ and $-B \cos(\alpha_d + \omega_u t_d) = K$. Therefore, Eq. F.13 simplifies to

$$\lambda \frac{d\alpha_\epsilon}{dt_\epsilon} = K\omega_u t_\epsilon - \frac{K\alpha_d}{2}(\alpha_\epsilon + \omega_u t_\epsilon)^2, \quad (\text{F.14})$$

or if we assume that for very slow displacement $\omega_u t_\epsilon \ll \alpha_\epsilon$,

$$\lambda \frac{d\alpha_\epsilon}{dt_\epsilon} = K\omega_u t_\epsilon - \frac{K\alpha_d}{2}\alpha_\epsilon^2. \quad (\text{F.15})$$

We can rescale the above equation with $\hat{\alpha} = a\alpha_\epsilon$ and $\hat{t} = bt_\epsilon$, where taking

$$a = \left(\frac{K\alpha_d^2}{4\lambda} \frac{1}{\omega_u} \right)^{1/3} \quad (\text{F.16})$$

$$b = \left(\frac{K^2(-\alpha_d)}{2\lambda^2} \omega_u \right)^{1/3} \quad (\text{F.17})$$

reduces Eq. F.15 to

$$\frac{d\hat{\alpha}}{d\hat{t}} = \hat{t} + \hat{\alpha}^2, \quad (\text{F.18})$$

which is a Riccati equation. Our solution should approach the quasi-static profile $\hat{\alpha}_{q.s}(\hat{t}) = -\sqrt{-\hat{t}}$ when $\hat{t} \rightarrow -\infty$. Therefore,

$$\hat{\alpha}(\hat{t}) = \text{Ai}'(-\hat{t})/\text{Ai}(-\hat{t}), \quad (\text{F.19})$$

where Ai is the Airy function of the first kind.

We plot Eq. F.19 along with the quasi-static profile in Fig. F-7. Here, point (0, 0) corresponds to (t_d, α_d) in Fig. F-6c; the solution $\hat{\alpha}(\hat{t})$ crosses abscissa at \hat{t}_1 , and it is singular at \hat{t}_2 . The contact line detaches from the pinning site somewhere between \hat{t}_1 and \hat{t}_2 and relaxes exponentially towards the new near-static state. Therefore, the disanchoring event takes place at $\hat{t} = \mathcal{O}(1)$ or $t_\epsilon \sim 1/b$. Then, we can approximate the integral in Eq. F.12 as $\bar{\omega}_0 - \bar{\omega}_{0,q.s} \approx \frac{\omega_u}{2\pi} K(\alpha_{d+} - \alpha_d) \frac{1}{b}$. In other words, at very slow displacement rates, the average extra force term (compared to quasi-static displacement) needed to move the slug scales as

$$\bar{\omega}_0 - \bar{\omega}_{0,q.s} \sim \omega_u^{2/3}. \quad (\text{F.20})$$

This scaling, however, relies on the $\omega_u t_\epsilon \ll \alpha_\epsilon$ assumption we have made to arrive at Eq. F.15. This, in our conditions of interest, is equivalent to $\frac{\omega_u}{B} \ll \frac{2K}{\alpha_d \lambda B} = \mathcal{O}(10)$.

Away from the depinning limit. While the force-velocity scaling is valid for a wide range of $\bar{\omega}/B$ in the constant force experiment (Fig. F-8a), the equivalent scaling in the constant velocity setting only applies for $\omega_u/B \ll \frac{2K}{\alpha_d \lambda B}$ (Fig. F-8b). In the latter case, the force-velocity relation is non-monotonous away from the depinning limit.

To rationalize the shape of the curve in Fig. F-8b we solve Eq. 8.17 and plot $\tilde{\alpha}_c(t)$ profiles for a wide range of ω_u/B in Fig. F-9. As ω_u/B increases, at first, only portion of the $\tilde{\alpha}_c(t)$ curve immediately after the disanchoring events deviates significantly from the quasi-static profile. In particular, the area between quasi-static and dynamic curves increases with ω_u/B (see Fig. F-6c and Fig. F-9), following scaling in Eq. F.20 for $\omega_u/B \ll 1$, where dynamics can be approximated by Eq. F.15. The area between the quasi-static and dynamic curves, increases a little more rapidly and reaches maximum as $\frac{\omega_u}{B}$ approaches $\frac{2K}{\alpha_d \lambda B}$.

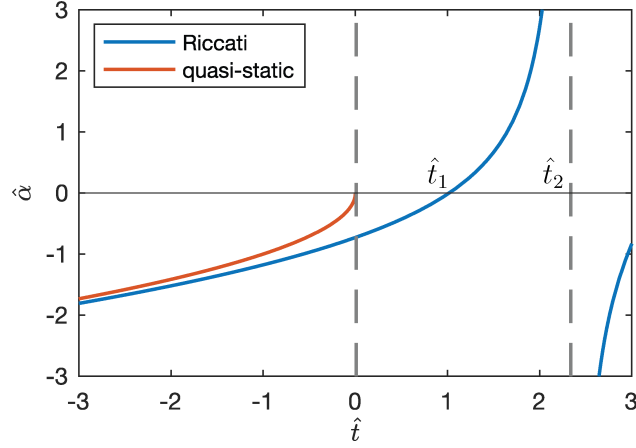


Figure F-7: Solution to equation F.18 (blue) as well as the quasi-static solution $\hat{\alpha}_{q.s}(\hat{t}) = -\sqrt{-\hat{t}}$ (red). Here, \hat{t}_1 is the first root of Eq. F.19 and \hat{t}_2 is its first singularity.

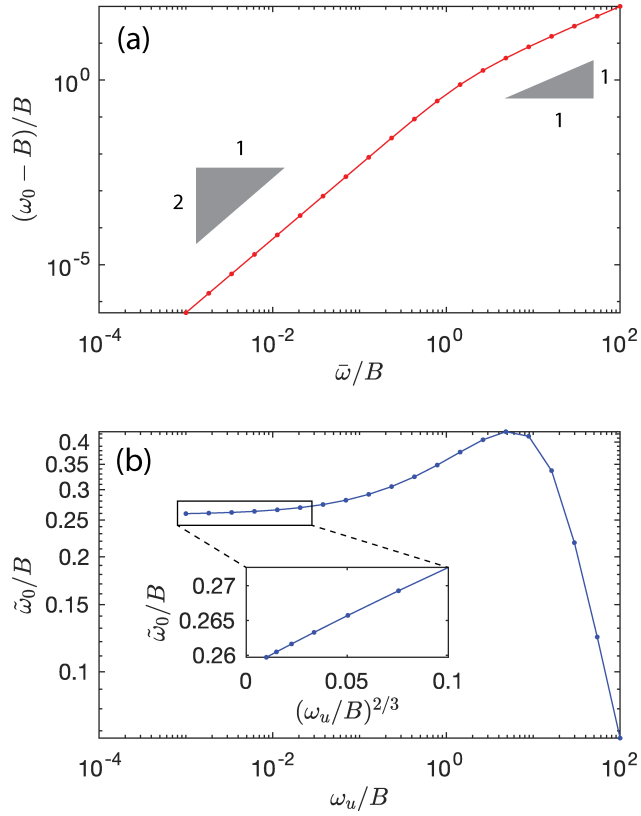


Figure F-8: Scaling of force-velocity terms in (a) constant force (Eqs. F.4-F.5) and (b) constant velocity settings, where inset demonstrates the scaling in Eq. F.20 for $\omega_u/B \ll 1$.

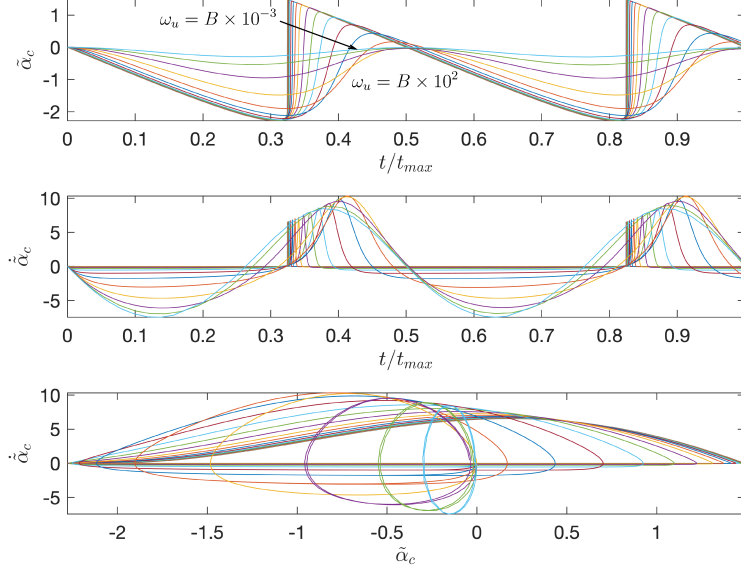


Figure F-9: Evolution of $\tilde{\alpha}_c$ in Eq. 8.17 for $\omega_u/B \in [10^{-3}, 10^2]$.

Eventually, the average value of $\tilde{\omega}_0/B$ starts diminishing with increasing ω_u when $\frac{\omega_u}{B} > \frac{2K}{\alpha_d \lambda B}$. This is the result of the oscillation amplitude dampening in $\tilde{\alpha}_c(t)$. In fact, when ω_u is sufficiently high, so that $\tilde{\alpha}_c \ll \omega_u t$, we can approximate Eq. 8.17 as

$$\lambda \frac{d\tilde{\alpha}_c}{dt} + K\tilde{\alpha}_c = -B \sin(\omega_u t), \quad (\text{F.21})$$

which is a first-order ODE with constant coefficients and periodic forcing. Then the solution to Eq. F.21 can be written as

$$\tilde{\alpha}_c(t) = -\frac{B}{\sqrt{K^2 + \lambda^2 \omega_u^2}} \sin(\omega_u t - \phi) + C e^{-Kt/\lambda}, \quad (\text{F.22})$$

where $\frac{B}{\sqrt{K^2 + \lambda^2 \omega_u^2}}$ is the amplitude of oscillations, $\phi = \text{Arg}(K + i\lambda\omega_u)$, and the transient solution constant C is determined by the initial conditions. When $\frac{\omega_u}{B} \gg \frac{2K}{\alpha_d \lambda B}$, the amplitude of oscillations would scale as

$$\frac{B}{\sqrt{K^2 + \lambda^2 \omega_u^2}} \sim \frac{B}{\lambda \omega_u}. \quad (\text{F.23})$$

This is consistent with the simulation results in Fig. F-10.

F.2.3 Total force

The force-velocity scaling relations we showed until now do not represent the total force one would need to apply to move the slug inside the capillary tube (Fig. 8-1). The scaling relation in section F.2.1 is for the force above the static threshold ($\omega_0 - B$). The scaling relation in section F.2.2 is for the force above the quasi-static threshold ($\bar{\omega}_0 - \bar{\omega}_{0,qs}$). Additionally, the relation in section F.2.2 was derived in a moving frame of reference and does not account for the bulk viscous force. This can be remedied by taking $\omega_0 = \bar{\omega}_0 + \omega_u$.

We plot the force-velocity curves for the total force in Fig. F-11 for both constant-rate and

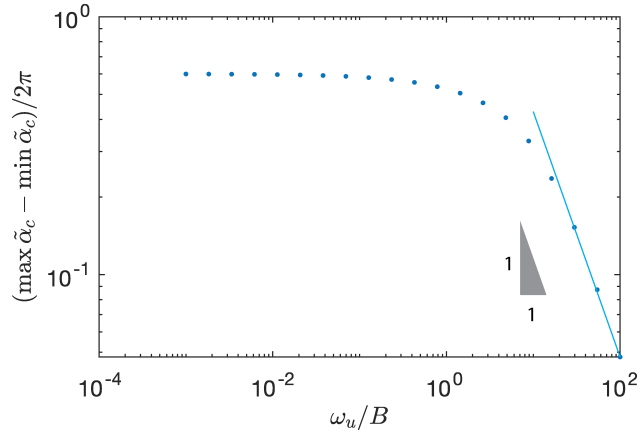


Figure F-10: Change in the amplitude of oscillations of $\tilde{\alpha}_c$ with increasing ω_u/B . Data is obtained through numerical solution of Eq. 8.17.

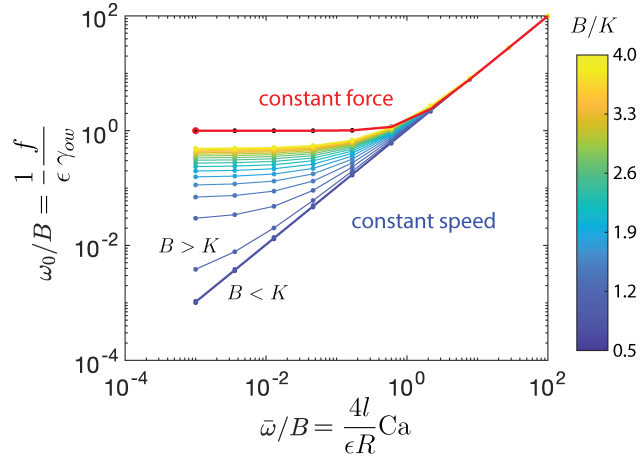


Figure F-11: Total force scaling for both constant-force (red) and constant-velocity (color-scaled) settings.



Figure F-12: Phase-field simulation of constant-rate fluid-fluid displacement in a 2D channel ($R = 290 \mu\text{m}$), where the top boundary is the plane of symmetry.

constant-force settings. In constant-force setting, the dominant contribution to the total force comes from the contact line interaction with surface imperfections until $\frac{\tilde{\omega}}{B} = \frac{4L}{\epsilon R} \text{Ca} = \mathcal{O}(1)$. In constant-rate setting, the crossover from stick–slip dominated to bulk-viscous force dominated dynamics depends on relative magnitudes of parameters B and K . The relative importance of surface imperfections can be negligible for weakly pinning surfaces (small B) and/or stiff oil/water interface (large K).

F.3 Phase-field simulations of the viscous slug displacement at a constant rate

Fig. F-12 shows a typical 2D phase-field simulation of fluid-fluid displacement, where invading fluid is marked with phase-field parameter $\phi = 1$, defending fluid with $\phi = -1$, and diffuse interface has values of ϕ in between. Spatio-temporal changes in ϕ are governed by the Cahn-Hilliard equation Cahn & Hilliard (2004) in the form

$$\frac{\partial \phi}{\partial t} + \underbrace{\mathbf{u} \cdot \nabla \phi}_{\text{transport from flow field}} = \underbrace{\nabla \cdot \frac{\tilde{\gamma} \tilde{\lambda}}{\tilde{\epsilon}^2} \nabla (\phi(\phi^2 - 1) - \nabla \cdot \tilde{\epsilon}^2 \nabla \phi)}_{\text{transport from chemical potential}}, \quad (\text{F.24})$$

where $\tilde{\gamma}$ is the mobility, $\tilde{\lambda}$ is the mixing energy density, and $\tilde{\epsilon}$ is the interface thickness. The coupled flow field \mathbf{u} is obtained using the creeping flow approximation

$$\rho \frac{\partial \mathbf{u}}{\partial t} = \nabla \cdot [-p \mathbf{I} + \mu (\nabla \mathbf{u} + (\nabla \mathbf{u})^T)] + \underbrace{\frac{\tilde{\lambda}}{\tilde{\epsilon}^2} (\phi(\phi^2 - 1) - \tilde{\epsilon}^2 \nabla^2 \phi) \nabla \phi}_{\text{interfacial tension term}}, \quad (\text{F.25})$$

where p , ρ , and μ are the fluid pressure, density, and viscosity. We set the constant flowrate on the left boundary and constant pressure on the right boundary (Fig. F-12). We set a space-varying contact angle $\theta_b(z)$ at the impermeable wall (bottom), such that $\cos \theta_b(z) = \cos \theta_{b0} - \epsilon \sin(2\pi z/q)$ by imposing

$$-\nabla \phi \cdot \mathbf{n} = |\nabla \phi| (\cos \theta_{b0} - \epsilon \sin(2\pi z/q)), \quad (\text{F.26})$$

as well as no-slip boundary condition, where \mathbf{n} is the normal unit vector at the wall.

Phase-field modeling of a viscous oil slug that is preceded by air and displaced by water would require a relatively long channel with reasonably fine mesh. That would translate into a significant computational cost. Since we are only interested in the dynamics of the stick–slip motion near the contact line, we instead model viscosity-matched displacement inside the 2D channel. This way the total pressure drop $\Delta p_{\text{total}}(t)$ across the channel has three components for any given simulation: time-dependent pressure due to stick–slip dynamics $\Delta p_{\text{slip}}(t)$, time-independent pressure due to Poiseuille flow in the bulk of the channel Δp_{pois} , and the time-independent pressure due to sharp

velocity gradients near the mean contact line geometry $\Delta p_{c.l.}$. For a given capillary number Ca , we find $\Delta p_{\text{pois}} + \Delta p_{c.l.}$ by running a simulation on a smooth surface ($\epsilon = 0$ in Eq. 8.11). Then, we can isolate $\Delta p_{\text{slip}}(t)$ through

$$\Delta p_{\text{slip}}(t) = \Delta p_{\text{total}}(t) - (\Delta p_{\text{pois}} + \Delta p_{c.l.}) \quad (\text{F.27})$$

for any combination of ϵ and Ca of interest. Then, we compute the total dissipation due to oscillatory motion of the contact line in Figure 8-4b as

$$\Xi = \frac{\langle \Delta p_{\text{slip}} \rangle}{\langle \Delta p_{\text{total}} \rangle}, \quad (\text{F.28})$$

where $\langle \Delta p_{\text{total}} \rangle = \frac{1}{t_{\text{max}}} \int_0^{t_{\text{max}}} \Delta p_{\text{total}}(t) dt$. We set the static contact θ_{b0} to $\pi/2$ (see Eq. 8.11) to match our assumptions in the analytic model.

While our phase-field simulations reported in Fig. 8-4b reproduce the main dynamic regimes of the drum analog (Fig. 8-4a), the mean value of the contact angle θ_{b0} increases with Ca due to viscous bending of the fluid-fluid interface. We marked a Ca region where this angle reaches π on a smooth surface with green shading in Fig. 8-4b. A film of defending fluid is deposited on the channel walls in this region. We neglected the dependence of the wetting transition on ϵ in Fig. 8-4 Golestanian (2004).

Bibliography

- ADLER, ROBERT 1946 A Study of Locking Phenomena in Oscillators. *Proceedings of the IRE* **34** (6), 351–357.
- AHN, CHONG H., CHOI, JIM WOO, BEAUCAGE, GREGORY, NEVIN, JOSEPH H., LEE, JEONG BONG, PUNTAMBEKAR, ANIRUDDHA & LEE, JAE Y. 2004 Disposable smart lab on a chip for point-of-care clinical diagnostics. *Proceedings of the IEEE* **92** (1), 154–173.
- AKER, EYVIND, MÅLØY, KNUT JØRGEN & HANSEN, ALEX 1998*a* Simulating temporal evolution of pressure in two-phase flow in porous media. *Physical Review E* **58** (2), 2217–2226.
- AKER, EYVIND, MÅLØY, KNUT JØRGEN, HANSEN, ALEX & BATROUNI, GEORGE 1998*b* A Two-Dimensional Network Simulator for Two-Phase Flow in Porous Media. *Transport in Porous Media* **32**, 163–186.
- AL-GHARBI, MOHAMMED S. & BLUNT, MARTIN J. 2005 Dynamic network modeling of two-phase drainage in porous media. *Physical Review E* **71**, 016308.
- ALAVA, MIKKO, DUBÉ, MARTIN & ROST, MARTIN 2004 Imbibition in disordered media. *Advances in Physics* **53** (2), 83–175.
- ANDERSON, RYAN, ZHANG, LIFENG, DING, YULONG, BLANCO, MAURICIO, BI, XIAOTAO & WILKINSON, DAVID P. 2010 A critical review of two-phase flow in gas flow channels of proton exchange membrane fuel cells. *Journal of Power Sources* **195** (15), 4531–4553.
- ARNÉODO, A., COUDER, Y., GRASSEAU, G., HAKIM, V., RABAUD, M., ARNEODO, A, COUDER, Y., GRASSEAU, G., HAKIM, ' V & RABAUD~, M 1989 Uncovering the analytical Saffman-Taylor finger in unstable viscous fingering and diffusion-limited aggregation. *Physical Review Letters* **63** (9), 984–987.
- AUSSILLOUS, PASCALE & QUÉRÉ, DAVID 2000 Quick deposition of a fluid on the wall of a tube. *Physics of Fluids* **12** (10), 2367–2371.
- AUSSILLOUS, P. & QUÉRÉ, D. 2001 Liquid marbles. *Nature* **411** (6840), 924–927.
- BAK, PER 2013 *How Nature works: the science of self-organized criticality*. Springer Science & Business Media.
- BAK, PER & CHEN, KAN 1989 The physics of fractals. *Physica D: Nonlinear Phenomena* **38** (1-3), 5–12.
- BAK, PER, TANG, CHAO & WIESENFELD, KURT 1987 Self-organized criticality: An explanation of the 1/f noise. *Physical Review Letters* **59** (4), 381–384.

- BAK, PER, TANG, CHAO & WIESENFELD, KURT 1988 Self-organized criticality. *Physical Review A* **38** (1), 364–374.
- BEN AMAR, MARTINE 1991*a* Exact self-similar shapes in viscous fingering. *Physical Review A* **43** (10), 5724–5727.
- BEN AMAR, MARTINE 1991*b* Viscous fingering in a wedge. *Physical Review A* **44** (6), 3673–3685.
- BENSIMON, DAVID, KADANOFF, LEO P., LIANG, SHOUDAN, SHRAIMAN, BORIS I. & TANG, CHAO 1986 Viscous flows in two dimensions. *Reviews of Modern Physics* **58** (4), 977–999.
- BERG, STEFFEN, OTT, HOLGER, KLAPP, STEPHAN A, SCHWING, ALEX, NEITELER, ROB, BRUSSEE, NIELS, MAKURAT, AXEL, LEU, LEON, ENZMANN, FRIEDER, SCHWARZ, JENS-OLIVER, KERSTEN, MICHAEL, IRVINE, SARAH & STAMPANONI, MARCO 2013 Real-time 3D imaging of Haines jumps in porous media flow. *Proceedings of the National Academy of Sciences of the United States of America* **110** (10), 3755–9.
- BICO, JOSÉ & QUÉRÉ, DAVID 2001 Falling Slugs. *Journal of Colloid and Interface Science* **243** (1), 262–264.
- BICO, JOSÉ & QUÉRÉ, DAVID 2002 Self-propelling slugs. *Journal of Fluid Mechanics* **467**, 101–127.
- BIRD, JAMES C., MANDRE, SHREYAS & STONE, HOWARD A. 2008 Short-time dynamics of partial wetting. *Physical Review Letters* **100** (23), 234501.
- BIROVLJEV, A., FURUBERG, L., FEDER, J., JSSANG, T., MLY, K. J. & AHARONY, A. 1991 Gravity invasion percolation in two dimensions: Experiment and simulation. *Physical Review Letters* **67** (5), 584.
- BISCHOFBERGER, IRMGARD, RAMACHANDRAN, RADHA & NAGEL, SIDNEY R. 2015 An island of stability in a sea of fingers: emergent global features of the viscous-flow instability. *Soft Matter* **11** (37), 7428–7432.
- BISWAS, SOUMYAJYOTI, FANTINEL, PAOLO, BORGMAN, OSHRI, HOLTZMAN, RAN & GOEHRING, LUCAS 2018 Drying and percolation in correlated porous media. *Physical Review Fluids* **3** (12), 124307.
- BLUNT, MARTIN J. 1998 Physically-based network modeling of multiphase flow in intermediate-wet porous media. *Journal of Petroleum Science and Engineering* **20** (3-4), 117–125.
- BLUNT, MARTIN J. 2001 Flow in porous media — pore-network models and multiphase flow. *Current Opinion in Colloid & Interface Science* **6** (3), 197–207.
- BLUNT, MARTIN J. 2017 *Multiphase flow in permeable media: A pore-scale perspective..* Cambridge University Press.
- BLUNT, MARTIN J. & SCHER, HARVEY 1995 Pore-level modeling of wetting. *Physical Review E* **52** (6), 6387–6403.
- BONN, DANIEL, EGGERS, JENS, INDEKEU, JOSEPH, MEUNIER, JACQUES & ROLLEY, ETIENNE 2009 Wetting and spreading. *Reviews of Modern Physics* **81** (2), 739–805.

- BORGMAN, OSHRI, DARWENT, THOMAS, SEGRE, ENRICO, GOEHRING, LUCAS & HOLTZMAN, RAN 2019 Immiscible fluid displacement in porous media with spatially correlated particle sizes. *Advances in Water Resources* **128**, 158–167.
- BRACE, W. F. & BYERLEE, J. D. 1966 Stick-Slip as a Mechanism for Earthquakes. *Science* **153** (3739), 990–992.
- BRETHERTON, F. P. 1961 The motion of long bubbles in tubes. *Journal of Fluid Mechanics* **10**, 166–188.
- BROCHARD-WYART, F. & DE GENNES, P. G. 1992 Dynamics of partial wetting. *Advances in Colloid and Interface Science* **39**, 1–11.
- CAHN, JOHN W. & HILLIARD, JOHN E. 2004 Free Energy of a Nonuniform System. I. Interfacial Free Energy. *The Journal of Chemical Physics* **28** (2), 258.
- CAI, T. TONY 2002 ON BLOCK THRESHOLDING IN WAVELET REGRESSION: ADAPTIVITY, BLOCK SIZE, AND THRESHOLD LEVEL.
- CALHOUN, R. B. & MORTENSEN, A. 1992 Infiltration of fibrous preforms by a pure metal:. *Metallurgical Transactions A* **23** (8), 2291–2299.
- CELIA, MICHAEL A., REEVES, PAUL C. & FERRAND, LIN A. 1995 Recent advances in pore scale models for multiphase flow in porous media. *Reviews of Geophysics* **33** (S2), 1049–1057.
- CHANDLER, RICHARD, KOPLIK, JOEL, LERMAN, KENNETH & WILLEMSSEN, JORGE F. 1982 Capillary displacement and percolation in porous media. *Journal of Fluid Mechanics* **119**, 249–267.
- CHEN, J. D. 1987 Radial viscous fingering patterns in Hele-Shaw cells. *Experiments in Fluids* **5** (6), 363–371.
- CHEN, JING DEN 1989 Growth of radial viscous fingers in a Hele-Shaw cell. *Journal of Fluid Mechanics* **201**, 223–242.
- CHEN, JING DEN & WILKINSON, DAVID 1985 Pore-scale viscous fingering in porous media. *Physical Review Letters* **55** (18), 1892–1895.
- CHENG, HUNG 2007 *Advanced Analytic Methods in Applied Mathematics, Science, and Engineering*. LuBan Press.
- CHIARELLO, R., PANELLA, V., KRIM, J. & THOMPSON, C. 1991 X-ray reflectivity and adsorption isotherm study of fractal scaling in vapor-deposited films. *Physical Review Letters* **67** (24), 3408.
- CHUOKE, R. L., VAN MEURS, P. & VAN DER POEL, C. 1959 The Instability of Slow, Immiscible, Viscous Liquid-Liquid Displacements in Permeable Media. *Petrol. Trans. AIME* **216**, 188–194.
- CIEPLAK, MAREK, MARITAN, AMOS & BANAVAR, JAYANTH R. 1996 Invasion percolation and Eden growth: Geometry and universality. *Physical Review Letters* **76** (20), 3754–3757.
- CIEPLAK, MAREK & ROBBINS, MARK O. 1988 Dynamical Transition in Quasistatic Fluid Invasion in Porous Media. *Physical Review Letters* **60** (20), 2042–2045.

- CIEPLAK, MAREK & ROBBINS, MARK O. 1990 Influence of contact angle on quasistatic fluid invasion of porous media. *Physical Review B* **41** (16), 11508–11521.
- CINAR, YILDIRAY, RIAZ, AMIR & TCHELEPI, HAMDI A. 2007 Experimental Study of CO₂ Injection Into Saline Formations. In *SPE Annual Technical Conference and Exhibition*. Society of Petroleum Engineers.
- CONSTANTINIDES, GEORGE N. & PAYATAKES, ALKIVIADES C. 2000 Effects of precursor wetting films in immiscible displacement through porous media. *Transport in Porous Media* **38** (3), 291–317.
- CONTI, M. & MARCONI, U. M. B. 2010 Diffusion limited propagation of burning fronts. In *WIT Transactions on Ecology and the Environment*, , vol. 137, pp. 37–45. WIT Press.
- COX, R. G. 1986 The dynamics of the spreading of liquids on a solid surface. Part 1. Viscous flow. *Journal of Fluid Mechanics* **168**, 169–194.
- DACCORD, GERARD GÉRARD, NITTMANN, JOHANN & STANLEY, H. EUGENE 1986 Radial viscous fingers and diffusion-limited aggregation: Fractal dimension and growth sites. *Physical Review Letters* **56** (4), 336–339.
- DALBE, MARIE-JULIE & JUANES, RUBEN 2018 Morphodynamics of Fluid-Fluid Displacement in Three-Dimensional Deformable Granular Media. *Physical Review Applied* **9** (2), 024028.
- DATTA, SUJIT S., RAMAKRISHNAN, T. S. & WEITZ, DAVID A. 2014 Mobilization of a trapped non-wetting fluid from a three-dimensional porous medium. *Physics of Fluids* **26** (2), 22002.
- DE CONINCK, J. & BLAKE, T.D. 2008 Wetting and Molecular Dynamics Simulations of Simple Liquids. *Annual Review of Materials Research* **38** (1), 1–22.
- DELAMARCHE, E., JUNCKER, D. & SCHMID, H. 2005 Microfluidics for Processing Surfaces and Miniaturizing Biological Assays. *Advanced Materials* **17** (24), 2911–2933.
- DELANNOY, JOACHIM, LAFON, SUZANNE, KOGA, YUKINA, REYSSAT, ETIENNE & QUÉRÉ, DAVID 2019 The dual role of viscosity in capillary rise. *Soft Matter* **15** (13), 2757–2761.
- DENIS BARTOLO, GUILLAUME DEGRÉ, PHILIPPE NGHE & VINCENT STUDER 2008 Microfluidic stickers. *Lab on a Chip* **8** (2), 274–279.
- DEVRIES, PHOEBE M. R., VIÉGAS, FERNANDA, WATTENBERG, MARTIN & MEADE, BRENDAN J. 2018 Deep learning of aftershock patterns following large earthquakes. *Nature* **560** (7720), 632–634.
- DUCLAUX, VIRGINIE, CLANET, CHRISTOPHE & QUÉRÉ, DAVID 2006 The effects of gravity on the capillary instability in tubes. *Journal of Fluid Mechanics* **556**, 217–226.
- EGGERS, JENS & STONE, HOWARD A. 2004 Characteristic lengths at moving contact lines for a perfectly wetting fluid: The influence of speed on the dynamic contact angle. *Journal of Fluid Mechanics* **505** (505), 309–321.
- EGGERS, JENS & VILLERMAUX, EMMANUEL 2008 Physics of liquid jets. *Reports on Progress in Physics* **71** (3), 036601.

- EMSLIE, ALFRED G., BONNER, FRANCIS T. & PECK, LESLIE G. 1958 Flow of a Viscous Liquid on a Rotating Disk. *Journal of Applied Physics* **29** (5), 858–862.
- FATT, I. 1956 The Network Model of Porous Media. *Petroleum Transactions, AIME* **207**, 144–177.
- FEDER, JENS, HINRICHSEN, EINAR L., MÅLØY, KNUT JØRGEN & JØSSANG, TORSTEIN 1989 Geometrical crossover and self-similarity of DLA and viscous fingering clusters. *Physica D: Nonlinear Phenomena* **38** (1-3), 104–111.
- FERER, M., JI, CHUANG, BROMHAL, GRANT S., COOK, JOSHUA, AHMADI, GOODARZ & SMITH, DUANE H. 2004 Crossover from capillary fingering to viscous fingering for immiscible unstable flow: Experiment and modeling. *Physical Review E* **70** (1), 016303.
- FERMIGIER, MARC & JENFFER, PATRICE 1991 An experimental investigation of the dynamic contact angle in liquid-liquid systems. *Journal of Colloid And Interface Science* **146** (1), 226–241.
- FERNÁNDEZ, JULIO F., ALBARRÁN, JESÚS M., FERNANDEZ, JULIO F & ALBARRAN, JESUS M 1990 Diffusion-limited aggregation with surface tension: Scaling of viscous fingering. *Physical Review Letters* **64** (18), 2133–2136.
- FERNANDEZ, JULIO F, RANGEL, RAFAEL & RIVERO, JUAN 1991 Crossover length from invasion percolation to diffusion-limited aggregation in porous media. *Physical Review Letters* **67** (21), 2958–2961.
- FISHER, LEN 1999 Physics takes the biscuit. *Nature* **397** (6719), 469–469.
- FRETTE, VIDAR, FEDER, JENS, JØSSANG, TORSTEIN & MEAKIN, PAUL 1992 Buoyancy-driven fluid migration in porous media. *Physical Review Letters* **68** (21), 3164.
- FURUBERG, LIV, FEDER, JENS, AHARONY, AMNON & JØSSANG, TORSTEIN 1988 Dynamics of invasion percolation. *Physical Review Letters* **61** (18), 2117–2120.
- FURUBERG, LIV, MÅLØY, KNUT JØRGEN & FEDER, JENS 1996 Intermittent behavior in slow drainage. *Physical Review E* **53** (1), 966–977.
- DE GENNES, P. G. 1985 Wetting: statics and dynamics. *Reviews of Modern Physics* **57** (3), 827–863.
- DE GENNES, PIERRE-GILLES, BROCHARD-WYART, FRANÇOISE & QUÉRÉ, DAVID 2004 *Capillarity and Wetting Phenomena*. Springer Science & Business Media.
- GJENNESTAD, MAGNUS AA., VASSVIK, MORTEN, KJELSTRUP, SIGNE & HANSEN, ALEX 2018 Stable and Efficient Time Integration of a Dynamic Pore Network Model for Two-Phase Flow in Porous Media. *Frontiers in Physics* **6**, 56.
- GOLDENFELD, NIGEL & KADANOFF, LEO P. 1999 Simple lessons from complexity. *Science* **284** (5411), 87–89.
- GOLDSMITH, HARRY L. & SPAIN, SAMIRA 1984 Margination of leukocytes in blood flow through small tubes. *Microvascular Research* **27** (2), 204–222.
- GOLESTANIAN, RAMIN 2004 Moving Contact Lines on Heterogeneous Substrates. *Philosophical Transactions: Mathematical, Physical and Engineering Sciences* **362** (1821).

- GOREN, SIMON L. 1962 The instability of an annular thread of fluid. *Journal of Fluid Mechanics* **12** (02), 309–319.
- GUO, WEIJIN, HANSSON, JONAS & VAN DER WIJNGAART, WOUTER 2018 Capillary pumping independent of the liquid surface energy and viscosity. *Microsystems and Nanoengineering* **4**, 2.
- HAINES, WILLIAM B. 1930 Studies in the physical properties of soil. V. The hysteresis effect in capillary properties, and the modes of moisture distribution associated therewith. *The Journal of Agricultural Science* **20** (1), 97–116.
- HESHMATI, MOHAMMAD & PIRI, MOHAMMAD 2014 Experimental investigation of dynamic contact angle and capillary rise in tubes with circular and noncircular cross sections. *Langmuir* **30** (47), 14151–14162.
- HILL, S. 1952 Channeling in packed columns. *Chemical Engineering Science* **1** (6), 247–253.
- HILPERT, MARKUS 2009 Effects of dynamic contact angle on liquid infiltration into horizontal capillary tubes: (Semi)-analytical solutions. *Journal of Colloid and Interface Science* **337** (1), 131–137.
- HILPERT, MARKUS 2010 Explicit analytical solutions for liquid infiltration into capillary tubes: Dynamic and constant contact angle. *Journal of Colloid and Interface Science* **344** (1), 198–208.
- HINRICHSEN, E. L., MÅLØY, K. J., FEDER, J. & JØSSANG, T. 1989 Self-similarity and structure of DLA and viscous fingering clusters. *Journal of Physics A: Mathematical and General* **22** (7), 271–277.
- HOFFMAN, RICHARD L 1975 A study of the advancing interface. I. Interface shape in liquid–gas systems. *Journal of Colloid and Interface Science* **50** (2), 228–241.
- HOLTZMAN, RAN 2016 Effects of Pore-Scale Disorder on Fluid Displacement in Partially-Wettable Porous Media. *Scientific Reports* **6** (1), 36221.
- HOLTZMAN, RAN & JUANES, RUBEN 2010 Crossover from fingering to fracturing in deformable disordered media. *Physical Review E* **82** (4), 046305.
- HOLTZMAN, RAN & SEGRE, ENRICO 2015 Wettability Stabilizes Fluid Invasion into Porous Media via Nonlocal, Cooperative Pore Filling. *Physical Review Letters* **115** (16), 164501.
- HOLTZMAN, RAN, SZULCZEWSKI, MICHAEL L. & JUANES, RUBEN 2012 Capillary Fracturing in Granular Media. *Physical Review Letters* **108** (26), 264504.
- HOMSY, G. M. 1987 Viscous Fingering in Porous Media. *Annual Review of Fluid Mechanics* **19** (1), 271–311.
- HU, RAN, LAN, TIAN, WEI, GUAN JU & CHEN, YI FENG 2019 Phase diagram of quasi-static immiscible displacement in disordered porous media. *Journal of Fluid Mechanics* **875**, 448–475.
- HU, RAN, WAN, JIAMIN, YANG, ZHIBING, CHEN, YI-FENG & TOKUNAGA, TETSU 2018 Wettability and Flow Rate Impacts on Immiscible Displacement: A Theoretical Model. *Geophysical Research Letters* **45** (7), 3077–3086.
- HUH, CHUN & SCRIVEN, L. E. 1971 Hydrodynamic model of steady movement of a solid/liquid/fluid contact line. *Journal of Colloid And Interface Science* **35** (1), 85–101.

- IANNACCONE, PHILIP M & KHOKHA, MUSTAFA 1996 *Fractal Geometry in Biological Systems: an Analytical Approach*. CRC Press.
- JAIN, A. K. & JUANES, R. 2009 Preferential Mode of gas invasion in sediments: Grain-scale mechanistic model of coupled multiphase fluid flow and sediment mechanics. *Journal of Geophysical Research* **114** (B8), B08101.
- JOANNY, J. F. & ROBBINS, MARK O. 1990 Motion of a contact line on a heterogeneous surface. *The Journal of Chemical Physics* **92**, 3206.
- JOEKAR-NIASAR, V. & HASSANIZADEH, S. M. 2012 Analysis of Fundamentals of Two-Phase Flow in Porous Media Using Dynamic Pore-Network Models: A Review. *Critical Reviews in Environmental Science and Technology* **42** (18), 1895–1976.
- JOEKAR-NIASAR, V., HASSANIZADEH, S. M. & DAHLE, H. K. 2010 Non-equilibrium effects in capillarity and interfacial area in two-phase flow: dynamic pore-network modelling. *Journal of Fluid Mechanics* **655**, 38–71.
- JOHNSON, MARK, KAMM, ROGER D., HO, LEE WING, SHAPIRO, ASCHER & PEDLEY, T. J. 1991 The nonlinear growth of surface-tension-driven instabilities of a thin annular film. *Journal of Fluid Mechanics* **233**, 141–156.
- JUNG, MICHAEL, BRINKMANN, MARTIN, SEEMANN, RALF, HILLER, THOMAS, SANCHEZ DE LA LAMA, MARTA & HERMINGHAUS, STEPHAN 2016 Wettability controls slow immiscible displacement through local interfacial instabilities. *Physical Review Fluids* **1** (7), 074202.
- KADANOFF, LEO P. 1985 Simulating hydrodynamics: A pedestrian model. *Journal of Statistical Physics* **39** (3-4), 267–283.
- KENKEL, N. C. & WALKER, D. J. 1996 Fractals in the Biological Sciences. *Coenoses* **11**, 77–100.
- KIM, JUNGCHUL, MOON, MYOUNG-WOON, LEE, KWANG-RYEOL, MAHADEVAN, L. & KIM, HO-YOUNG 2011 Hydrodynamics of Writing with Ink. *Physical Review Letters* **107** (26), 264501.
- KNACKSTEDT, MARK A., SAHIMI, MUHAMMAD & SHEPPARD, ADRIAN P. 2002 Nonuniversality of invasion percolation in two-dimensional systems. *Physical Review E - Statistical Physics, Plasmas, Fluids, and Related Interdisciplinary Topics* **65** (3), 035101.
- KNUDSEN, HENNING ARENDT & HANSEN, ALEX 2002 Relation between pressure and fractional flow in two-phase flow in porous media. *Physical Review E* **65** (5), 056310.
- LAKE, LARRY W. 1989 *Enhanced oil recovery*. Englewood Cliffs, N.J.: Prentice Hall.
- LAN, TIAN, HU, RAN, YANG, ZHIBING, WU, DONG-SHENG & CHEN, YI-FENG 2020 Transitions of Fluid Invasion Patterns in Porous Media. *Geophysical Research Letters* **47** (20), e2020GL089682.
- LANDAU, L. & LEVICH, B. 1988 Dragging of a Liquid by a Moving Plate. In *Dynamics of Curved Fronts*, pp. 141–153. Elsevier.
- LEE, CHUNG HYUK, ZHAO, BENZHONG, ABOUATALLAH, RAMI, WANG, RAINEY & BAZYLAK, AIMY 2019 Compressible-Gas Invasion into Liquid-Saturated Porous Media: Application to Polymer-Electrolyte-Membrane Electrolyzers. *Physical Review Applied* **11** (5), 054029.

- LEE, HYUNDO, GUPTA, ANKUR, HATTON, T. ALAN & DOYLE, PATRICK S. 2017 Creating Isolated Liquid Compartments Using Photopatterned Obstacles in Microfluidics. *Physical Review Applied* **7** (4), 044013.
- LEE, SUNGYON, LEE, JEREMY, LE MESTRE, ROBIN, XU, FENG & MACMINN, CHRISTOPHER W. 2020 Migration, trapping, and venting of gas in a soft granular material. *Physical Review Fluids* **5** (8), 084307.
- LÉGER, ALAIN, WEBER, LUDGER & MORTENSEN, ANDREAS 2015 Influence of the wetting angle on capillary forces in pressure infiltration. *Acta Materialia* **91**, 57–69.
- LENORMAND, R 1990 Liquids in porous media. *Journal of Physics: Condensed Matter* **2** (S), SA79–SA88.
- LENORMAND, R & BORIES, S 1980 Description d’un mecanisme de connexion de liaison destine a l’etude du drainage avec piegeage en milieu poreux. *Comptes Rendus de l’Acad{\'e}mie des Sciences* **291**, 279–282.
- LENORMAND, ROLAND, TOUBOUL, ERIC & ZARCONE, CESAR 1988 Numerical models and experiments on immiscible displacements in porous media. *Journal of Fluid Mechanics* **189**, 165–187.
- LENORMAND, ROLAND & ZARCONE, CESAR 1985 Invasion Percolation in an Etched Network: Measurement of a Fractal Dimension. *Physical Review Letters* **54** (20), 2226–2229.
- LENORMAND, R., ZARCONE, C. & SARR, A. 1983 Mechanisms of the displacement of one fluid by another in a network of capillary ducts. *Journal of Fluid Mechanics* **135**, 337–353.
- LEVACHÉ, BERTRAND, AZIOUNE, AMMAR, BOURREL, MAURICE, STUDER, VINCENT & BARTOLO, DENIS 2012 Engineering the surface properties of microfluidic stickers. *Lab on a Chip* **12** (17), 3028–3031.
- LEVACHÉ, BERTRAND & BARTOLO, DENIS 2014 Revisiting the Saffman-Taylor Experiment: Imbibition Patterns and Liquid-Entrainment Transitions. *Physical Review Letters* **113** (4), 044501.
- LI, SHUWANG, LOWENGRUB, JOHN S., FONTANA, JAKE & PALFFY-MUHORAY, PETER 2009 Control of Viscous Fingering Patterns in a Radial Hele-Shaw Cell. *Physical Review Letters* **102** (17), 174501.
- LI, ZIDA, MAK, SZE YI, SAURET, ALBAN & SHUM, HO CHEUNG 2014 Syringe-pump-induced fluctuation in all-aqueous microfluidic system implications for flow rate accuracy. *Lab on a Chip* **14** (4), 744–749.
- LØVOLL, GRUNDE, MÉHEUST, YVES, TOUSSAINT, RENAUD, SCHMITTBUHL, JEAN & MÅLØY, KNUT JØRGEN 2004 Growth activity during fingering in a porous Hele-Shaw cell. *Physical Review E* **70** (2), 026301.
- LUCAS, RICHARD 1918 Ueber das Zeitgesetz des kapillaren Aufstiegs von Flüssigkeiten. *Kolloid-Zeitschrift* **23** (1), 15–22.
- MACMINN, CHRISTOPHER W., DUFRESNE, ERIC R. & WETTLAUFER, JOHN S. 2015 Fluid-Driven Deformation of a Soft Granular Material. *Physical Review X* **5** (1), 011020.

- MACMINN, C. W., SZULCZEWSKI, M. L. & JUANES, R. 2010 CO₂ migration in saline aquifers. Part 1. Capillary trapping under slope and groundwater flow. *Journal of Fluid Mechanics* **662**, 329–351.
- MACMINN, C. W., SZULCZEWSKI, M. L. & JUANES, R. 2011 CO₂ migration in saline aquifers. Part 2. Capillary and solubility trapping. *Journal of Fluid Mechanics* **688**, 321–351.
- MAJUMDAR, A. & TIEN, C. L. 1990 Fractal characterization and simulation of rough surfaces. *Wear* **136** (2), 313–327.
- MÅLØY, KNUT JØRGEN, FEDER, JENS & JØSSANG, TORSTEIN 1985 Viscous fingering fractals in porous media. *Physical Review Letters* **55** (24), 2688–2691.
- MÅLØY, KNUT JØRGEN, FURUBERG, LIV, FEDER, JENS & JØSSANG, TORSTEIN 1992 Dynamics of slow drainage in porous media. *Physical Review Letters* **68** (14), 2161–2164.
- MANNETJE, D. J.C.M., MUGELE, F. & VAN DEN ENDE, D. 2013 Stick-slip to sliding transition of dynamic contact lines under ac electrowetting. *Langmuir* **29** (48), 15116–15121.
- MARKOVIĆ, DIMITRIJE & GROS, CLAUDIUS 2014 Power laws and self-organized criticality in theory and nature. *Physics Reports* **536** (2), 41–74.
- MARTYS, NICOS, ROBBINS, MARK O. & CIEPLAK, MAREK 1991 Scaling relations for interface motion through disordered media: Application to two-dimensional fluid invasion. *Physical Review B* **44** (22), 12294–12306.
- MASLOV, SERGEI 1995 Time directed avalanches in invasion models. *Physical Review Letters* **74** (4), 562–565.
- MEAKIN, PAUL, BIROVLJEV, ALEKSANDAR, FRETTE, VIDAR, FEDER, JENS & JØSSANG, TORSTEIN 1992 Gradient stabilized and destabilized invasion percolation. *Physica A: Statistical Mechanics and its Applications* **191** (1-4), 227–239.
- MEAKIN, PAUL & TARTAKOVSKY, ALEXANDRE M. 2009 Modeling and simulation of pore-scale multiphase fluid flow and reactive transport in fractured and porous media. *Reviews of Geophysics* **47** (3), RG3002.
- MEAKIN, P., TOLMAN, S. & BLUMEN, A. 1989 Diffusion-Limited Aggregation. *Proceedings of the Royal Society A: Mathematical, Physical and Engineering Sciences* **423** (1864), 133–148.
- MENG, YUE, PRIMKULOV, BAUYRZHAN K., YANG, ZHIBING, KWOK, CHUNG YEE & JUANES, RUBEN 2020 Jamming transition and emergence of fracturing in wet granular media. *Physical Review Research* **2** (2), 022012.
- MOEBIUS, FRANZISKA & OR, DANI 2012 Interfacial jumps and pressure bursts during fluid displacement in interacting irregular capillaries. *Journal of Colloid and Interface Science* **377** (1), 406–415.
- MØLLER, P. C.F. & BONN, D. 2007 The shear modulus of wet granular matter. *EPL* **80** (3), 38002.
- MORROW, NORMAN R & MASON, GEOFFREY 2001 Recovery of oil by spontaneous imbibition. *Current Opinion in Colloid & Interface Science* **6** (4), 321–337.

- MOULINET, S., GUTHMANN, C. & ROLLEY, E. 2004 Dissipation in the dynamics of a moving contact line: effect of the substrate disorder. *The European Physical Journal B* **37**, 127–136.
- MOURA, MARCEL, MÅLØY, KNUT JØRGEN, FLEKKØY, EIRIK GRUDE & TOUSSAINT, RENAUD 2017a Verification of a Dynamic Scaling for the Pair Correlation Function during the Slow Drainage of a Porous Medium. *Physical Review Letters* **119** (15), 154503.
- MOURA, M., MÅLØY, K. J. & TOUSSAINT, R. 2017b Critical behavior in porous media flow. *EPL* **118** (1), 14004.
- MUGELE, FRIEDER & BARET, JEAN-CHRISTOPHE 2005 Electrowetting: from basics to applications. *Journal of Physics: Condensed Matter* **17** (28), R705–R774.
- MUMLEY, THOMAS E, RADKE, C.J & WILLIAMS, MICHAEL C 1986 Kinetics of liquid/liquid capillary rise: I. Experimental observations. *Journal of Colloid and Interface Science* **109** (2), 398–412.
- NIEMEYER, L., PIETRONERO, L. & WIESMANN, H. J. 1984 Fractal Dimension of Dielectric Breakdown. *Physical Review Letters* **52** (12), 1033–1036.
- NITTMANN, JOHANN, DACCORD, GÉRARD & STANLEY, H. EUGENE 1985 Fractal growth viscous fingers: quantitative characterization of a fluid instability phenomenon. *Nature* **314** (6007), 141–144.
- ODIER, CÉLESTE, LEVACHÉ, BERTRAND, SANTANACH-CARRERAS, ENRIC & BARTOLO, DENIS 2017 Forced Imbibition in Porous Media: A Fourfold Scenario. *Physical Review Letters* **119** (20), 208005.
- ØREN, P. E., BAKKE, STIG & ARNTZEN, O. J. 1998 Extending Predictive Capabilities to Network Models. *SPE Journal* **3** (4), 324–336.
- ORON, ALEXANDER, DAVIS, STEPHEN H. & BANKOFF, S. GEORGE 1997 Long-scale evolution of thin liquid films. *Reviews of Modern Physics* **69** (3), 931–980.
- PAHLAVAN, AMIR A., CUETO-FELGUEROSO, LUIS, MCKINLEY, GARETH H. & JUANES, RUBEN 2015 Thin Films in Partial Wetting: Internal Selection of Contact-Line Dynamics. *Physical Review Letters* **115** (3), 034502.
- PARK, C. W. & HOMSY, G. M. 1984 Two-phase displacement in Hele Shaw cells: Theory. *Journal of Fluid Mechanics* **139**, 291–308.
- PATERSON, LINCOLN 1981 Radial fingering in a Hele Shaw cell. *Journal of Fluid Mechanics* **113**, 513–529.
- PATERSON, LINCOLN 1984 Diffusion-limited aggregation and two-fluid displacements in porous media. *Physical Review Letters* **52** (18), 1621–1624.
- PATMONOAJI, ANINDITYO, MUHARRIK, MUSHLIH, HU, YINGXUE, ZHANG, CHUNWEI & SUEKANE, TETSUYA 2020 Three-dimensional fingering structures in immiscible flow at the crossover from viscous to capillary fingering. *International Journal of Multiphase Flow* **122**, 103147.

- PATZEK, T.W. & KRISTENSEN, J.G. 2001 Shape Factor Correlations of Hydraulic Conductance in Noncircular Capillaries: II. Two-Phase Creeping Flow. *Journal of Colloid and Interface Science* **236** (2), 305–317.
- PATZEK, T. W. 2001 Verification of a complete pore network simulator of drainage and imbibition. *SPE Journal* **6** (2), 144–156.
- PEEK, R. L. & MCLEAN, D. A. 1934 Capillary Penetration of Fibrous Materials. *Industrial & Engineering Chemistry Analytical Edition* **6** (2), 85–90.
- PERRIN, H., BELARDINELLI, D., SBRAGAGLIA, M. & ANDREOTTI, B. 2018a Response function of a moving contact line. *Physical Review Fluids* **3** (4), 044001.
- PERRIN, HUGO, LHERMEROUT, ROMAIN, DAVITT, KRISTINA, ROLLEY, ETIENNE & ANDREOTTI, BRUNO 2016 Defects at the Nanoscale Impact Contact Line Motion at all Scales. *Physical Review Letters* **116** (18), 184502.
- PERRIN, HUGO, LHERMEROUT, ROMAIN, DAVITT, KRISTINA, ROLLEY, ETIENNE & ANDREOTTI, BRUNO 2018b Thermally activated motion of a contact line over defects. *Soft Matter* **14** (9), 1581–1595.
- PLATEAU, JOSEPH. 1873 *Statique Expérimentale et Théorique des Liquides Soumis aux Seules Forces Moléculaires*. Gauthier-Villars.
- PONOMARENKO, ALEXANDRE, QUÉRÉ, DAVID DAVIF & CLANET, CHRISTOPHE 2011 A universal law for capillary rise in corners. *Journal of Fluid Mechanics* **666**, 146–154.
- PRIES, A. R., NEUHAUS, D. & GAEHTGENS, P. 1992 Blood viscosity in tube flow: dependence on diameter and hematocrit. *The American journal of physiology* **263**, H1770–H1778.
- PRIMKULOV, B. K., CHUI, J. Y. Y., PAHLAVAN, A. A., MACMINN, C. W. & JUANES, R. 2020a Characterizing dissipation in fluid-fluid displacement using constant-rate spontaneous imbibition. *Physical Review Letters* **125** (17), 174503.
- PRIMKULOV, B. K., PAHLAVAN, A. A., BOUROUBA, L., BUSH, J. W. M. & JUANES, R. 2020b Spin coating of capillary tubes. *Journal of Fluid Mechanics* **886**, A30.
- PRIMKULOV, BAUYRZHAN K., PAHLAVAN, AMIR A., FU, XIAOJING, ZHAO, BENZHONG, MACMINN, CHRISTOPHER W. & JUANES, RUBEN 2019 Signatures of fluid-fluid displacement in porous media: wettability, patterns and pressures. *Journal of Fluid Mechanics* **875**, R4.
- PRIMKULOV, BAUYRZHAN K., PAHLAVAN, AMIR A., FU, XIAOJING, ZHAO, BENZHONG, MACMINN, CHRISTOPHER W. & JUANES, RUBEN 2021 Wettability and Lenormand’s Diagram. *Journal of Fluid Mechanics* **923**, A34.
- PRIMKULOV, BAUYRZHAN K., TALMAN, STEPHEN, KHALEGHI, KEIVAN, RANGRIZ SHOKRI, ALIREZA, CHALATURNYK, RICK, ZHAO, BENZHONG, MACMINN, CHRISTOPHER W. & JUANES, RUBEN 2018 Quasistatic fluid-fluid displacement in porous media: Invasion-percolation through a wetting transition. *Physical Review Fluids* **3** (10), 104001.
- PRIMKULOV, BAUYRZHAN K., ZHAO, BENZHONG, MACMINN, CHRISTOPHER W. & JUANES, RUBEN 2022 Avalanches in strong imbibition. *Communications Physics* 2022 5:1 **5** (1), 1–6.

- RABBANI, HARRIS SAJJAD, ZHAO, BENZHONG, JUANES, RUBEN & SHOKRI, NIMA 2018 Pore geometry control of apparent wetting in porous media. *Scientific Reports* **8** (1), 15729.
- RAPHAËL, E. & DE GENNES, P. G. 1989 Dynamics of wetting with nonideal surfaces. The single defect problem. *The Journal of Chemical Physics* **90**, 7577.
- RAYLEIGH, R. S. 1892 On the instability of cylindrical fluid surfaces. *Philosophical Magazine and Journal of Science* **34**, 177–180.
- RICHARD, D. & QUÉRÉ, D. 1999 Viscous drops rolling on a tilted non-wettable solid. *Europhysics Letters* **48** (3), 286–291.
- RICHEFEU, VINCENT, EL YOUSOUFI, MOULAY SAÏD & RADJAÏ, FARHANG 2006 Shear strength properties of wet granular materials. *Physical Review E* **73** (5), 051304.
- ROSS, ZACHARY E., TRUGMAN, DANIEL T., HAUKSSON, EGILL & SHEARER, PETER M. 2019 Searching for hidden earthquakes in Southern California. *Science* **364** (6442), 767–771.
- ROSSEN, WILLIAM R 2000 Snap-off in constricted tubes and porous media. *Colloids and Surfaces A: Physicochemical and Engineering Aspects* **166** (1-3), 101–107.
- ROUX, S. & GUYON, E. 1989 Temporal development of invasion percolation. *Journal of Physics A: Mathematical and General* **22** (17), 3693–3705.
- SAFFMAN, P. G. & TAYLOR, G. 1958 The Penetration of a Fluid into a Porous Medium or Hele-Shaw Cell Containing a More Viscous Liquid. *Proceedings of the Royal Society A: Mathematical, Physical and Engineering Sciences* **245** (1242), 312–329.
- SANDNES, B., FLEKKØY, E.G., KNUDSEN, H.A., MÅLØY, K.J. & SEE, H. 2011 Patterns and flow in frictional fluid dynamics. *Nature Communications* **2** (1), 288.
- SAVVA, NIKOS, PAVLIOTIS, GRIGORIOS A. & KALLIADASIS, SERAFIM 2011 Contact lines over random topographical substrates. Part 1. Statics. *Journal of Fluid Mechanics* **672**, 358–383.
- SCHÄFFER, ERIK & WONG, PO ZEN 1998 Dynamics of contact line pinning in capillary rise and fall. *Physical Review Letters* **80** (14), 3069–3072.
- SCHÄFFER, ERIK & WONG, PO ZEN 2000 Contact line dynamics near the pinning threshold: A capillary rise and fall experiment. *Physical Review E* **61** (5), 5257–5277.
- SCRIVEN, L. E. 1988 Physics and Applications of Dip Coating and Spin Coating. *MRS Proceedings* **121**, 717–729.
- SEAVER, ALBERT E. & BERG, JOHN C. 1994 Spreading of a droplet on a solid surface. *Journal of Applied Polymer Science* **52** (3), 431–435.
- SHENG, PING & ZHOU, MINYAO 1992 Immiscible-fluid displacement: Contact-line dynamics and the velocity-dependent capillary pressure. *Physical Review A* **45** (8), 5694–5708.
- SHEPPARD, ADRIAN P., KNACKSTEDT, MARK A., PINCZEWSKI, W. V. & SAHIMI, MUHAMMAD 1999 Invasion percolation: New algorithms and universality classes. *Journal of Physics A: Mathematical and General* **32** (49), 521–529.

- SINGH, KAMALJIT, SCHOLL, HAGEN, BRINKMANN, MARTIN, MICHIEL, MARCO DI, SCHEEL, MARIO, HERMINGHAUS, STEPHAN & SEEMANN, RALF 2017 The Role of Local Instabilities in Fluid Invasion into Permeable Media. *Scientific Reports* **7** (1), 444.
- SNOEIJER, JACCO H. & ANDREOTTI, BRUNO 2013 Moving Contact Lines: Scales, Regimes, and Dynamical Transitions. *Annual Review of Fluid Mechanics* **45** (1), 269–292.
- SPARROW, COLIN & MANDELBROT, B. 1984 The Fractal Geometry of Nature. *Journal of the Royal Statistical Society. Series A (General)* **147** (4).
- STAUFFER, DIETRICH & AHARONY, AMNON 1985 *Introduction to Percolation Theory*. Taylor & Francis Group.
- STOKES, J. P., WEITZ, D. A., GOLLUB, J. P., DOUGHERTY, A., ROBBINS, M. O., CHAIKIN, P. M. & LINDSAY, H. M. 1986 Interfacial Stability of Immiscible Displacement in a Porous Medium. *Physical Review Letters* **57** (14), 1718–1721.
- STRANG, GILBERT. 2007 *Computational Science and Engineering*. Wellesley-Cambridge Press.
- SYGOUNI, VARVARA, TSAKIROGLOU, CHRISTOS D. & PAYATAKES, ALKIVIADES C. 2006 Capillary pressure spectrometry: Toward a new method for the measurement of the fractional wettability of porous media. *Physics of Fluids* **18** (5), 053302.
- SYGOUNI, V., TSAKIROGLOU, C. D. & PAYATAKES, A. C. 2007 Using wavelets to characterize the wettability of porous materials. *Physical Review E* **76** (5), 056304.
- SZULCZEWSKI, MICHAEL L, MACMINN, CHRISTOPHER W, HERZOG, HOWARD J & JUANES, RUBEN 2012 Lifetime of carbon capture and storage as a climate-change mitigation technology. *Proceedings of the National Academy of Sciences of the United States of America* **109** (14), 5185–9.
- TALLAKSTAD, KEN TORE, KNUDSEN, HENNING ARENDT, RAMSTAD, THOMAS, LØVOLL, GRUNDE, MÅLØY, KNUT JØRGEN, TOUSSAINT, RENAUD & FLEKKØY, EIRIK GRUDE 2009a Steady-state two-phase flow in porous media: Statistics and transport properties. *Physical Review Letters* **102** (7), 074502.
- TALLAKSTAD, KEN TORE, LØVOLL, GRUNDE, KNUDSEN, HENNING ARENDT, RAMSTAD, THOMAS, FLEKKØY, EIRIK GRUDE & MÅLØY, KNUT JØRGEN 2009b Steady-state, simultaneous two-phase flow in porous media: An experimental study. *Physical Review E* **80** (3), 036308.
- TANNER, L. H. 1979 The spreading of silicone oil drops on horizontal surfaces. *Journal of Physics D: Applied Physics* **12** (9), 1473.
- TAYLOR, G. I. 1961 Deposition of a viscous fluid on the wall of a tube. *Journal of Fluid Mechanics* **10** (02), 161–165.
- THIELE, UWE & KNOBLOCH, EDGAR 2006a Driven drops on heterogeneous substrates: Onset of sliding motion. *Physical Review Letters* **97** (20), 204501.
- THIELE, UWE & KNOBLOCH, EDGAR 2006b On the depinning of a driven drop on a heterogeneous substrate. *New Journal of Physics* **8** (12), 313.

- THIELICKE, WILLIAM & STAMHUIS, EIZE J. 2014 {PIVlab} {\textendash} Towards User-friendly, Affordable and Accurate Digital Particle Image Velocimetry in {MATLAB}. *Journal of Open Research Software* **2** (1), e30.
- THOMPSON, KARSTEN E. 2002 Pore-scale modeling of fluid transport in disordered fibrous materials. *AIChE Journal* **48** (7), 1369–1389.
- TOUSSAINT, R, LØVOLL, G, MÉHEUST, Y, MÅLØY, K. J & SCHMITTBUHL, J 2005 Influence of pore-scale disorder on viscous fingering during drainage. *Europhysics Letters (EPL)* **71** (4), 583–589.
- TROJER, MATHIAS, SZULCZEWSKI, MICHAEL L. & JUANES, RUBEN 2015 Stabilizing Fluid-Fluid Displacements in Porous Media Through Wettability Alteration. *Physical Review Applied* **3** (5), 054008.
- TRYGGVASON, GRETAR & AREF, HASSAN 1983 Numerical experiments on Hele Shaw flow with a sharp interface. *Journal of Fluid Mechanics* **136**, 1–30.
- TZIMAS, G. C., MATSUURA, T., AVRAAM, D. G., VAN DER BRUGGHEN, W., CONSTANTINIDES, G. N. & PAYATAKES, A. C. 1997 The combined effect of the viscosity ratio and the wettability during forced imbibition through nonplanar porous media. *Journal of Colloid and Interface Science* **189** (1), 27–36.
- VALVATNE, PER H. & BLUNT, MARTIN J. 2004 Predictive pore-scale modeling of two-phase flow in mixed wet media. *Water Resources Research* **40** (7), W07406.
- VAN MEURS, P. 1957 The Use of Transparent Three-Dimensional Models for Studying the Mechanism of Flow Processes in Oil Reservoirs. *Transactions of the AIME* **210** (01), 295–301.
- VARAGNOLO, S., FERRARO, D., FANTINEL, P., PIERNO, M., MISTURA, G., AMATI, G., BIFERALE, L. & SBRAGAGLIA, M. 2013 Stick-slip sliding of water drops on chemically heterogeneous surfaces. *Physical Review Letters* **111** (6), 066101.
- VASILIEV, L. L. 2008 Micro and miniature heat pipes - Electronic component coolers. *Applied Thermal Engineering* **28** (4), 266–273.
- VIZIKA, O., AVRAAM, D. G. & PAYATAKES, A. C. 1994 On the role of the viscosity ratio during low-capillary-number forced imbibition in porous media. *Journal of Colloid And Interface Science* **165** (2), 386–401.
- VOINOV, O. V. 1977 Hydrodynamics of wetting. *Fluid Dynamics* **11** (5), 714–721.
- WALLS, PETER L. L., DEQUIDT, GRÉGOIRE & BIRD, JAMES C. 2016 Capillary Displacement of Viscous Liquids. *Langmuir* **32** (13), 3186–3190.
- WASHBURN, EDWARD W. 1921 The Dynamics of Capillary Flow. *Physical Review* **17** (3), 273–283.
- WILKINSON, DAVID 1984 Percolation model of immiscible displacement in the presence of buoyancy forces. *Physical Review A* **30** (1), 520.
- WILKINSON, D. & WILLEMSSEN, J. F. 1983 Invasion percolation: a new form of percolation theory. *Journal of Physics A: Mathematical and General* **16** (14), 3365–3376.

- WITTEN, T. A., SANDER, L. M. & SANDER, I. M. 1981 Diffusion-Limited Aggregation, a Kinetic Critical Phenomenon. *Physical Review Letters* **47** (19), 1400–1403.
- YANG, XIAOSONG, DU, SHUMING & MA, JIN 2004 Do earthquakes exhibit self-organized criticality? *Physical Review Letters* **92** (22), 228501.
- YETISEN, ALI KEMAL, AKRAM, MUHAMMAD SAFWAN & LOWE, CHRISTOPHER R. 2013 Paper-based microfluidic point-of-care diagnostic devices. *Lab on a Chip* **13** (12), 2210.
- YORTSOS, Y. C., XU, B. & SALIN, D. 1997 Phase Diagram of Fully Developed Drainage in Porous Media. *Physical Review Letters* **79** (23), 4581.
- YU, TONY S., BULOVIĆ, VLADIMIR & HOSOI, A. E. 2013 Coarsening and solidification via solvent-annealing in thin liquid films. *Journal of Fluid Mechanics* **723**, 69–90.
- ZENG, WEN, JACOBI, IAN, BECK, DAVID J., LI, SONGJING & STONE, HOWARD A. 2015 Characterization of syringe-pump-driven induced pressure fluctuations in elastic microchannels. *Lab on a Chip* **15** (4), 1110–1115.
- ZHAO, BENZHONG, A. PAHLAVAN, AMIR, CUETO-FELGUEROSO, LUIS & JUANES, RUBEN 2018 Forced Wetting Transition and Bubble Pinch-Off in a Capillary Tube. *Physical Review Letters* **120** (8), 084501.
- ZHAO, BENZHONG, MACMINN, CHRISTOPHER W. & JUANES, RUBEN 2016 Wettability control on multiphase flow in patterned microfluidics. *Proceedings of the National Academy of Sciences* **113** (37), 10251–10256.
- ZHAO, BENZHONG, MACMINN, CHRISTOPHER W, PRIMKULOV, BAUYRZHAN K, CHEN, YU, VALOCCHI, ALBERT J, ZHAO, JIANLIN, KANG, QINJUN, BRUNING, KELSEY, MCCLURE, JAMES E, MILLER, CASS T, FAKHARI, ABBAS, BOLSTER, DIOGO, HILLER, THOMAS, BRINKMANN, MARTIN, CUETO-FELGUEROSO, LUIS, COGSWELL, DANIEL A, VERMA, RAHUL, PRODANOVIĆ, MAŠA, MAES, JULIEN, GEIGER, SEBASTIAN, VASSVIK, MORTEN, HANSEN, ALEX, SEGRE, ENRICO, HOLTZMAN, RAN, YANG, ZHIBING, YUAN, CHAO, CHAREYRE, BRUNO & JUANES, RUBEN 2019 Comprehensive comparison of pore-scale models for multiphase flow in porous media. *Proceedings of the National Academy of Sciences of the United States of America* **116** (28), 13799–13806.
- ZIMMERMANN, MARTIN, SCHMID, HEINZ, HUNZIKER, PATRICK & DELAMARCHE, EMMANUEL 2007 Capillary pumps for autonomous capillary systems. *Lab on a Chip* **7** (1), 119–125.
- ZUO, BIAO, ZHENG, FAN FAN, ZHAO, YU RONG, CHEN, TIANYU, YAN, ZHUO HUA, NI, HUANGANG & WANG, XINPING 2012 Stick–Slip Phenomenon in Measurements of Dynamic Contact Angles and Surface Viscoelasticity of Poly(styrene-*b*-isoprene-*b*-styrene) Triblock Copolymers. *Langmuir* **28** (9), 4283–4292.